The Multidisciplinary Design Optimization of a Distributed Propulsion Blended-Wing-Body Aircraft

By

Yan-Yee Andy Ko

A dissertation submitted to the Faculty of the

Virginia Polytechnic Institute and State University

In partial fulfillment of the requirements for the degree of

Doctor of Philosophy

In

Aerospace Engineering

W.H. Mason, Chair

B. Grossman

J.A. Schetz

R. T. Haftka

R. K. Kapania

April 14, 2003

Blacksburg, Virginia

Keywords: Multidisciplinary Design Optimization, Aircraft Design,

Blended-Wing-Body, Distributed Propulsion, Jet Wing, Jet Flap

The Multidisciplinary Design Optimization of a Distributed Propulsion Blended-Wing-Body Aircraft

Yan-Yee Andy Ko

(ABSTRACT)

The purpose of this study is to examine the multidisciplinary design optimization (MDO) of a distributed propulsion blended-wing-body (BWB) aircraft. The BWB is a hybrid shape resembling a flying wing, placing the payload in the inboard sections of the wing. The distributed propulsion concept involves replacing a small number of large engines with many smaller engines. The distributed propulsion concept considered here ducts part of the engine exhaust to exit out along the trailing edge of the wing.

The distributed propulsion concept affects almost every aspect of the BWB design. Methods to model these effects and integrate them into an MDO framework were developed. The most important effect modeled is the impact on the propulsive efficiency. There has been conjecture that there will be an increase in propulsive efficiency when there is blowing out of the trailing edge of a wing. A mathematical formulation was derived to explain this. The formulation showed that the jet 'fills in' the wake behind the body, improving the overall aerodynamic/propulsion system, resulting in an increased propulsive efficiency.

The distributed propulsion concept also replaces the conventional elevons with a vectored thrust system for longitudinal control. An extension of Spence's Jet Flap theory was developed to estimate the effects of this vectored thrust system on the aircraft longitudinal control. It was found to provide a reasonable estimate of the control capability of the aircraft.

An MDO framework was developed, integrating all the distributed propulsion effects modeled. Using a gradient based optimization algorithm, the distributed propulsion BWB aircraft was optimized and compared with a similarly optimized conventional BWB design. Both designs are for an 800 passenger, 0.85 cruise Mach number and 7000 nmi mission. The MDO results found that the distributed propulsion

BWB aircraft has a 4% takeoff gross weight and a 2% fuel weight. Both designs have similar planform shapes, although the planform area of the distributed propulsion BWB design is 10% smaller. Through parametric studies, it was also found that the aircraft was most sensitive to the amount of savings in propulsive efficiency and the weight of the ducts used to divert the engine exhaust.

Acknowledgements

First and foremost, I would like to thank my Lord and Savior, Jesus Christ, without whom life would not be worth living. I owe everything I have, known and do to Him. The more I consider the science around me, and try to understand it, the more I am struck in amazement by the complexity and efficiency of His creation.

Next, I would like to acknowledge the love of my life, my wife, Teresa Edwards Ko. God has blessed me beyond measure by providing her to me. Her firm belief in me, encouragement and unwavering support has fueled me to complete this work, even when at times I had doubted myself. This work would not have been completed in this amount of time without her. She is truly my encourager, counselor and helper. I love her with all my life.

I have worked with my advisor, Dr. William Mason for almost five years to date, working on both this work and on various other different projects. My current knowledge in aerospace engineering will not be as complete as it is without his patience, insight and instruction. His attention to detail and constant search for excellence has many times prompted me to stop and think, and saved me from embarrassment. I also treasure him as a friend, and I will certainly miss working with him.

The members of the Virginia Tech Blended-Wing-Body research team, especially the faculty, have contributed much to the success of this work. I would like to thank Dr. Schetz, who never misses the forest for the trees. I truly appreciate his ideas and insight, and our numerous discussions concerning distributed propulsion has in a large part resulted in this work. I would also like to thank Dr. Raphael Haftka, from the University of Florida for participation in this work. He has an exceptional ability to visualize, understand and scrutinize every detail of our work, even in fields not familiar with. His brilliant intuition and vast experience has many times brought me out 'show stopper' problems and steered the direction of this work in the right and wise direction. Finally, I would like to thank Dr. Bernard Grossman for his thoughtful advice and support for this work. Through the amazing advances in telecommunications, I am glad that I can tap his advice and experience even when he is physically not here at Virginia Tech. I will also sorely miss his wit and humor.

I would also like to acknowledge the student members of the Virginia Tech Blended-Wing-Body research team, especially Serhat Hosder and Vance Dippold. Their friendship, suggestions, and research have propelled this work to where it is now today. I will miss the many hours spent in discussion, solving major hurdles in this research.

I would like to thank Dr. Rakesh Kapania for being on my doctoral committee, and supporting me in this work. His willingness to help me in every aspect is greatly appreciated.

It would not be fair if I did not acknowledge the people at NASA Langley for their support. Without their financial support, this work would not be possible. Their help with information, insight and material has helped a great deal in making this work a success. I would like to specifically acknowledge William M. Kimmel and Mark Guynn at NASA Langley for their support and help in this work

The support from Phoenix Integration for this work is invaluable. I am especially grateful to them for allowing me to use their ModelCenter® and Analysis Server® software for free. I am confident that their excellent support and customer driven philosophy will continue to be the backbone of their success. I would specifically acknowledge Dr. Hongman Kim and Dr. Brett Malone for their support of this work.

I would like to thank my family for their encouragement and support. I am grateful to my parents for encouraging me to pursue my dreams and ambitions even if it meant to be separated on the other side of the world. I will never take their love for me for granted. I thank my sister, Sharon, for being an excellent role model and a friend. Her success in all she does is a blueprint for me to follow.

Finally, I would like to thank my friends: The Dodsons and everyone at housegroup – their prayers and support has kept me going all these years; Mark McCann for keeping accountable and being an ever helping friend; John Garner and Josh Sessler

for serving with me in leading Boy’s Brigade; and finally, the boy’s in Battalion in Boy’s Brigade, working and know all of you has been an honor.

Contents

List of Figures

List of Tables

Nomenclature

a	Speed of sound at altitude
a_1	Speed of sound at initial cruise altitude
a_{mn}	Coefficients to solve for jet flap theory Fourier coefficients
A	Equation simplification factor
A_n	Jet flap theory Fourier coefficients
AR	Aspect ratio
AR_{Cabin}	Aspect ratio of the passenger cabin
AR_{Cabin_min}	Minimum passenger cabin aspect ratio
ATM_{Engine}	Engine advanced technology multiplier factor
b	Wing span
b_{cabin}	Span of the passenger cabin
b_{mn}	Coefficients to solve for jet flap theory Fourier coefficients
b_J	Jet height
b_W	Wake height
$b_{winglet}$	Winglet span
B	Equation simplification factor
B_n	Jet flap theory Fourier coefficients
BFL	Balanced field length
c	Chord length
c_1	Chord length of the first span-station
c_2	Chord length of the second span station
c_3	Chord length of the third span station
c_4	Chord length of the fourth span station
c_5	Chord length of the fifth span station

$\bar{c}$	Average chord
c_m	Coefficients to solve for jet flap theory Fourier coefficients
C_{dwave}	Wave drag coefficient
C_{Di}	Induced drag coefficient
$C_{Di_{Distributed\ Propulsion}}$	Distributed propulsion induced drag coefficient
$C_{D_{Profile}}$	Profile drag coefficient
$C_{D_{Wave}}$	Wave drag coefficient
$C_{D_{Total}}$	Total drag coefficient
C_J	Jet coefficient
$C_{\bar{J}}$	Jet momentum flux coefficient
C_l	Two-dimensional lift coefficient
C_L	Three-dimensional lift coefficient
$C_L^{(2)}$	Two-dimensional lift coefficient predicted by jet flap theory
C_{L_a}	Three-dimensional lift coefficient slope wrt. angle-of-attack
C_{L_0}	Three-dimensional lift coefficient at zero angle of attack
$C_{L_{de}}$	Three-dimensional lift coefficient slope wrt. elevon deflection angle
C_{Lclimb}	Climb three-dimensional lift coefficient
C_{Lmax}	Maximum three-dimensional lift coefficient
C_M	Three-dimensional moment coefficient
C_{M_a}	Three-dimensional moment coefficient slope wrt. angle-of-attack
$C_{M_{de}}$	Three-dimensional moment coefficient slope wrt elevon deflection angle
C_{M_0}	Three-dimensional moment coefficient at zero angle of attack
$C_{M_{Jet\ Flap}}$	Moment coefficient from the jet flap system
Constraint_max	Maximum constraint value
Constraint_min	Minimum constraint value
Constraint_value	Constraint value

C_{Tip}	Tip chord length
$C_{winglet}$	Winglet chord length
CG_{fuel}	Fuel weight center of gravity
d_m	Coefficients to solve for jet flap theory Fourier coefficients
d_{nac}	Nacelle diameter
D_i	Induced drag
e_m	Coefficients to solve for jet flap theory Fourier coefficients
f	ratio of the engine jet velocity to the freestream velocity
$\boldsymbol{F}$	Force vector
F_{wing}	Wing weight technology factor
F_{ldg}	Landing gear weight technology factor
F_x	Force in the freestream direction
g	Acceleration due to gravity
G	g_{climb} - g_{min}
h	Altitude
h_{cruise}	Cruise altitude
$h_{obstacle}$	Obstacle height
i	Fuel weight CG calculation tank index
I	Total number of tanks for fuel weight CG calculation
I_n	Jet flap theory coefficients
I_W	Wing weight geometric factor
l_{nac}	Nacelle length
J	Jet thrust
$\bar{J}$	Jet momentum flux
DKE	rate of kinetic energy added to the flow
L	Lift force
L'	Lift per unit span
L_R	Lapse rate
L/D	Lift to drag ratio
$\dot{m}_a$	Airflow rate
M	Mach number

$M_{2D@LE}(h)$	Two-dimensional moment about the leading edge
$M_{2D@X=0}(h)$	Two-dimensional moment about X=0 position
$M_{3D@X=0}(h)$	Three-dimensional moment about X=0 position
M_{crit}	Critical Mach number
M_{dd}	Drag divergence Mach number
n	Ultimate load factor
N_{pass}	Number of passengers
p	Local pressure
p_{∞}	Freestream pressure
q	Dynamic pressure
$\boldsymbol{q}$	Velocity vector perturbation from the freestream comprising of components u, v, w
R	Gas constant
$Range$	Calculated aircraft range
$Ratio_{Jet}$	Ratio of jet thrust to total thrust
ROC	Top of climb rate of climb
sfc	Thrust specific fuel consumption
sfc_1	Uncorrected thrust specific fuel consumption
sfc_2	Corrected thrust specific fuel consumption
sfc_{cruise}	Cruise thrust specific fuel consumption
$sfc_{cruise,SL}$	Cruise thrust specific fuel consumption at sea level
sfc_{new}	Thrust specific fuel consumption adjusted for distributed propulsion
sfc_{old}	Thrust specific fuel consumption not adjusted for distributed propulsion
S_{cabin}	Passenger cabin planform area
S_{CS}	Planform area of the control surfaces
S_{ref}	Wing planform reference area
S_{strip}	Strip reference area
$S_{wet,nac}$	Nacelle wetted area
t	Airfoil section thickness

t/c	Thickness to chord ratio
t/c_1	Thickness to chord ratio of the first span-station
t/c_2	Thickness to chord ratio of the second span-station
t/c_3	Thickness to chord ratio of the third span-station
t/c_4	Thickness to chord ratio of the fourth span-station
t/c_5	Thickness to chord ratio of the fifth span station
T	Total aircraft thrust
T_0	Engine thrust per engine
T_{bleed}	Engine bleed thrust
T_{excess}	Engine thrust minus the engine bleed thrust
T_{jet}	Jet thrust
T_{total}	Total thrust
T_{useful}	Thrust from the engine after accounting for losses in the ducts
T/W	Thrust to weight ratio
$Temp$	Temperature at altitude
$Temp_{36089}$	Temperature at Tropopause (36089 ft)
$Temp_{cruise}$	Cruise altitude temperature
$Temp_{SL}$	Temperature at sea level
$\tilde{u}$	Velocity perturbation from U_{∞}
u	Velocity perturbation in the x direction
U	Correction factor for flaps in the balanced field length calculation
U_{∞}	Freestream velocity
U_J	Jet velocity
U_W	Wake velocity
v	y component of the velocity
V	Aircraft speed
V_1	Cruise velocity at initial altitude
V_{stall}	Aircraft stall speed
V_{min}	Minimum velocity at approach
w	z component of the velocity
$\dot{w}_f$	Weight fuel flow rate

$w_{i¥}$	induced downwash velocity
W_1	Aircraft weight at initial cruise
W_{ai}	Anti-icing weight
W_{cabin}	Passenger cabin weight
$W_{controls}$	Controls weight
W_{eng}	Engine weight
$W_{engines}$	Propulsion weight (includes nacelle and pylon weight)
W_{final}	Weight of aircraft at the end of the calculated mission range
W_{fuel}	Fuel weight
$W_{fuel\ remaining}$	Remaining fuel weight in the tanks
$W_{fuel\ total}$	Total fuel weight
$W_{fuel}(i)$	Fuel weight in the i^{th} fuel tank
W_{fixed}	Fixed weights
$W_{initial}$	Weight of aircraft at start of the calculated mission range
W_{lg}	Landing gear weight
W_{nac}	Nacelle weight
W_{other}	Sum of weights unaffected by wing weight formulation
$W_{payload}$	Payload weight
W_{pyl}	Pylon weight
W_{wing}	Wing weight
x_{CP}	Position of the center of pressure
x_{CG}	Aircraft center of gravity x-coordinate
x_{gap}	Distance between the leading edge position at the root and X=0.
x_{LE}	Distance between the leading edge position at the root and the local leading edge position
$X_{CG}(i)$	X-coordinate center of gravity location of the i^{th} fuel tank

Greek Symbols

a	Angle of attack
a_{3D}	Three dimensional angle of attack for jet flap theory

$a_{i\infty}$	induced angle of attack due to the jet flap
d_e	Elevon deflection angle
DKE	rate of kinetic energy added to the flow
f	90° - winglet dihedral angle
f_m	Fourier coefficient pivotal points for jet flap theory
$G(y)$	Circulation distribution in the Trefftz plane
g	Ratio of specific heats
g_{climb}	Second segment climb gradient
g_{min}	Minimum second segment climb gradient
h	Semi-spanwise position
h_2	Position of the second span-station
h_3	Position of the third span-station
h_4	Position of the fourth span-station
h_{duct}	Duct efficiency
h_P	Froude propulsive efficiency
h_{P1}	Uncorrected Froude propulsive efficiency
h_{P2}	Corrected Froude propulsive efficiency
V_{dia}	Diameter scaling factor
k_a	Airfoil technology factor
l	Taper ratio
$l*$	Jet flap theory factor
l_J	$4/C_J$
k	Correction term for flight acceleration
$L_{1/4c}$	Quarter chord sweep angle
L_2	Quarter chord sweep angle
L_3	Quarter chord sweep angle
L_4	Quarter chord sweep angle
L_{LE}	Leading edge sweep angle
L_{TE1}	Quarter chord sweep angle

$L_{winglet}$	Winglet sweep angle
r	Density at altitude
r_{1}	Density at the initial cruise altitude
r_{36089}	Density at the tropopause (36089 ft)
r_{SL}	Density at sea level
s	Jet flap theory factor
t	Jet flap deflection angle
y	Fraction of savings in propulsive efficiency

Abbreviations

ACSYNT	AirCraft SYNThesis
ADP	Advanced Ducted Propeller
BWB	Blended-Wing-Body
CFD	Computational Fluid Dynamics
CG	Center of Gravity
DOT	Design Optimization Tools
FAR	Federal Aviation Regulations
FLOPS	FLight OPtimization System
LH_2	Liquid hydrogen
MDO	Multidisciplinary design optimization
NASA	National Aeronautics and Space Administration
OEW	Operational Empty Weight
SFC	Specific fuel consumption
STOL	Short takeoff and landing
TOGW	Takeoff gross weight
WZF	Zero fuel weight

Chapter 1: Introduction

Multidisciplinary Design Optimization has been receiving increased interest in the aerospace industry as a valuable tool in aircraft design [1], [2], [3]. The use of MDO in conceptual and preliminary design of innovative aircraft concepts is but one application where it provides the designer with better insight into the coupled nature of different aerospace disciplines related to aircraft design. In a general MDO aircraft design framework, different analysis modules or their surrogates representing the different disciplines, such as structures and aerodynamics, are linked to an optimizer to either minimize or maximize a certain objective function (such as take-off gross weight) subject to specified design constraints. By coupling these disciplines, the optimizer is allowed to take advantage of the synergism of the different disciplines. The key issue in using MDO in aircraft design is the difficulty of implementing high-fidelity, computationally-intensive analysis methods into the early stages of the design process [4]. There are codes such as ACSYNT [5] and FLOPS [6] that attempt to do this by using simplified models of the various disciplines. Mason et al. [7] suggest a response surface method to implement high fidelity computational fluid dynamics (CFD) results into the MDO process.

This dissertation will describe the use of an MDO framework to design a distributed propulsion Blended-Wing-Body (BWB) transport aircraft as well as a discussion on the formulation of the effects of distributed propulsion on the design of the aircraft. Our distributed propulsion concept involves replacing fewer large engines with more smaller engines on the aircraft. These engines will be integrated within the structure of the aircraft, and part of the engine exhaust (usually the cold air exhaust from a high bypass ratio turbofan engine) will be ducted out the trailing edge of the wing. This arrangement has a possible advantage of increasing propulsive efficiency, reducing airframe trailing edge noise and increasing engine redundancy. The BWB is a unique, tailless aircraft that combines the passenger and cargo structure into the aerodynamic inboard wing, resulting in an integral aircraft design. The high level of integration between the wing, fuselage, engines, and control surfaces inherent in the BWB design allows it to take advantage of the synergistic nature between the different aircraft design disciplines resulting in an aircraft with better performance than a conventional design. Figure 1-1 shows a picture of the BWB concept. With the distributed propulsion concept integrated into the BWB aircraft design, MDO will be used to reveal the advantages of this aerodynamics-propulsion integration and highlight its benefits.

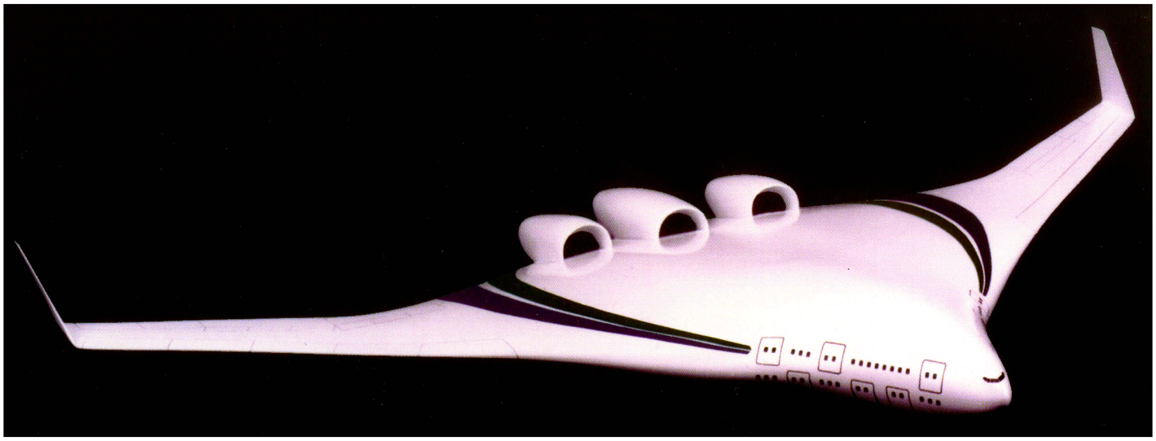

Figure 1-1: The Blended-Wing-Body aircraft

1.1. Statement of the problem

This dissertation describes the integration of the advanced propulsion concept of distributed propulsion into the BWB aircraft. A discussion on the history and previous design work on the BWB aircraft and distributed propulsion is provided in Chapter 2.

The distributed propulsion BWB aircraft will have the propulsion system integrated by using a modest number of engines (about eight engines) buried inside the structure, distributed across the span. High bypass ratio turbofan engines will be assumed to be the engine type of choice in this application. Part of the engine cold air exhaust will be ducted to exit out the trailing edge of the wing. This arrangement is reminiscent of the jet wing concept. The rest of the engine exhaust (the rest of the cold air exhaust and the hot core exhaust) will be ejected through a conventional nozzle. Figure 1-2 shows a drawing of a cross section of the wing illustrating this concept. The configuration also replaces the use of conventional flaps and elevons with a vectored thrust control system along the now blown aircraft trailing edge. An illustration of the planform view of this configuration is shown in Figure 1-3. It should be noted that the jet wing could extend across the entire span (i.e. blowing out of the trailing edge across the entire span) or only across part of the span as shown in Figure 1-3.

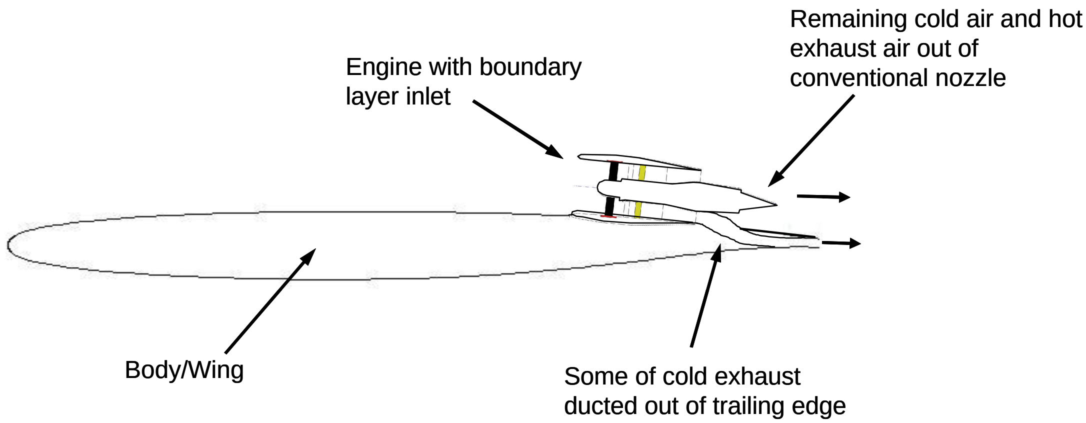

Figure 1-2: Drawing of a cross section of the wing illustrating the distributed propulsion concept.

It should be noted here that NASA makes the distinction between the concepts of distributed propulsion and distributed exhaust [8]. Distributed propulsion refers to replacing a few large engines with more smaller engines. Distributed exhaust refers to the concept of distributing the exhaust across a large area, much like the jet-wing concept [9]. The concept that is proposed here is a hybrid between the two. This dissertation will not make this distinction and we will refer to the proposed concept as a ‘distributed propulsion’ concept.

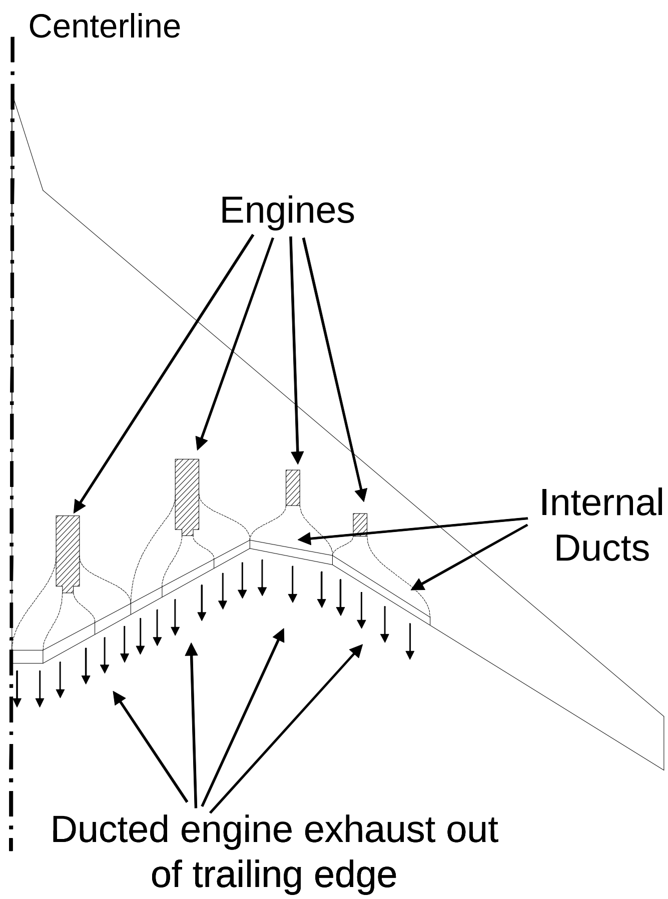

Figure 1-3: Drawing of the planform view of the distributed propulsion BWB configuration illustrating the distributed propulsion concept.

This study will use low to medium fidelity analytical models to estimate the various aerodynamic and propulsion effects of this aerodynamic-propulsion integration. This will include extensions to existing theories and formulations, together with innovative representations of various aircraft systems. Where possible, programs already developed in previous Virginia Tech studies were used within the distributed propulsion BWB MDO software tool. Commercial code integration software was also used to speed up the MDO tool development process.

Once the MDO tool was developed, it was validated by comparing the analytic design of the conventional BWB aircraft with existing BWB designs available in the literature. Then, an optimized distributed propulsion BWB was designed and compared to the optimized conventional BWB design and parametric studies were performed to assess the sensitivities of the design with respect to their critical design parameters. These sensitivities helped us identify critical aspects of the design, and pointed out areas in the concept that need further investigation.

This dissertation is organized as follows:

- Chapter 2 presents the background and a survey of the literature about the BWB aircraft concept, and distributed propulsion configurations
- Chapter 3 provides the concept description of the distributed propulsion blended-wing body aircraft. The optimization problem statement will be presented including a description of the objective function, design variables and constraints. A discussion on the evolution of the optimization setup will be provided, as a documentation of the lessons learned.
- Chapter 4 describes the MDO model that is used for a general BWB aircraft. Here, detailed descriptions of the analytical methods used in the MDO framework are presented.
- Chapter 5 describes the theoretical foundation and analytical models that are used to integrate the distributed propulsion concept with the BWB aircraft design.
- Chapter 6 presents the MDO results. Design comparisons between the optimized conventional BWB design and distributed propulsion BWB design will be made. Results of parametric studies that were done to understand the sensitivities of the distributed propulsion BWB to certain key parameters will also be presented.
- Chapter 7 will provide some concluding remarks about this effort
- Chapter 8 will provide some recommendations for future development in this research field.

Chapter 2: Background and Literature Review

2.1. The Blended-Wing Body Aircraft

The BWB is an innovative aircraft concept that integrates the wing, fuselage, engines and tail to achieve a significant improvement in performance over a conventional transport. It is a hybrid shape that resembles a flying wing, dispensing with the need for a conventional tail and cylindrical fuselage.

The flying wing configuration is not a new concept. In 1912, a pusher propeller tailless biplane was designed by John W. Dunne [10]. Later, other low speed flying wing configurations were built and flown. These include the AW-52 of the German Horten aircraft family and the YB-49 by Northrop. Figures for both these aircraft can be found at http://www.cranfield.ac.uk/coa/tech-avt/avt-4.htm. These programs faced major challenges, and ultimately Northrop's dream of having a flying wing airliner was not realized. However, with current and emerging technologies, such as the digital flight control system, these major challenges can be solved, making the flying wing concept a feasible. One example of a successful flying wing design today is that of the B-2 Stealth Bomber.

2.1.1. Recent and current design studies on the BWB concept

The most extensive study on using the BWB as a feasible alternative to the conventional cantilever wing transport aircraft was done in the United States by the McDonnell Douglas Company (now Boeing) and NASA. This started in 1988, when

Dennis Bushnell from NASA Langley challenged academia and industry to consider innovative concepts in aircraft designs for long-haul transport. In response to this challenge, an initial design study done by Callaghan and Liebeck in 1990 [11] showed that a BWB configuration with an 800 passenger capacity, cruising at Mach 0.85 and a 7000 nmi range, offered a 40% increase in lift to drag ratio (*L/D*) and a 25% reduction in fuel burn when compared to an advanced technology conventional transport.

A subsequent investigation by Liebeck et al. [12] showed that a BWB configuration sized for 800 passengers and a range of 7000 nautical miles achieved a reduction of 16% in takeoff gross weight and a 35% reduction in required fuel weight when compared to a similarly designed conventional aircraft. This significant improvement in performance was possible for several reasons. Due to the absence of a fuselage, the BWB configuration has low interference drag resulting in a higher *L/D* ratio. The thick airfoil sections and favorable span loading of the aircraft allow for more efficient structures, resulting in a lighter wing weight. A substantial improvement in aerodynamic efficiency is attainable due to a reduction in wetted area compared to a conventional cylindrical fuselage/wing design.

The early design studies [12] also considered using engines with boundary layer ingesting inlets to improve the over-all propulsive efficiency of the airplane. The designs in these studies also place the passenger cabin and cargo area within the inboard aircraft wing sections. Fuel was stored in the outboard wing sections. The studies indicated that the BWB configuration integration was exceptionally challenging due to the high level of coupling between different disciplines. The report concluded that MDO would be unavoidable in the further development of the BWB configuration. It concluded further that emergency egress issues were also a key challenge.

In these studies, it was clear that the non-circular pressurized cabin structure would pose a major technical challenge. In a BWB configuration, the square-cube law results in a low cabin surface area to volume ratio. This poses a challenge, as it reduces the available surface area for passenger emergency egress. Also, the non-cylindrical shape of the passenger cabin poses a challenge when designing for pressurization. The early configuration in 1990 [11] used a design with four parallel cylindrical tubes as the passenger cabin, similar to the double bubble concept (Figure 2-1). The multiple cylinder cabin concept was later abandoned [12], and a cabin pressure vessel structure was adopted. The cabin was designed with a combination single and double deck design, with the double deck inboard and the single deck outboard as the fuselage blends into the wing. Two structural concepts were considered. The first concept used a thin, arched pressure vessel above and below each cabin, also known as the multi-bubble concept. The pressure vessel skin takes the load in tension and is independent of the wing skin. For the second concept, the pressure vessel and wing skin are integrated via a thick sandwich structure. Figure 2-2 illustrates these two cabin structural concepts. As a first step in the detailed design of the cabin pressure vessel, Vitali et al. [13] optimized a laminated composite panel for the integrated cabin/wing skin structure. Mukhopadhyay et al. [14] performed an analysis, design and optimization of the pressurized cabin, comparing the two different concepts. It was found that the multi-bubble concept balanced the internal cabin pressure load efficiently, through the membrane stress in the cylindrical segment shells and inter-cabin walls. In addition to this, the outer shell provided an additional redundancy by being able to withstand operational cabin pressure during a cabin pressure leak. They concluded that the proper design of the multi-bubble concept design could reduce the overall weight by as much as 20-30% compared to the integrated design, making the multi-bubble design the concept of choice.

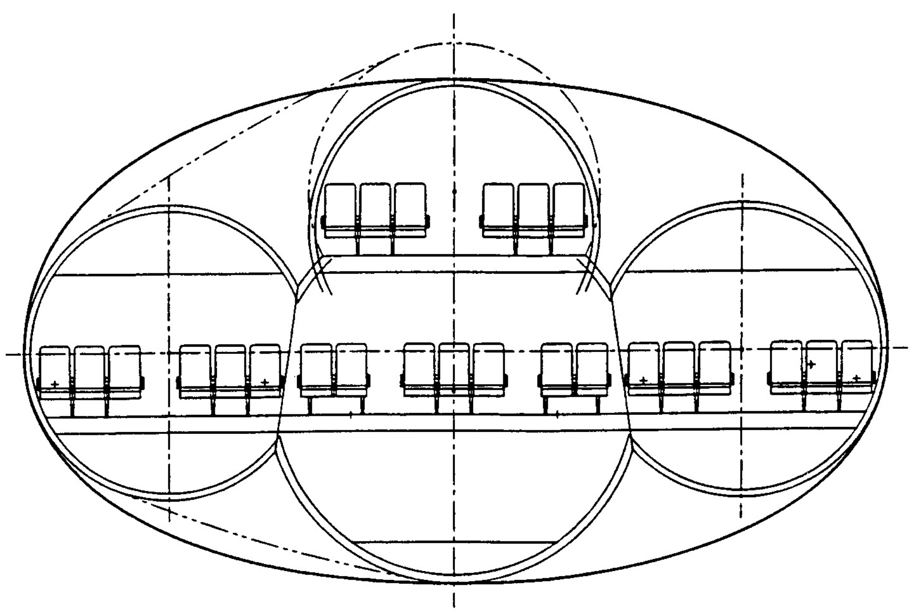

Figure 2-1: Fuselage cross section of initial BWB concept [11].

To take advantage of the high level of synergism, Boeing pursued the BWB program using MDO with their Wing Multidisciplinary Optimization Design code (WingMOD) [15]. This code was originally developed at Stanford University for conventional wing and tail design [16], but was modified to be used for the BWB. In WingMOD, the design is controlled with design variables that include wing span, chords, thicknesses, and twist at several control stations. Other non-geometric design variables such as skin thicknesses, fuel distribution, spar location and control surface deflections were also used. Constraints on range, trim, balance, stability and control power were enforced [15]. To allow for a faster cycle time, low fidelity analysis such as a vortex lattice method was used to estimate aerodynamic loads. Empirical data were used to estimate profile and wave drag within the WingMOD optimization. Higher fidelity methods such as finite element analysis and Navier-Stokes CFD codes were used in conjunction to the optimization and provided a means of correcting the lower fidelity analysis [17]. Results that were presented [18] showed a 15% reduction in TOGW and a 28% reduction in fuel burned. References [14] to [25] provide details on the BWB design work done at Boeing.

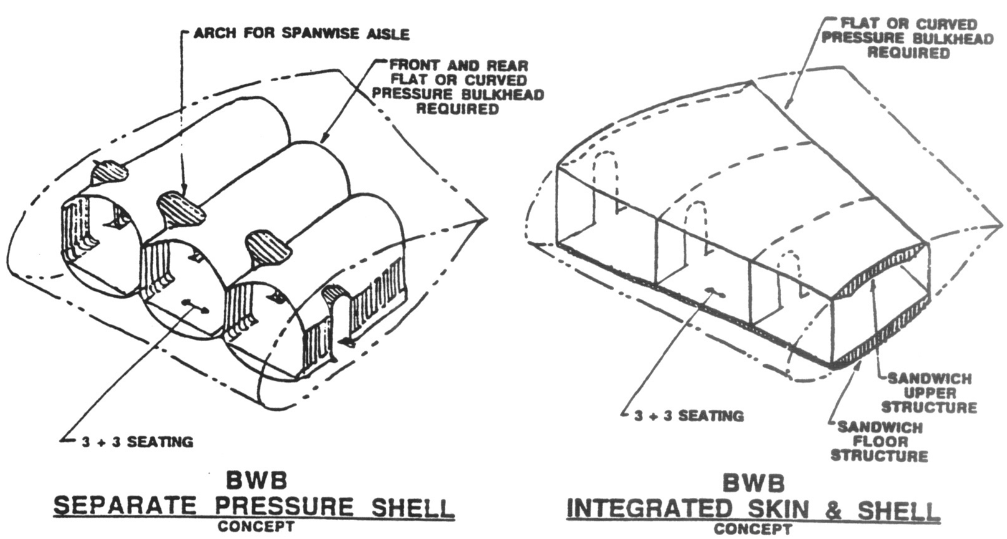

Figure 2-2: BWB cabin structural concept [12].

In conjunction with the MDO design work, transonic and low-speed wing tunnel tests on the BWB configuration were done at the NASA LaRC National Transonic Facility. These tests were performed to validate the CFD results performed throughout the design phase. The wind tunnel tests showed excellent agreement for lift, drag, and pitching moment as well as wing pressure distribution [18]. The low speed test verified trimmed C_{Lmax} estimates and showed favorable stall characteristics for the configuration.

To address concerns about the performance of the boundary layer ingesting engine inlets at the rear of the aircraft, CFD was used to perform a multidisciplinary design of the engine inlet. It was theorized that the low-momentum flow would improve propulsive efficiency, but it was noted that poor inlet performance could offset or negate the potential advantage. Two-dimensional [26] and three-dimensional multidisciplinary inlet design studies [27] were carried out at Stanford University to address that concern. The study showed that the inlet could be tailored to improve the inlet performance while maintaining the improved propulsive efficiency. Details on the CFD aerodynamic design of these boundary layer ingesting inlets can be found in References [26] to [30]. Experimental work done at the University of Southern California also provided significant data on boundary layer ingesting inlets (References [31] to [33])

Another notable effort on the BWB configuration is the MOB (Multi-Disciplinary Design and Optimization for Blended Wing Body configurations) project funded by the European Union. The MOB project is a multi-national and multi-company consortium in Europe comprised of three aerospace companies, four research institutes and eight universities. Its purpose is to create methods and tools to allow distributed design teams to design innovative new aircraft with the potential of entering the aerospace market. As a demonstration case, the MOB project selected the BWB configuration to study. Of particular interest is the preliminary BWB design done by Cranfield University [10]. Details of the MOB project can be found in References [34] to [39]. While no comparison of results were provided in the publications from the MOB project were given, the preliminary study by Cranfield University found that the BWB aircraft had a savings of 10-19% in terms of direct operating cost per seat mile when compared to the Boeing 747-400 aircraft.

Other work done on the BWB configuration includes research by TsAGI [40], [41] in Russia. It was found that the most critical design issue was meeting the FAR requirements for emergency egress. However, a feasible design was created, which had a cruise high lift to drag ratio (*L/D*) of 25 at a Mach number of 0.85. Tohoku University [42] in Japan performed an aerodynamic design of a BWB aircraft using an inverse design method where target pressure distributions are specified.

2.2. Distributed Propulsion and Jet Wings

The idea of distributed propulsion for aircraft was originally conceived with the objective of reducing airframe noise [43]. Distributing the propulsion system using a number of small engines instead of a few large ones reduces the total propulsion system noise [8]. This is partly because smaller engines produce a higher frequency range noise, which can be easily absorbed by materials and dissipates faster. It was also suggested that a distributed propulsion concept could be employed as a seamless high-lift system, dispensing with conventional high-lift systems that are major sources of airframe noise.

There are several other potential benefits of distributed propulsion. One advantage is its improved safety due to engine redundancy. With numerous engines, an engine out condition is not as critical to the aircraft's performance in terms of loss of available thrust and controllability. The load redistribution provided by the engines has the potential to alleviate gust load/flutter problems, while providing passive load alleviation resulting in a lower wing weight. There is also the possible improvement in affordability due to the use of small, easily-interchangeable engines.

There are potential aerodynamic benefits of distributed propulsion when there is a synergistic integration between the propulsion system and aircraft airframe. The idea of an integrated propulsion/lift system is already evident in nature, where animals in flight generate lift and thrust using the same organs. Kuchemann[1] [9], suggested a 'jet wing' configuration to improve propulsive efficiency. A jet wing configuration combines the propulsion system by burying the engine in the wing and exhausting the engine flow out

[1] The original reference to Kuchemann introducing the jet wing concept has been cited to be in: "On the Possibility of Connecting the Production of Lift with that of Propulsion," *M.A.P. Volkenrode, Reports and Translations* No. 941 – 1 Nov., 1947, APPENDIX I, Kuchemann, D., "The Jet Wing,". However, we were unable to obtain a copy of this reference.

of the trailing edge as shown in Figure 2-3. Kuchemann [44] describes a version of the jet wing where air enters an intake at the leading edge of the wing and is ducted to a device that can add energy to the flow. This device, integrated inside the wing, could be a turbofan engine, where the bypass ducts are non-annular, but divided into two cold air ducts on either side of the engine core. He suggests that this jet wing arrangement may be more efficient than a conventional engine arrangement where the engine nacelles are installed somewhere away from the wings and body. To reduce duct losses, and maintain low duct and jet velocities, a large number of lightly-loaded fans would be needed within the bypass ducts.

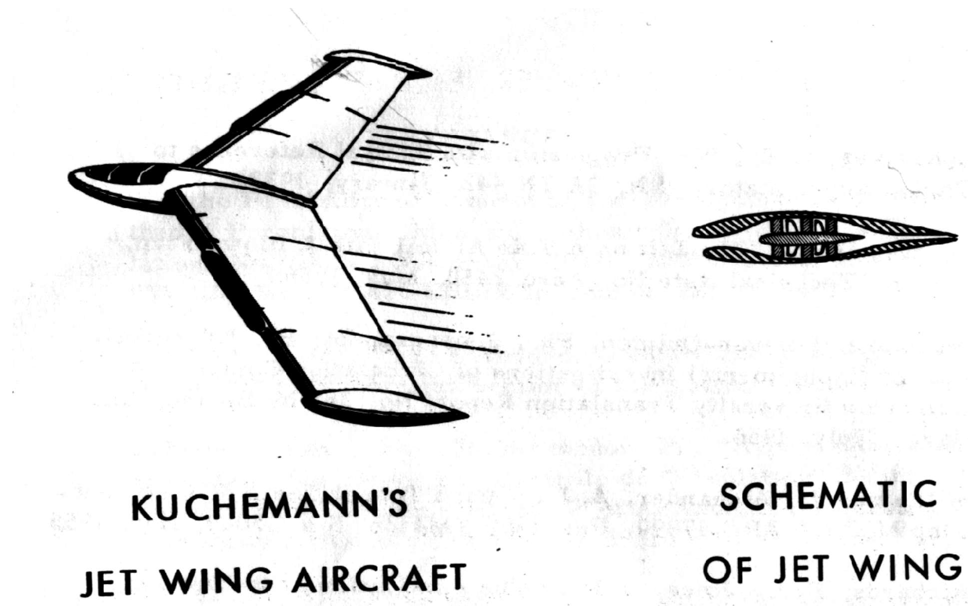

Figure 2-3: Kuchemann's Jet Wing Aircraft concept [9].

The jet wing concept can be describes as an arrangement on a wing where a thin sheet of air from the engine is ejected out of a slot near or at the trailing edge. This utilizes the available power of the engine for thrust and lift augmentation. This is similar in overall concept to the jet flap. The jet flap is an arrangement that ejects a thin sheet of high velocity air with a downward inclination out of a slot near or at the trailing edge to obtain high lift. Its application is associated with the generation of powered or high lift capabilities. While both concepts are similar in the sense that air from the engine is ejected out of the trailing edge (near it) of the wing, their differences lie in their application. The jet flap concept involves a large downward deflection of the jet sheet at an angle with respect to the free stream, usually in the context of STOL (Short takeoff and landing) aircraft configurations. The jet wing concept does not usually employ a deflection in the angle of the jet sheet. One could use both the term ‘jet wing’ and ‘jet flap’ in referring to the distributed propulsion concept that is considered here. It is not uncommon that both terms are used interchangeably. For example, Davidson [45] uses the term ‘jet flap’ while Attinello refers to Davidson’s jet flap as a true ‘jet wing’ [9].

The concept of jet wings and jet flaps is well documented [46],[47]. Experimental aircraft such as the Ball-Bartoe JW-1 JetWing STOL Research aircraft [48], and the Hunting HS 126 research aircraft [49], [50] have shown the advantages of this configuration at low-speed, high lift conditions. At transonic speeds, two-dimensional numerical results show that there is an increase in the suction peak near the leading edge, resulting in higher obtainable lift [51],[52]. Three-dimensional numerical calculations also show that there is significant lift augmentation due to blowing of the jet [53],[54]. Experimental results by Yoshihara provide additional details on the interference effects on the performance of a jet wing [55]. He shows that fuselage interference effects reduce the potential benefits of jet wings. While this result is not encouraging for conventional aircraft designs, it shows that the BWB concept is a good application for this technology.

Chapter 3: Distributed Propulsion BWB Concept Description

The purpose of this work is to provide a low to medium fidelity BWB MDO design tool for the investigation of advanced propulsion concepts. This chapter will provide a description of the distributed propulsion BWB aircraft. The optimization problem statement will also be presented including a listing of all the design variables and constraints. A detailed description of the analysis methods that are used in the distributed propulsion MDO program can be found in Chapters 4 and 5.

3.1. Geometry Description

The BWB planform is described by defining a parametric model with a relatively small number of design parameters. The geometric properties at five span stations along the half-span of the aircraft are used. Figure 3-1 shows the location of those span stations. The chord length (*c*), thickness to chord ratio (*t/c*) and quarter-chord sweep ($L_{¼c}$) are the geometric properties that are used as design variables at those span stations. The positions of the defining span-stations (except for the root and tip stations) as functions of the half-span of the aircraft are also used as design variables. The geometric properties of the aircraft in between the span-stations (resulting in four wing sections) are determined using a straight line wrap method. The location of the aircraft systems, passenger cabin and aircraft fuel tanks are all described using the span stations and the wing sections they define. In addition to the span stations, the aircraft span is also used to describe the BWB planform.

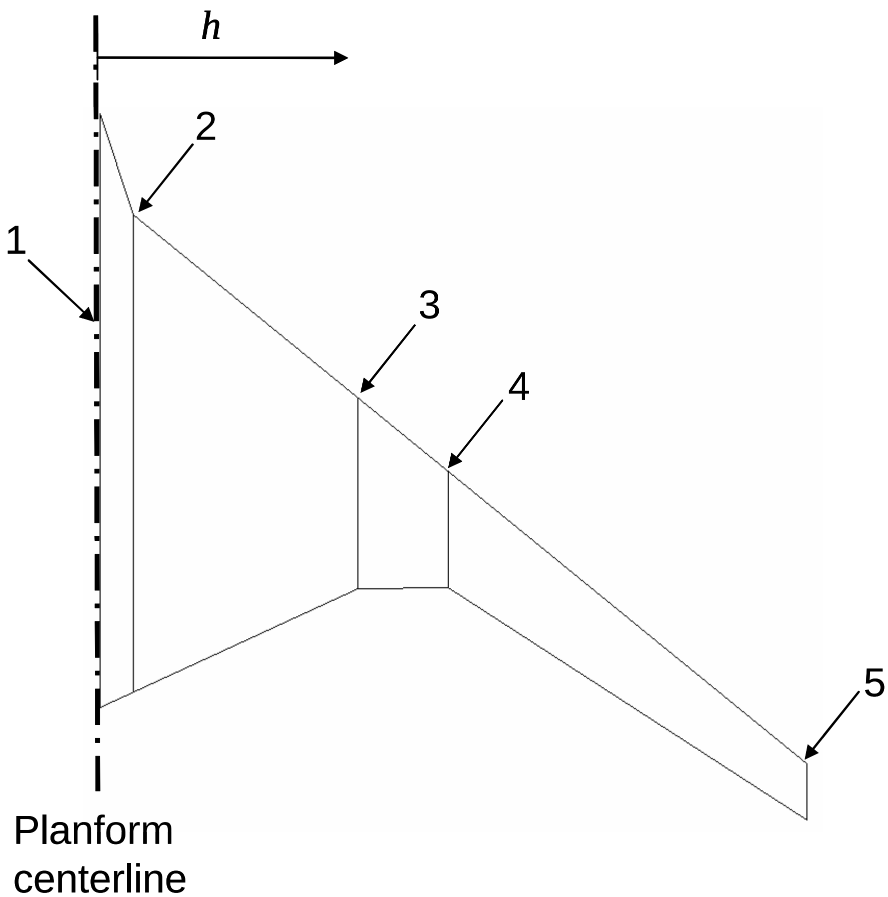

Figure 3-1: The BWB planform showing the five span stations. They are defined as a function of the half-span from the root section (h). Numbers show the span-station number.

3.1.1. Passenger cabin

It is assumed that the passenger cabin is placed at the center inboard section of the BWB. Its location is defined to be in the wing sections inboard of the third span-station (first two wing sections). The passenger cabin occupies the forward 60% of the chord in these sections. The remaining rear 40% of the chord is defined as the afterbody section that houses the aircraft systems, and emergency exit tunnels. Figure 3-2 shows the position of both the passenger cabin and the afterbody section schematically.

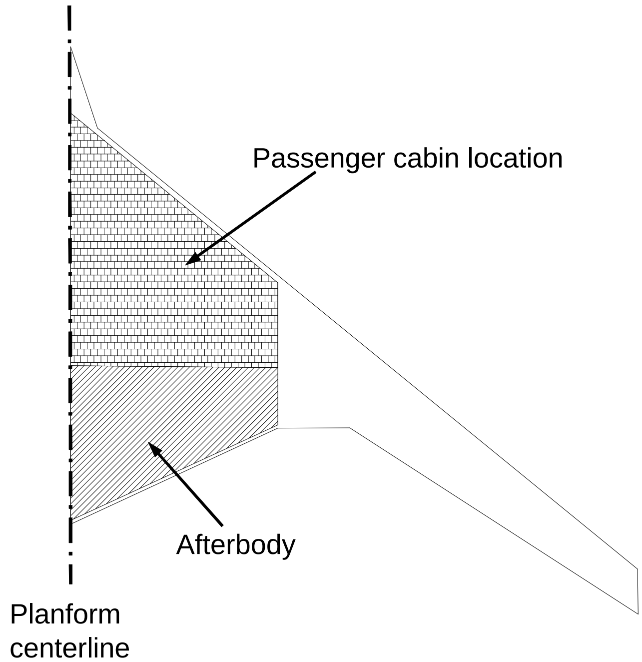

Figure 3-2: Planform schematic of the BWB showing the position of the passenger cabin and afterbody section.

To ensure that there is enough cabin space for the number of passengers carried on the BWB, an average of 10 ft^2 of cabin floor area per passenger is assigned [12]. It is also assumed that a portion of the passenger cabin comprises a double deck configuration. The double deck section is defined to be located inboard of the second span-station (the first wing section). Figure 3-3 gives a schematic of this arrangement. By enforcing a minimum thickness constraint at the first three span stations, we ensure that there is enough height in the passenger cabin to accommodate the passengers.

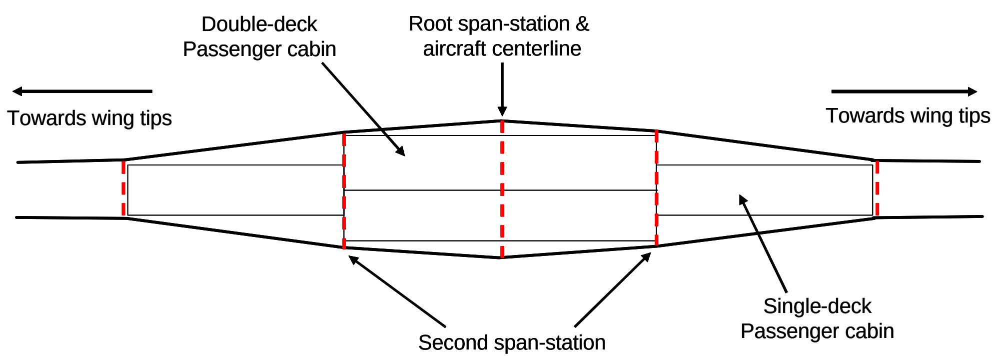

Figure 3-3: Front view planform of the BWB showing the position of the double- and single deck passenger cabin.

3.1.2. Fuel tanks

We assume that the fuel tanks are located in the outboard wing sections starting from the third span stations to the 95% semi-span location. Figure 3-4 shows the locations of the fuel tanks. Within these sections, only 60% of the chord length can be used to store fuel, starting from the forward 10% chord location. The rear 20% chords of the outboard sections are used for the hydraulic systems and in the distributed propulsion configuration, including the ductwork.

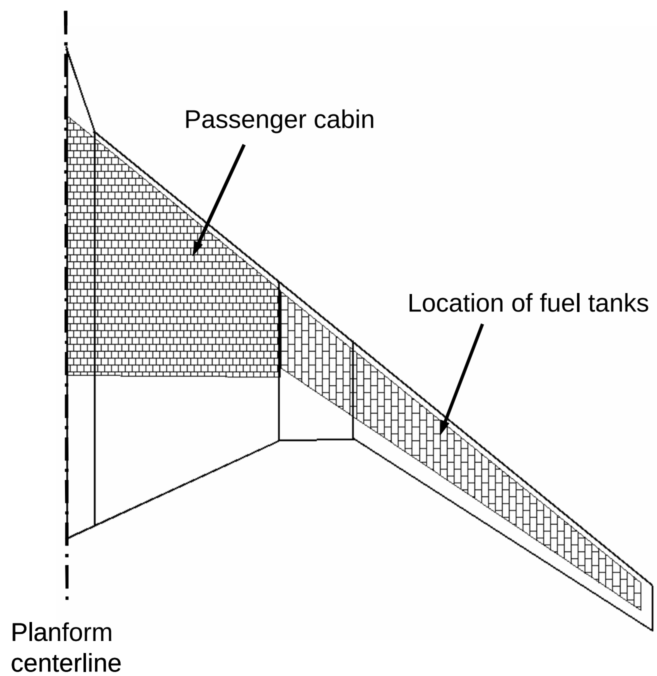

Figure 3-4: Planform schematic of the BWB aircraft showing the position of the fuel tanks and passenger cabin.

Winglets are modeled only in the calculation of the induced drag. The geometric details of the winglets are described in Chapter 4. No account for the weight of the winglets is included.

3.2. Optimization Problem Statement

3.2.1. Objective Function

The distributed propulsion BWB MDO program has been designed to accommodate different objective functions, and even combinations of objective functions. Of most interest in this research is the takeoff gross weight (TOGW).

However, if one wishes, other measures of fitness, such as the fuel weight or lift to drag ratio (*L/D*) can be used.

3.2.2. Design Variables

A total of 21 design variables are used in the distributed propulsion BWB MDO setup. These include aircraft geometric properties as well as other necessary variable such as engine thrust. Table 3-1 gives a list of the design variables that are used, their descriptions and the maximum and minimum values imposed.

The design variables are normalized before being input into the optimizer. This procedure is important in the optimization process to ensure that the relative magnitudes of the design variables are on the same scale.

3.2.3. Constraints

There are 19 inequality constraints that are imposed in the distributed propulsion BWB setup[1]. The constraints, to be described in more detail next, are:

- Range constraint
- Fuel volume constraint
- Balanced field length constraint
- Landing distance constraint
- Second segment climb gradient constraint
- Missed approach climb gradient
- Approach velocity constraint
- Top of climb rate of climb constraint
- Maximum allowable section C_l
- Cabin area constraint
- Cabin aspect ratio constraint
- Section thickness constraint (3 constraints)
- Stability and control constraints (4 constraints)

[1] Although a maximum allowable section C_l constraint is imposed, a constraint on the three-dimensional lift coefficient, C_L, was not considered.

Table 3-1: Design variables used in the distributed propulsion BWB MDO program

	Design Variable	Description	Minimum value	Maximum value
1	h_2	Position of the second span station as a function of semi-span	0.01	0.19
2	h_3	Position of the third span station as a function of semi-span	0.2	0.4
3	h_4	Position of the fourth span station as a function of semi-span	0.45	0.99
4	c_1	Chord length of the root span station (ft.)	30	300
5	c_2	Chord length of the second span station (ft.)	30	200
6	c_3	Chord length of the third span station (ft.)	30	200
7	c_4	Chord length of the fourth span station (ft.)	30	200
8	c_5	Chord length of the tip span station (ft.)	10	200
9	t/c_1	Thickness to chord ratio at the root span station	0.1	0.4
10	t/c_2	Thickness to chord ratio at the second span station	0.1	0.4
11	t/c_3	Thickness to chord ratio at the third span station	0.1	0.4
12	t/c_4	Thickness to chord ratio at the fourth span station	0.1	0.4
13	t/c_5	Thickness to chord ratio at the tip span station	0.1	0.4
14	L_{TE1}	Sweep angle at the trailing edge of the first wing section (deg.)	-45	0
15	L_2	Quarter-chord sweep angle for the second wing section (deg.)	0	60
16	L_3	Quarter-chord sweep angle for the third wing section (deg.)	0	60
17	L_4	Quarter-chord sweep angle for the fourth wing section (deg.)	0	60
18	b	Wing span (ft.)	20	600
19	W_{fuel}	Fuel weight (lbs.)	148000	592000
20	T_0	Engine thrust per engine (lbs.)	5560	111200
21	h_{cruise}	Average cruise altitude (ft.)	17500	70000

The constraints are normalized using Equation (3.1) based on their maximum and minimum allowable values. Although the optimizer allows the user to specify directly input maximum and minimum values for each inequality constraint, the constraints here are normalized to be feasible if they are negative for consistency.

$$\begin{aligned} &\frac{\text{Constraint\_min} - \text{Constraint\_value}}{\text{Constraint\_min}} \leq 0 \text{ for minimum} \\ &\frac{\text{Constraint\_value} - \text{Constraint\_max}}{\text{Constraint\_max}} \leq 0 \text{ for maximum} \end{aligned} \tag{3.1}$$

3.2.3.1. Range Constraint

The range constraint ensures that the calculated range of the aircraft can meet the mission range including a 500 nmi reserve range.

3.2.3.2. Fuel Volume Constraint

The fuel volume constraint ensures that the volume available to store fuel in the wings is greater than the required fuel volume needed to complete the aircraft mission.

3.2.3.3. Balanced Field Length constraint

The balanced field length constraint ensures that the calculated balanced field length does not exceed a maximum limit. Nominally, this limit is set at 11,000 ft.

3.2.3.4. Landing distance constraint

The landing distance constraint ensures that the calculated aircraft landing distance does not exceed a maximum limit. Nominally, this limit is set at 11,000 ft.

3.2.3.5. Second segment climb constraint

This constraint requires that the second segment climb gradient of the aircraft is not smaller than the FAR specifications. These minimums are shown in Table 3-2.

Table 3-2: Minimum Second Segment Climb Gradients

Number of Engines	Minimum Second Segment Climb Gradient
2	0.024
3	0.027
4	0.030

The second segment climb gradient is defined as the ratio of the rate of climb to the forward velocity at full throttle while one engine is inoperative and the gear retracted, over a 50 foot obstacle. The FAR regulations for aircraft with more than 4 engines are currently unclear. For the distributed propulsion BWB, the minimum for 3 engines is used.

3.2.3.6. Missed Approach Climb Gradient Constraint

This constraint restricts the missed approach climb gradient to be greater than the specified minimum value. The FAR minimum is given in Table 3-3.

Table 3-3: Minimum Missed Approach Climb Gradients

Number of Engines	Minimum Second Segment Climb Gradient
2	0.021
3	0.024
4	0.027

As with the second segment climb gradient, the FAR regulations for a transport aircraft with more than 4 engines are currently unclear. For the distributed propulsion BWB, the minimum for 3 engines is used.

3.2.3.7. Approach velocity constraint

The approach velocity constraint limits the approach velocity of the aircraft to a minimum set limit. Nominally, this limit is set to 140 knots for large transport aircraft. The approach speed is calculated to be 1.3 times the stall speed [69][1].

3.2.3.8. Top of climb rate of climb constraint

This constraint requires that the available rate of climb at the initial cruise altitude be greater than 500 ft/s.

[1] Page 85-87

3.2.3.9. Maximum Allowable Section C_l constraint

This constraint makes sure that the required maximum two dimensional lift coefficient at cruise is less than the given maximum lift coefficient. In this case, the maximum lift coefficient is set to a value of 0.65.

3.2.3.10. Cabin area constraint

The cabin area constraint ensures that the available cabin floor area is greater than the needed cabin area at 10 ft^2 per passenger [12].

3.2.3.11. Cabin aspect ratio constraint

The cabin aspect ratio constraint is included to simulate a cabin egress constraint. Cabin egress is an important factor for the BWB aircraft, with limited side surface area to place emergency exits. If the passenger cabin aspect ratio is too small (i.e. the passenger cabin is too slender), there will not be enough emergency exits at the front and exit tunnels in the rear to meet FAR requirements. Also, the distance between passengers in the middle of the cabin and the emergency exits will be too large to meet the mandated FAR requirements. The cabin aspect ratio constraint limits the cabin aspect ratio to a minimum of 0.45. This aspect ratio is defined as the ratio of the square of the cabin width to the cabin planform area.

3.2.3.12. Section thickness constraints

The section thickness constraints ensure that there is sufficient thickness in the aircraft inboard sections to accommodate the passenger cabin. These constraints apply to the first three span stations. The first two span stations are constrained to a minimum thickness of 22 feet to accommodate the double passenger decks. The third span station is constrained to a minimum thickness of 9 feet.

3.2.3.13. Stability and control constraints

There are four longitudinal stability and control constraints. This corresponds to constraints at four different weight conditions: Zero fuel weight, Takeoff gross weight, operational empty weight and the operational empty weight with full fuel. These constraints make sure that the center of gravity location of the aircraft is within necessary limits to ensure acceptable longitudinal control. A detailed discussion of these constraints is given in Chapter 4.

Chapter 4: An MDO model for a Blended-Wing-Body Aircraft

4.1. Software Architecture

In an aircraft conceptual or preliminary aircraft design, various disciplinary design teams have access to various design and analytical tools. Often, the results from these different disciplines conflict in requirements. To resolve these conflicting requirements, simple iterations amongst the disciplines are done, making minor changes to a baseline aircraft, until all the design constraints are met. In traditional engineering environments, this iteration is done by physically allowing each disciplinary expert to perform some measure of analysis and design, then passing it on to the next expert, under the control of a chief aircraft designer, until a final converged design is produced. In preliminary or detailed design effort, this process can take as long as months at a time, expending large amounts of man-hours and resources. In addition to this, the suite of available tools to the designer keeps increasing and current tools are often upgraded or modified. These tools often run on different computational platforms, and are coded in different programming languages. Analysis fidelity and run-time also varies greatly between these tools.

MDO seeks to link, organize and automate these analysis tools, providing the designer the ability to take advantage of the synergism between different disciplines. From an integration standpoint, previous Virginia Tech MDO efforts have met with varying levels of success. Often, each integrated code is 'custom built' for a certain application or problem. Modifications are then made to this code to adapt it for other applications where needed. Also, the code continues to evolve, with changes made by different users at different times. What results is a collection of different variants of the same integrated design program, with varying levels of changes and upgrades made to the variants. Each frequently only works for a specific design problem. Also, the program is often platform and language specific. Any cross language integration efforts require a high level of expertise and are likely to contain programming bugs. The process of integration also requires many man hours of programming, requiring the programmer to keep track of individual variables as they are passed between individual analysis routines. Program debugging time is long and often difficult.

Engineering integration software, also known as integrated design framework packages, seeks to overcome these problems, providing the user with more time to devote to analysis and design. In the design of the BWB MDO tool, ModelCenter® is used as the engineering integration software.[70] ModelCenter® is a product by Phoenix Integration. It provides the means to help wrap, link and schedule multiple software applications. Based on a client and server methodology, wrapped software is 'published' on a server, allowing a user to have access to the individual software to integrate, much like web server hosting. ModelCenter® requires the use of an auxiliary program, called Analysis Server® which acts as the software server. Since ModelCenter® and Analysis Server® are written in Java, they are portable across different hardware and software platforms.[1]

Figure 4-1 shows the general architecture of the BWB MDO code. A variety of optimization techniques are available, including gradient based optimization techniques and global optimization strategies such as genetic search algorithms [71]. In this MDO architecture, only gradient based search methods are used, although it is fairly easy to implement other optimization techniques through ModelCenter®. The optimization process begins with an initial baseline design. This is the so-called optimization baseline design. From here, based on the configuration, the geometry parameters are calculated to be used by the various modules. The aerodynamics module calculates the wing load and the drag of the aircraft. The structures module calculates the wing weight while the weights module calculates the weights of the individual systems in the entire aircraft. The

---

[1] More information on ModelCenter® can be found at their web-site at http://www.phoenix-int.com.

propulsion module provides the thrust specific fuel consumption, engine weight and thrust performance of the propulsion system. The other modules such as fuel volume, performance, stability and control and balance are used to calculate the objective function and various constraint values. With this information, the optimizer is then able to determine the 'next step' for the optimization, be it a new search direction (for gradient based optimization algorithms) or a new location to be evaluated in the design space. This process is repeated until convergence to a minimum objective function is achieved. In the distributed propulsion MDO framework, the built in optimizer in ModelCenter® is used to perform this function. This optimizer was developed by Vanderplaats R. & D. and is similar to the DOT optimization software that they market.

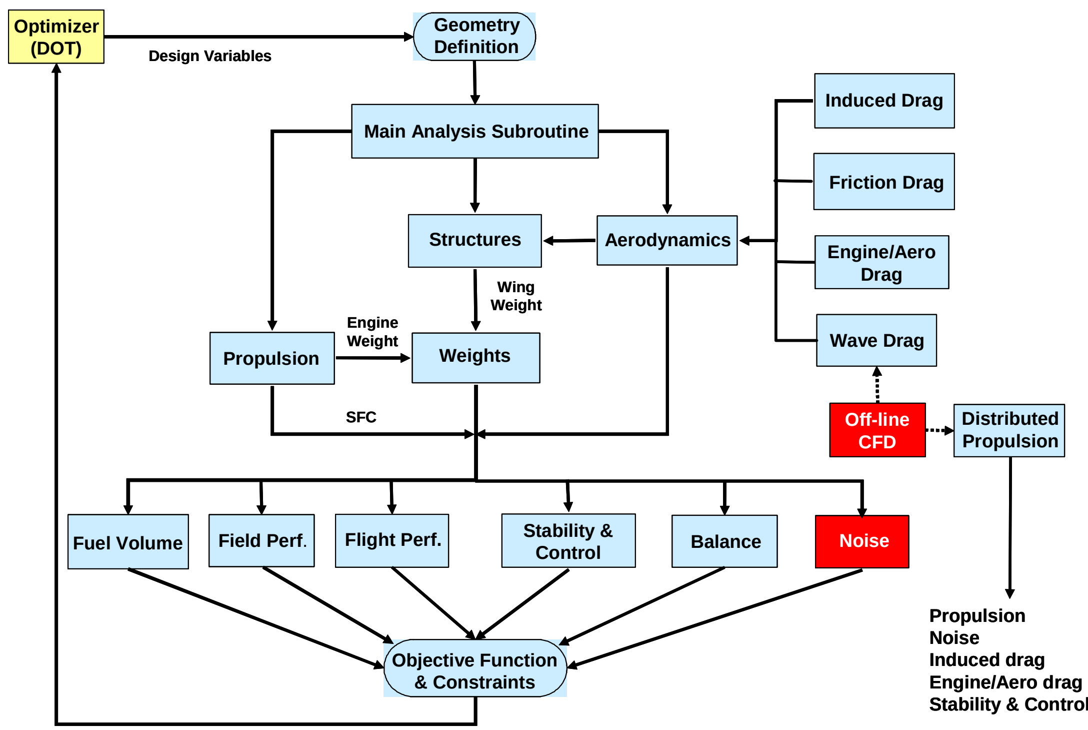

Figure 4-1: Flowchart showing the MDO framework of the distributed propulsion BWB MDO program. Boxes in blue are those that are in place in the MDO framework while those in red are ones that are still under development. Modules in yellow are built-in ModelCenter® functions.

4.2. Analysis methods

Analysis methods of different levels of fidelity are used in the distributed propulsion BWB MDO program. Where possible, methods that have already been developed in previous research studies were modified and used. This helped in reducing the development time of the MDO framework.

4.2.1. Aerodynamics

The aerodynamics module is comprised of three different aerodynamic analysis programs, executed by a main analysis subroutine. The following are the aerodynamic analysis programs that are used.

- idrag
  - idrag is a vortex panel code written by Joel Grasmeyer. It calculates the load distribution on a wing having a given a lift coefficient and also the induced drag associated with that condition. The geometry input allows for non-planar surfaces, which provides the capability to model the winglets on the BWB. The load distribution information calculated from idrag is then used as input into other analyses (e.g. transonic wave drag estimation). Reference [72] provides additional detail on idrag.
- wdrag
  - wdrag is a subroutine that uses the Korn equation to estimate the transonic wave drag for a wing. Here, simple sweep theory is used [73] to account for sweep in the geometry. First, the geometry is divided into a number of spanwise strips. Then, the wave drag model estimates the drag divergence Mach number as a function of airfoil technology factor, thickness to chord ratio, section lift coefficient and sweep angle for each individual strip. With the drag divergence Mach number, the critical Mach number can be calculated, from which the wave drag coefficient is obtained. The total wave drag is found by integrating the wave drag of all the strips along the planform. Reference [74], [75] provides additional detail on wdrag
- Friction
  - This program was written to calculate the friction drag due to individual components on a body [76]. It is based on applying form factors to an equivalent flat plate skin friction drag analysis. The amount of laminar flow on the BWB is estimated by interpolating results from the Reynolds number vs.

sweep data obtained from the F-14 Variable Sweep Transition Flight Experiment (1984-1987) [77] and wind tunnel test data from Boltz et al. [78]. Details on Friction can be obtained from Reference [76] and [79]

In the aerodynamic analysis, the drag at five different conditions is found to provide the necessary data required by other analysis modules in the BWB program. These conditions are listed below:

1. TOGW condition at cruise altitude (This is the limit cruise lift coefficient)
2. Cruise condition => Zero fuel weight + 0.5 Fuel weight
3. Initial climb configuration ($V = 1.2\ V_{stall}$ at takeoff)
4. Approach and missed approach configuration ($V = 1.3\ V_{stall}$)
5. Touch down configuration ($V = 1.15\ V_{stall}$)

Additional drag due to the landing gear at landing and take-off conditions are added to the calculated drag later during the calculation of the field performance constraints. This is done by assuming a nominal landing gear drag coefficient and reference area. This drag is then scaled based on the aircraft reference area and added to the necessary field performance calculations. These nominal landing gear drag coefficient and reference area were obtained from our previous Strut-Braced Wing aircraft MDO design program. Additional drag due to the high lift systems can also be included in the field performance calculation via this method.

The next sections discuss the specific modeling details that are used as inputs into the individual aerodynamics disciplines. The assumptions that were made are also described.

4.2.1.1. Induced Drag

The general geometry input into idrag is shown in Figure 4-2. As can be seen, five sections are modeled. The first four define the shape of the BWB, while the fifth section models the winglet. Based on the chord lengths and sweep information (that are input as design variables in the BWB program), the coordinates describing each of the first four sections can be calculated. For the winglet, its dimensions are based on assumed quantities that were obtained from the 1994 Boeing BWB design that was published in

Reference [12]. The size of the winglet is then scaled based on the tip chord length of the BWB geometry that is analyzed for each design iteration.

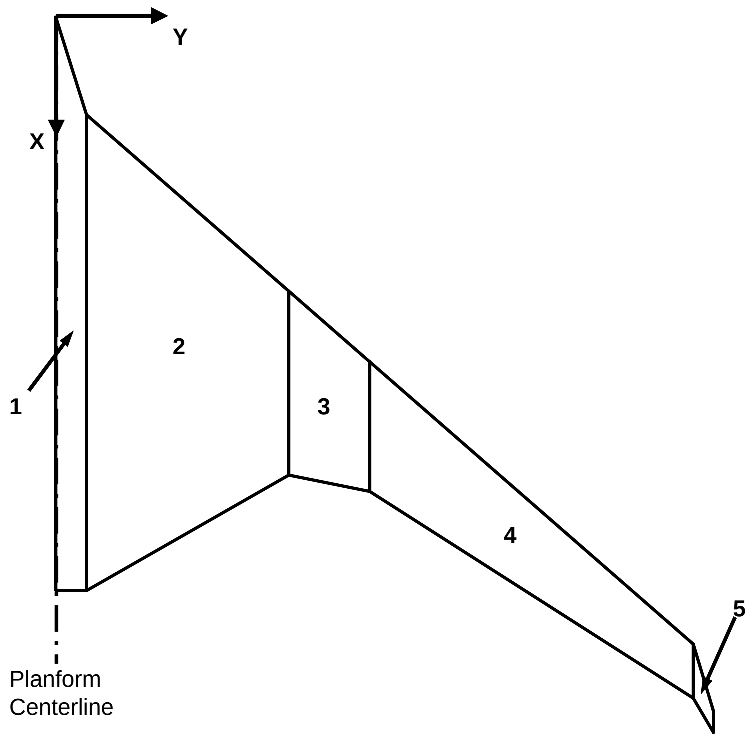

Figure 4-2: Geometry planform input into idrag. Numbers indicate planform sections. Planform 5 represents the winglet.

The assumed dimensions of the winglets based on the 1994 Boeing BWB design are as follows:

$f = 30°$

$L_{winglet} = 72°$

$C_{winglet} = 0.4\ C_{Tip}$

$b_{winglet} = 0.4\ C_{Tip}$

Figure 4-3 shows the geometric definitions that are used to model the winglet.

Once the geometry sections have been defined, the number of panels for each section is selected. A total of 160 panels are used for the entire geometry, 10 of which are assigned to the winglet section. The remaining 150 panels are distributed among the four wing sections based on the span of each section (relative to the wing half-span). The *spacing_flag* parameter for all the sections is set at 0, which evenly spaces the vortex control points.

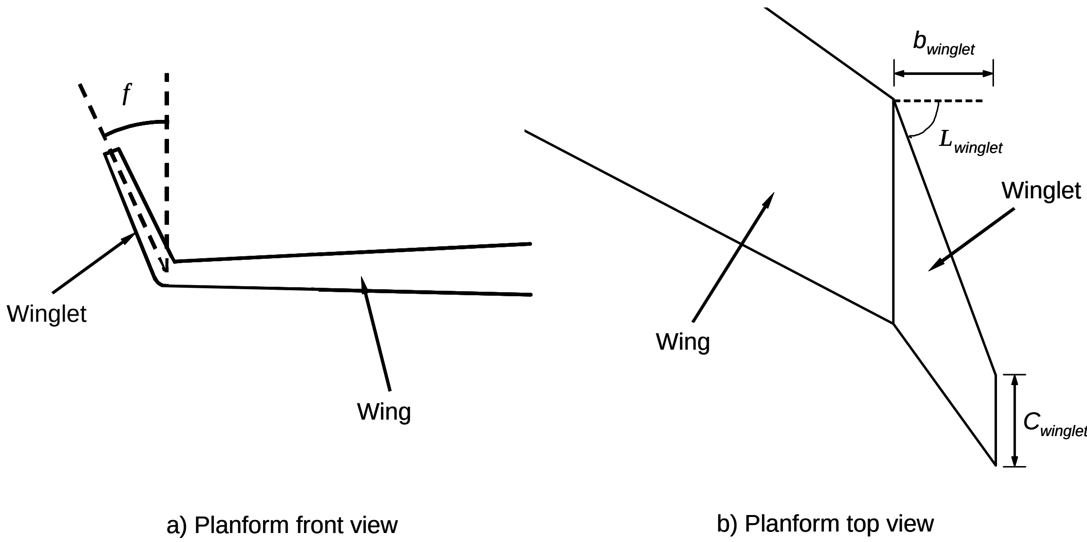

Figure 4-3: Geometric definitions of the BWB winglet

4.2.1.2. Friction Drag

To calculate friction drag, the BWB geometry is divided into a number of sections for input into the <u>Friction</u> subroutine. The number of planar surfaces on the BWB is selected by the parameter *Strips_Fdrag_Max*. Currently, this parameter is set at a value of 25 for a half span of the BWB.

The input to <u>Friction</u> requires that the calculation of the wetted area of each planar surface be done. With the thick airfoil sections used in the BWB, the assumption that the wetted area is approximately twice the planform area does not hold (covering the top and bottom surfaces). To calculate the wetted area, a generic airfoil section is used as a template for the wetted area calculation. For each wing planar surface, the template airfoil section is scaled to the required thickness at its corresponding location. The wetted area of that surface then can be calculated given the coordinates of the scaled airfoil section. By using a single template airfoil section, a close approximate to the actual wetted area of the BWB aircraft can be obtained without the need for the actual airfoil section information that will be used in the BWB design.

<u>Friction</u> is also used to estimate the friction drag on the engine nacelles. Using equations found in Isikveren [80], estimates for nacelle length, diameter and wetted area can be obtained given the thrust of an individual engine. These equations were obtained from correlation expressions and engine data compiled from *Aviation Week* [81], *Janes*

All the World's Aircraft [82] and that from Svoboda [83]. Equations (4.1) to (4.3) give the details of these equations. To account for buried internal engines, a factor *engine_expose_fact* is applied to the nacelle wetted area calculation. This factor represents the fraction of 'exposed' nacelle area of a buried engine compared to an engine mounted on pylons.

$$d_{nac} = 4\left[0.0625 + \frac{1}{4\sqrt{2}}\left(1.730 \ln T_0 - p\right)^{\frac{1}{2}}\right] \tag{4.1}$$

$$l_{nac} = 5\left[\frac{T_0^{\;0.9839}}{6p\,(1.730 \ln T_0 - p)}\right] \tag{4.2}$$

$$S_{wet,nac} = 2p^{\,2} V_{dia} d_{nac} \begin{bmatrix} \left(0.2057 l_{nac}^2 + 0.04661 d_{nac}^2\right)^{\frac{1}{2}} \\ + \left(0.18531 l_{nac}^2 + 0.07557 d_{nac}^2\right)^{\frac{1}{2}} \\ - \left(0.005077 l_{nac}^2 + 0.01611 d_{nac}^2\right)^{\frac{1}{2}} \\ - \left(0.01651 l_{nac}^2 + 0.03666 d_{nac}^2\right)^{\frac{1}{2}} \end{bmatrix} \tag{4.3}$$

where V_{dia}, the diameter scaling factor, was determined by Isikveren [80] to be 0.2028.

4.2.1.3. Wave Drag

As mentioned earlier, the total wave drag is calculated by estimating the wave drag on individual spanwise strips that make up the geometry. For simplicity, the same spanwise strips that were used for Friction are used to estimate the wave drag. The lift coefficient at each strip is obtained from information calculated in idrag. The quarter chord sweep is also input into the wave drag calculation. To save computation time, wave drag is only calculated for the cruise configuration (zero fuel weight + 0.5 fuel weight configuration) since the other configurations (such as takeoff and landing) occur at low Mach numbers, and the contribution of wave drag to the total drag would be negligible.

At each strip, the drag divergence Mach number is estimated using the Korn equation, extended to include sweep using simple sweep theory [74], [75] as shown in Equation (4.4).

$$M_{dd} = \frac{k_a}{\cos \Lambda_{1/4c}} - \frac{(t/c)}{\cos^2 \Lambda_{1/4c}} - \frac{C_l}{10 \cos^3 \Lambda_{1/4c}} \tag{4.4}$$

With the drag divergence Mach number known, the critical Mach number can be found assuming the empirically-derived shape of the drag rise by Lock [84]. The equation for the drag divergence Mach number is given in Equation (4.5).

$$M_{crit} = M_{dd} - \left(\frac{0.1}{80}\right)^{1/3} \tag{4.5}$$

With this, we can calculate the wave drag coefficient with Equation (4.6).

$$C_{d_{wave}} = 20\left(M - M_{crit}\right)^4 \frac{S_{strip}}{S_{ref}} \quad for\ \ M > M_{crit} \tag{4.6}$$

It was found during the implementation of this method, that the Korn equation formulation is not suitable for estimating the wave drag at high sweep angles. Figure 4-4 shows the variation of critical Mach number and wave drag coefficient, given a certain airfoil technology factor, thickness to chord ratio and lift coefficient.

From Figure 4-4 we see that at high sweep angles (> 50°), the estimation for the critical Mach number reaches a maximum and then rapidly decreases. As a result, the wave drag coefficient increases rapidly with increasing sweep. This behavior is caused by the cosine terms in the denominator of the terms in Equation (4.4). Knowing that this behavior is not consistent with reality, a limit is set on the formulation such that if the sweep angle is above 50°, and the critical Mach number is beyond the maximum point, the wave drag coefficient for that particular strip is not taken into account.

The use of the modified Korn equation in Equation (4.4) assumes small *t/c* ratios (approximately less than 15%) to be valid. However, to accommodate passengers in the BWB aircraft, the *t/c* ratios at the inboard wing sections are large (18%-20%). Therefore, although this formulation is used in our BWB code to estimate the transonic wave drag of the aircraft, the fidelity of this method is possibly too crude to provide an accurate value of the wave drag coefficient. CFD data should be used to adjust and modify this method in the future, allowing for better wave drag coefficient estimates.

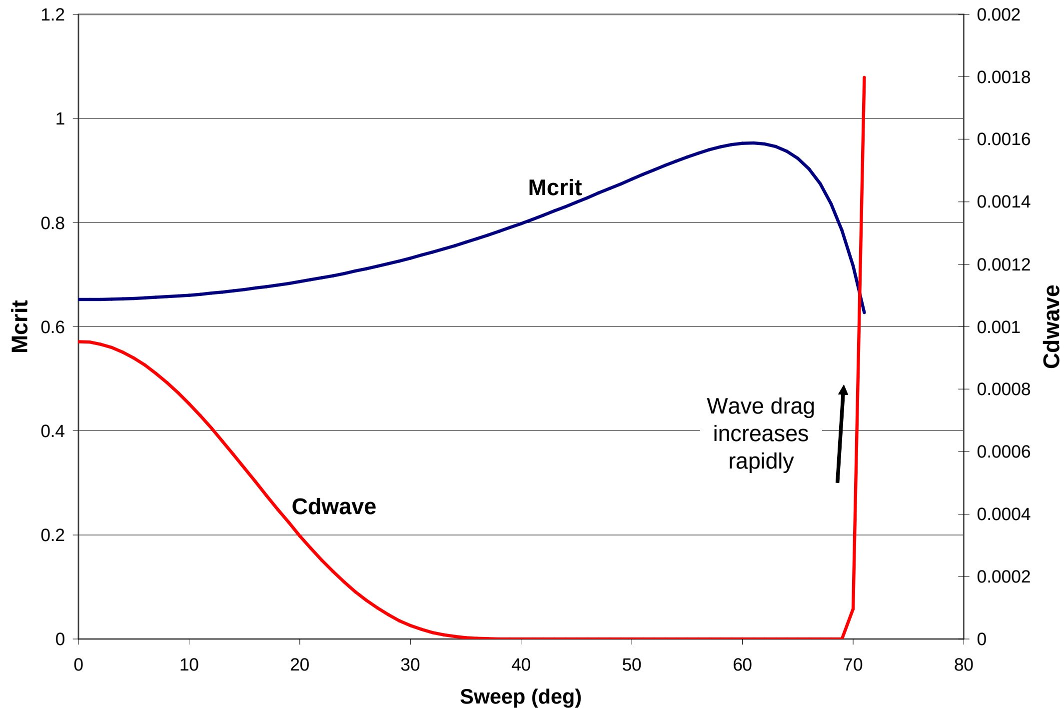

Figure 4-4: Chart shows the variation of critical Mach number and wave drag coefficient for an increasing sweep angle. The Korn equation formulation breaks down at high sweep angles when the critical Mach number rapidly decreases after reaching a maximum. This leads to a rapidly increasing wave drag coefficient.

4.2.2. Structures (Wing weight estimation)

Initially, the wing weight equation provided by Beltramo et al. [85] was used to evaluate the wing weight of the Blended-Wing Body. This approach was used by Liebeck et al. to design the 1994 BWB design [12]. This equation is given in Equation (4.7).

$$W_{Wing} = z_1 I_W + z_2 S_{ref} + z_3$$

$$I_W = \frac{n(AR)^{1.5}\left(\dfrac{WZF}{TOGW}\right)^{0.5}(1+2l)\left(\dfrac{TOGW}{S_{ref}}\right)S_{ref}^{1.5}\left(1\times10^{-6}\right)}{\mathrm{t/c}\left(\cos\Lambda_{\frac{1}{4}c}\right)(1+l)}\left(\mathrm{lbs-ft^2}\right) \tag{4.7}$$

where ζ_1 = 0.930 (1/lbs-ft$^{0.5}$)

ζ_2 = 6.44 (1/ft^2)

ζ_3 = 390. lbs

S_{ref} = Reference wing area

n = Ultimate load factor

AR = Aspect ratio

WZF = Zero fuel weight

TOGW = Takeoff gross weight

l = taper ratio

t/c = thickness to chord ratio

$L_{¼c}$ = quarter chord sweep

Although this approach was adequate at an analysis level, we found that it does not provide the level of fidelity necessary for optimization. Average (or even weighted average) values of the taper ratio (l), aspect ratio (AR), thickness to chord ratio (t/c), wing sweep, and wing area (S_{ref}) were not adequate to describe the geometric properties that are used in the BWB aircraft. In addition to this, the reference area used by Liebeck et al. [12] for the wing weight calculation uses the trapezoidal wing area and not the planform area. Since the trapezoidal wing area is only dependant on the outer wing section, using this definition in an optimization setup neglects the effects of the inboard sections and over emphasizes the role of the outboard wing sections.

As a replacement for the wing weight formulation from Beltramo et al. [85], we used the wing weight formulation from FLOPS [86]. In addition to this formulation being a higher fidelity model, it takes into account the geometry of the individual wing sections, and takes into account the number and position of the engines for load alleviation.

Table 4-1 shows the difference in wing weight and takeoff gross weight estimation for the 1994 BWB design between the Beltramo et al. [85] formulation (using the trapezoidal and planform area) and that from FLOPS. It shows that the difference between using the planform area and the trapezoidal wing area using the same wing weight formulation (Beltramo et al. [85]) is only 2%. The wing weight estimation increases by 41% when the formulation in FLOPS is used. It should be noted the wing weight using the formulation by Beltramo et al. [85] (trapezoidal wing area) is the one that was used by Liebeck et al. [12] to design the 1994 BWB aircraft. It should be noted that the values in Table 4-1 are for the analysis of the same aircraft configuration and not an optimized design. No change in the design was made including that of the aircraft fuel weight. Therefore, the takeoff gross weight reflects only the effect of using the different reference area and wing weight formulation on the aircraft weight calculation.

Table 4-1: Difference in the wing weight calculation methods for the 1994 BWB design

Wing weight calculation method	Wing Weight (lbs)	Takeoff Gross Weight (lbs)	Wing reference area (ft^2)
Beltramo (trapezoidal wing area)	124,609	1,010,587	10,432
Beltramo (planform wing area)	127,045	1,017,074	16,477
FLOPS (planform wing area)	176,011	1,068,804	16,477

Mukhopadhyay et al. [14] provides an alternate estimation for the wing weight for the BWB aircraft. In their publication, a set of structural concepts for a pressurized fuselage for a BWB type aircraft was considered. It was found that an unintegrated pressurized cabin and wing structure offered the best weight savings, while providing redundancy in the case of a pressure leak. Although this wing weight estimation is not included in the present distributed propulsion BWB analysis, the current estimation method used also models the structure with an unintegrated passenger cabin and wing.

4.2.3. Weights

The calculations of the individual component weights for the BWB are based on the analysis done by Liebeck et al. (NASA CR-4624) [12]. With the exception of the wing weight, the equations provided in this NASA contract report were used. For the wing weight, the formulation used in FLOPS is used. Where no specific weight computation information was given in the report, the weights provided in the report were scaled (information on how they are scaled will be provided later). The following sections provide the equations and assumptions that were used throughout the calculation of the weight of the BWB. Technology factors can also be applied to the individual weights that are calculated.

4.2.3.1. Cabin Weight

In the design of the BWB, it is assumed that the cabin area is contained in the inboard section of the wing up to the third span station. It is also assumed that only 60%

of the chord length in this inboard section is used for the cabin area. This is because the height inside the aircraft towards the trailing edge would likely be too small to fit passengers. The cabin weight calculation is divided into two sections, the pressure membrane weight, and the cabin vertical web weight. The total cabin weight is calculated from the sum of the pressure membrane and cabin vertical web weights.

4.2.3.1.1. Pressure membranes

The pressure membrane weight is the estimate of the weight of the upper and lower pressure membranes enclosing the passenger cabin. A graphite composite skin is assumed to be used designed at a thickness to withstand an ultimate pressure loading of 18 psi. Based on the analysis by Liebeck et al. [12], a skin thickness of 0.05 inch is used. A density of 0.057 lb/in^3 is used for the graphite composite. Based on the planform area of the cabin, the weight of the upper and lower pressure membranes can be calculated.

4.2.3.1.2. Cabin vertical webs

The cabin vertical webs run from the forward to the aft of the cabin area, at a spacing of 12.5 ft between webs. From the analysis by Liebeck et al. [12], it was determined that a web thickness of 0.05 inches should be used (using graphite composite materials). With the width of the cabin known, the number of cabin vertical webs can be determined and therefore their weight.

4.2.3.1.3. Secondary Structure

The secondary structure weight is scaled to the number of passengers at 61.25 lbs per passenger, scaling the weights used by Liebeck et al. [12].

4.2.3.2. Pressure Barriers

The pressure barrier is also known as the bulkhead of the aircraft cabin. The pressure barrier weight is scaled to the side area (not covered by the pressure membrane) around the passenger cabin. In the calculation of the side area, the passenger cabin height is assumed to be 90% of the maximum thickness of the airfoil section. Figure 4-5 shows an illustration of this assumption. Three different areas for the pressure barriers are calculated. They are the forward pressure barrier, the cabin tip pressure barrier and the aft pressure barrier.

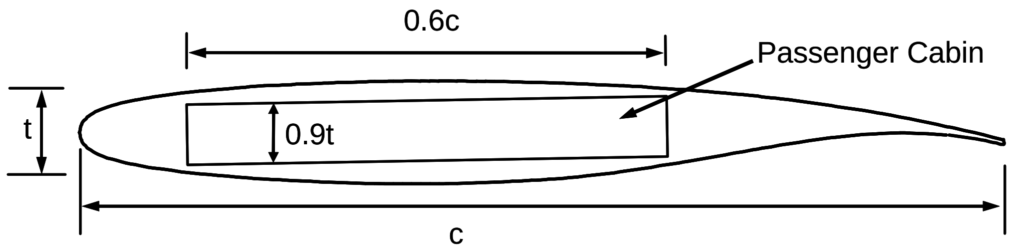

Figure 4-5: Diagram of the cross section of the BWB where the passenger cabin is located. It illustrates the assumption that 90% of the maximum thickness of the airfoil section is taken to be the average height of the cabin.

4.2.3.3. Afterbody

The afterbody section is defined as the remaining area behind the passenger compartment in the inboard section of the BWB wing. Just like the passenger cabin, it is assumed that the afterbody section ends at the third spanwise station. The weight of the afterbody section is scaled to the planform area of that section at 5.54 lbs/ft^2 based on the weights obtained from Liebeck et al. [12].

4.2.3.4. Nose shell weight

The nose shell weight is estimated at 1300. lbs. based on the weights used by Liebeck et al. [12]

4.2.3.5. Anti-icing weight

The anti-icing weight is scaled to the reference wing area at 0.120 lbs/ft^2 based on the weights used by Liebeck et al. [12].

4.2.3.6. Fixed weights

The fixed weights are the total sum of the following items:

- Pneumatics
- Auxiliary power plant
- Electrical
- Furnishings and equipment

- Air conditioning
- Avionics & autopilot
- Instruments

The total fixed weights are scaled to the number of passengers using Equation (4.8).

$$W_{fixed} = 201.9\,N_{pass} + 4000\;(lbs) \tag{4.8}$$

4.2.3.7. Operational Items

The operational items weight is scaled to the number of passengers at 60.0 lbs per passenger.

4.2.3.8. Flight controls and hydraulics

The flight controls and hydraulics weights are estimated based on the Equation (4.9) provided in NASA-CR151970.

$$W_{controls} = 360.0 + a_{CS} S_{CS} \tag{4.9}$$

where S_{CS} is the planform area of the control surfaces and a_{CS} = 2.525 lbs/ft^2.

4.2.3.9. Payload weight

The payload weight is estimated at 220 lbs per passenger.

4.2.3.10. Landing gear weight

The landing gear weight is estimated using Equation (4.10).

$$W_{\lg} = a_{\lg} \left(TOGW\right)^{1.1} \tag{4.10}$$

where TOGW is the takeoff gross weight and a_{lg} = 0.0135 lbs$^{-0.1}$

4.2.4. Total Aircraft weight

After calculating the individual weights, the Takeoff gross weight (TOGW) and other functional weights can be determined. The TOGW is the sum of all the individual weights (except the operational items weight since the fixed weights equation includes the operational items weight already), including the fuel weight. The zero fuel weight is the TOGW minus the fuel weight. The Operational empty weight is calculated as the zero fuel weight minus the payload weight. The manufacturer's empty weight is estimated as the operational empty weight minus the operational items weight.

4.2.4.1. Calculating the weights

Since the landing gear and wing weights are functions of the TOGW, a Newton's method is employed to solve the implicit weight formulation. To simplify the calculation, we define factors A and B in Equation (4.11).

$$A = (0.930\times10^{-6})\,F_{wing}\,\frac{n\,AR^{1.5}(1+2\,l\,)\,S_{Ref}^{\;\;0.5}}{t/c\,(Cos\Lambda_{\frac{1}{4}c})(1+\,l\,)} \tag{4.11}$$
$$B = (6.44\,S_{Ref}+390)\,F_{wing}+W_{other}$$

where F_{wing} = Wing weight technology factor. W_{other} is defined as the sum of the weights shown in Equation (4.12).

$$W_{other} = W_{cabin} + W_{engines} + W_{controls} + W_{ai} + W_{fixed} + W_{payload} + W_{fuel} \tag{4.12}$$

where
W_{cabin} = Cabin weight
$W_{engines}$ = Total weight of the engines including nacelles
$W_{controls}$ = Flight controls and hydraulics weight
W_{ai} = Anti-icing weight
W_{fixed} = Fixed items weight
$W_{payload}$ = Payload weight
W_{fuel} = Fuel weight

Hence, the takeoff gross weight formulation will become

$$TOGW = A\left[TOGW(TOGW - W_{fuel})\right]^{0.5} + 0.0135\,F_{ldg}\,(TOGW)^{1.1} + B \tag{4.13}$$

where F_{ldg} = Landing gear weight technology factor

Therefore, in the Newton's method formulation, the function to be solved is:

$$f\,(TOGW) = A\left[TOGW(TOGW - W_{fuel})\right]^{0.5} + 0.0135\,F_{ldg}\,(TOGW)^{1.1} + B - TOGW = 0 \tag{4.14}$$

where the derivative with respect to TOGW is

$$f\,'(TOGW) = \frac{0.5\,A(2\,TOGW - W_{fuel})}{\left[TOGW(TOGW - W_{fuel})\right]^{0.5}} + 0.01485\,F_{ldg}\;TOGW^{\,0.1} - 1 \tag{4.15}$$

This formulation provides all the pieces required to perform a Newton iteration to obtain the TOGW. It should be noted that the fuel weight and engine weight (for one engine and pod) is an input into this subroutine. The convergence criterion for the solution of the Takeoff Gross weight is currently set to within one pound.

4.2.5. Propulsion

As mentioned before, the distributed propulsion arrangement adopted here for the BWB aircraft calls for some of the engine exhaust to be ducted out the aircraft trailing edge. It also calls for a modest number of engines (about 8) buried in the structure along the span. This arrangement would inevitably place the inlets in the path of the boundary layer developing on the body of the aircraft. Special boundary layer ingestion inlets would be used to minimize the ram drag incurred by the placement of these engines. Some experimental and computational work has been done to design an optimal inlet for this application. Papers written concerning this work are listed in References [26] to [33]. For the distributed propulsion BWB MDO program, it is assumed that the inlets have the same performance as a regular nacelle inlet on pylons.

The propulsion analysis subroutine calculates the weight, thrust and specific fuel consumption (SFC) performance for the engines used in the distributed propulsion BWB. The analysis method uses semi-empirical equations and engine models to estimate these quantities of the BWB aircraft based on data collected by Isikveren [80]. They are capable of producing estimates for both a conventional BWB configuration and a distributed propulsion BWB configuration.

4.2.5.1. Engine weight

All the weight equations for the propulsion system were obtained from Isikveren [80]. These regression equations were based on a compiled database of current available turbofan engines.

Equation (4.16) shows the engine weight equation used.

$$W_{eng} = a_{eng}\, T_0^{1.0572} \tag{4.16}$$

where T_0 is the engine thrust in Newtons and a_{eng} = 0.0177 lbs$^{-0.0572}$.

Equation (4.17) accounts for the additional weight due to the nacelles.

$$W_{nac} = 0.345\,ATM_{Engine}\,W_{eng} \tag{4.17}$$

where ATM_{Engine} is an advanced technology multiplier factor for the engines. It simulates the savings in nacelle weight due to future enabling technologies.

If the engines are mounted on pylons, the additional pylon weight is estimated using Equation (4.18).

$$W_{pyl} = a_{pyl}\,W_{eng}^{0.736} \tag{4.18}$$

where a_{pyl} = 0.574 lbs$^{0.264}$.

Equation (4.16) was verified with our current database of engine weights. However, without a database on nacelle and pylon weights, Equations (4.17) and (4.18) were not verified.

4.2.5.2. Engine specific fuel consumption model

The specific fuel consumption model is based on a GE-90-like engine deck provided by NASA. The relation given in Equation (4.19) describes the given engine deck as a function of altitude and Mach number [87].

$$sfc_{cruise} = \left(\frac{Temp_{cruise}}{Temp_{SL}}\right)^{0.4704}\left(sfc_{static,SL} + 0.4021M\right) \tag{4.19}$$

The 1994 Boeing BWB design (which is used as a verification and reference BWB) uses advanced ducted propeller (ADP) engines and not a GE-90-like engine platform. By specifying the static sea level specific fuel consumption of the ADP engine, we assume that the SFC behavior of the ADP engine is similar to that of the GE-90 (with respect to altitude and Mach number).

4.2.6. Fuel volume

The BWB configuration assumes that the outboard wing sections (defined as the wing sections outboard from the third spanwise station) are used to store fuel. The fuel volume module calculates the available volume for fuel storage in the outboard wings, and the fuel center of gravity (CG) locations if the fuel is shifted completely inboard and outboard. These two CG locations provide the range of possible CGs of the aircraft fuel if the BWB aircraft uses fuel pumping for CG control. The available fuel volume is used in the fuel volume constraint, where it is compared to the fuel volume needed to carry the necessary fuel required for the aircraft mission. The CG locations are used in the calculation of the longitudinal control constraint analysis that determines the aircraft's overall CG location and its ability to meet longitudinal control requirements.

4.2.6.1. Available fuel volume

To calculate the available volume within the wing, the wing fuel tank is divided into a number of spanwise strips. The volume in each of these wing strips is then calculated. In this calculation, we assume that only 60% of the wing chord can be used to store fuel in the wing. Within this 60%, we assume that the average thickness of the wing is 90% of the maximum thickness of that wing section. Figure 4-6 shows an illustration that explains the assumptions. It is also assumed that fuel tanks extend only up to 95% of the wing span.

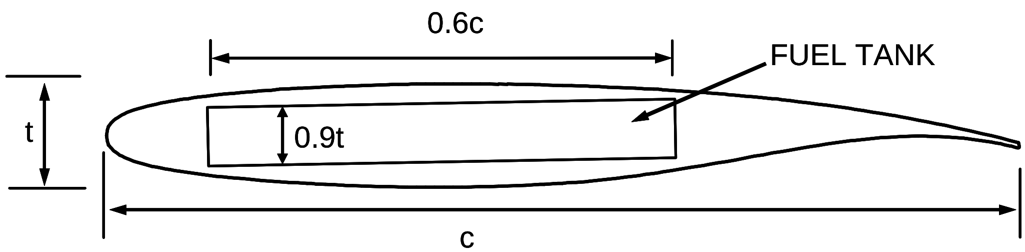

Figure 4-6: Diagram shows the position of the fuel tank in a cross section of the wing.

With the available volume calculated for each of the strips, a volume loss factor of 85% is applied to the volume to account for the volume taken by the construction of the fuel tank. This factor is used in accordance with Raymer's suggestion [69][1]. If hydrogen fuel is considered, this volume loss factor will have to be increased to account for the additional insulation and construction to accommodate cryogenic fuel. A fuel density of 6.8 lb/gallon is used, which is the nominal density of Jet-A fuel. No account for ullage in the fuel tanks is included.

[1] Page 226-228

4.2.6.2. Fuel weight center of gravity (CG) locations

To calculate the fuel weight CG location, the actual fuel volume needed to hold the fuel required for the aircraft mission is compared to the available volume calculated in the previous section. If the fuel volume exceeds the volume available in the wing fuel tanks, both CG locations (one for fuel that is shifted inboard and the other for fuel shifted outboard) are set to be at the location of the wing tanks center of gravity. Although this condition violates the fuel volume constraint (since the aircraft cannot carry all the fuel that it needs), the CG locations are still computed so as to prevent any discontinuities or computational run-time errors in the optimization procedure.

If the fuel volume does not exceed the available volume, the calculation procedures to shift the fuel both fully inboard and outboard are started. Note that this calculation procedure is only to determine the CG location when the aircraft is fully fueled. It is not related to the fuel use or pumping schedule of the aircraft during cruise. For the fuel fully shifted inboard CG location, the calculation procedure is as follows:

1. Fill the first inboard fuel tank (first wing fuel strip in wing) with fuel needed for the mission. This tank is for $i = 1$
2. Is there any remaining fuel after filling the tank? If yes, then fill the next fuel tank (indexed as i+1). If no, go to step 3.
3. Partially fill in the last tank. This tank is indexed as the I^{th} fuel tank.
4. Calculate the CG location of the fuel in the individual tanks.

   Equation (4.20) is used to calculate step 4.

$$CG_{Fuel} = \frac{\sum_{i=1}^{I-1}\left[X_{CG}(i)W_{fuel}(i)\right] + X_{CG}(I)W_{fuel\ remaining}}{W_{fuel\ total}} \tag{4.20}$$

where $X_{CG}(i)$ = the CG location of the n^{th} fuel tank

$W_{fuel}(i)$ = the total weight of the fuel that can be held in the i^{th} fuel tank

$W_{fuel\ total}$ = Total weight of the fuel needed to complete the aircraft mission

$\mathrm{W}_{\mathrm{fuel\ remaining}} = W_{fuel\ total} - \sum_{i=1}^{I-1} W_{fuel}(i)$

Then, the CG location calculation for the fuel fully shifted outboard is performed using the same procedure.

4.2.7. Performance

The performance subroutine contains calculation to provide two performance variables, the rate of climb at initial cruise altitude, more known as top of climb rate of climb, and the aircraft total range.

4.2.7.1. Top of climb rate of climb

In the aircraft performance calculation, we assume that the average cruise condition is when the aircraft is at half fuel capacity (i.e. Aircraft weight = Zero fuel weight + 0.5 fuel weight). Thus, with the average cruise altitude and the weight at the initial cruise altitude known, we can calculate the initial cruise altitude. This method is based on that used by Gundlach [87], modified to solve for the initial cruise altitude analytically.

First, we assume a straight and level flight condition, hence obtaining Equation (4.21).

$$\begin{aligned} W_1 &= \frac{C_L}{\frac{1}{2} r_1 V_1^{2} S_{ref}} \\ &= \frac{2 C_L}{r\, M^2 a_1^2 S_{ref}} \end{aligned} \tag{4.21}$$

where C_L = aircraft lift coefficient at initial cruise altitude

W_1 = weight at the initial cruise

r_1 = density at the initial cruise altitude

V_1 = Cruise velocity at initial cruise

M = Cruise Mach number

a_1 = Speed of sound at the initial cruise altitude

S_{ref} = Aircraft reference area

With Equation (4.21), we can solve for the altitude since the density and speed of sound are functions of altitude. This is done by considering the standard atmosphere equations which are applied to Equation (4.22), which is Equation (4.21) rearranged to reflect the terms dependant on altitude on the left hand side.

$$r(h)\,a(h)^2 = \frac{2C_L}{W_1 M^2 S_{ref}} \tag{4.22}$$

Once the initial cruise altitude is calculated, the rate of climb can be calculated using Equation (4.23).

$$ROC = \left(\frac{T}{W_1} - \left(\frac{L}{D}\right)^{-1}\right)\left(\frac{V_1}{1+k}\right) \tag{4.23}$$

where k = correction term for flight acceleration. For constant Mach number, below 36089 ft, k= -0.1332 M^2. The correction factor is not applied for altitudes above 36089 ft.

4.2.7.2. Range

In the range calculation, a weight fraction method is used to account for the warm-up, taxi, takeoff and climb performance. Although the calculation for this segment of the mission needs to be improved or replaced with a higher fidelity method, it is sufficient for the range calculation at this present time. The range for the cruise segment is calculated using the Breguet range equation, shown in Equation (4.24).

$$Range = \frac{L}{D}\left[\frac{V}{sfc_{cruise}}\right]\ln\left(\frac{W_{initial}}{W_{final}}\right) \tag{4.24}$$

No fuel allotment is provided for the descent and landing segment of the mission. Also, a reserve range of 500 nmi is removed from the calculated value.

4.2.8. Field Performance

The field performance section is used to provide the metrics for the field performance constraints. There are five different field performance metrics that are considered:

- Second segment climb gradient
- Balanced Field Length
- Landing distance
- Missed approach climb gradient
- Approach velocity

4.2.8.1. Second segment climb gradient

The second segment climb gradient is defined as the ratio of the rate of climb to the forward velocity at full throttle while one engine is inoperative and the gear retracted, over a 50 foot obstacle. This can be approximated using Equation (4.25) at the conditions specified.

$$g_{climb} = \arcsin\left(\frac{T}{W} - \frac{1}{L/D}\right) \tag{4.25}$$

4.2.8.2. Balanced Field Length

The balanced field length calculation is made based on the empirical estimation from Torenbeek [88]. This equation is given in Equation (4.26).

$$BFL = \frac{0.863}{1+2.3G}\left(\frac{W/S}{r\,gC_{L_{climb}}} + h_{obstacle}\right)\left(\frac{1}{T/W-U} + 2.5\right) + \left(\frac{655}{\sqrt{\frac{r}{r_{SL}}}}\right) \tag{4.26}$$

where BFL = Balanced field length (ft)

G = g_{climb} - g_{min}

g_{climb} = Second segment climb gradient as calculated in previous section

g_{min} = Minimum second segment gradient limits as given in Chapter 3

C_{Lclimb} = C_L at climb speed (1.2 V_{stall})

$h_{obstacle}$ = obstacle height (50 ft)

U = 0.01 C_{Lmax} + 0.02 for flaps in takeoff position

4.2.8.3. Landing distance

The landing distance is determined using methods suggested by Roskam and Lan [89]. It defines the three legs in the landing distance calculation, which are the air distance, free roll distance, and brake distance. The air distance is the distance from the 50 foot obstacle to the point of wheel touchdown, including the flare distance. The free roll distance is the distance between touchdown and the application of the brakes. The brake distance is the distance covered while the brakes are applied. Although landing distance is usually associated with the approach velocity, both are considered separately in the MDO formulation.

4.2.8.4. Missed approach climb gradient

The calculation of the missed approach climb gradient is similar to that of the second segment climb gradient with the exception that all the engines are operating, and the weight of the aircraft is at a landing configuration.

4.2.8.5. Approach velocity

The approach velocity is taken to be the same as the missed approach velocity. This velocity is evaluated during the missed approach climb gradient calculation.

4.2.9. Stability and Control

The absence of a tail on the BWB demands careful attention to the longitudinal control authority of the design. The stability and control analysis establishes maximum and minimum center of gravity (CG) limits on the BWB aircraft based on certain criterion for longitudinal control. During the mission profile of the aircraft, the actual CG travel of the aircraft must lie within the aforementioned CG limits. To establish the design constraints to achieve this, the determination of two critical quantities are needed:

- The CG travel on the BWB during the entire mission of the aircraft
- The maximum and minimum center of gravity limits based on certain control criteria

4.2.9.1. BWB CG travel

The BWB CG travel calculation is based in part on methods and guidelines provided by Chai et al. [90]. This method involves identifying individual component weights and defining the longitudinal CG location for each component. Some of these components will be assigned a maximum and minimum longitudinal CG location. Figure 4-7 provides a planform schematic showing the placement of the fuel tanks, passenger cabin and afterbody on the aircraft. The final goal is to be able to calculate the CG travel at four different weight conditions:

- Operational empty weight

- Zero fuel weight
- Operational empty weight with full fuel
- Takeoff gross weight

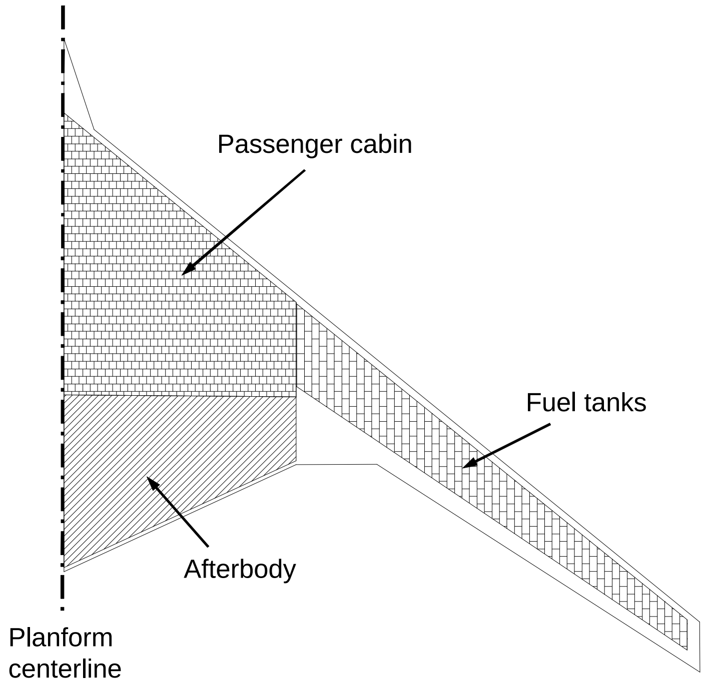

Figure 4-7: Planform schematic of the BWB showing placement of the fuel tanks, passenger cabin and afterbody

4.2.9.1.1. Wing CG location

The CG location of the wing should lie between the fore and aft wing spars. The wing CG location is calculated by considering the average CG location of the front and rear spars in each of the four span sections. Since the spar densities and thickness distributions are unknown, we assume a constant material thickness and span distribution. This reduces the calculation to a consideration of only the planform geometry of the section. We also assume that the front spar lies at the 10% chord location and the rear spar at the 70% chord location. For each individual section, the CG location of the front and rear spars in that section is determined, and the overall location is determined by a weighted average (of the section areas).

4.2.9.1.2. Cabin CG location

The cabin CG location is assumed to be acting through the centroid of the passenger cabin area. The passenger cabin area is defined to extend from the leading edge of the first and second span sections to the 60% chord location of those sections.

4.2.9.1.3. Afterbody CG location

The afterbody is defined as the section of the aircraft directly behind the passenger cabin. The CG location of the afterbody is assumed to lie at the average forward 1/3 afterbody chord location.

4.2.9.1.4. Anti-icing system CG location

The anti-icing system CG location is assumed to be between the forward spar (10% chord location) and the rear spar (70% chord location) of the wing.

4.2.9.1.5. Fixed weights CG location

The fixed weights are defined to include the pneumatics, auxiliary power, electrical, air-conditioning and avionics weight. Without any specific details on the placement locations of these systems, it is assumed that they will be located in the afterbody of the aircraft, and therefore its CG location is the same as the afterbody's.

4.2.9.1.6. Furnishing CG location

The furnishing CG location is set to be the same as the passenger cabin CG location.

4.2.9.1.7. Instruments CG location

The instruments CG location is assumed to be located 5 feet from the nose of the aircraft. This should place the instrument CG location inside the aircraft cockpit.

4.2.9.1.8. Flight controls and hydraulics CG location

The flight controls and hydraulics systems are most likely to be located behind the rear spar of the wing. Therefore, their CG locations are assumed to be at the 1/3 of the chord of the wing section behind the rear spar. This CG location is calculated from only the third and fourth span sections of the BWB.

4.2.9.1.9. Payload CG location

Since the payload is assumed to be located directly under the passenger cabin, its CG location is set the same as the passenger cabin CG location.

4.2.9.1.10. Propulsion CG location

At present, the exact location of the propulsion system is not determined. Hence, the propulsion CG location is assumed to be centered at the 95% root chord location. This assumption should be changed once the propulsion system location is determined. However, based on previous BWB designs, their propulsion systems usually lie at about the 95% root chord location.

4.2.9.1.11. Landing gear CG location

The landing gear CG location is especially difficult to ascertain. This is mainly because its position is dependant on the overall aircraft CG location. In this assessment, it is assumed that the landing gear CG location is located at the centroid of the entire BWB planform.

4.2.9.1.12. Operational empty weight and zero fuel weight CG locations

With the component weight provided by the weight estimation routine, and the CG locations as explained above, the overall CG location of the BWB aircraft at operational empty weight (OEW - weight of the aircraft without fuel and payload) and zero fuel weight (WZF - weight of the aircraft without fuel but with payload) can be determined. Both the possible front and rear CG locations are determined, but the average of the two locations is used in the final control constraint assessment. This is done to allow future modifications to the program to use the front and rear CG location calculations. When higher fidelity CG estimation formulations are implemented in the future, it is likely that the front and rear CG locations will provide a better representation of the CG location of the entire aircraft [90].

4.2.9.1.13. Fuel weight CG location and fuel pumping

Fuel pumping in aircraft for CG control is not a new concept. For example, the Concorde relies on fuel pumping to keep the aircraft CG within acceptable limits during flight. The same concept will be used in the BWB to control the CG travel of the aircraft to lie within the acceptable control limits of the aircraft. Based on the geometry of the aircraft fuel tanks, their maximum capacity and the volume of fuel required for the aircraft mission, the CG locations of the fuel when packed fully inboard and fully outboard can be determined. An explanation of this calculation procedure is given in Section 4.2.6.2.

4.2.9.1.14. Takeoff gross weight (TOGW) and operational empty weight with full fuel weight (OEW + Fuel weight) possible CG locations

With the fuel weight CG locations when the fuel is shifted both fully inboard and outboard, and the OEW and WZF CG locations, the possible CG location range of the BWB at TOGW and OEW + Fuel weight can be determined. At these two weight conditions, only a range of CG locations are prescribed, within which fuel pumping for CG control is used.

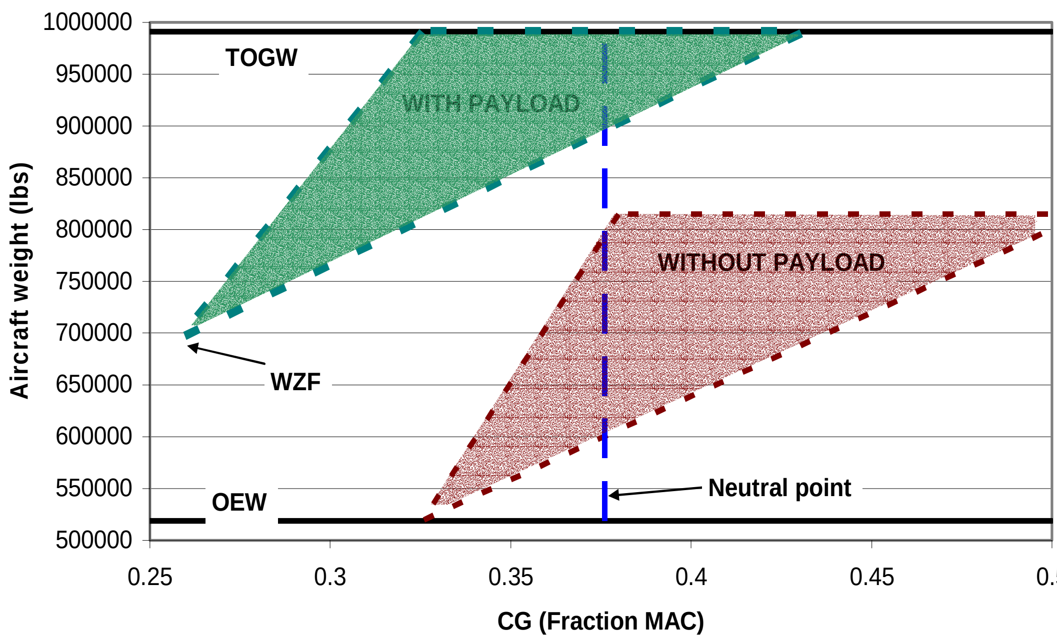

Figure 4-8: Plot of the range of possible CG location using fuel pumping for the 1994 BWB design in two weight configurations: with and without payload.

The CG locations calculated at the four weight conditions provide a comprehensive representation of the CG travel in the BWB aircraft throughout the entire mission of the aircraft. The OEW and OEW + Fuel weight conditions provide CG travel locations when the aircraft is without any payload. The WZF and TOGW conditions are when the aircraft is with full payload. Figure 4-8 shows the CG travel for the 1994 BWB configuration. The shaded areas represent the achievable CG location at a certain fuel weight condition by using fuel pumping.

4.2.9.2. CG limits for acceptable longitudinal control

Longitudinal control center of gravity limits are determined by two assessment criteria. These criteria are based in part on those used by the European MOB project [36] to design a BWB aircraft. The two criteria are evaluated at the approach flight phase. Based on a minimum approach velocity of 140 knots, a minimum velocity, V_{min} of 110 knots is used for the evaluation of the constraints. This is done to provide a 30% safety margin on approach. The two criterions that are used are:

- Maximum elevon deflection boundary at V_{min}
- Maximum angle-of attack boundary at V_{min}

A detailed explanation of the two criterions will be given later.

To evaluate the longitudinal control characteristics of the BWB aircraft, a Vortex Lattice Method (VLM) program, <u>JKayVLM</u> is used to estimate the elevon control derivatives as well as the lift and moment coefficient derivatives. These derivatives are expressed as linear expansions of the lift and moment coefficients. These expressions will then help in determining the CG location limits subject to the aforementioned criteria.

4.2.9.2.1. Maximum elevon deflection boundary at V_{min} criteria

The maximum elevon deflection boundary at V_{min} criteria requires that the CG location of the aircraft should be within limits such that the aircraft elevon trim angles do not exceed the maximum deflection angles of ± 20°. The angle of attack at this condition is that required to provide lift at 1G flight. This criterion sets a forward and rear CG limit for the aircraft.

To calculate the CG limits, consider Equations (4.27) and (4.28) that describe the lift and moment coefficient (calculated about the nose of the aircraft).

$$C_L = C_{L_0} + C_{L_\alpha}\alpha + C_{L_{\delta_e}}\delta_e \tag{4.27}$$

$$C_M = C_L x_{CG} + C_{M_0} + C_{M_\alpha}\alpha + C_{M_{\delta_e}}\delta_e \tag{4.28}$$

Rearranging,

$$\alpha = \frac{C_L - \left(C_{L_0} + C_{L_{\delta_e}}\delta_e\right)}{C_{L_\alpha}} \tag{4.29}$$

$$x_{CG} = \frac{C_M - \left(C_{M_0} + C_{M_\alpha}\alpha + C_{M_{\delta_e}}\delta_e\right)}{C_L} \tag{4.30}$$

By setting δ_e equal to ±20°, and for trim conditions, C_M to 0, Equations (4.29) and (4.30) can be used to calculate the forward and rear CG limits given a certain lift coefficient (that is calculated based on the aircraft weight). Figure 4-9 shows a plot of the forward and rear CG limits set by the maximum elevon deflection criteria. The 1994 BWB design planform was used in this example.

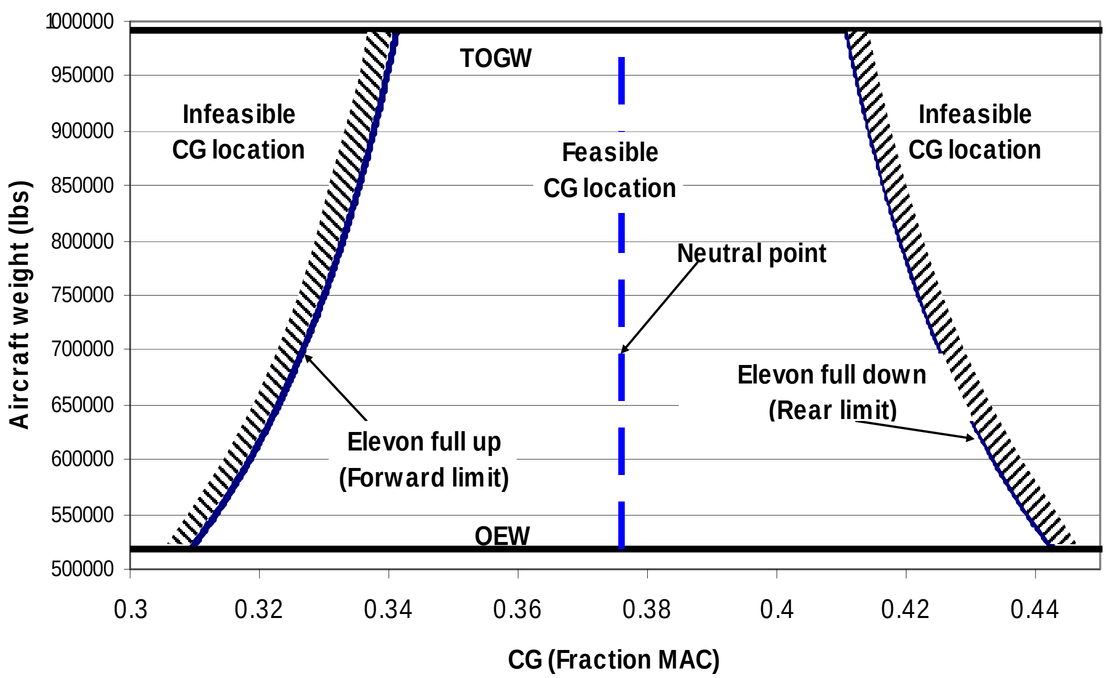

Figure 4-9: Forward and rear CG limits set by the maximum elevon deflection criteria. Results are for the 1994 BWB planform

From Equation (4.30), we see that the CG boundary is dependant on the zero angle of attack moment coefficient, C_{M_0}. Presently, we assume a thin, no camber shape for the calculation in JKayVLM. Therefore, C_{M_0} is calculated to be zero. In reality, C_{M_0} will not have a zero value, but we do not currently have a reliable method to estimate this value without incurring large computational costs. As more CFD calculations are being performed, a response surface method could be used to model the C_{M_0} behavior of the BWB design.

4.2.9.2.2. Maximum angle-of attack boundary at V_{min}

The maximum angle-of-attack boundary at V_{min} criteria requires that the aircraft CG is at a location such that the angle of attack of the elevon-trimmed aircraft does not exceed the stall angle of attack. This criterion sets a forward center of gravity limit. Currently, the stall angle of attack is taken to be at 27°.

To calculate the CG limit set by this criterion, consider again Equations (4.27) and (4.28). Rearranging the equations, we get

$$d_e = \frac{C_L - \left(C_{L_0} + C_{L_a} a\right)}{C_{L_{de}}} \tag{4.31}$$

Using Equation (4.30) and (4.31), the forward limit set by the maximum angle of attack boundary at V_{min} can be calculated. The conditions for the calculations are: C_M = 0.0, a = 27° and C_L as calculated based on the aircraft weight. Figure 4-10 shows a plot of the forward CG limit set by the maximum angle of attack boundary at V_{min} criteria. The 1994 BWB design planform was used in this example.

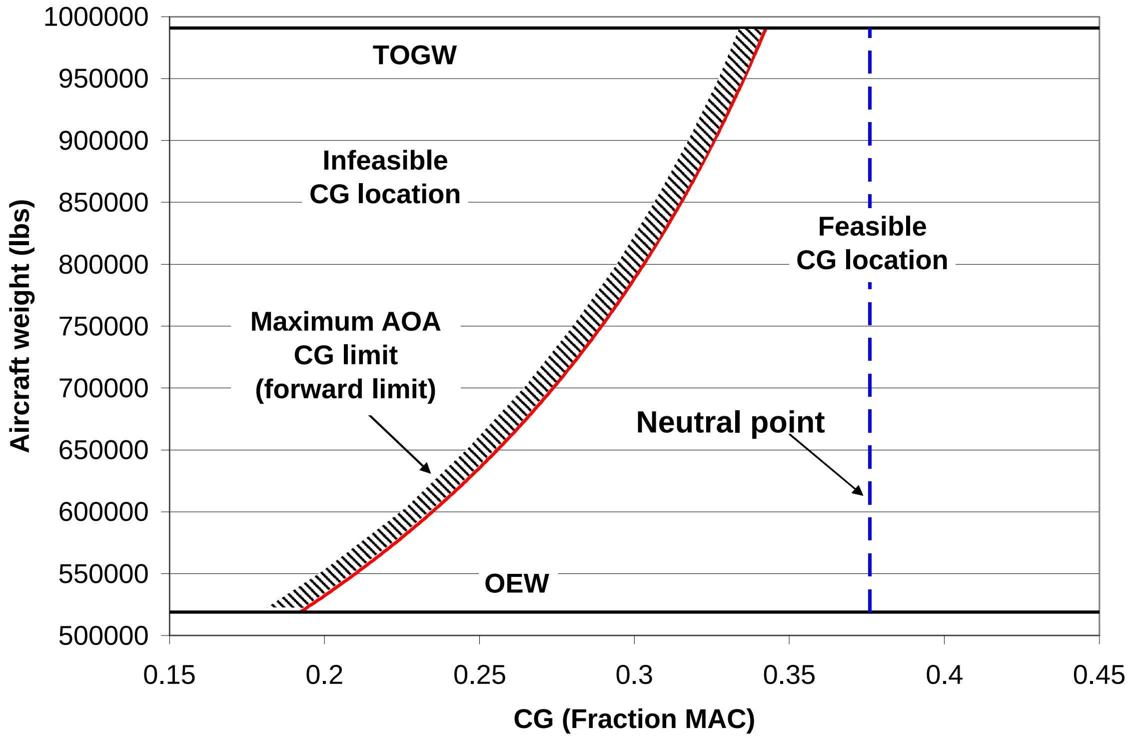

Figure 4-10: Forward CG limit determined by the maximum angle of attack criteria. Results are for the 1994 BWB planform.

4.2.9.2.3. Constraint value calculation

Figure 4-11 is a combination of Figures 4-8, 4-9 and 4-10. It shows that the maximum elevon deflection criteria CG limit is the critical forward CG limit at all aircraft weight configuration with the exception of weights close to TOGW. The rear CG limit is also set by the maximum elevon deflection criteria. By comparing these critical limits with the actual possible CG travel of the aircraft (shaded area), we find that the BWB aircraft can satisfy the longitudinal control constraints in weight configurations without payload. However, with a full payload, the BWB aircraft only satisfies the constraints at weights above approximately 830,000 lbs. The aircraft does not satisfy the constraints at weight configurations below 830,000 lbs. Therefore in the 1994 BWB design configuration case, not all the control constraints are satisfied.

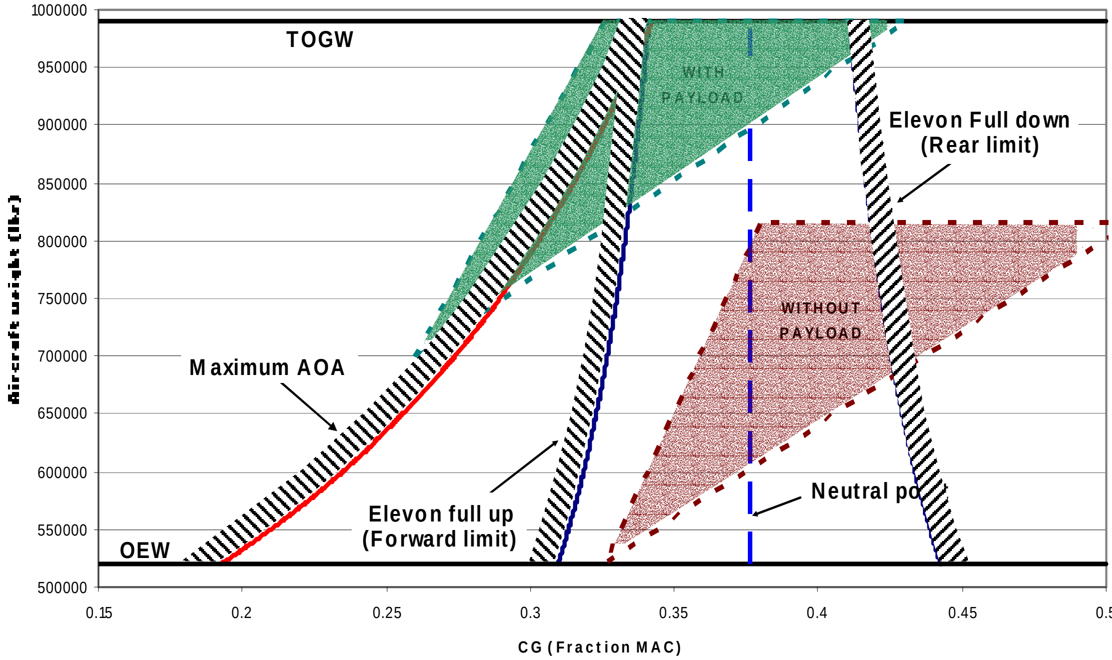

Figure 4-11: Plot shows the comparison between the aircraft CG limits for acceptable longitudinal control and the possible CG locations that can be achieved through fuel pumping. The figure shows that although the aircraft is within the CG limits without payload, it cannot satisfy the CG limits when the aircraft is below 830,000 lbs with payload.

Quantitatively, the control constraints are evaluated at the four mentioned weight conditions as critical conditions that represent the entire aircraft CG envelope. By evaluating the stability and control constraints at these aircraft weight conditions, we should be able to capture the entire CG travel of the aircraft compared to the CG limit profile. Listing these four weight conditions again for reference:

- Operational empty weight (OEW)
- Operational empty weight + Full fuel weight (OEW + Fuel weight)
- Zero fuel weight (WZF)
- Takeoff gross weight (TOGW)

To calculate the constraint values at WZF and OEW, the CG location of the aircraft at those weight conditions are compared to the critical forward and rear CG limits. A piecewise linear function is generated based on the distance between the neutral point and CG limits at that particular weight condition, with the constraint value reaching a maximum normalized value of 1 at the neutral point. Figure 4-12 shows the variation of the value of the constraint with respect to CG position, given a certain neutral point and CG limits. The value of the constraint is calculated based on this linear function given the position of the aircraft CG at the particular weight condition. A negative constraint value represents an infeasible design. It should be noted here that this function was formulated to represent the permissible aircraft CG envelope mathematically. As a result, the gradients of these constraints will be determined in part by the type of function that is used. Practically, no difficulty has been encountered in the optimization process as a result of the choice of using a linear piecewise function to represent the CG envelope. We have not yet tested the use of other mathematical functions such as a continuous quadratic function.

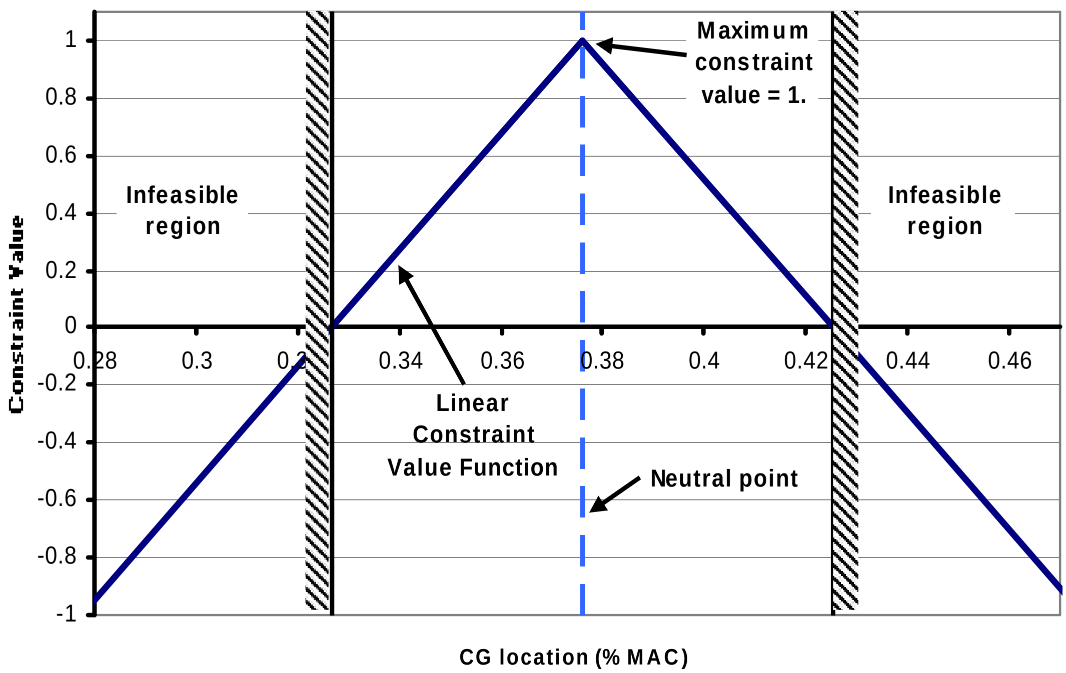

Figure 4-12: Plot showing the linear piecewise function that is used to determine the control constraint value at a certain weight configuration.

A slightly more involved treatment needs to be applied in determining the constraint value at the TOGW and OEW + Fuel weight conditions. We must account for the range of CG locations that can be achieved using fuel pumping. If the neutral point lies within the aircraft possible CG range, the constraint will automatically be assigned a value of 1. However, if the neutral point lies outside the aircraft's possible CG range, a ‘critical’ CG location will be calculated. This critical CG location will be determined by the closest possible CG location to the neutral point that can be achieved using fuel pumping. As with the WZF and OEW constraints, a piecewise linear function will be generated based on the distance between the neutral point and the CG limits at that particular weight condition. The constraint value will be evaluated based on the piecewise linear function and the ‘critical’ CG location. As before, a negative constraint value represents an infeasible design.

Since the aircraft CG is allowed to be forward or aft of the neutral point, this arrangement allows for the BWB aircraft design to be statically stable or unstable. We assume that if the aircraft is unstable at any point, the flight control software will be designed to take this into account. It is entirely possible that the static stability of the aircraft will change from a stable to an unstable configuration (or vice versa) during the course of the aircraft mission. In the distributed propulsion BWB MDO framework, the aircraft static stability is not taken into account.

4.3. MDO Implementation

All the methods are implemented in FORTRAN as individual stand alone programs. Using Phoenix Integration’s Analysis Server®, the compiled codes are wrapped and published on Analysis Server® to be used. Phoenix Integration’s ModelCenter® is then used to integrate the different programs to create the distributed propulsion BWB MDO code. The built-in DOT optimizer is used as the optimization tool to perform the optimizations. In ModelCenter®, we use the ‘geometry component’ to create a quick three dimensional geometry representation of the BWB planform, which aids in visualizing the design variables.

4.3.1. Formulation changes due to sub-optimal solutions

The current version of the distributed propulsion BWB MDO program contains several formulation changes from the original MDO formulation. All these changes were made to avoid sub-optimal solutions that were encountered while performing optimization studies. The following sections describe the changes in formulation that were made.

4.3.1.1. Trailing edge sweep angle at the first wing section

During the development of the distributed propulsion BWB MDO code, we found that the optimizer would design a conventional BWB aircraft with a positively swept trailing edge at the first wing section. This was deemed to be undesirable. The BWB MDO code does not account for the chordwise placement of the engines. For a conventional BWB, the engines are placed towards the trailing edge at spanwise positions close to the root. With this in mind, it would not be desirable to have a swept trailing edge section, although a forward swept trailing edge would be tolerable. To prevent the optimizer from designing the BWB aircraft with a swept trailing edge at the first wing section, a constraint was implemented. This constraint calculated the trailing edge sweep at the first wing section, preventing it from being positive.

Later, while performing parametric optimization studies, we found the presence of a sub-optimal solution. Figure 4-13 shows the TOGW variation of an optimized distributed propulsion BWB aircraft with changing duct weight factor. The duct weight factor will be explained in Chapter 5. The first line at a higher TOGW variation corresponds to the optimal solution after having started from the 1994 BWB design. As we can see, there is an indication of the presence of this sub-optimal solution with the sudden increase and decrease in TOGW with varying duct weight factor. The second line of a lower TOGW variation is a result of the optimization starting from a different design. This line indicates that there is a lower optimum design that cannot be reached by the optimizer when started with the 1994 BWB design.

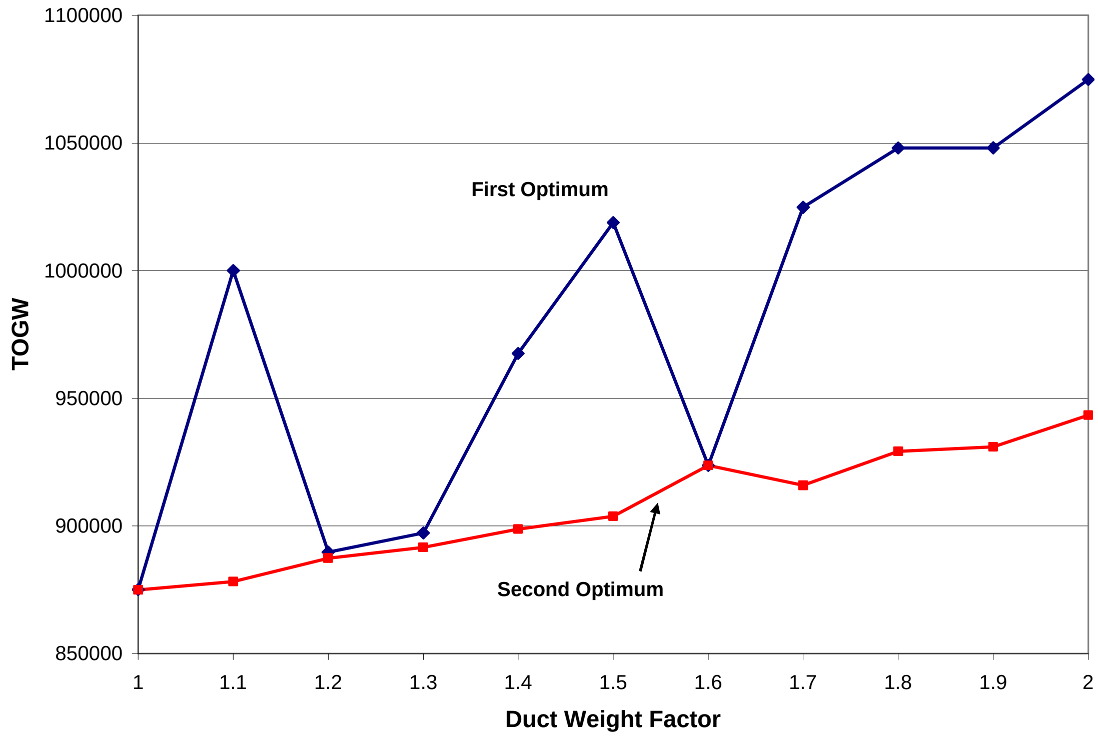

Figure 4-13: Figure shows the variation of the TOGW with varying duct weight factor. The blue line is the optimum design if started from the 1994 BWB design planform. The red line is the optimum design if started from the optimum design planform at duct weight factor = 1.6. This figure shows the presence of a sub-optimal solution.

To understand the cause of the presence of the sub-optimal solution, the results at both optimum designs at a duct weight factor of 1.6 was considered. Using these two points, an alpha plot [91] was created. An alpha plot is created by examining the design along a linear interpolation line of the design variable between the two optimum points. Mathematically, the design variables vector is represented in Equation (4.32)

$$\boldsymbol{X} = (1-a)\boldsymbol{X}_1 + a\boldsymbol{X}_2 \tag{4.32}$$

where $\boldsymbol{X}$ = Design variables vector for a certain value of α

$\boldsymbol{X}_1$ = Design variables vector of the first design

$\boldsymbol{X}_2$ = Design variables vector of the second design

a = Alpha varying between 0.0 and 1.0.

The variation of the objective function and constraints are examined along this line. Figure 4-14 shows the alpha plot between these two points, showing the constraint value of selected critical constraints.

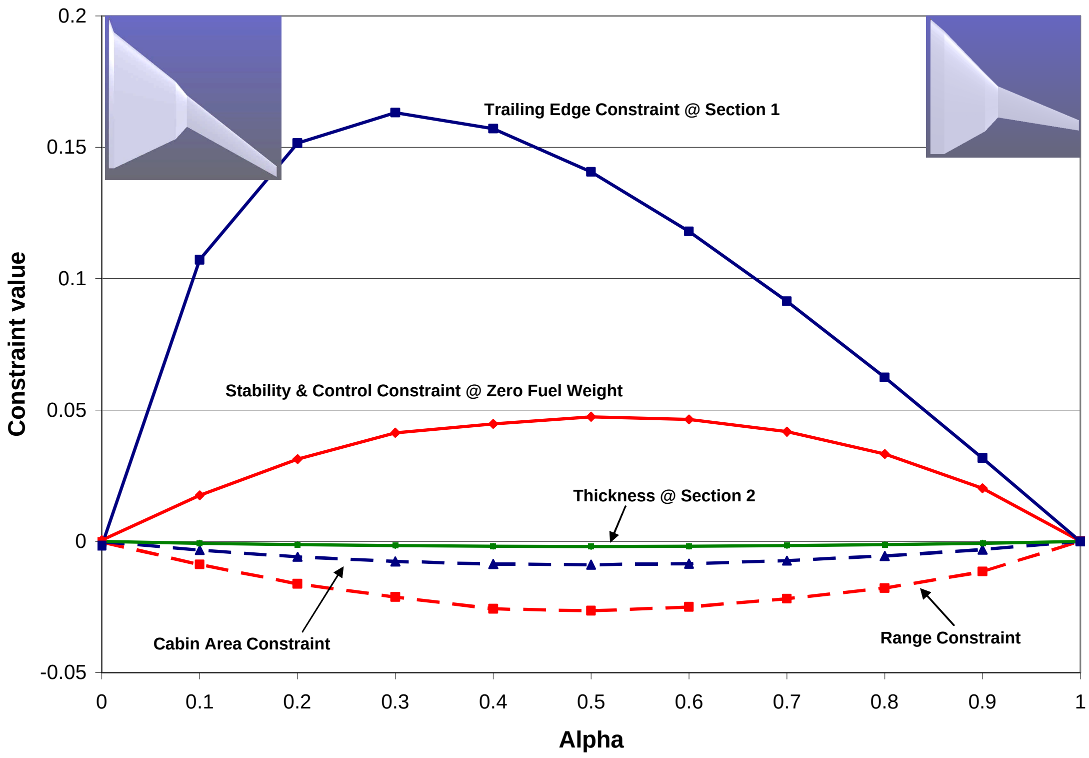

Figure 4-14: Alpha plot showing the variation of selected constraints between two optimum designs. The design at alpha = 0, is the higher TOGW design while the design at alpha = 1.0 is the higher TOGW design. Positive constraint values represent a violated constraint. The planform on the upper left hand corner corresponds to the design at alpha = 0, and the planform on the upper right hand corner corresponds to the design at alpha = 1.

It is clear from the alpha plot that the trailing edge constraint at the first wing section is the critical constraint that is preventing the optimizer from reaching the lower TOGW design.

To avoid this sub-optimal solution, several changes were made. First the trailing edge at the first wing section constraint was eliminated. Then, the quarter-chord sweep angle at the first wing section was replaced by the trailing edge sweep angle as a design variable. A side constraint imposed on the design variable then prevents the sweep angle from becoming positive. In effect, this replaces the non-linear inequality constraint with a linear side constraint. However, an additional constraint has to be added to prevent the quarter-chord sweep at this section from being negative. The quarter chord sweep design variable that was replaced had a side constraint imposed on it that prevented the sweep angle from being negative. Hence, an inequality constraint has to be implemented to replicate this effect.

Figure 4-15 shows the result of this formulation change. It is similar to Figure 4-14 except with a new line which represents the optimum design using the new formulation, starting from the 1994 BWB design. It is clear that this formulation change has prevented the optimizer from stopping prematurely at the higher TOGW optimum point.

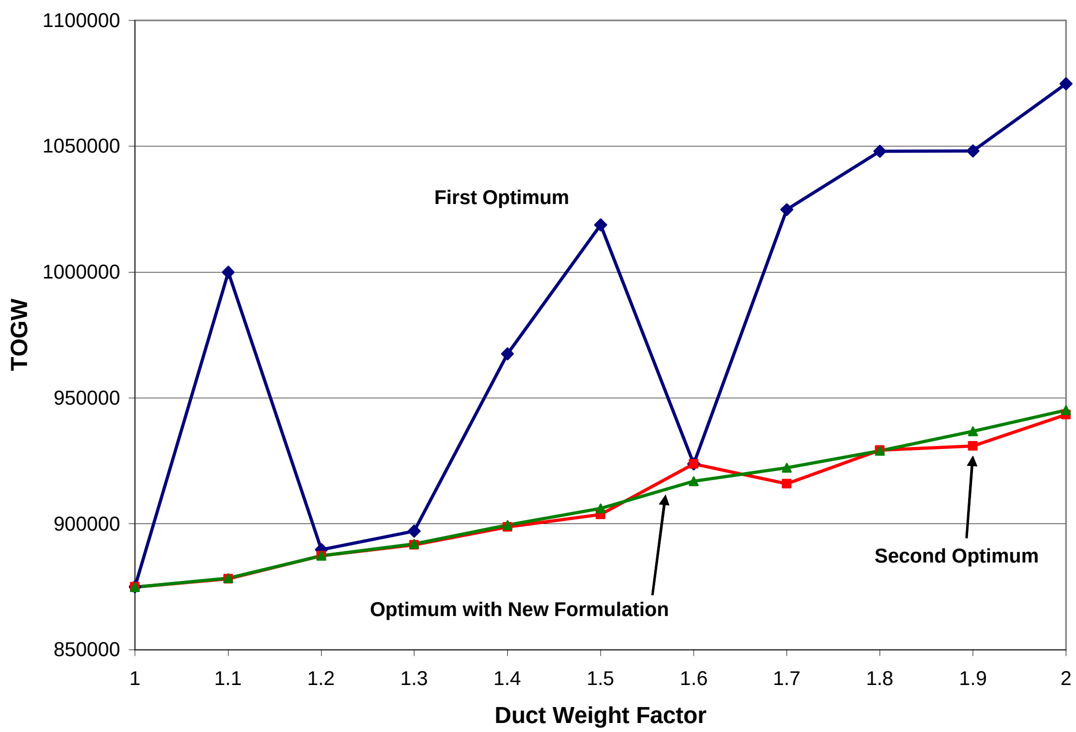

Figure 4-15: Figure shows the variation of the TOGW of the BWB aircraft with varying duct weight factor. This figure is similar to Figure 4-14, except that the green line represents the optimum design using the new formulation, starting from the same point as that used for the blue line.

4.3.1.2. Cabin Aspect ratio

While performing some of the optimization parametric studies, we found the presence of another sub-optimal solution even after implementing the changes outlined in

Section 4.3.1.1. Figure 4-16 shows the TOGW variation of an optimized distributed propulsion BWB aircraft with changing duct efficiency factor. The duct efficiency factor will be explained in Chapter 5. We see that the optimizer stops at a higher TOGW optimum when starting from point 1, as opposed to the solution obtained starting from point 2. The non-monotonic variation in the TOGW behavior also suggests that the optimization problem is ill-formed.

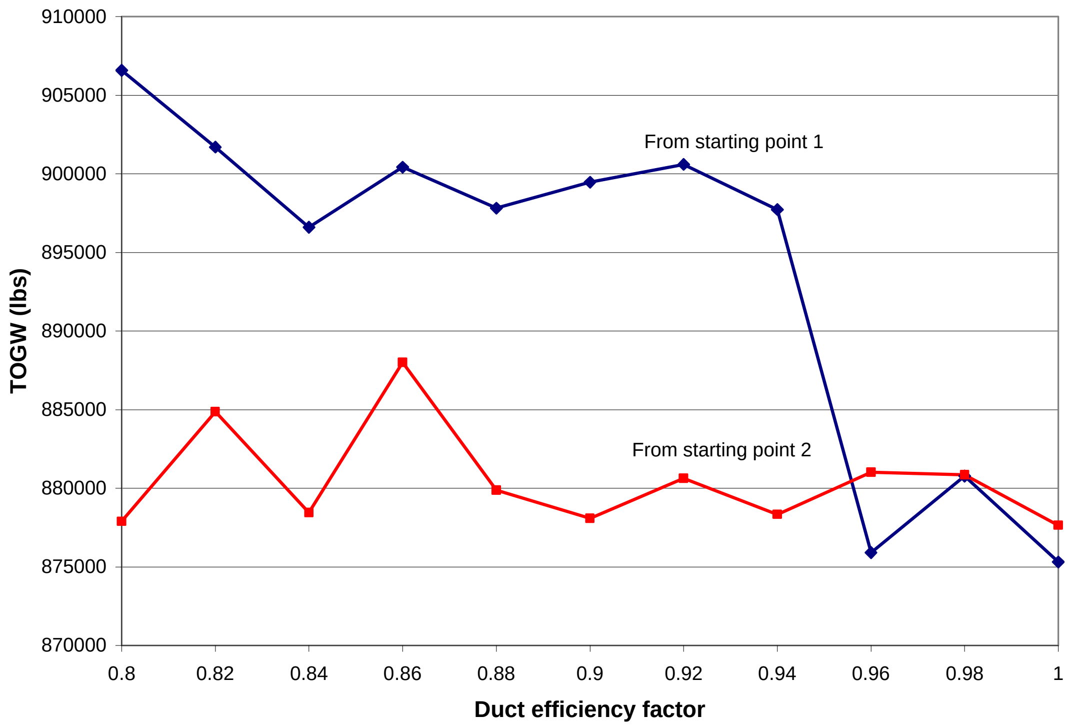

Figure 4-16: Figure shows the variation of the TOGW with varying duct efficiency factor. The blue line is the optimum design if started from design point 1. The red line is the optimum design if started from a different design point, point 2. The presence of a sub-optimal solution can be seen by noticing that the optimization stops prematurely in most cases when starting at point 1.

To identify the cause of the sub-optimal solution, the results at a duct efficiency of 0.9 was examined. An alpha plot was created to look at intermediate designs between the optimum obtained from starting at point 1 and optimum obtained from starting at point 2. Figure 4-17 shows the alpha plot between these two points, showing the constraint value at selected constraints that were deemed important. In Figure 4-17 a negative constraint value represents the feasible design region while a positive value represents the infeasible region. It is clear that the cabin aspect ratio constraint is preventing the optimizer from reaching the lower TOGW optimum.

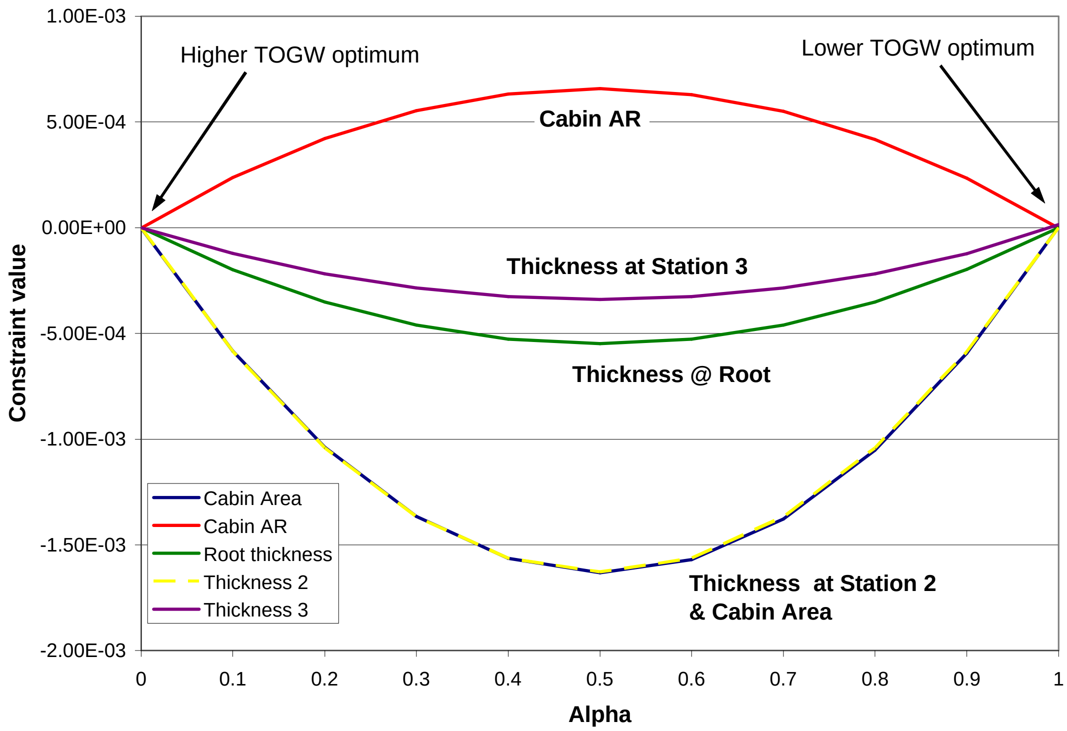

Figure 4-17: Alpha plot showing the variation of selected constraints between two optimum designs. The design at alpha = 0, is the higher TOGW design while the design at alpha = 1.0 is the higher TOGW design. Positive constraint values represent a violated constraint.

To understand the behavior of this constraint, further examination into the formulation of this constraint was required. The cabin aspect ratio is defined as:

$$AR_{Cabin} = \frac{b_{cabin}}{S_{cabin}} \tag{4.33}$$

where b_{cabin} = the passenger cabin span

S_{cabin} = the passenger cabin planform area.

Figure 4-18 shows the alpha plot of the passenger cabin span and planform area in. We can see that the two variables seem to behave linearly between the two optimum designs. However, when we take the ratio of the two to obtain the cabin aspect ratio, the behavior ceases to become linear. This is shown in Figure 4-19. It is this non-linear variation in the cabin aspect ratio that is causing the sub-optimal solution. A reformulation of this constraint is needed.

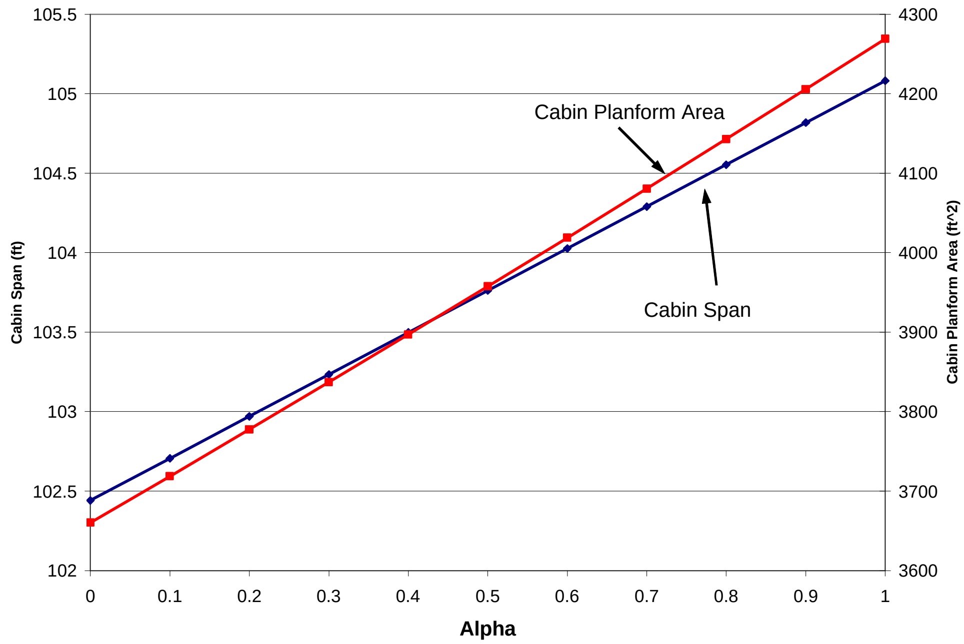

Figure 4-18: Alpha plot showing the variation of the aircraft cabin span and cabin planform area between two optimum designs. The design at alpha = 0, is the lower TOGW design while the design at alpha = 1.0 is the higher TOGW design

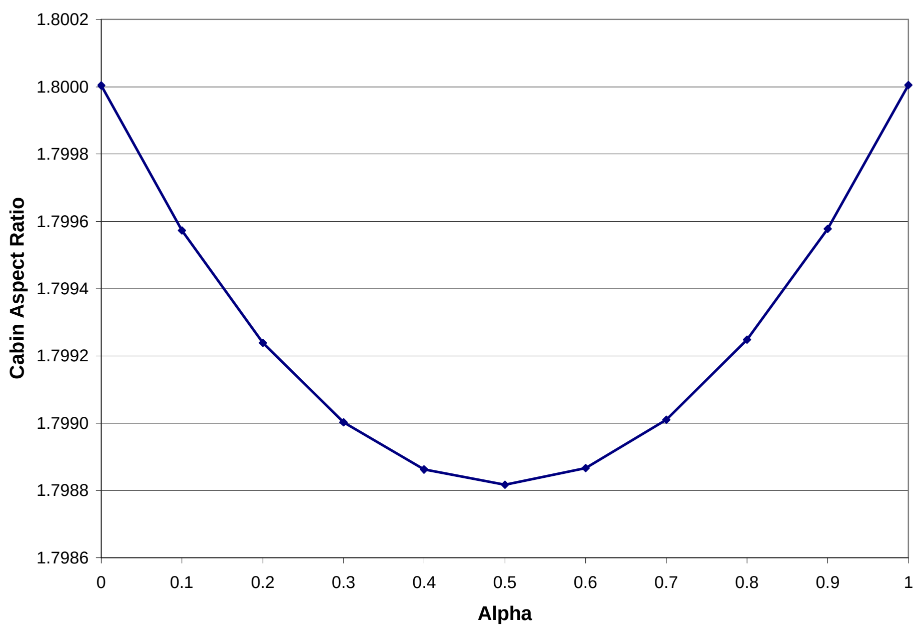

Figure 4-19: Alpha plot showing the variation of the aircraft cabin aspect ratio between two optimum designs. The design at alpha = 0, is the lower TOGW design while the design at alpha = 1.0 is the higher TOGW design

Consider the constraint formulation as shown in Equation (4.34). It specifies that the cabin aspect ratio is constrained to a prescribed minimum value.

$$AR_{cabin} = \frac{b_{cabin}}{S_{cabin}} \geq AR_{cabin\_min} \tag{4.34}$$

By rearranging Equation (4.34), we can rewrite it in the form shown in Equation (4.35).

$$b_{cabin} - AR_{cabin\_min} S_{cabin} \geq 0 \tag{4.35}$$

Doing this preserves the linearity of both the cabin span and cabin area variation. However, although mathematically true, rearranging the constraint equation to that in Equation (4.35) had resulted in the constraint value not being normalized. To normalize the constraint value, it is divided by a nominal value of the cabin planform area. Therefore, the new cabin aspect ratio constraint formulation is shown in Equation (4.36)

$$-\frac{b_{cabin} - AR_{cabin\_min} S_{cabin}}{S_{cabin\_nominal}} \leq 0 \tag{4.36}$$

Figure 4-20 shows the result of this new formulation. The green line is the variation of the aircraft TOGW with respect to the duct weight factor, optimized starting from point one. Here, we see that the TOGW behavior is smooth, and that the optimum range is close to that obtained from starting at point 2 previously. We can conclude from this figure that the reformulation has resulted in preventing the optimizer from stopping prematurely at the sub-optimal solution. The optimization problem is also better formed compared to that previously as indicated by the smooth variation in the TOGW behavior.

Although this formulation is better, Figure 4-20 shows that there is a possibility that a lower TOGW optimum (than that obtained with the new formulation) is present at least in two instances. These situations occur when the duct efficiency factor is equal to 0.8 and 0.84. We can see that the results from the old formulation at these two instances seem to result in a lower TOGW than with the new formulation. Upon closer inspection, we found that at each instance, both optimum designs were similar. The differences were a result of small variations in the design variable values, well within the modeling uncertainty of this study. In fact, the TOGW difference between the two optima at duct efficiency factor = 0.8 is only by 0.7%. We can expect that this difference is well within the modeling uncertainty of the program.

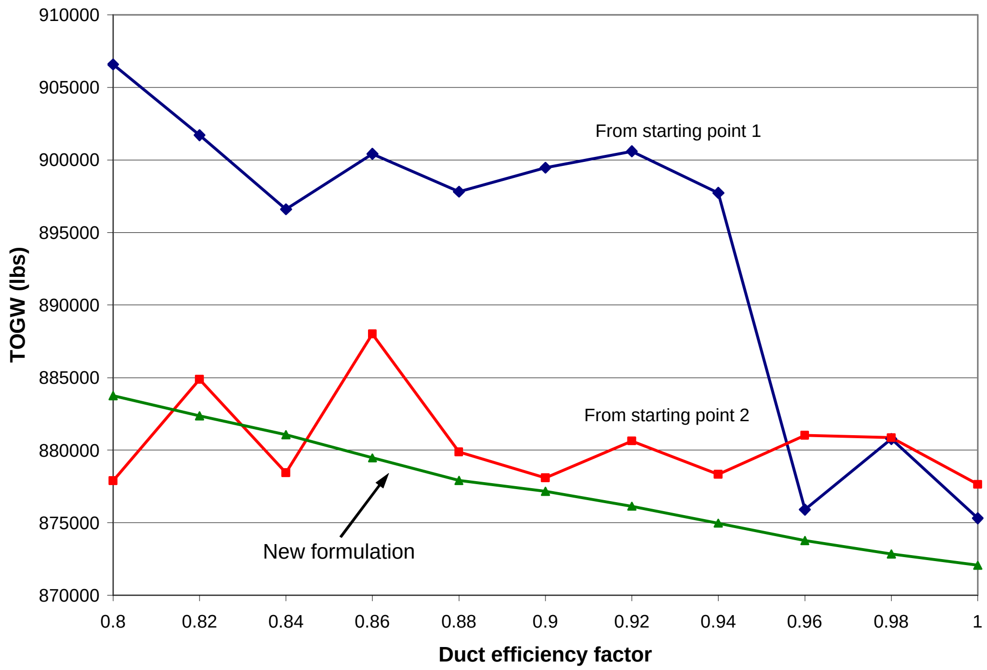

Figure 4-20: Figure shows the variation of the TOGW of the BWB aircraft with varying duct efficiency factor. This figure is similar to Figure 4-17, except that the green line represents the optimum design using the new formulation, starting from the same point as that used for the blue line.

4.3.2. Optimization strategies

The default constrained optimization method in ModelCenter® is the Method of Modified Feasible Directions. However, two other methods are available to the user: the Sequential Linear Programming method and the Sequential Quadratic Programming method. Based on previous experience with the Strut-Braced Wing MDO code [92], the Method of Modified Feasible Directions seems to give the best results in terms of avoiding sub-optimal solutions and fewest function evaluations. However, in a seminar by Gary Vanderplatts [93] from Vanderplatts R. & D., the Sequential Quadratic Programming method was recommended as a first choice in picking an optimization algorithm in ModelCenter®. In the distributed propulsion BWB MDO code, several optimization strategies have been adopted, including using a combination of the two aforementioned optimization methods and restarting optimization runs to force convergence. It is up to the user, and dependant on the MDO setup as to which strategy will work the best. The next sections will discuss ways the user can improve the optimization process.

It should be noted here that with a local optimization algorithm, it is not possible to determine if the optimum design found is the global optimum design. However, to increase the chances of reaching the global optimum design, the user should perform optimizations starting from different multiple starting designs. The best design is determined by selecting the optimum design with the lowest objective function out of the number of optimizations performed. With the distributed propulsion BWB MDO program, most of the optimizations will reach the lowest TOGW (the objective function) design of all the optimizations. To ensure that the optimizer did not stop prematurely at a sub-optimal design, the following optimization strategies should also be employed to see if it results in a better design.

4.3.2.1. Restarting optimization

From previous experience in the Strut-Braced Wing MDO program, the Method of Modified Feasible Directions seems to stop at a solution prematurely. The solution to this possibility was to restart the optimization process from the point at which the previous optimization stopped [92]. This process was found to result in the optimizer converging to a single optimum most of the time.

This method has also been adopted with the distributed propulsion BWB MDO program. However, unlike the results from the Strut-Braced Wing MDO program, this optimization strategy has not necessarily resulted in the optimizer converging to a single optimum when started from different initial designs. However, in certain instances, this method was found to help in the optimization process, when the optimizer seems to stop prematurely. Figure 4-21 shows the convergence history of one such case.

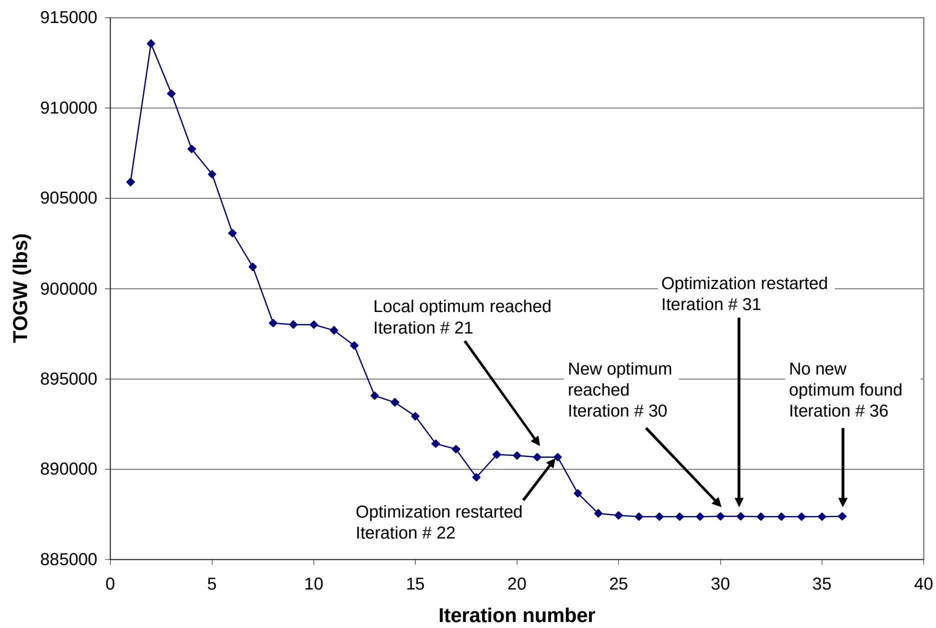

Figure 4-21: Plot showing the optimization iteration history of a distributed propulsion BWB aircraft design. It shows that a sub-optimal solution was reached at iteration number 21. The optimization was restarted and a new optimum was reached at iteration number 30. Although the optimization was restarted again, no new optimum was found.

4.3.2.2. Increasing the optimum design variables by a certain factor

If the strategy of restarting the optimization results in the optimizer stopping at a sub-optimal solution, another strategy adopted is to increase the optimum design variables by a certain factor and restarting the optimization. In some cases, an increase of approximately 1% would shift the initial design baseline away from the sub-optimal solution, but within the feasible design space. This shift places the initial design far enough away from the sub-optimal solution to allow the optimizer to look for a better optimum point. This strategy is a variation of starting the optimization at different design points.

It should be noted that when increasing the optimum design variables by a factor (say, by 1%), the fuel weight design variable usually would have to be increased by twice or three times that amount to satisfy the range constraint, and place the design point in a feasible design space. In practice, all the design variables should be increased, and then the fuel weight design variable would be increased until the range constraint is satisfied.

Figure 4-22 shows an instance where increasing the optimum design variable point resulted in finding a better optimum point.

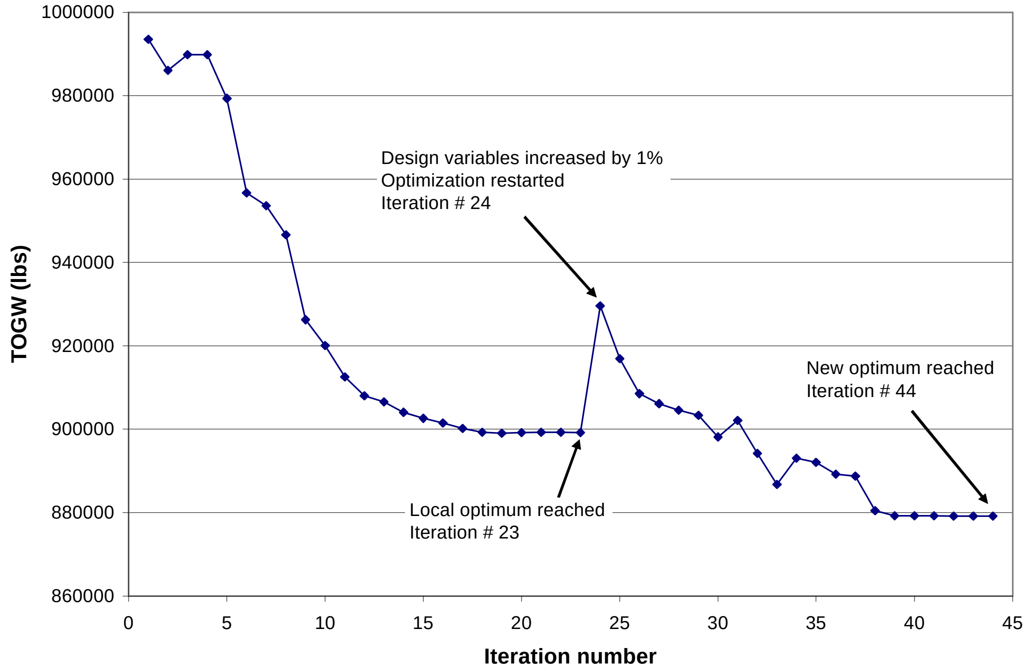

Figure 4-22: Plot showing the optimization iteration history of a distributed propulsion BWB aircraft design. It shows that a sub-optimal design was reached at iteration number 23. By increasing the stopping design variables by 1%, and restarting the optimization, a new optimum is reached.

4.3.2.3. Using a combination of optimizers

Another optimization strategy that can be used is to employ a combination of different optimization algorithms in succession. In some instances, the Sequential Quadratic Programming optimization algorithm will be used first, and then, using the Modified Method of Feasible Directions, the optimization will be restarted from where the previous algorithm stopped. In other instances, the opposite is done. Figure 4-23 shows an instance where the optimization strategy of restarting using different optimization algorithms has worked.

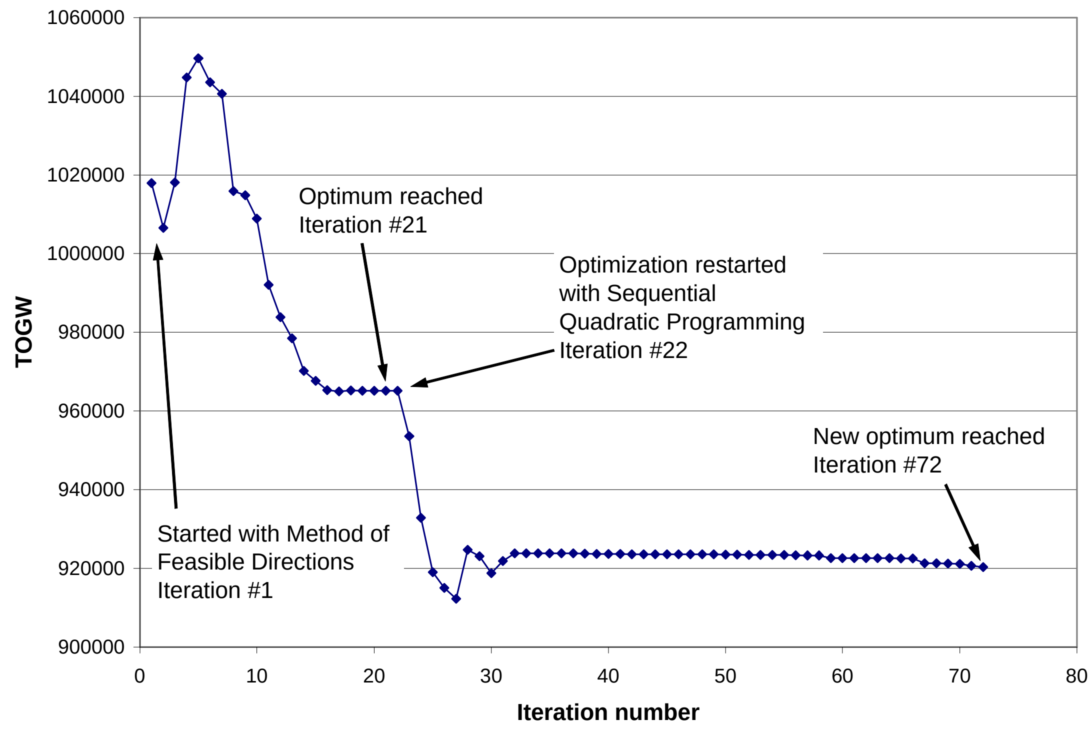

Figure 4-23: Plot showing the optimization iteration history of a conventional BWB aircraft design. It shows that a sub-optimal solution was reached at iteration number 21 after being optimized using the Method of Feasible Directions algorithm. The optimization was restarted using the Sequential Quadratic Programming algorithm at iteration number 22. This results in a new lower TOGW optimum reached at iteration number 72.

4.3.2.4. Strategy if optimizer fails to find a feasible design space

Occasionally, the optimizer fails to find the feasible design space. Most of the time when this happens, the infeasible design point where the optimizer fails is close to the feasible design space. What the user should do in this instance is to examine the constraints that are violated at the failed optimization stopping point. Then, by ‘tweaking’ certain design variables, the design point can be moved either closer or into the feasible design space. Table 4-2 gives a list of constraints that are usually found to be violated, and a corresponding design variable that can be ‘tweaked’ to change the value of that constraint. It should be noted here that these constraints are not only a function of their primary design variable, and often, changing the value of a design variable will change the value of two or three constraints. It is up to the user to decide the magnitude a certain design variable needs to be tweaked to strike a balance between letting one constraint move towards a feasible region while not causing other constraints to be violated. Experience has indicated that making changes as small as 0.1% to 0.5% of the design variable value is preferable.

Table 4-2: Table of probable violated constraints and their corresponding primary design variable

Violated constraint	Primary design variable
Range constraint	Fuel weight
Fuel volume constraint	*t/c* ratio at the fourth span station
Second segment climb gradient constraint	Thrust
Cabin area constraint	Position of the second or third span station
Cabin aspect ratio constraint	Position of the third span station
Thickness constraints	*t/c* ratios at the corresponding span stations

Chapter 5: MDO distributed propulsion models

As mentioned in previous chapters, the distributed propulsion concept that is considered here is one that ducts some amount of the cold engine exhaust out through the trailing edges of the wings (shown earlier in Figure 1-2). This arrangement is very similar to that of a jet wing or jet flap.

Jet flap applications are usually associated with STOL applications, with their need for high lift coefficients. There has been extensive theoretical and experimental work done investigating the jet flap concept, especially concerning its use in STOL applications. A discussion of previous jet flap and jet wing research can be found in Chapter 2, but there has been little detailed analysis of this arrangement as a propulsion system.

Distributed propulsion affects almost every aspect of the aircraft design. Each of these influences has to be identified and quantified to fully understand the concept. The propulsion system is now integrated closely with the aircraft structure. Interaction effects are important, and need to be modeled. In this chapter, the various theories and methods that are used to include distributed propulsion into the BWB aircraft will be explained.

5.1. Aerodynamics/Propulsion integration

5.1.1. Distributed propulsion and propulsive efficiency

When Kuchemann introduced the jet wing concept in 1938 [9], it was suggested that this configuration would result in an improvement in propulsive efficiency. Although this conjecture is plausible in theory, no detailed assessment has been found in the literature. The improvement in propulsive efficiency comes from the general idea that the jet exiting the trailing edge of the wing ‘fills in the wake’ behind the aircraft. This approach is commonly implemented in ships and submarine, having a streamlined axisymmetric body (neglecting the sail and the control surfaces) and a single propeller on the axis. Although the wake is not perfectly filled, this arrangement tends to maximize the propulsive efficiency of the entire system [95]. It is expected that a similar improvement in propulsive efficiency can be achieved with the proposed distributed propulsion configuration for aircraft. For the distributed propulsion BWB configuration, part of the engine exhaust will be ducted out of the trailing edge of the aircraft (likely the cold air fan air, although ducting the hot air core exhaust is possible).

The Froude Propulsion Efficiency, h_P, can be defined as the ratio of useful power out of the propulsor to the rate of kinetic energy added to the flow (by the propulsor), as shown in Equation (5.1).

$$h_P = \frac{T U_\infty}{q S_{ref} U_\infty f (f^2 - 1)} \tag{5.1}$$

where T = Thrust

U_∞ = Freestream velocity

S_{ref} = Reference area

q = dynamic pressure

f = ratio of the engine jet velocity to the freestream velocity

For simplicity, consider initially a two-dimensional, non-lifting, self-propelled vehicle with an engine as shown in Figure 5-1. The wake of the body is independent of the jet from the engine. For the system to be self propelled, the drag associated with the velocity deficit due to the wake is balanced by the thrust of the engine. The loss in propulsive efficiency (from 100%) is due to any net kinetic energy left in the wake (characterized by the non-uniformities in the velocity profiles) compared to that of a uniform velocity profile. For this case, a typical Froude Propulsion Efficiency for a high bypass ratio turbofan at Mach 0.85 is 80% [96][1].

---

[1] Page 178.

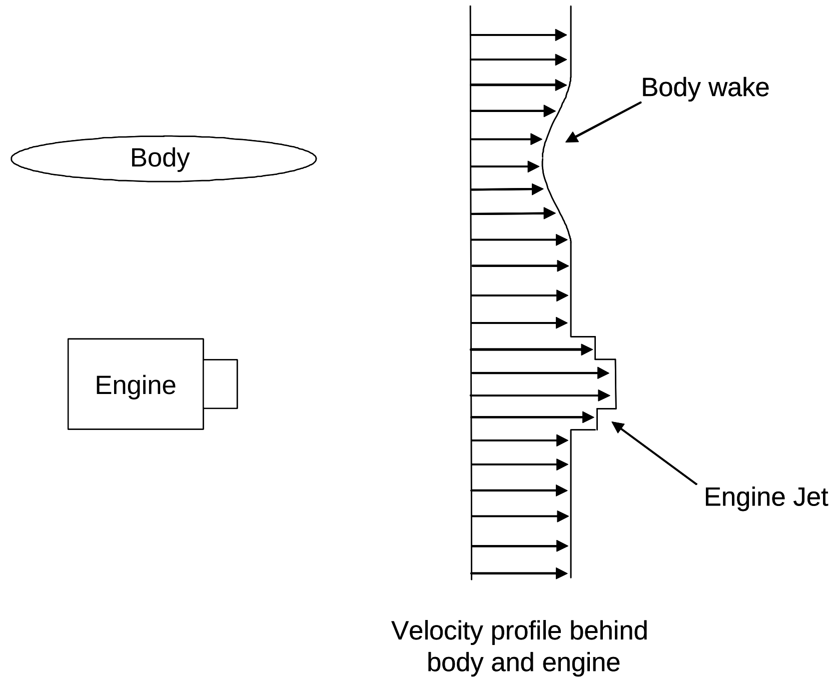

Figure 5-1: A typical velocity profile behind a body and engine

Now, consider a distributed propulsion configuration where the jet and the wake of the body are combined, as shown in Figure 5-2. In an ideal distributed propulsion system, the jet will perfectly ‘fill in’ the wake creating a uniform velocity profile. The kinetic energy added to the flow by the propulsor compared to that of a uniform velocity profile is therefore zero, which results in a Froude Propulsive Efficiency of 100%. In practice, the jet does not fully ‘fill in’ the wake but produces smaller non-uniformities in the velocity profile as illustrated in Figure 5-3. However, this velocity profile will result in a smaller net kinetic energy than that of the case where the body and engine are independent (shown in Figure 5-1). The efficiency associated with a distributed propulsion configuration will be bounded by the efficiency of the decoupled body/engine case (nominally at 80%) and the perfect distributed propulsion configuration of 100%. It should be noted, however, that we have not included the effect the jet has on the overall pressure distribution of the body. We expect that the jet will entrain the flow over the surface and increase the drag, but this effect is not modeled here.

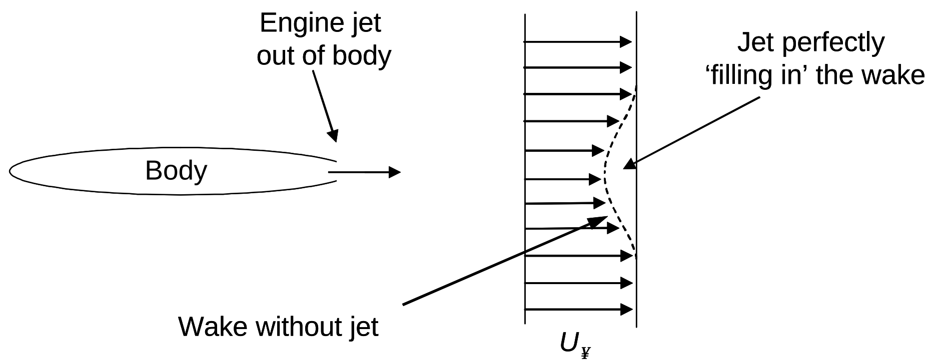

Figure 5-2: The velocity profile of a perfect distributed propulsion body/engine system. The jet perfectly 'fills in' the wake created by the body.

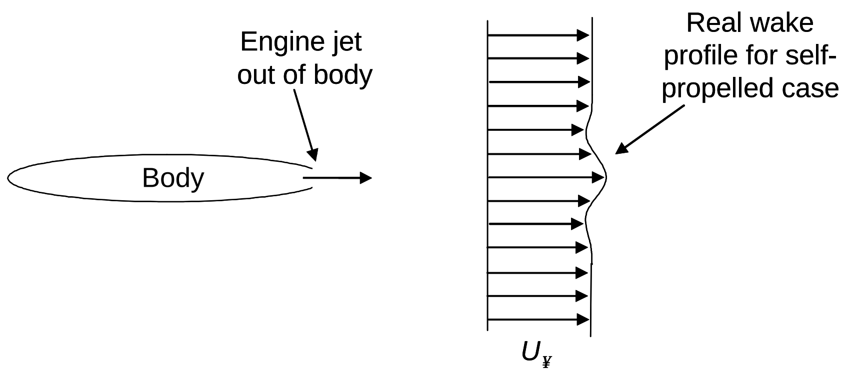

Figure 5-3: The velocity profile of a realistic distributed propulsion body/engine system. The non-uniformities in the distribution will contribute to a reduction in Froude Propulsive Efficiency although not as much as the separate body/engine case

Now consider a lifting body with an engine in a distributed propulsion configuration. In this case, the drag on the system is now not only due to the viscous drag but also the drag due to the downwash. This means that the engine jet now 'overfills' the wake. Therefore, even in a perfect system, a 100% Froude Propulsive Efficiency is not attainable. In the perfect system idealization of this configuration, part of the jet would be used to perfectly 'fill in' the wake while the remaining jet would be in the freestream away from the body. If the induced drag constitutes about 50% of the total drag (viscous drag + induced drag) as in well designed wings, then the maximum possible increase in Froude Propulsive Efficiency will be half of that in the non-lifting body case (i.e. the Froude Propulsive Efficiency using a nominal high bypass ratio turbofan in a distributed propulsion setting would be between 80% -90%).

From the above example for a subsonic lifting body, we see that the upper limit of the Froude propulsive efficiency is determined by the ratio of the viscous drag to the total drag. In the same way, for a lifting body in transonic flow, the upper limit of the Froude propulsive efficiency is determined by the ratio of the viscous and wave drag to the total drag. The wave drag is included because the presence of shocks on the body affects the size and shape of the wake downstream.

In an aircraft design performance assessment, the Froude Propulsive Efficiency can be reflected in the performance in terms of the thrust specific fuel consumption (SFC). We should expect that an increase in the Froude Propulsive Efficiency will result in a reduction in SFC, improving the aircraft’s overall performance. To relate the Froude Propulsive Efficiency with the Thrust Specific Fuel Consumption, consider the approximate relation given in Equation (5.2) by Stinton [97].

$$SFC = \frac{U_\infty}{k_1 h_p h_t} \tag{5.2}$$

where U_∞ = freestream velocity

k_1 = SFC factor. Stinton [97] determined this factor to be 4000 ft-hr/s.

h_p = Froude propulsive efficiency

h_t = the engine internal thermal efficiency

Assuming a constant freestream velocity, SFC factor and internal engine thermal efficiency, we can obtain Equation (5.3).

$$\frac{sfc_1}{sfc_2} = \frac{h_{P2}}{h_{P1}} \tag{5.3}$$

Hence, given a baseline propulsive efficiency and specific fuel consumption, a new specific fuel consumption can be calculated for an increase in propulsive efficiency.

In this model development, we have assumed that the jet is able to fill in the wake, and that the efficiencies that are proposed can be achieved. However, we still have not given an analysis illustrating this effect. To do this, we now provide an analysis of an idealized model problem.

5.1.1.1. Distributed Propulsion Theory

Consider a two-dimensional body in a flow that is self propelled by an engine whose jet does not influence the wake of the body. The thrust that is produced by the engine is described in Equation (5.4).

$$T = \dot{m}_a\left[(1+f)U_J - U_\infty\right] + \left(p_e - p_\infty\right)A_e \tag{5.4}$$

where T = engine thrust

$\dot{m}_a$ = airflow rate

f = fuel-air ratio

U_J = velocity out of the engine

U_∞ = freestream velocity

p_e = exhaust pressure

p_∞ = ambient pressure

A_e = exhaust area

The derivation of Equation (5.4) can be found in most propulsion text-books such as that by Hill and Peterson [96]. We will assume that the exhaust pressure is equal to the ambient pressure, and that the fuel mass added to the flow compared to the air mas flow rate is negligible. The thrust equation therefore reduces to:

$$T = \dot{m}_a\left(U_J - U_\infty\right) \tag{5.5}$$

The kinetic energy added to the flow by the propulsor is given in Equation (5.6).

$$\Delta KE = \tfrac{1}{2}\dot{m}_a\left[(1+f)U_J^2 - U_\infty^2\right] \tag{5.6}$$

Again, if we assume that the fuel mass added to the flow compared to the air mass flow rate is negligible, the equation reduces to

$$\Delta KE = \tfrac{1}{2}\dot{m}_a\left(U_J^2 - U_\infty^2\right) \tag{5.7}$$

Using the definition of the Froude Propulsive Efficiency as the ratio of the thrust power to the rate of kinetic energy added to the flow by the propulsor, using Equation (5.5) and (5.7), we get:

$$h_P = \frac{\dot{m}_a (U_J - U_\infty) U_\infty}{\frac{1}{2}\dot{m}_a (U_J^2 - U_\infty^2)} = \frac{2}{\frac{U_J}{U_\infty} + 1} \tag{5.8}$$

Now, let us consider the velocity profile of the jet and wake downstream. For simplicity, we shall assume that the wake of the body and jet of the engine takes on a square shape. This is shown in Figure 5-4.

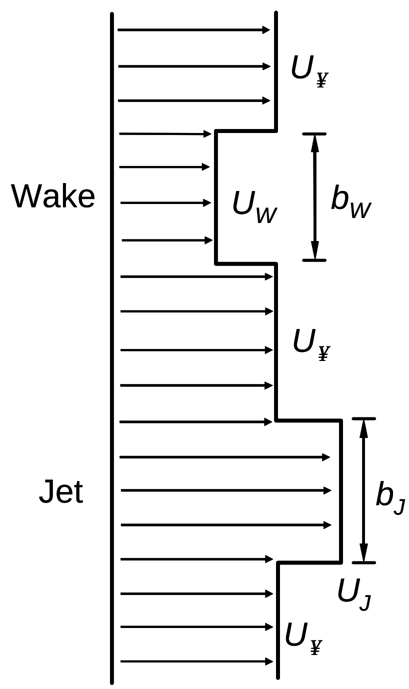

Figure 5-4: Figure shows the proposed velocity profile of the wake and jet downstream. The jet and wake profiles are decoupled

Now, consider the force vector, according to the momentum theorem and conservation of mass, as shown in Equation (5.9).

$$\boldsymbol{F} = -\iint_S (p - p_\infty) d\boldsymbol{S} - \iint_S r\, \boldsymbol{q} (U_\infty + \boldsymbol{q}) d\boldsymbol{S} \tag{5.9}$$

where $\boldsymbol{F}$ = force vector

p = pressure at the boundaries

p_∞ = ambient pressure

U_∞ = freestream velocity

$\boldsymbol{q}$ = velocity perturbation from U_∞ ,comprised of components u, v, w

r = density

S = Control surface

Consider a two dimensional control volume around the body and the engine, with a downstream velocity profile that is shown in Figure 5-4. This control volume is shown in Figure 5-5. As done before, for simplicity, we shall assume that the downstream pressure is undisturbed from the upstream (or ambient) pressure. For the force vector in the freestream direction, Equation (5.9) reduces to Equation (5.10).

$$F_x = -\int_{-h}^{h} r\, u\left(U_\infty + u\right) dy \tag{5.10}$$

where u is the velocity perturbation from U_8 in the freestream direction.

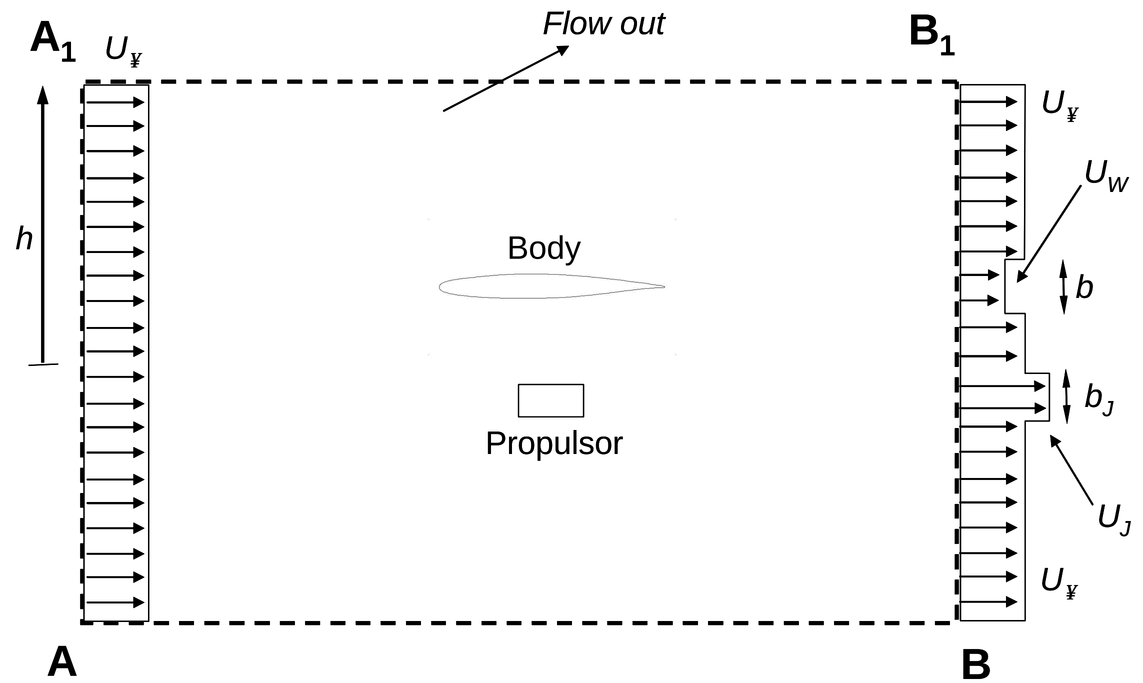

Figure 5-5: Control surface around the non-distributed propulsion configuration where the body is independent of the propulsor.

Performing the integration in Equation (5.10) for the profile in Figure 5-5, the force equation results in

$$F_x = r\left[b_W U_W \left(U_\infty - U_W\right) - b_J U_J \left(U_J - U_\infty\right)\right] \tag{5.11}$$

Equating the force to zero for a self-propelled case, and rearranging, we obtain

$$\left(\frac{U_J}{U_\infty}\right)^2 - \left(\frac{U_J}{U_\infty}\right) - \left(\frac{b_J}{b_W}\right)^{-1}\left(\frac{U_W}{U_\infty}\right)\left(1-\frac{U_W}{U_\infty}\right) = 0 \tag{5.12}$$

Solving for $\frac{U_J}{U_\infty}$, we get

$$\frac{U_J}{U_\infty} = \frac{1}{2} \pm \frac{1}{2}\sqrt{1+4\left(\frac{b_J}{b_W}\right)^{-1}\left(\frac{U_W}{U_\infty}\right)\left(1-\frac{U_W}{U_\infty}\right)} \tag{5.13}$$

Since $\frac{U_W}{U_\infty}$ is less than 1.0, the term in the square root will have a value greater than 1.0. Therefore, since we know that $\frac{U_J}{U_\infty}$ must have a value equal or greater than 1.0, the positive solution is applicable (shown in Equation (5.14)).

$$\frac{U_J}{U_\infty} = \frac{1}{2} + \frac{1}{2}\sqrt{1+4\left(\frac{b_J}{b_W}\right)^{-1}\left(\frac{U_W}{U_\infty}\right)\left(1-\frac{U_W}{U_\infty}\right)} \tag{5.14}$$

By substituting Equation (5.14) into Equation (5.8), we get a mathematical form of the propulsive efficiency shown in Equation (5.15), for the non-distributed propulsion configuration.

$$h_P = \frac{2}{\frac{3}{2} + \sqrt{1+4\left(\frac{b_J}{b_W}\right)^{-1}\left(\frac{U_W}{U_\infty}\right)\left(1-\frac{U_W}{U_\infty}\right)}} \tag{5.15}$$

This formulation is consistent with the discussions on propulsive efficiency in most propulsion textbooks such as that in Hill and Peterson [96][1]. We see that the propulsive efficiency is at 100%, if $\frac{U_J}{U_\infty} = 1.0$ (corresponding to $\frac{b_J}{b_W} = \infty$).

Now, consider the case where the jet of the engine is superimposed within the wake of the body, modeling the distributed propulsion configuration. This arrangement is shown in Figure 5-6.

[1] Page 149-150.

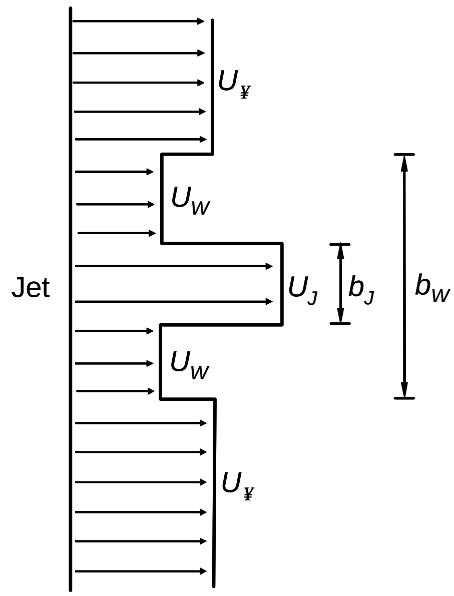

Figure 5-6: Figure shows the proposed velocity profile of the wake and jet downstream in a distributed propulsion configuration.

The propulsive efficiency for this case can still be evaluated using Equation (5.8). As before, consider the balance of momentum in this case. We will have a rectangular control surface around the body, and make the same assumptions as we did in the non-distributed propulsion calculation. This control surface is shown in Figure 5-7.

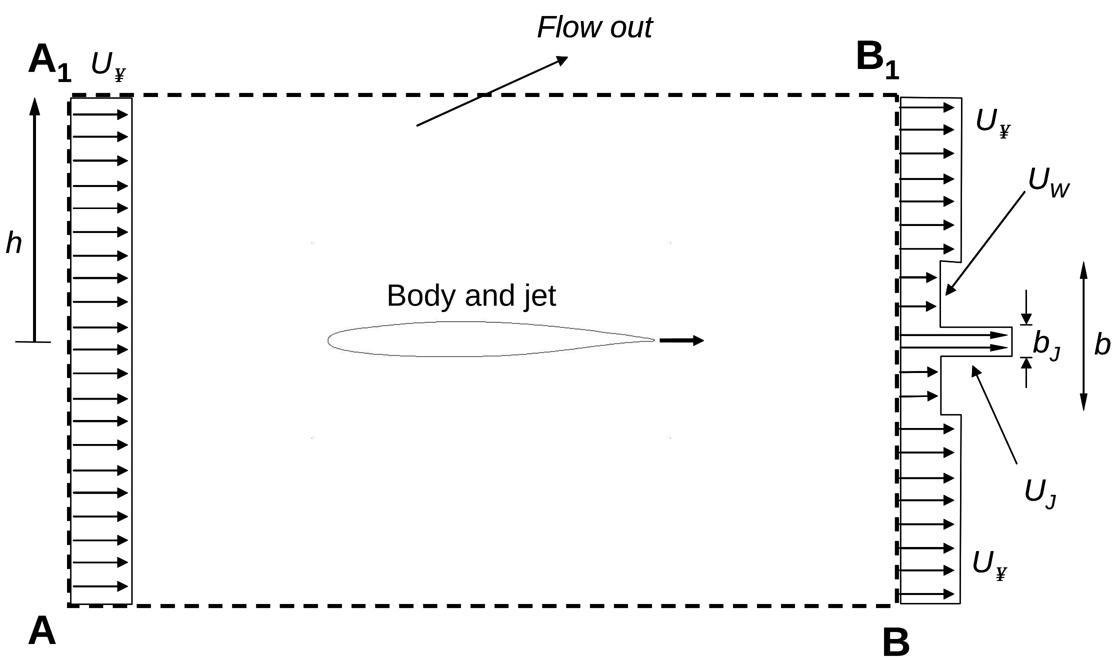

Figure 5-7: Control surface around the distributed propulsion configuration where the jet from the propulsor is combined with the wake of the body

Performing the integration in Equation (5.10) across the control surface for the profile in Figure 5-7, we get:

$$F_x = r\left[b_W\left(U_W^2 - U_\infty U_W\right) + b_J\left(U_J^2 - U_W^2 + U_\infty U_W - U_\infty U_J\right)\right] \qquad (5.16)$$

Equating the force to zero for a self propelled case, and rearranging, we get Equation (5.17)

$$\frac{U_J}{U_\infty} = \frac{1}{2} \pm \frac{1}{2}\sqrt{1 + 4\left(\frac{U_W}{U_\infty}\right)\left(1 - \frac{U_W}{U_\infty}\right)\left[\left(\frac{b_J}{b_W}\right)^{-1} - 1\right]} \qquad (5.17)$$

Again, since the value of $\frac{U_W}{U_\infty}$ is less than 1.0, and the value of $\frac{U_J}{U_\infty}$ greater than 1.0, the positive solution is applicable. This is given in Equation (5.18).

$$\frac{U_J}{U_\infty} = \frac{1}{2} + \frac{1}{2}\sqrt{1 + 4\left(\frac{U_W}{U_\infty}\right)\left(1 - \frac{U_W}{U_\infty}\right)\left[\left(\frac{b_J}{b_W}\right)^{-1} - 1\right]} \qquad (5.18)$$

Substituting Equation (5.18) into Equation (5.8), we get the mathematical formulation for a distributed propulsion case shown in Equation (5.19).

$$h_P = \frac{2}{\frac{3}{2} + \frac{1}{2}\sqrt{1 + 4\left[\left(\frac{b_J}{b_W}\right)^{-1} - 1\right]\left(\frac{U_W}{U_\infty}\right)\left(1 - \frac{U_W}{U_\infty}\right)}} \qquad (5.19)$$

Now, consider the limiting case in this arrangement. For the propulsive efficiency to be 100%, it is required that $\frac{b_J}{b_W} = 1.0$. This corresponds to $\frac{U_J}{U_\infty} = 1.0$. In essence, it is the case where the jet 'perfectly' fills in the wake of the body. This effect is consistent with our previous assertion that a perfectly filled wake corresponds to an efficiency of 100%. It should be noted that the value of $\frac{b_J}{b_W}$ is limited to a maximum value of 1.0, and a consideration of $\frac{b_J}{b_W}$ values larger than 1.0 would involve a new formulation. $\frac{U_J}{U_\infty}$ is limited to a minimum of 1.0, as the system cannot be self propelled for any value of $\frac{U_J}{U_\infty}$ less than 1.0.

Figure 5-8 shows a plot of the propulsive efficiency using Equations (5.15) and (5.19) for different values of $\frac{b_J}{b_W}$, at a specified representative value of $\frac{U_W}{U_\infty}$ = 0.5. It clearly shows that the distributed propulsion configuration achieves a higher propulsive efficiency than the non-distributed propulsion configuration for the same value of $\frac{b_J}{b_W}$.

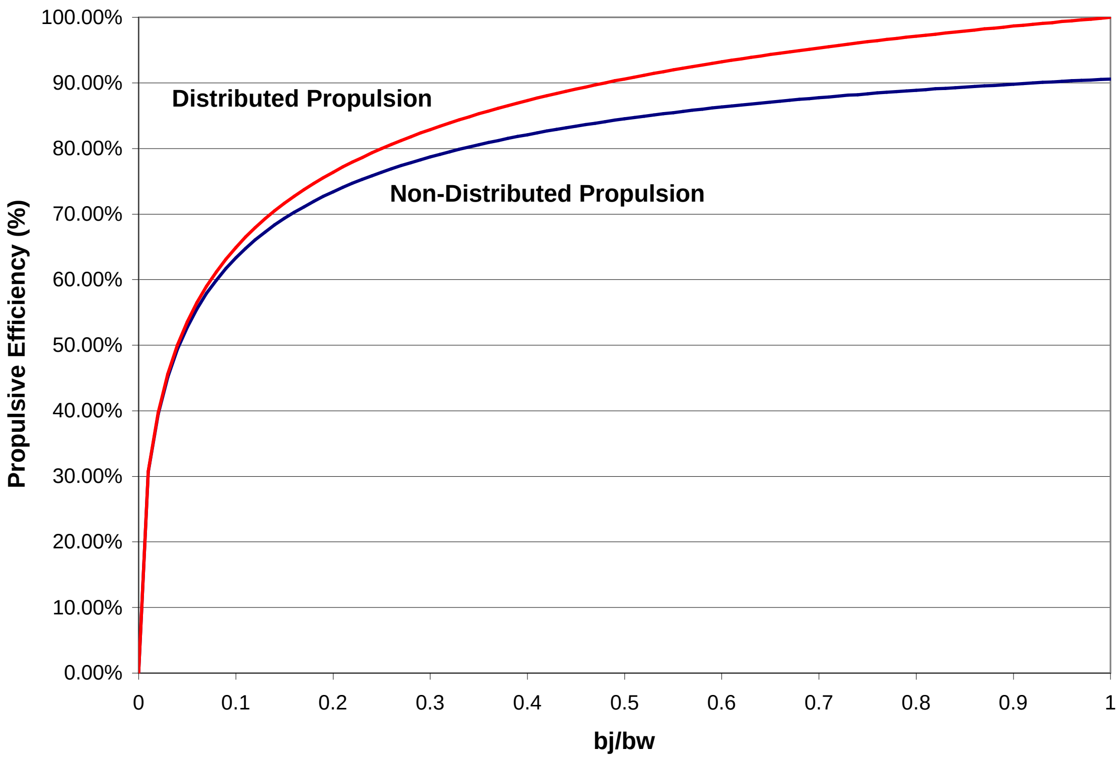

Figure 5-8: Comparison of Froude propulsive efficiency with the variation in $\frac{b_J}{b_W}$ between a distributed propulsion and non-distributed propulsion configuration. $\frac{U_W}{U_\infty}$ = 0.5.

Although Figure 5-8 plots values of $\frac{b_J}{b_W}$ of up to 1.0, $\frac{b_J}{b_W}$ is not limited to this maximum value for the non-distributed propulsion case. In fact, we find from Equation

(5.16) that as $\frac{b_J}{b_W}$ is increased towards infinity, the propulsive efficiency for the non-distributed propulsion case tends towards 100%.

Before we discuss the implications of this formulation, it is prudent to address the validity of the assumptions that were made and their influence in the overall context of the subject. First, we assumed that the jet exit pressures are equal to the surrounding ambient pressure. This assumption is usually made to represent a propulsion system that is working at its optimum design configuration. However, one could repeat the above formulation taking into account the pressure terms. Doing this though, complicates the equation, and does not provide any additional insight. Secondly, we assumed that the fuel mass flow rate compared to the air mass flow rate is negligible. This assumption is reasonable, and holds for most turbofan engines, especially for high bypass ratio turbofan engines. As for the previous assumption, no additional insight would be attained if we included the effect of the added mass due to the addition of fuel. Lastly, we assumed a square shaped velocity profile for the wake and the jet. This is probably the most crucial simplifying assumption made in the formulation that is not true to reality. However, the formulation was repeated assuming a triangular jet and wake profile. This formulation is given in Appendix A. The results show that there is a similar trend in the Froude propulsive efficiency plots between assuming a square and a triangular shaped wake and jet. For values of $\frac{b_J}{b_W}$ greater than approximately 0.3, the distributed propulsion formulation has a higher efficiency than the non-distributed propulsion case although the savings for a triangular shaped wake and jet is not as high as that for a square shaped wake and jet. For example, for $\frac{b_J}{b_W} = 0.4$ and $\frac{U_W}{U_\infty} = 0.5$, the difference in propulsive efficiencies between the distributed propulsion case and the non-distributed propulsion case by 1.75% using a triangular shaped jet and wake assumption. This difference is 5.19% for a square shaped jet and wake assumption. By considering both the square and triangular shaped velocity profiles, we essentially were considering the limiting profile shapes for a wake and a jet. A realistic wake and jet will possess a shape in between that of the square and triangular shape. Implied in the formulation of the theory, we had assumed a linear superposition of the jet and wake when considering the distributed propulsion configuration. Also, we assumed that the size of the wake remains the same as that in the non-distributed propulsion configuration. In reality, there will undoubtedly be interaction effects such as entrainment of the flow by the jet, altering the flow field on the airfoil, which may increase the drag.

Let us apply this theory to our distributed propulsion BWB configuration. Since the design is for a transonic passenger transport aircraft, it is assumed that supercritical airfoil sections will be used. One major characteristic of transonic airfoils is the presence of a thick (or even diverging) trailing edge. The presence of this thick trailing edge significantly decreases the wave drag at transonic Mach numbers if compared to a similar airfoil design with a closed trailing edge [98]. However, the presence of the thick trailing edge also results in the formation of a recirculation region immediately behind the airfoil, hence resulting in a base drag penalty. At transonic Mach numbers, the reduction in wave drag is much greater than the base drag due to the thick trailing edge, resulting in a better overall airfoil *L/D* performance. The penalties of this base drag are considered an 'expense' at sub critical Mach numbers in return for the drag performance at transonic Mach numbers [98]. A common trailing edge thickness for a supercritical airfoil is approximately 0.7% of the airfoil chord length. Although this seems to be a small percentage, the trailing edge thickness can still be quite substantial for large chord lengths. For example, a 20 ft chord length section will result in a 1.8 inch trailing edge thickness. In light of the distributed propulsion BWB, such a thickness is large enough to duct some of the engine exhaust out. By blowing out of the trailing edge, we reduce or even eliminate the base drag associated with the thick trailing edge.

Consider the velocity profile in Figure 5-9. In the non-distributed propulsion case, the drag of the body is represented by the velocity deficit area created by the wake, namely, Area A. In the distributed propulsion case, assuming the same sized wake (for the same body), the drag is now represented by the sum of Area B and C, which is smaller than area A. The difference between Area A and the sum of Area B and C (which is equal to Area E) represents the base drag that is not present in the distributed propulsion configuration.

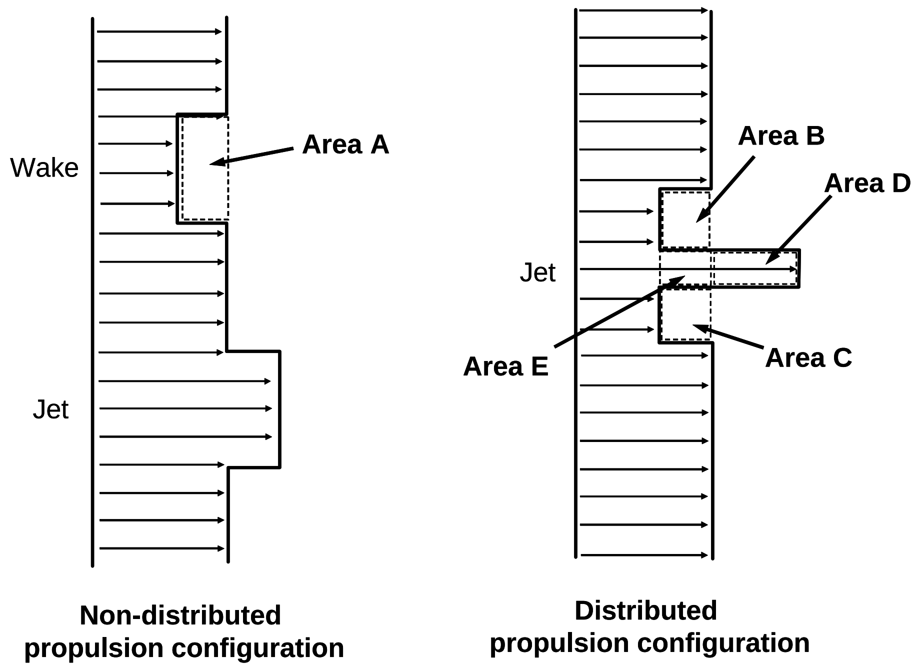

Figure 5-9: Illustration showing the difference between the velocity profile behind the body and jet for a non-distributed propulsion and distributed propulsion configuration.

Another way of visualizing this effect is by considering the velocity profile relative to the body. In Figure 5-10, in relation to the body, the wake creates a 'negative' velocity component in the chordwise direction. Similarly, the jet produces a positive velocity component. The section of the wake behind the thick trailing edge is not present because it is being 'filled' in by the jet.

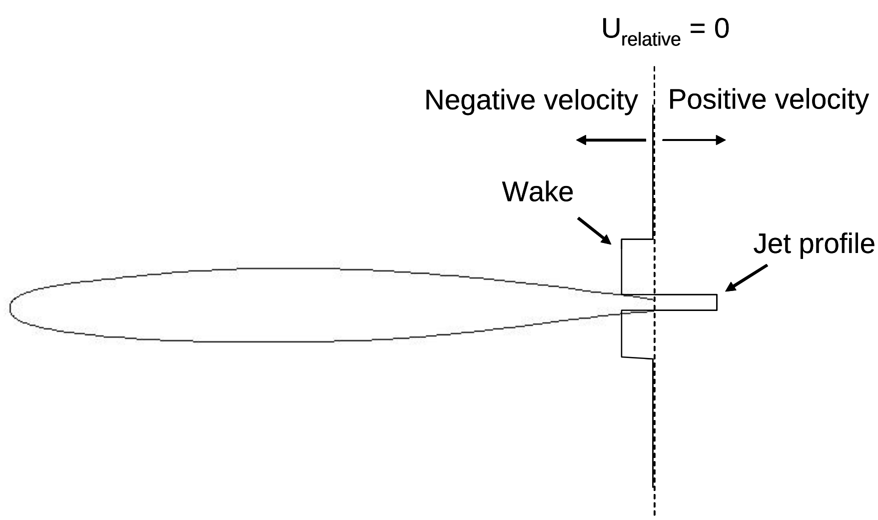

Figure 5-10: Figure shows relative velocity profile behind a streamlined body of a distributed propulsion configuration, relative to the body.

One important implication of this theory is that the propulsive efficiency is only dependent on the jet width and velocity of the propulsor, but recall that the two are connected by the self-propelled condition. Equation (5.8) shows that a smaller jet velocity relative to the freestream velocity results in a better propulsive efficiency. However, it is quite possible that a conventional propulsion arrangement could achieve a better propulsive efficiency by being able to generate the same amount of thrust at a smaller jet velocity. In a distributed propulsion system, the jet velocity is limited by the available exit area out of the trailing edge of the body. In a two-dimensional case, this is represented by the 'height' of the jet. A small jet height results in high jet velocities to produce the needed thrust. No such limit applies to the conventional arrangement, where the exit area out of the engine can be as large as needed to achieve a small jet velocity.

For a distributed propulsion system to do better than the conventional arrangement, the trailing edge of the wing has to be thick enough to allow a low jet velocity. The logical question then should be: how thick should the trailing edge of an airfoil be for a distributed propulsion system to achieve efficiencies better than conventional propulsion arrangements? To answer this, we considered a 10% *t/c* ratio supercritical airfoil as shown in Figure 5-11. This airfoil has a 0.5% chord thickness trailing edge. We found that to propel this airfoil at Mach 0.72 with a jet out of the trailing edge, a propulsive efficiency of 74% is achieved. It is projected that in order to achieve an 80% efficiency, the trailing edge of the airfoil has to be increased by another 50%, or a thickness of 0.75% of the chord length. Doubling the trailing edge thickness (1% chord length) will give a projected efficiency of 84%, but there may be adverse aerodynamic effects from increasing the trailing edge thickness.

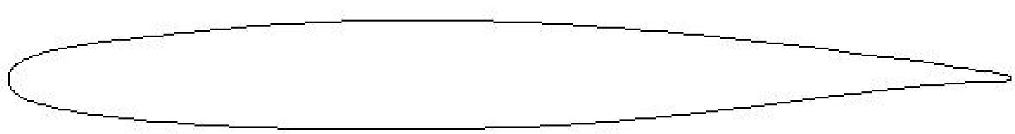

Figure 5-11: 10% thick supercritical airfoil with a 0.5% thick trailing edge.

The application of this theory is not solely limited to thick trailing edge wing sections. This theory can also be applied to wing sections with blowing out of the upper and lower wing surface close to the trailing edge, as shown in Figure 5-12. In this configuration, not only is the engine jet exhausted of the thick trailing edge, it is also exhausted out from the surface of the wing through slots or holes. This allows for more exhaust area, allowing for a smaller jet velocity (and hence a better propulsive efficiency) for the same thrust.

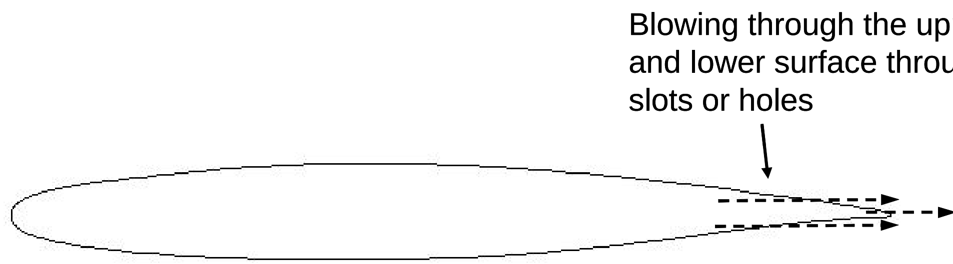

Figure 5-12: Concept to which the distributed propulsion theory can be applied to. Blowing through the upper and lower surface of the wing through slots or holes allows for a larger area to exhaust from, hence resulting in a lower jet velocity and better propulsive efficiency for the same required thrust.

5.1.2. Spence's Jet Flap Theory and Induced Drag

A key theory in describing and analyzing the jet flap is Spence's Jet Flap theory [99], [100], [101]. Spence extended thin airfoil theory to describe airfoil and wing performance with a jet flap in terms of the C_J, the jet coefficient. C_J is defined in Equation (5.20).

$$C_J = \frac{J}{\frac{1}{2} r U_\infty^2 S_{ref}} \tag{5.20}$$

where J is the total jet momentum flux.

For small jet angles (less than 30°), Spence's Jet Flap theory results compare well with experiment even at transonic speeds [55]. Although other computational analysis methods have been developed using higher order panel methods [54], potential flow methods [51], and transonic small disturbance theory [52], [53], we will use Spence's Jet Flap theory to estimate lift and moment coefficient characteristics for the calculation of the control constraints, and to evaluate the effect of the distributed propulsion system on the induced drag of the aircraft. Using Spence's Jet Flap theory will allow for an adequate level of fidelity in the initial performance analysis of a distributed propulsion system without the computational expense and long development and analysis time required with higher fidelity methods.

Spence's Jet Flap Theory can be used to estimate the effect of a jet flap on the induced drag of an aircraft. The following discussion is based on that presented by Spence in Reference [100].

Consider a finite span wing with a jet stream exiting at the trailing edge. For a jet momentum flux, J, the horizontal and vertical components of the jet momentum far behind the wing can be approximated to be $\left(1-\frac{1}{2}a_{i\infty}^{2}\right)J$ and $a_{i\infty}J$ respectively, where $a_{i\infty}$ is the induced angle of attack due to the jet flap.

Assuming an elliptical lift distribution, the circulation distribution in Trefftz plane can be written as:

$$\Gamma(y) = U_{\infty} a_{i\infty} b\sqrt{1-h^{2}} \tag{5.21}$$

where the induced downwash, $w_{i\infty}$ is equal to $U_{\infty}a_{i\infty}$.

Summing the momentum equations over the yz-plane, we get the lift and drag components

$$D_i = \tfrac{1}{2}a_{i\infty}J - \iint (p - p_{\infty})\,dy\,dz \tag{5.22}$$

$$L = a_{i\infty}J + rU_{\infty}\iint w\,dy\,dz \tag{5.23}$$

Notice that the integrals

$$\iint w\,dy\,dz \text{ and } \iint (p - p_{\infty})\,dy\,dz = -\tfrac{1}{2}r\iint\left(v^{2}+w^{2}\right)dy\,dz$$

can be evaluated by considering the two-dimensional flow in the Trefftz plane, and are similar to the integrals obtained when considering a non-jet-flapped wing. Hence, these integrals can be evaluated to be

$$\iint w\,dy\,dz = \tfrac{1}{4}p\,b^{2}w_{i\infty} \tag{5.24}$$

$$\iint (v^{2}+w^{2})\,dy\,dz = \tfrac{1}{4}p\,b^{2}w_{i\infty}^{2} \tag{5.25}$$

By combining Equation (5.22) and (5.25), we obtain an expression for the induced drag

$$D_i = \tfrac{1}{2}a_{i\infty}^{2}\left(J + \tfrac{1}{4}pr\,b^{2}U_{\infty}^{2}\right) \tag{5.26}$$

Similarly, by combining Equation (5.23) and (5.24), we can obtain an expression for the lift

$$L = a_{i\infty}\left(J + \tfrac{1}{4} p r b^2 U_{\infty}^2\right) \tag{5.27}$$

By using the definition of the force coefficients and aspect ratio,

$$J = \tfrac{1}{2} r U_{\infty}^2 S_{ref} C_J \tag{5.28}$$

$$L = \tfrac{1}{2} r U_{\infty}^2 S_{ref} C_L \tag{5.29}$$

$$D_i = \tfrac{1}{2} r U_{\infty}^2 S_{ref} C_{Di} \tag{5.30}$$

$$AR = \frac{b^2}{S_{ref}} \tag{5.31}$$

Equations (5.26) and (5.27) can be written as

$$C_{Di} = \tfrac{1}{4} a_{i\infty}^2 (p\,AR + 2C_J) \tag{5.32}$$

$$C_L = \tfrac{1}{2} a_{i\infty} (p\,AR + 2C_J) \tag{5.33}$$

Therefore,

$$C_{Di} = \frac{C_L^2}{p\,AR + 2C_J} \tag{5.34}$$

Comparing Equation (5.34) with the induced drag coefficient equation for a non-jet-flapped wing with an elliptical load distribution (Equation (5.35)), we find the addition of the factor $2C_J$ in the denominator that describes the influence of the jet flap on the induced drag of the wing. The equation also reduces to the non-jet-flapped wing equation when $C_J = 0$, which serves as a check to the validity of the equation.

$$C_{Di} = \frac{C_L^2}{p\,AR} \tag{5.35}$$

To implement the effects of the jet on the induced drag of the wing, the induced drag is calculated using <u>idrag</u> for a non-jet-flapped wing and then corrected with the ratio in Equation (5.36).

$$\frac{C_{Di_{\text{Distributed Propulsion}}}}{C_{Di}} = \frac{p\,AR}{p\,AR + 2C_J} \tag{5.36}$$

5.2. Controls/Propulsion Integration

In the distributed propulsion BWB configuration, the elevon controls are replaced with a vectored jet wing control system. This system controls the BWB longitudinally by changing the deflection angle of the jet exiting the trailing edge of the wing. We expect that the changes in this deflection angle will be enough to change the lift and pitching moment characteristics of the aircraft to achieve comparable control capabilities with that of the conventional BWB configuration.

To estimate the effects of the jet deflection angle on the lift and pitching moment of the aircraft, Spence's jet flap theory [99],[100],[101] will be used. Spence's two dimensional jet flap theory [99] extends the methods of thin-airfoil theory to give a solution for the inviscid, incompressible flow past a thin airfoil at a small angle of attack (a), when a thin jet exits the trailing edge at a small deflection angle (t). The method provides an estimate of the lift and moment coefficient of the airfoil in terms of the jet coefficient, C_J. Comparisons of these quantities for jet coefficients of up to 4 show good agreement with experimental results [99]. Spence, together with Maskell [100], later introduced the three-dimensional jet flap theory that considers the case of a thin unswept wing of finite aspect ratio. This wing possesses a deflected jet sheet of zero thickness emerging at a small deflection angle, t at the trailing edge. This theory is a result of the extension of the two dimensional jet flap theory and Prandlt's lifting line theory. However, this theory is limited to conditions where the jet momentum flux per unit span is elliptically distributed and the jet deflection angle and angle of attack distributions are constant across the span. For a thin, unswept jet wing with a high aspect ratio, the lift coefficient can be estimated using Equations (5.37) and (5.38) obtained from Reference [99].

$$C_L = \frac{C_L^{(2)}\left(\pi AR + 2C_J\right)}{\pi AR + 2\dfrac{\partial C_L^{(2)}}{\partial \alpha} - 2\pi(1+\sigma)}$$

$$\sigma = \frac{\left(1-\lambda^*\right)\left(\dfrac{C_J}{\pi AR}\right)}{\lambda^* - \left(1-\lambda^*\right)\left(\dfrac{C_J}{\pi AR}\right)} \tag{5.37}$$

$$\lambda^* \approx \frac{\left(\dfrac{2}{\pi}\right)\dfrac{C_L^{(2)}}{\tau + \alpha_{3D}}}{AR + \left(\dfrac{2}{\pi}\right)\dfrac{\partial C_L^{(2)}}{\partial \alpha} - 2}$$

$$C_L^{(2)} = \frac{\partial C_L^{(2)}}{\partial \alpha}\alpha_{3D} + \frac{\partial C_L^{(2)}}{\partial \tau}\tau$$

$$\frac{\partial C_L^{(2)}}{\partial \tau} = 2\left(\pi C_J\right)^{\frac{1}{2}}\left(1 + 0.151C_J^{\frac{1}{2}} + 0.139C_J\right)^{\frac{1}{2}} \tag{5.38}$$

$$\frac{\partial C_L^{(2)}}{\partial \alpha} = 2\pi\left(1 + 0.151C_J^{\frac{1}{2}} + 0.219C_J\right)$$

To account for sweep, we will apply simple sweep theory [73] by multiplying the equation for C_L (in Equation (5.37)) with $\cos^2 \Lambda_{1/4c}$

To check the validity of the theory, we consider a case where $C_J = 0$. Physically, this represents the case of a simple wing without a jet. For an unswept wing, the estimate of the lift coefficient reduces to Equation (5.39).

$$C_L = \frac{2\pi AR}{2 + AR}\alpha \tag{5.39}$$

This result is similar to Prandlt's equation for an elliptic finite wing [103]. To further check the validity of the theory, estimates of the lift coefficient is compared to estimates obtained using a VLM program. Three test cases were set up to examine the comparisons for changes in aspect ratio, taper ratio and sweep. For small values of C_J, we should expect the jet flap theory to compare closely with results from the VLM program. We also expect an increase in the lift coefficient with increasing values of C_J.

In the first test case, a rectangular wing with no sweep and camber is considered. An elliptical load distribution is assumed and a taper ratio of unity is used. Various aspect ratios can be considered by varying the span of the planform. Figure 5-13a shows the planform geometry for the first test case.

In the second test case, a trapezoidal wing with no quarter chord sweep and camber is considered. An elliptical load distribution is assumed and the aspect ratio is kept constant. Various taper ratios can be considered by varying the root chord of the planform. Figure 5-13b shows the planform geometry for the second test case.

For the last case, a rectangular wing with no camber is considered. An elliptical load distribution is assume, the aspect ratio is kept constant and taper ratio of 1 is used. This planform is used to test the theory at various sweep angles. Figure 5-13c shows the planform geometry for the third test case.

Figures 5-14, 5-15 and 5-16 show the results of the comparisons of the lift coefficient between estimates from the jet flap theory and from the VLM program. Results from two values of C_J were used: 1×10^{-11}, and 1.0. From Figure 5-14, we find that the difference between Spence's jet flap theory and VLM is larger at lower aspect ratios. However, even at an aspect ratio of 5, there is only a 1% difference in the lift coefficient estimation. Figure 5-15 also shows close agreement with varying taper ratios. The maximum difference in lift coefficient estimation is 2.6% at a taper ratio of 0.9. Figure 5-16 shows the comparison at different sweep angles. Here, the difference is the greatest between the test cases. The results show that the jet flap theory over predicts the effect of sweep on the lift coefficient. However, this is not unexpected since simple sweep theory was used to account for the effects of sweep. Doing this assumes that the chordwise pressure distribution across the span remains the same. As the sweep angle is increased, this assumption starts to break down.

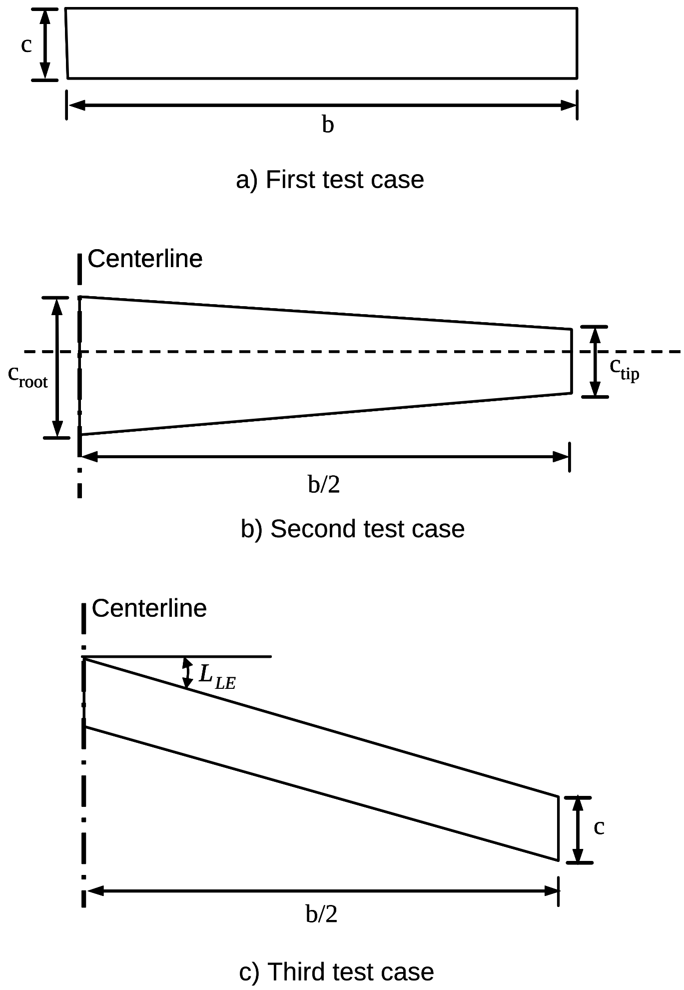

Figure 5-13: Figure shows planform details for the three test cases. In the first test case, the aspect ratio can be changed by varying *b*, the span. In the second test case, the taper ratio can be changed by varying C_{root}, the root chord. In the third test case, the sweep angle can be varied by changing the leading edge sweep angle, L_{LE}.

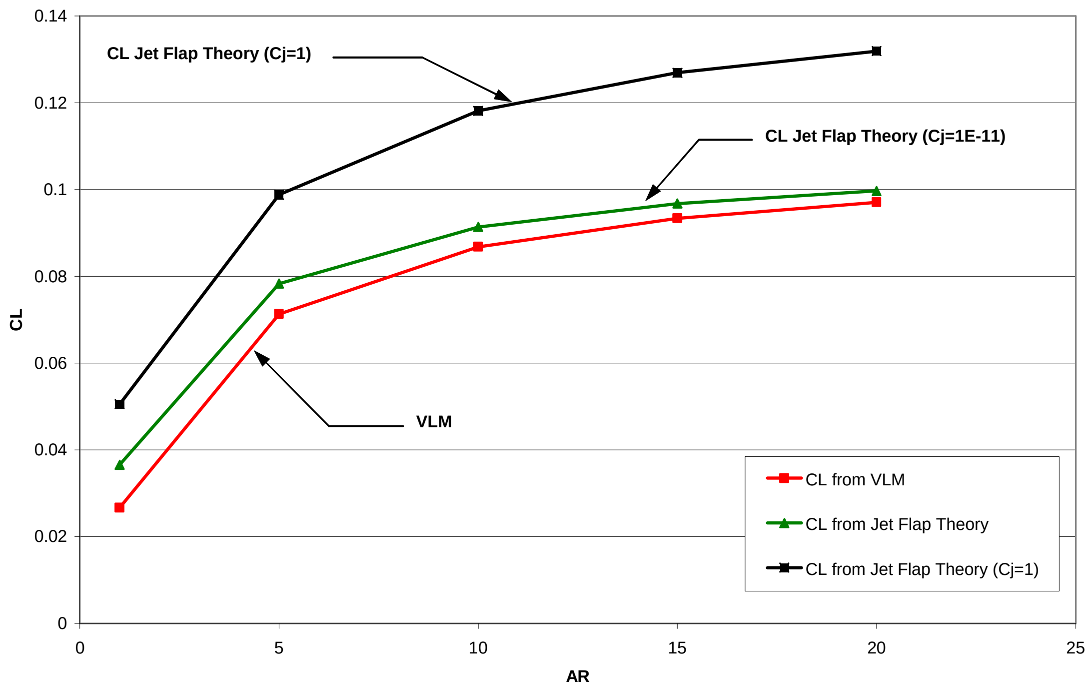

Figure 5-14: Comparison of lift coefficient estimation between Spence's jet flap theory and VLM results with varying aspect ratio.

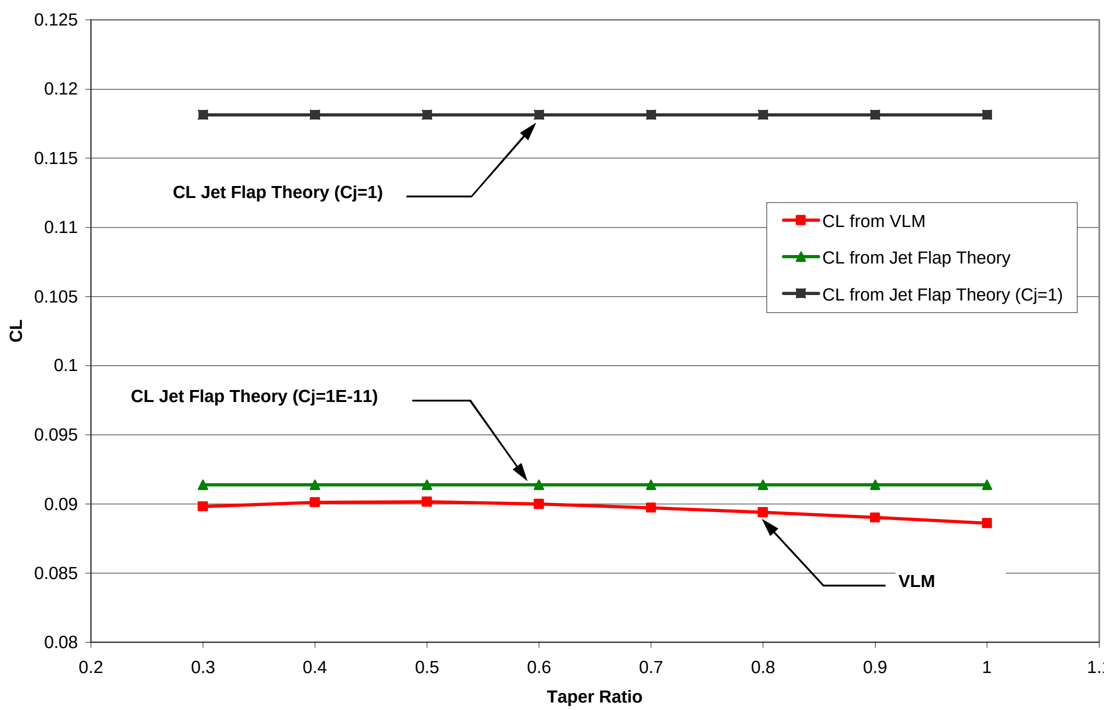

Figure 5-15: Comparison of the lift coefficient estimation between Spence's jet flap theory and VLM results with varying taper ratio.

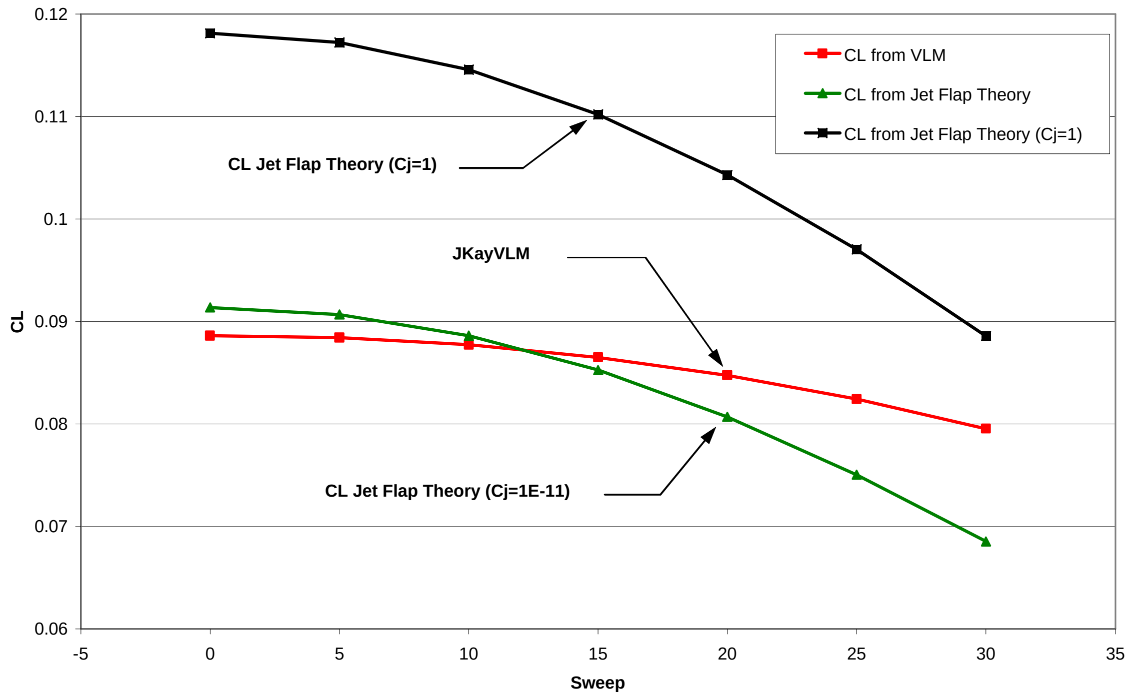

Figure 5-16: Comparison of the lift coefficient estimation between Spence's jet flap theory and VLM results with varying wing sweep.

5.2.1. 3-D moment coefficient calculation: Extension of Spence's jet flap theory

Although the three-dimensional jet flap theory provides estimates of the lift coefficient for an unswept finite aspect ratio wing, it does not provide a procedure to estimate the moment coefficient for a swept finite aspect ratio jet wing. To obtain the three-dimensional jet wing moment coefficient for this configuration, an extension of the two dimensional jet flap theory is needed.

5.2.1.1. General Formulation

Consider the wing planform shown in Figure 5-17. At any spanwise station, the moment about the leading edge in defined as:

$$M_{2D@LE}(h) = L' x_{CP} \tag{5.40}$$

where L' is the lift per unit span. The moment about an origin (X = 0) generated by the cross section can be formulated as shown in Equation (5.41).

$$M_{2D@X=0}(h) = L'\left(x_{gap} + x_{LE} + x_{CP}\right) \tag{5.41}$$

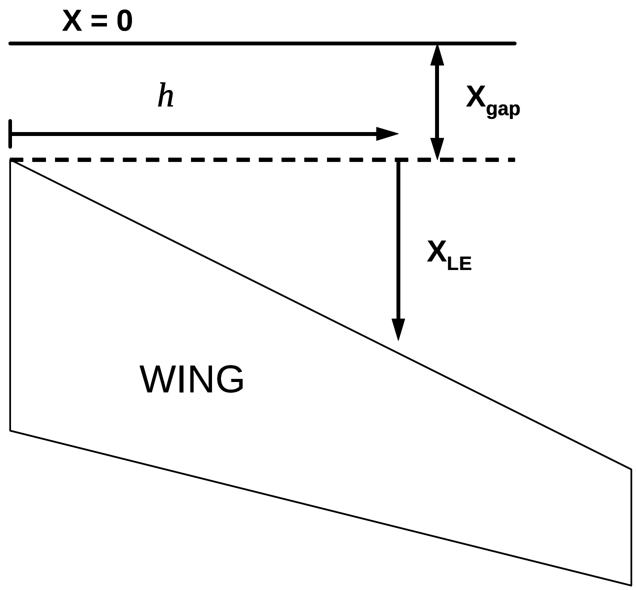

Figure 5-17: Diagram shows a general wing planform and geometry basis for the formulation of the 3D moment coefficient.

Combining Equations (5.40) and (5.41), we get

$$M_{2D@X=0}(h) = \frac{x_{gap} + x_{LE} + x_{CP}}{x_{CP}} M_{2D@LE}(h) \tag{5.42}$$

At this juncture, we will define the moment coefficients both in two-dimensions and three-dimensions,

$$C_{M_{2D@LE}} = \frac{M_{2D@LE}}{q c^2} \tag{5.43}$$

$$C_{M_{3D@LE}} = \frac{M_{3D@X=0}}{q S_{ref} \bar{c}} \tag{5.44}$$

We know that the three dimensional moment is equal to the integration of the two dimensional moment across the span. This is described mathematically in Equation (5.45).

$$
\begin{aligned}
M_{3D@X=0} &= \int_{-\frac{b}{2}}^{\frac{b}{2}} M_{2D@X=0}(h)\,dy \\
&= \int_{-\frac{b}{2}}^{\frac{b}{2}} \frac{x_{gap} + x_{LE} + x_{CP}}{x_{CP}} M_{2D@LE}(h)\,dy
\end{aligned}
\tag{5.45}
$$

Using the definitions to the moment coefficients, Equation (5.45) can be rearranged to give an equation for the three dimensional moment coefficient.

$$
\begin{aligned}
C_{M_{3D@X=0}} &= \frac{1}{S_{ref}\bar{c}} \int_{-\frac{b}{2}}^{\frac{b}{2}} \frac{x_{gap} + x_{LE} + x_{CP}}{x_{CP}} \left(c^2 C_{M_{2D@LE}}(h)\right) dy \\
&= \frac{b}{S_{ref}\bar{c}} \int_{0}^{1} \frac{x_{gap} + x_{LE} + x_{CP}}{x_{CP}} \left(c^2 C_{M_{2D@LE}}(h)\right) dh
\end{aligned}
\tag{5.46}
$$

5.2.1.2. Spence's Jet Flap Theory

For a thin two dimensional wing at a small angle of attack and jet deflection angle, Spence's Jet Flap theory [99] provides a formulation for the two dimensional lift and moment coefficient about the leading edge. This formulation is given in Equations (5.47) to (5.50).

$$
C_l = \frac{\partial C_l}{\partial a} a + \frac{\partial C_l}{\partial t} t \tag{5.47}
$$

$$
\frac{\partial C_l}{\partial a} = 2p + 1.152 C_J^{\frac{1}{2}} + 1.106 C_J + 0.051 C_J^{\frac{3}{2}} \tag{5.48}
$$

$$
\frac{\partial C_l}{\partial t} = 3.54 C_J^{\frac{1}{2}} + 0.325 C_J + 0.156 C_J^{\frac{3}{2}} \tag{5.49}
$$

$$
C_{M_{2D@LE}} = t\,(C_J + I_{-1}) + \tfrac{1}{2} p a + \sum_{n=0}^{N-1} \left(t A_n + a B_n\right) I_n \tag{5.50}
$$

It should be noted that Equations (5.48) and (5.49) differ from that in Equation (5.38), as these equations are formulations for the two-dimensional lift coefficient slopes with respect to the angle of attack and jet deflection angle. The formulation in Equation (5.38) is solely for the calculation of the three dimensional lift coefficient of an unswept, finite aspect ratio thin wing.

The constant factors I_n used in the calculation of the two dimensional moment coefficient are given to be, I_{-1}, I_0,…, I_8 = 1.563, 1.717, 1.133, 0.401, 0.193, 0.117, 0.076, 0.054, 0.040, 0.031. These values were obtained by solving for a set of nine Fourier coefficients that are independent of the value of C_J [99]. The determination of the other Fourier coefficients, A_n and B_n come by numerically solving two sets of 9 linear equations based on the jet coefficient, C_J. These sets of equations are described in Equation (5.51) and (5.52).

$$\sum_{n=0}^{N-1}(a_{mn} + l_J b_{mn})A_n = c_m + l_J\ d_m \tag{5.51}$$

$$\sum_{n=0}^{N-1}(a_{mn} + l_J\ b_{mn})B_n = e_m \tag{5.52}$$

where N = 9 and l_J is defined as $4/C_J$.

For n = 0, 1, 2, …, N-1 and m = 0, 1, 2, …, N-1, the formulation for the system of equation can be obtained from Equation (5.53)

$$\begin{aligned}
f_m &= \frac{mp}{N},\ m = 0,1,2,\ldots,N-1 \\
a_{m0} &= \sin f_m \\
a_{mn} &= (1+\cos f_m)\sin n f_m,\ \ (n>0) \\
b_{mn} &= \frac{4\left(\cos n f_m + 2n\tan\tfrac{1}{2} f_m \sin n f_m\right)}{\left(4n^2-1\right)} \\
c_m &= -(1+\cos f_m) \\
d_m &= \frac{8}{p}\left[\sec\tfrac{1}{2} f_m \ln\left(\tan\tfrac{1}{4} f_m\right) - \ln\left(\tan\tfrac{1}{2} f_m\right)\right] \\
e_m &= -2\sec\tfrac{1}{2} f_m \left(1-\sin\tfrac{1}{2} f_m\right)
\end{aligned} \tag{5.53}$$

The chordwise location of the center of pressure is given by

$$x_{CP} = \frac{C_{M_{2D@LE}}}{C_l} \tag{5.54}$$

By assuming that the there is no variation in the two dimensional moment coefficient across the span, we can substitute Equation (5.50) and Equation (5.54) into Equation (5.46) to obtain the three dimensional moment coefficient given a certain angle of attack distribution, jet deflection angle and jet coefficient.

The angle of attack distribution can be found by considering the local streamwise two dimensional lift coefficient distribution (via the wing load distribution). By assuming a certain jet deflection angle, Equation (5.47) can be used to determine the angle of attack distribution. This formulation is for full span blowing. For partial span blowing, this formulation can be easily modified by setting the jet coefficient to a small number (numerically setting C_J equal to zero makes the calculation of l impossible) at sections along the span where blowing is not present.

5.2.1.2.1. Comparison with standard test cases

To check the validity of this formulation, the same test cases that were used with the three-dimensional lift coefficient were applied to this formulation. As mentioned before, the lift coefficient of these three test cases compare well with the results from a VLM program at different aspect ratios, taper ratios and sweep angles. As with the comparison of the moment coefficient, we expect the results of the formulation to be close to the results of the VLM program at small jet coefficients and at a zero jet deflection angle.

The first test case makes the comparison at different aspect ratios. Figure 5-18 shows the result of the comparison. Here, we see that the difference between the formulation and the VLM program is large at low aspect ratios. This is expected as three dimensional effects are more dominant at low aspect ratios. However, the formulation captures the general trend of the moment coefficient with changes in aspect ratio, and compares well at high aspect ratios.

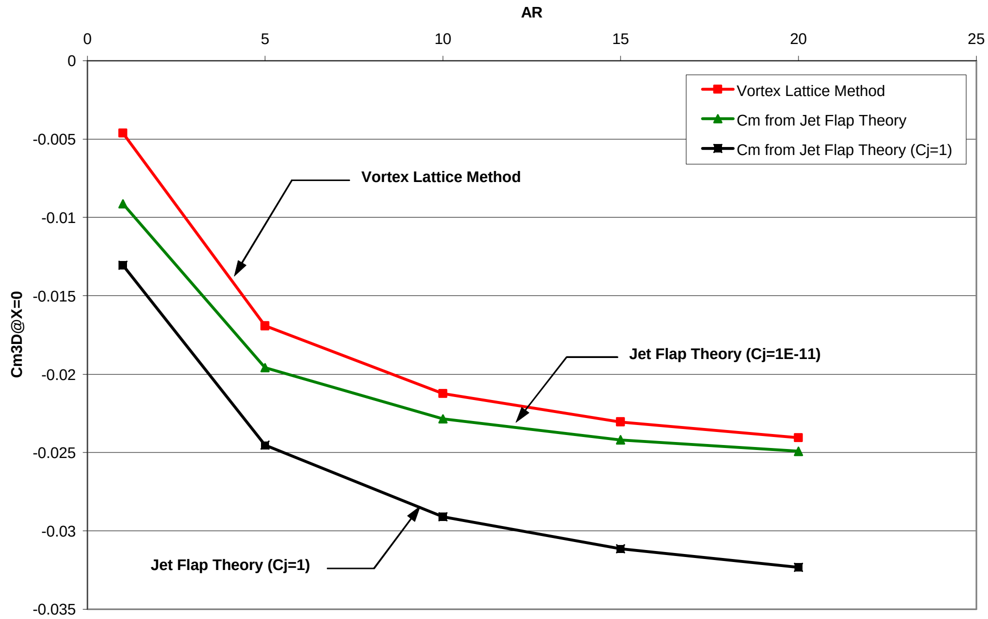

Figure 5-18: Comparison of moment coefficient estimation between Spence's jet flap theory and VLM with varying aspect ratio.

The second test case makes the comparison at different taper ratios. Figure 5-19 shows the results of that comparison. We can see that the estimates obtained from the formulation matches very closely with that obtained from the VLM program.

Figure 5-20 shows the comparison at various sweep angles. The differences between the formulation estimates and VLM program results grow with an increasing sweep angles. This difference can be traced to the assumption that the sectional moment coefficient is uniform across the span. Hence, we do expect deviation from the correct result as this assumption breaks down as the sweep increases.

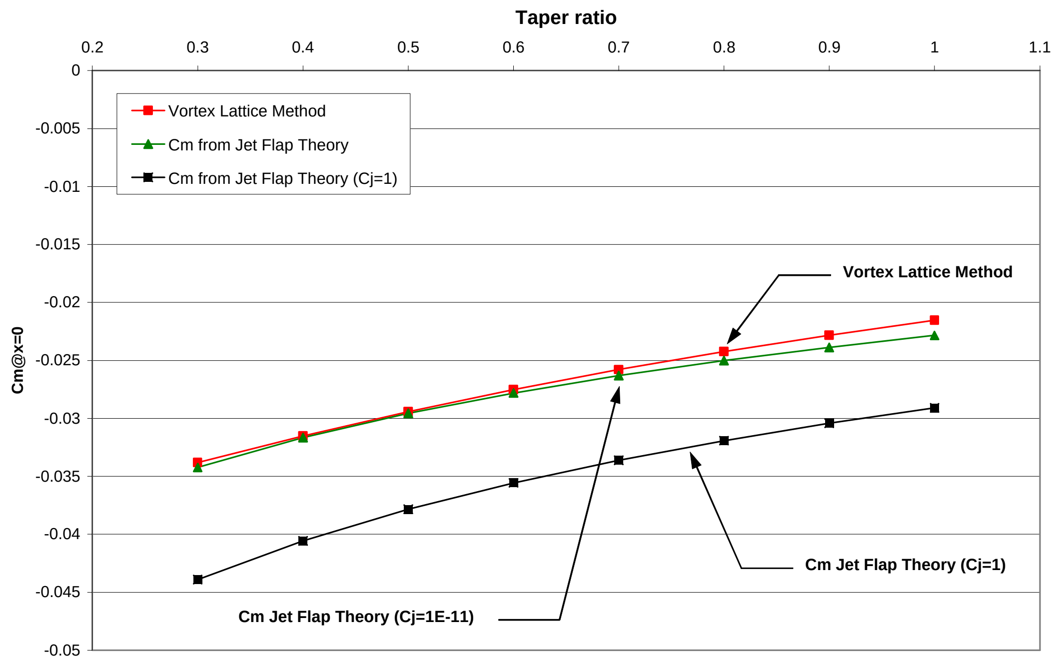

Figure 5-19: Comparison of moment coefficient estimation between Spence's jet flap theory and VLM with varying taper ratio.

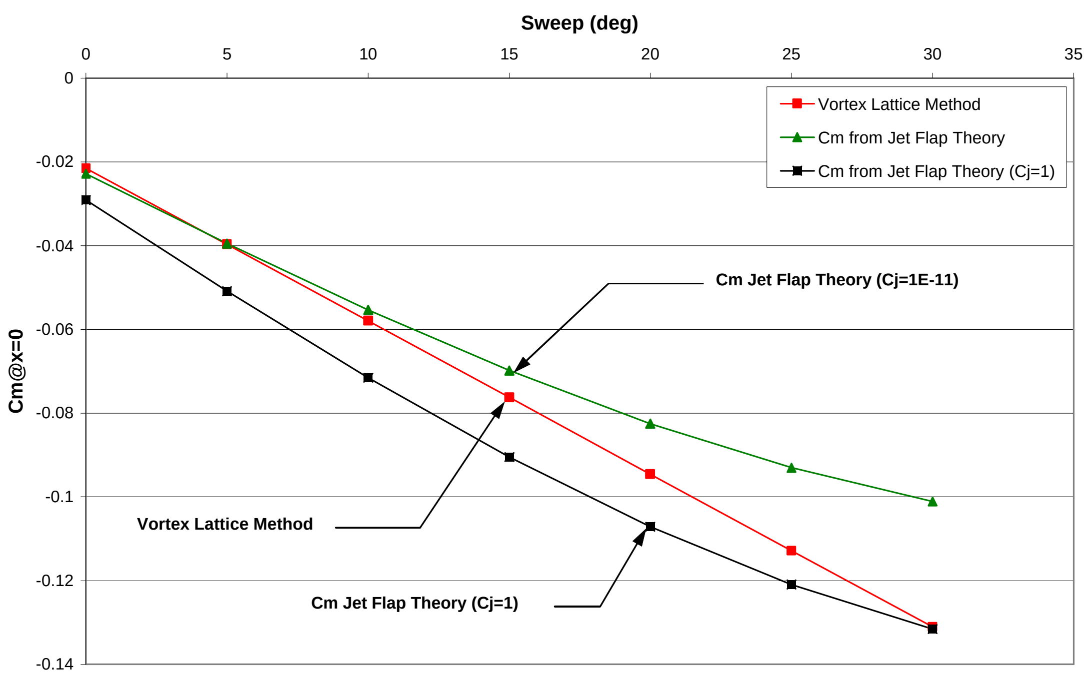

Figure 5-20: Comparison of moment coefficient estimation between Spence's jet flap theory and VLM with varying sweep angles.

5.2.1.2.2. Comparison for a BWB planform

In addition to the three test cases, the extension to Spence's Jet Flap theory was used to estimate the lift and moment coefficients as applied to the 1994 BWB design planform. Different values of the jet coefficient are used including one that is close to zero (to compare to results from a VLM program). Figure 5-21 and 5-22 give comparisons of both lift and moment coefficients as a function of angle of attack. Comparing results from the VLM program and that with a jet coefficient of $1\text{x}10^{-20}$, there is a clear difference in both the C_L-$\boldsymbol{a}$ and C_M-$\boldsymbol{a}$ slope. This leads to a difference of 8.7% difference in the calculation of the neutral point. To address this difference, in the implementation of jet flap theory approximation, both the C_L-$\boldsymbol{a}$ and C_M-$\boldsymbol{a}$ slopes will be adjusted to match that obtained from the VLM program. It is hoped that this adjustment will account for most of the differences between the approximate estimation of the lift and moment coefficients and with results from VLM.

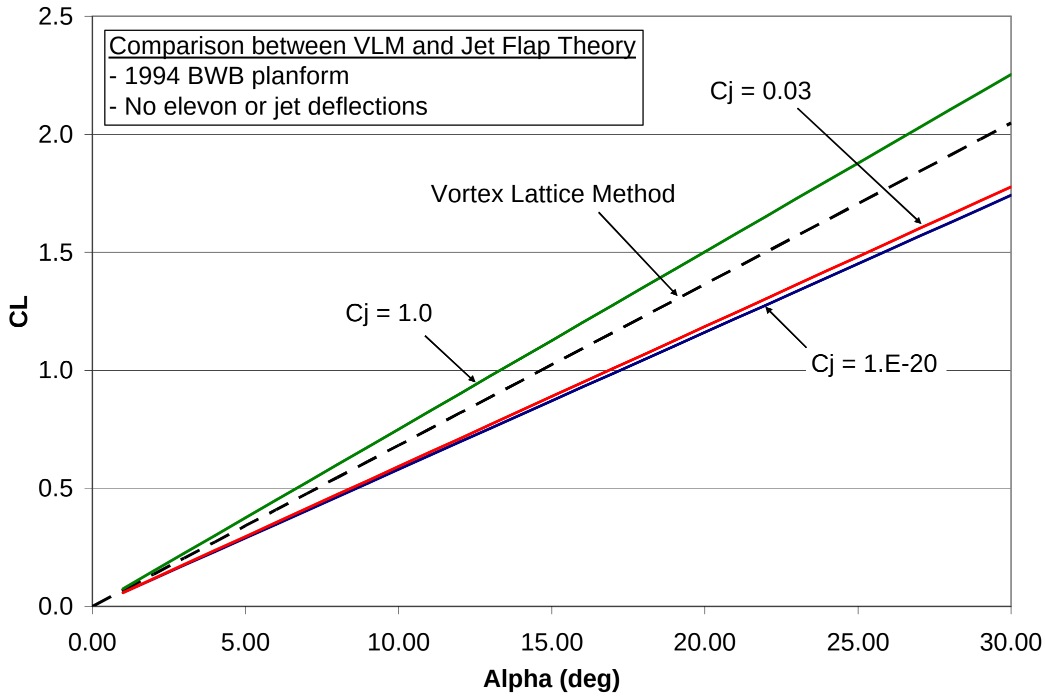

Figure 5-21: Comparison of the C_L-α curve between VLM results and Spence's jet flap theory at different jet coefficients.

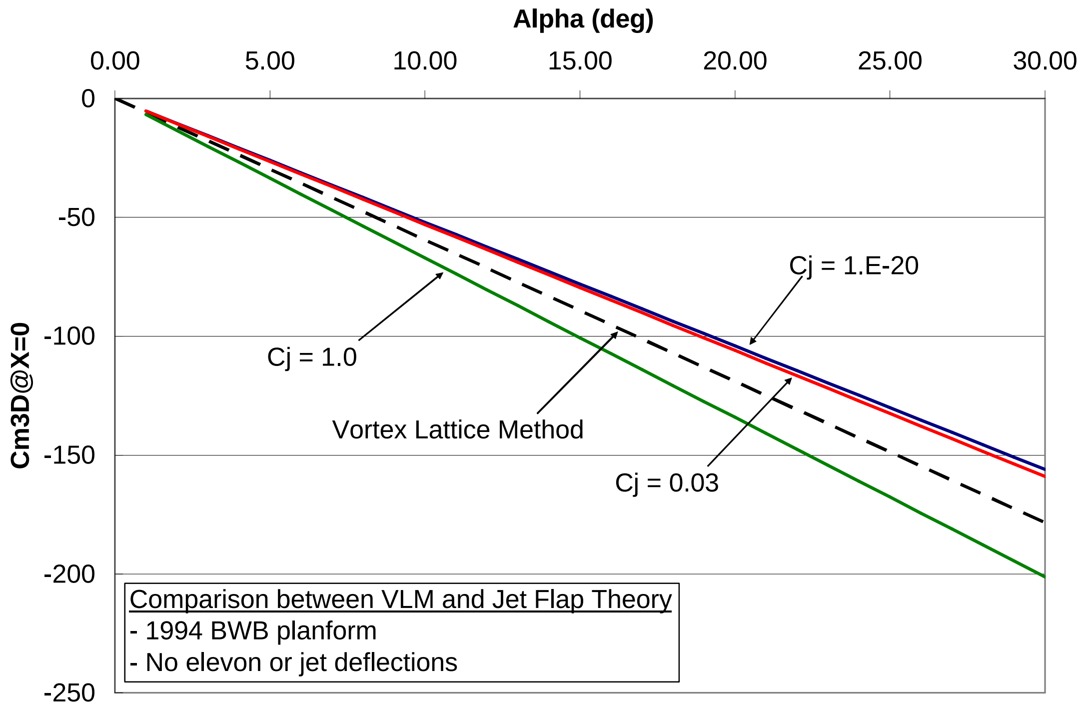

Figure 5-22: Comparison of the C_M-α curve between VLM results and Spence's jet flap theory at different jet coefficients.

A comparison of the C_L-a and C_M-a plots for configurations where the jet is deflected by 10° was also done. The results from VLM with the elevons deflected by 10° are also given for comparison.Figure 5-23 and 5-24 give that comparison. As expected, the zero angle of attack lift and moment coefficient for small jet coefficients are close to zero. Also as expected, increasing the jet coefficient increases the zero angle of attack lift and moment coefficients.

5.2.1.3. Calculation of the CG limits for a jet wing

For a conventional BWB configuration, the lift and moment coefficients are evaluated through a linearized form shown in Equation (4.27) and (4.28). These equations are repeated here in Equation (5.55) and (5.56) for reference.

$$C_L = C_{L_0} + C_{L_a} a + C_{L_{de}} d_e \tag{5.55}$$

$$C_M = C_L x_{CG} + C_{M_0} + C_{M_a} a + C_{M_{de}} d_e \tag{5.56}$$

Unlike that in Equation (5.55) and (5.56), the lift and moment coefficient formulation for the entire BWB aircraft takes on a nonlinear form. Therefore, the calculation of the CG limits for a distributed propulsion configuration requires a slightly different treatment than that explained in Chapter 4.

Consider the moment coefficient equation shown in Equation (5.57).

$$C_M = C_L x_{CG} + C_{M_{\text{Jet Flap}}}\left(C_J, a(h), t\right) \tag{5.57}$$

For the maximum elevon deflection boundary at V_{min}, Equation (5.57) can be directly solved for the upper and lower CG boundary locations, knowing the lift and moment coefficients. The maximum jet deflection angle is set at ± 20° (similar to the maximum elevon deflection for the conventional BWB configuration).

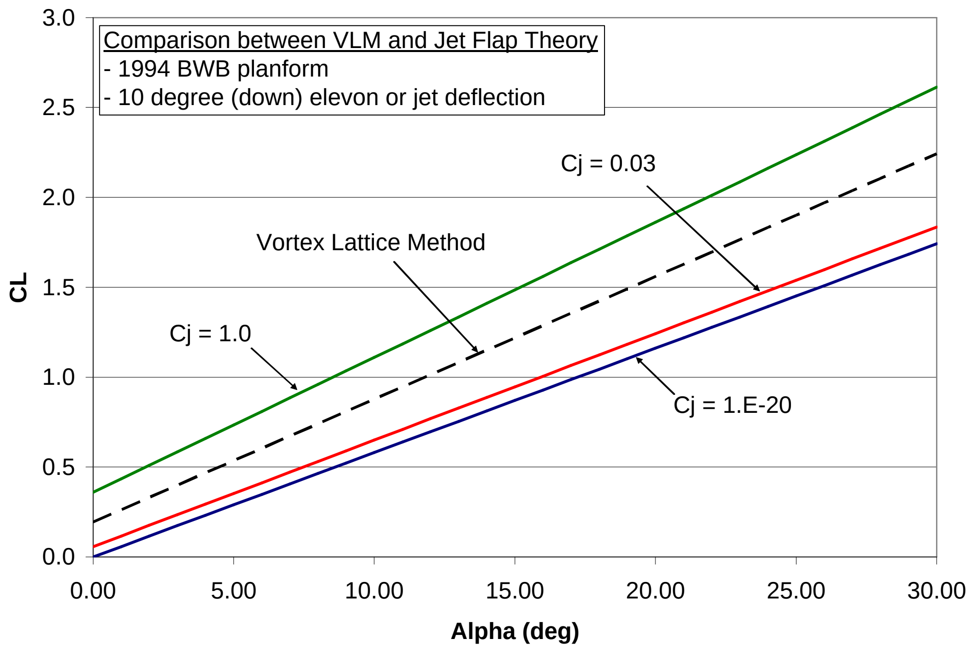

Figure 5-23: Comparison of the CL-α curve between VLM results and Spence's jet flap theory at different jet coefficients. A 10° elevon or jet deflection is used, changing the zero angle of attack lift coefficient.

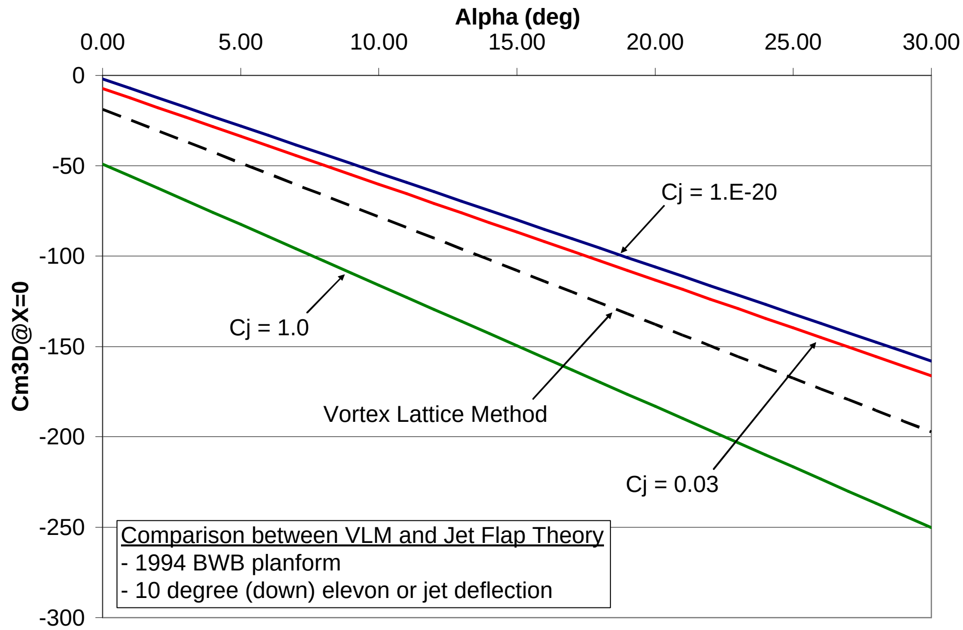

Figure 5-24: Comparison of the C_M-α curve between VLM results and Spence's jet flap theory at different jet coefficients. A 10° elevon or jet deflection is used, changing the zero angle of attack moment coefficient.

For the maximum angle attack of boundary at V_{min}, the jet deflection angle has to be determined given a lift coefficient and stall angle of attack (set at 27°). To do this, we use Equations (5.37) and (5.38) to solve for the jet deflection angles. The explicit equations were obtained by symbolically solving the equations using Mathematica. Once the jet deflection angle was obtained, Equation (5.37) was used to solve for the forward CG boundary.

Figure 5-25 shows a comparison of the CG limits for a conventional configuration with that of a distributed propulsion configuration with C_J = 0.03. This value of C_J was obtained by determining the required jet thrust (therefore leading to the calculation of C_J) using the method outlined in Section 5.1.1., for the 1994 BWB planform geometry, at Mach 0.85, cruising at 35000 ft. We consider this to be a typical value of C_J for the distributed propulsion BWB aircraft at cruise. In this comparison, the 1994 BWB planform was used. As can be seen, the distributed propulsion configuration provides just as much control authority as the conventional configuration at this jet coefficient.

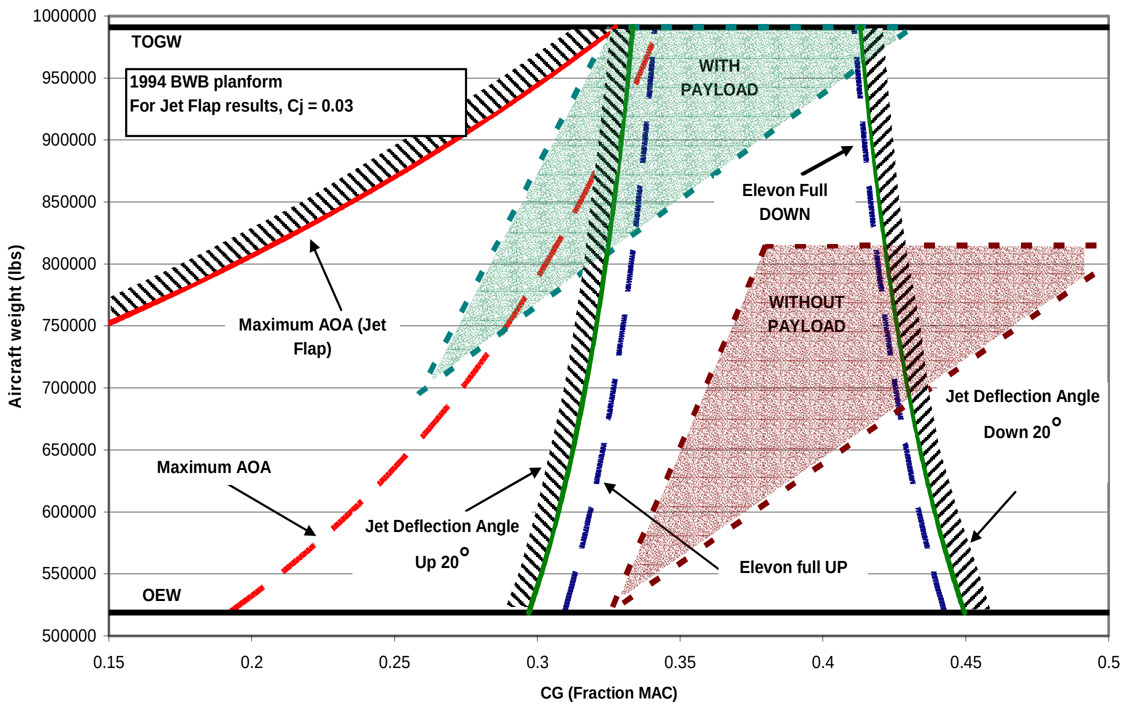

Figure 5-25: Comparison between the CG limits for a distributed propulsion BWB configuration and a conventional BWB configuration. Shaded areas show the possible CG location for the aircraft using fuel pumping.

5.2.2. Design Issues

In Figure 5-25, the jet coefficient of 0.03 that was used is typical of jet coefficients for the distributed propulsion BWB at cruise conditions. However, the conditions at which the control constraints are calculated are at much lower dynamic pressure (approach condition at sea level). Therefore, for the same jet thrust, the jet wing has a higher jet coefficient at approach than at cruise, which translates into greater control authority for the jet wing at approach than at cruise. This result is opposite from the behavior of conventional elevons where their effectiveness is smaller at the approach condition than at cruise[1]. Therefore, it could be that the limiting control case for distributed propulsion case would be at the cruise condition instead of approach. However, no criterion has been established for control limit at cruise conditions. One would expect that the control requirements at cruise would not be as great as that at

[1] Ironically, the loss of effectiveness of the elevons at approach condition (compared to cruise condition) is due to the lower dynamic pressures at this conditions. This is the same reason that gives the jet wing an advantage.

approach conditions. Presently, the approach condition is used as the critical condition for the distributed propulsion configuration.

5.3. *Thrust loss due to Ducting*

As a consequence of ducting some of the engine exhaust through the trailing edges of the BWB aircraft, there will be some thrust losses in those ducts. To simulate the duct losses on the portion of the thrust that is exhausted out the trailing edge, a duct efficiency factor is applied to the thrust of the aircraft. A schematic of the propulsion arrangement is shown in Figure 5-26.

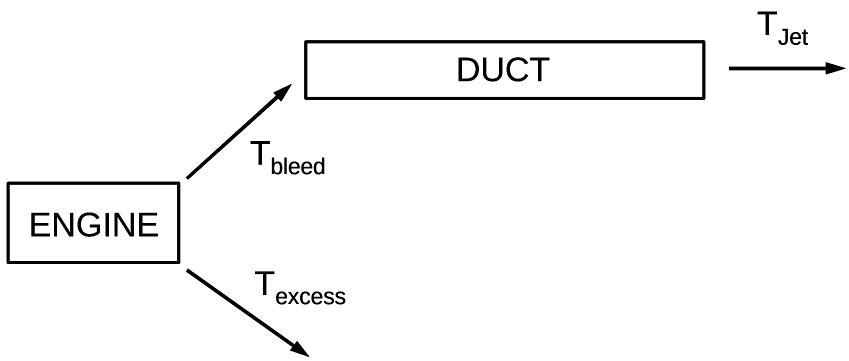

Figure 5-26: Schematic of the propulsion arrangement for the distributed propulsion BWB

We will define T_{useful} as the thrust from the engine already accounted for losses in the ducts. T_{Total} will be the total thrust that is produced by the engine (not accounting for duct losses. Equations (5.58) and (5.59) show this mathematically.

$$T_{useful} = h_{duct} T_{bleed} + T_{excess} \tag{5.58}$$

$$T_{Total} = T_{bleed} + T_{excess} \tag{5.59}$$

Therefore, the useful thrust can be formulated as shown in Equation (5.60).

$$T_{useful} = T_{bleed} (h_{duct} - 1) + T_{Total} \tag{5.60}$$

For the jet thrust, it is defined as

$$T_{jet} = h_{duct} T_{bleed} \tag{5.61}$$

Defining the jet thrust ratio as the ratio of the jet thrust to the useful thrust,

$$Ratio_{Jet} = \frac{T_{Jet}}{T_{useful}} \tag{5.62}$$

Therefore,

$$T_{Jet} = Ratio_{Jet}\, T_{useful} \tag{5.63}$$

Combining Equation (5.61) and (5.63), we get

$$T_{bleed} = \frac{Ratio_{Jet}}{h_{duct}} T_{useful} \tag{5.64}$$

Substituting Equation (5.64) into Equation (5.60), and rearranging, we get

$$\frac{T_{useful}}{T_{Total}} = \frac{1}{1 - \dfrac{h - 1}{h} Ratio_{Jet}} \tag{5.65}$$

In the present formulation, $Ratio_{Jet}$ is determined by the ratio of the profile and wave drag (or total drag minus the induced drag) to the total drag.

$$Ratio_{Jet} = \frac{C_{D_{Profile}} + C_{D_{Wave}}}{C_{D_{Total}}} \tag{5.66}$$

With this formulation, this thrust correction can be included into the BWB MDO design program, for a given duct efficiency factor.

An alternate formulation can be applied, by accounting the duct losses in the engine SFC instead of the thrust. Consider the definition of the engine SFC in Equation (5.67).

$$sfc = \frac{\dot{w}_f}{T} \tag{5.67}$$

Substituting Equation (5.65) into (5.67) by replacing the thrust T, with the useful thrust T_{useful}. Simplifying, we obtain Equation (5.68).

$$\begin{aligned} sfc_{new} &= \left(1 + \frac{1-h}{h} Ratio\right) \frac{\dot{w}_f}{T_{Total}} \\ &= \left(1 + \frac{1-h}{h} Ratio\right) sfc_{old} \end{aligned} \tag{5.68}$$

SFC_{old} is the specific fuel consumption before the losses in the ducts are accounted for. The formulation in Equation (5.68) can be used in lieu of that in Equation

(5.65). Both essentially account for the thrust losses in the ducts. However, only one of these two formulations should be used, so as to avoid accounting for the losses twice. In the current distributed propulsion BWB framework, the formulation in Equation (5.66) is used.

5.4. Structural/Ducting weight

To simulate the duct weight associated with diverting some of the engine exhaust out of the trailing edges, a duct weight factor is applied to the propulsion system weight. There is a possibility that the duct weight does not scale linearly with the propulsion weight. It has been suggested that perhaps the duct weight scales better with the jet velocity or the mass flow rate of the engine. However, without any compelling information to do otherwise, the distributed propulsion BWB MDO framework scales the duct weight through the use of a factor applied to the propulsion system weight.

Chapter 6: MDO Results

The goal of this study is to use MDO to study the design effects of integrating the distributed propulsion concept with the BWB aircraft. This involves identifying key propulsion integration effects with various aircraft design disciplines and formulating analysis methods to quantify their effects. This also involves developing an MDO framework to design a distributed propulsion BWB aircraft. Future research into the distributed propulsion BWB aircraft will involve using the framework to implement noise and emissions considerations into the design process. This chapter will discuss the results obtained from the MDO design optimization of the distributed propulsion aircraft.

Before performing distributed propulsion MDO, it is prudent to verify the integrated low to medium fidelity analysis methods and our MDO methodology against known designs. Doing this provides a level of confidence in the MDO program and reveals any inconsistencies within the integration process. Two published BWB designs will be used to verify the MDO analysis methods that are used. The first is the BWB design by Liebeck et al. [12], published in 1994. The other design was designed at Boeing, also by Liebeck et al., [21] published in 1996.

6.1. Verification Mission Profile

The mission profiles for the two BWB designs are identical. They call for a 7000 nmi range mission with a 500 nmi reserve range, cruising at a Mach number of 0.85. The passenger capacity of the aircraft is 800 passengers in a three-class configuration. The field performance requires a maximum 11,000 ft takeoff and landing field length. Figure 6-1 gives an overview of the mission profile.

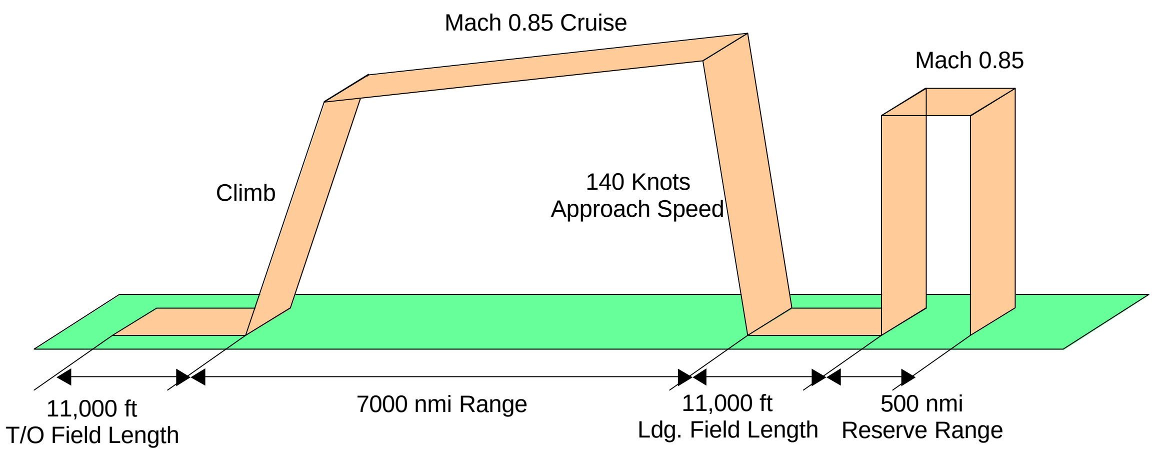

Figure 6-1: Verification mission profile

6.2. BWB verification results

6.2.1. 1994 BWB design analysis comparison

Figure 6-2 and 6-3 shows the 1994 BWB design planform as given in Liebeck et al. [12]. The geometric dimensions for this design are given in Table 6-1. Using these geometric dimensions and the verification mission profile, the 1994 BWB design was analyzed using the distributed propulsion BWB program, configured for a conventional BWB. In the initial development of the distributed propulsion BWB MDO code, the same method used to calculate the wing weight for the 1994 BWB design was used in our MDO code. This calculation method is from a formulation given in Beltramo et al. [85]. Later, it was replaced by the analysis methodology from FLOPS [86]. Therefore, the results using the initial wing weight formulation will be presented with that from our present methodology. Table 6-2 shows the comparison between the published design values and those obtained from our MDO code.

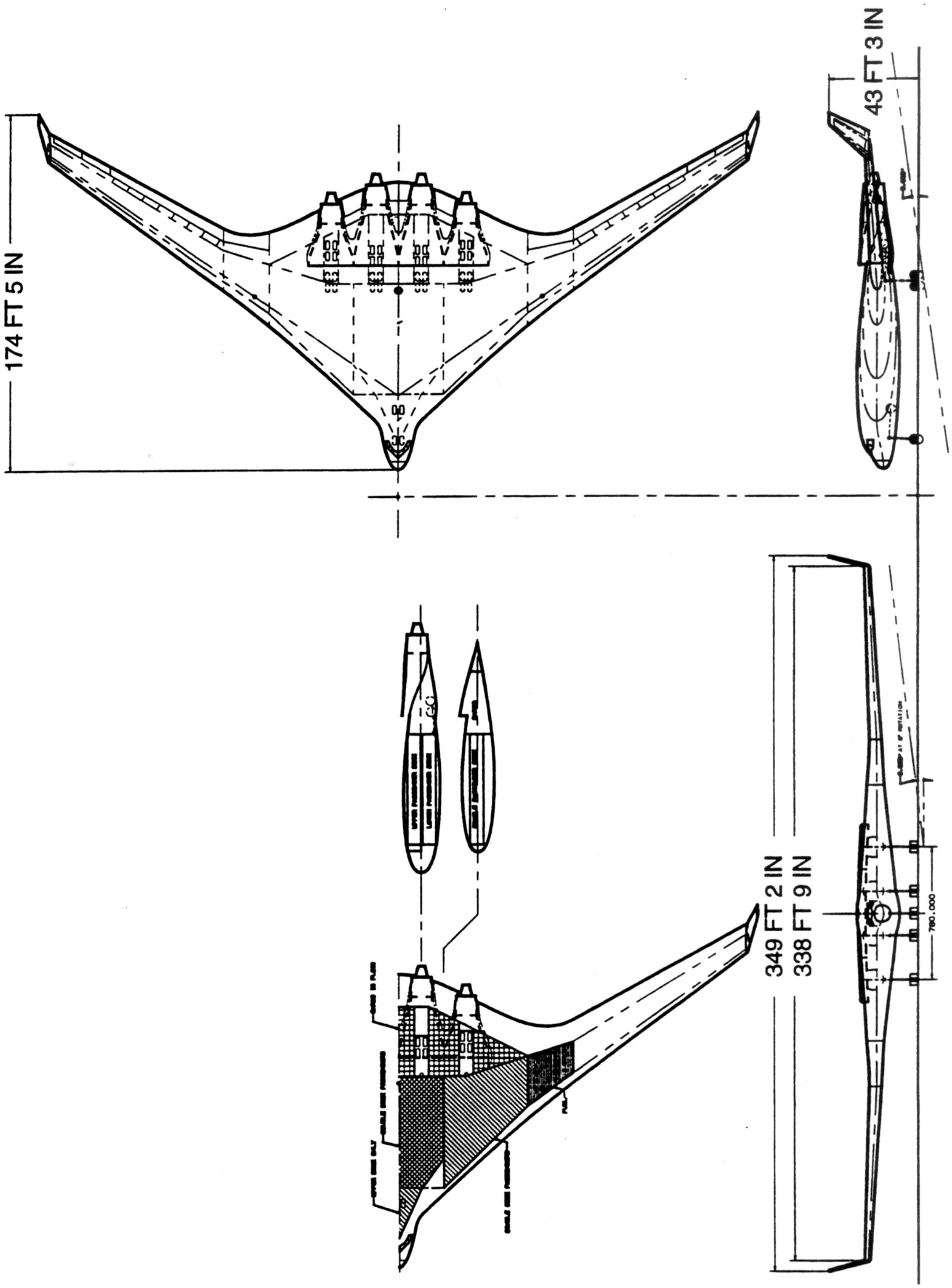

Figure 6-2: General design planform of the 1994 BWB design [12]

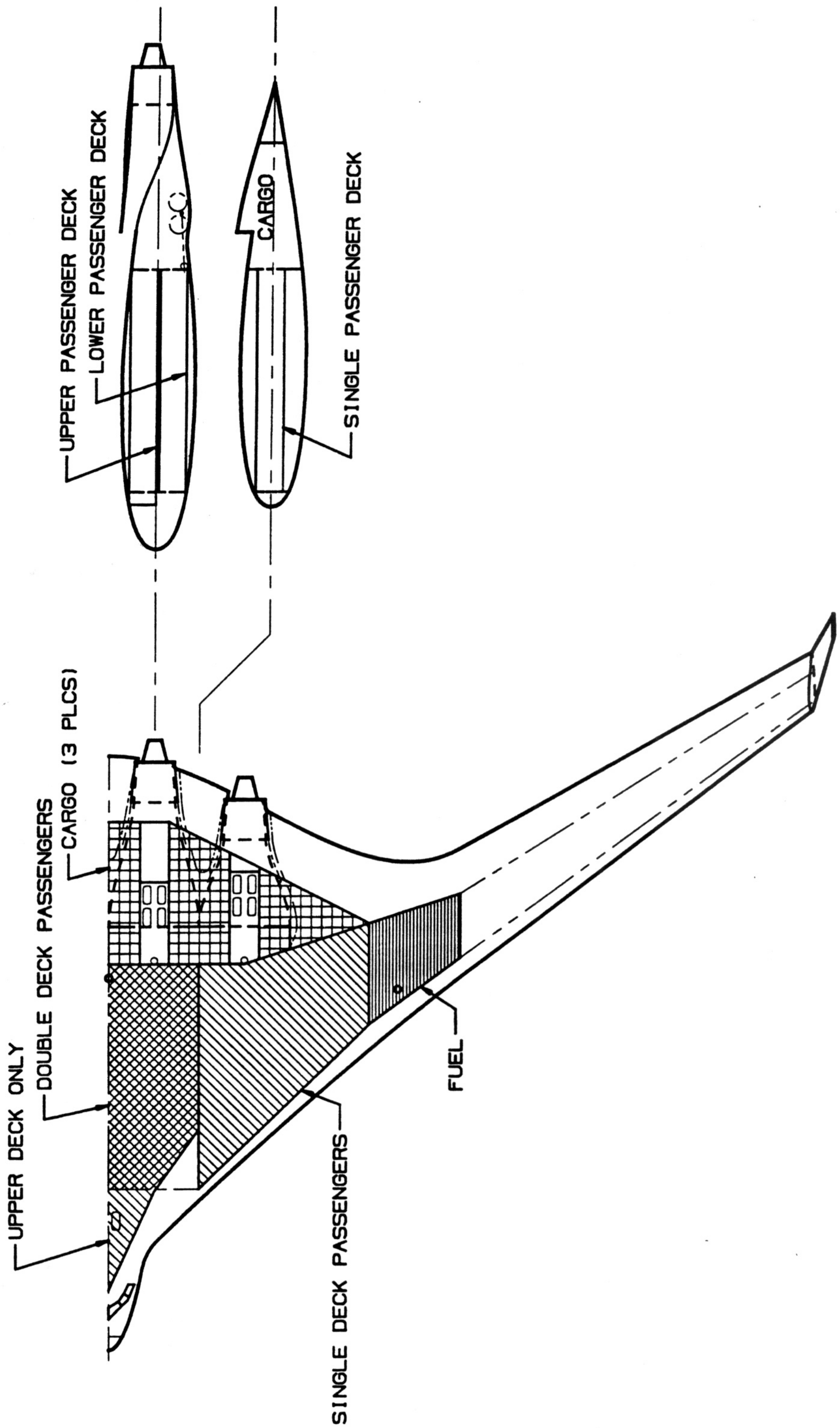

Figure 6-3: Detailed design planform of the 1994 BWB design[12]

Table 6-1: Table describing the design variable properties of the 1994 BWB design [12]

		1994 BWB design
Chord (ft)	Root	142.1
	Section 2	117.9
	Section 3	45.56
	Section 4	32.17
	Tip	13.4
t/c	Root	0.16*
	Section 2	0.15*
	Section 3	0.15*
	Section 4	0.14*
	Tip	0.14*
Sweep (deg)	Section 1-2	66.1
	Section 2-3	25.5
	Section 3-4	33.3
	Section 4-5	37.2
Wing Span (ft)		338.75
Thrust per engine (lbs)		55600
Fuel Weight (lbs)		296000
Number of Engines		4

Table 6-2: Comparison between published results and BWB MDO analysis of the 1994 conventional BWB design.

	1994 BWB design (Boeing)	BWB MDO analysis (Beltramo wing weight eqn.)	BWB MDO analysis (current wing weight analysis)
TOGW (lbs)	991000	968444	1010343
Wing Weight (lbs)	133800	120923	160595
T/W	0.22	0.23	0.22
W/S (lbs/ft^2)	95.0*	58.77	61.3
Engine SFC (lb/hr/lb)	0.578	0.575	0.575
Cruise CL	0.6	0.23	0.24
L/D at cruise	27.2	29.3	29.8
Calculated Range	7000	7432.2	7108

* Calculated based on trapezoidal area and not planform area

From Table 6-2, we see that there is less than a 2% difference in the TOGW calculation between that reported by Liebeck et al. [12] and the analysis of that configuration using our BWB MDO code. There is a large difference between the cruise lift coefficient that is reported and that which was obtained by the MDO code. Part of this difference can be accounted for with the difference in wing reference area calculation. If corrected for the difference in wing area, the cruise C_L becomes 0.38. Also, although not mentioned, it is quite possible that the value reported is the maximum cruise lift coefficient and not the average cruise lift coefficient, obtained from the MDO code. However, the *L/D* ratio at cruise values compares well. Overall, the MDO BWB analysis code compares satisfactorily with this case.

6.2.2. 1996 BWB design analysis comparison

Figure 6-4 shows the general arrangement drawing of the 1996 BWB design [21]. Table 6-3 provides the design variable data for this design that is input into the MDO code. Comparing this design with that of the 1994 BWB design, we see a noticeable difference between the two planforms. Using the planform area definition, the 1996 BWB design has a smaller aspect ratio of 4.9 compared to the aspect ratio of the 1994 BWB at 7.0. From a code validation standpoint, this difference is good, as it provides the opportunity to test the analysis methods with a different design planform.

Table 6-3: Table describing the design variable properties of the 1996 BWB design [21]

		1996 BWB design
Chord (ft)	Root	148.9
	Section 2	100.0
	Section 3	45.45
	Section 4	26.14
	Tip	11.36
t/c	Root	0.17
	Section 2	0.18
	Section 3	0.11
	Section 4	0.090
	Tip	0.095
Sweep (deg)	Section 1-2	51.7
	Section 2-3	32.0
	Section 3-4	29.3
	Section 4-5	34.2
Wing Span (ft)		280.0
Thrust per engine (lbs)		61900
Fuel Weight (lbs)		213447
Number of Engines		3

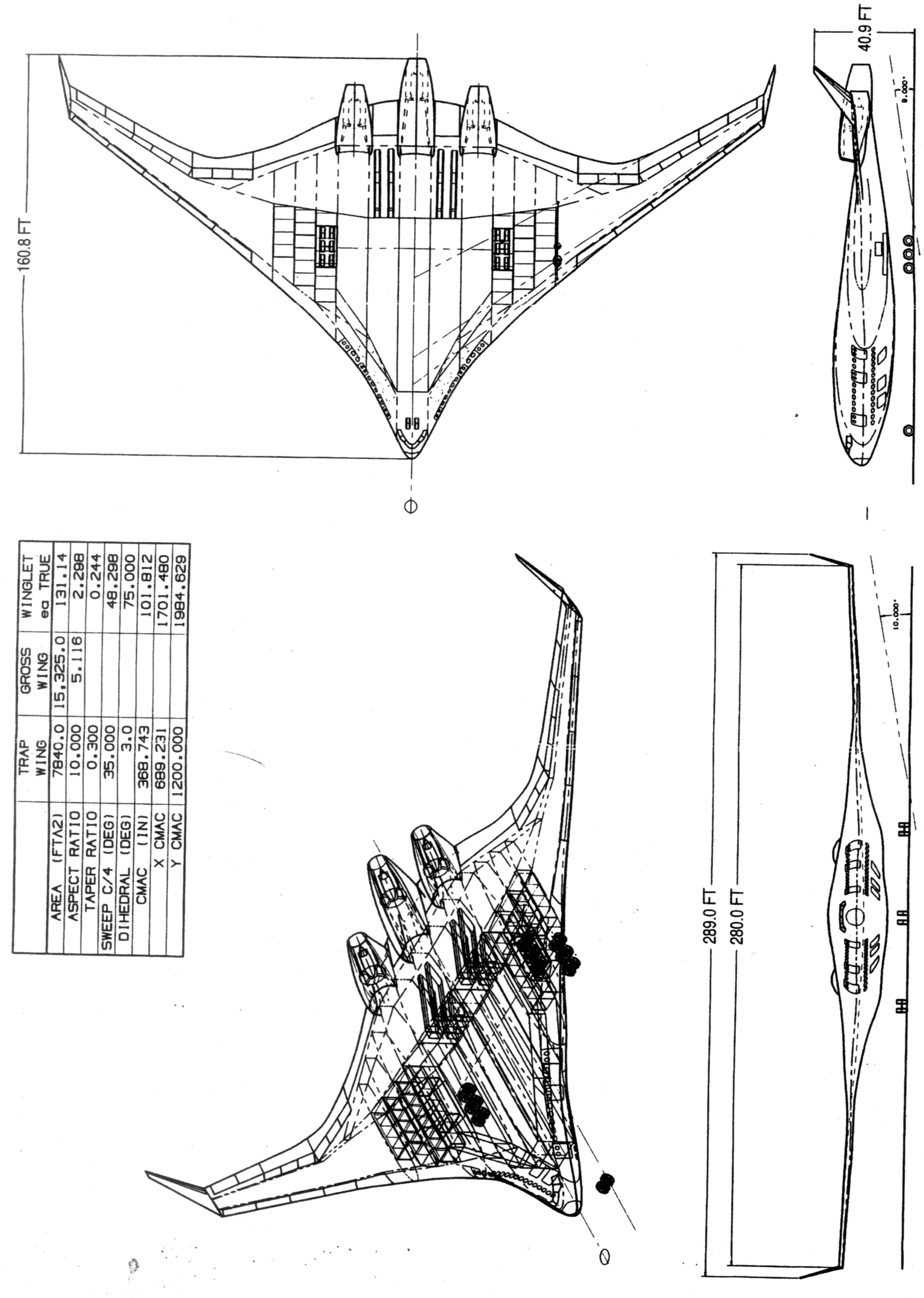

Figure 6-4: Arrangement drawing of the Boeing 1996 BWB design [21].

Table 6-4 compares the analysis from our MDO code with those published in the 1996 BWB report [21]. We see that our MDO code over predicts the TOGW of the aircraft by 7.6%. This difference is acceptable, considering the difference in the level of fidelity in modeling the aircraft weight. A major difference is in the wing weight where the MDO code over predicts the published value by 25%. This is probably because we are using the wing weight formulation from FLOPS that is intended for wings in a conventional fuselage/wing configuration. Also, an integrated design of the wing and cabin was not adopted in the MDO code (as done with the 1996 BWB design) which we would expect to reduce the wing weight estimates. Another difference is in the range calculation. The MDO code under predicts the range of the aircraft by 2000 nmi. This is due to two reasons. First, the engine SFC in the MDO code is much higher than that of the 1996 BWB aircraft. When the engine SFC of the BWB aircraft was reduced to the levels used in the 1996 design, the calculated range increased to 6300 nmi. Secondly, the 1996 BWB aircraft design does not take into account the 500 nmi reserve range that is adopted in the BWB MDO code. Hence, if the engine SFC were reduced, and the 500 nmi range were taken into account, there would only be a 200 nmi difference between that from the MDO code and that in the report. Although it is easy to adjust the engine SFC to match that which was used in the 1996 report, it was decided that the current model was sufficient for this study. If it is decided to do otherwise in the future, the distributed propulsion BWB MDO code is designed to be flexible enough to allow such a change without significant effort.

Table 6-4: Comparison between published results and BWB MDO analysis of the 1996 conventional BWB design.

	1996 BWB design (Boeing)	**BWB MDO analysis**
TOGW (lbs)	822632	884941
Wing Weight (lbs)*	184877	231837
T/W	0.226	0.21
W/S (lbs/ft^2)**	105*	55.5
Engine SFC (lb/hr/lb)	0.466	0.575
Cruise CL	0.39	0.23
L/D at cruise	22.97	28
Calculated Range	7000	4963.4

* Wing weight includes weight of passenger cabin

** Calculated based on trapezoidal area and not planform area

With the favorable validation results obtained using both the 1994 and 1996 BWB designs, we decided that the distributed propulsion BWB MDO code was mature enough to be used as a tool to examine the distributed propulsion BWB aircraft. An optimized conventional BWB aircraft design will be used as a comparator.

6.3. Optimization results: Distributed propulsion BWB vs. Conventional BWB designs

Once the distributed propulsion BWB MDO program was validated, both the conventional BWB and the distributed propulsion BWB designs were optimized. Using the optimum conventional BWB design as a comparator, an assessment of the effects of distributed propulsion was made. Using the same MDO framework allows for an 'apples to apples' comparison.

An eight engine configuration is used for the distributed propulsion BWB aircraft design. The conventional BWB aircraft has a four engine configuration, like that of the 1994 BWB design. For the optimum distributed propulsion BWB design, the engines are evenly spaced inboard of the 70% semi-span location on the wing. Some of the engine exhaust will exit through the trailing edge across the entire span of the aircraft. It is assumed that only 25% of the possible savings in propulsive efficiency due to 'filling in the wake' is attainable, and that the ducts used to divert the engine exhaust out the trailing edge have an efficiency of 95%. To account for the weight of the ducts, the weight of the propulsion system is increased by 10%. Although no detailed studies have yet been done to determine a nominal value for these parameters, these values are considered to be realistic. Results of parametric studies will be presented later that examine the sensitivities of these parameters to the design of the distributed propulsion aircraft.

To examine the individual distributed propulsion effects on the BWB design, four additional optimized BWB designs were made. These designs were created by adding each effect individually to the conventional BWB configuration and obtaining an optimum solution. The five distributed propulsion effects that were examined are:

- Number of engines
- Distributed propulsion induced drag effects

- Savings in propulsive efficiency
- Duct efficiency
- Duct weight factor

Table 6-5 and 6-6 shows the optimization results of both the conventional BWB configuration and distributed propulsion BWB configuration together with the 'intermediate' distributed propulsion configurations.

6.3.1. Comparison of final designs

Before we examine the optimization results in detail, consider Figure 6-5, which graphically shows the difference in planform shape between the optimum conventional BWB design and the optimum distributed propulsion BWB design. Both designs share similar planform shapes and it is difficult to visually distinguish the differences between the designs.

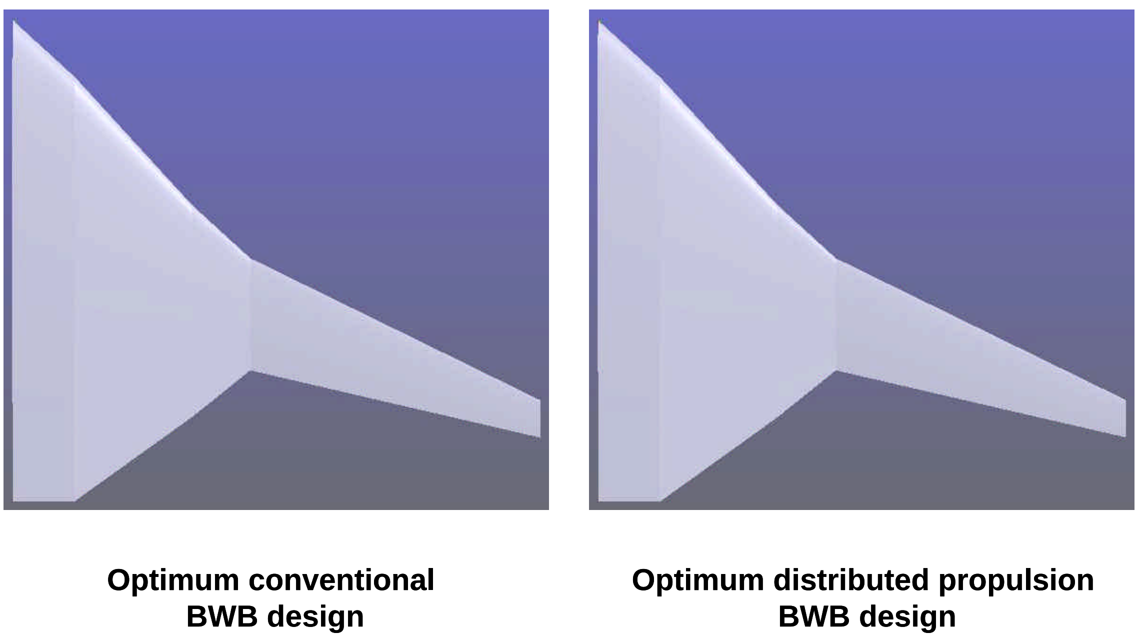

Figure 6-5: Comparison of the optimum configuration design of the conventional and distributed propulsion BWB aircraft.

Table 6-5: Optimum configuration comparisons between the conventional BWB design and the distributed propulsion BWB design, together with 'intermediate' optimum designs to show the individual distributed propulsion effects. The conventional BWB design in Column 1 is used as the reference design for calculating all the percentage comparisons.

Column number		1	2	3	4	5	6
		Conv. BWB design (4 engines)	Conv. BWB design (8 engines)	Dist. Prop. BWB design (induced drag effects only)	Dist. Prop. BWB design (perfect duct eff. & no duct weights)	Dist. Prop. BWB design (no duct weights)	Distributed Propulsion BWB design
Parameters							
Number of engines		4	8	8	8	8	8
Distributed propulsion factor		NA	NA	0.00	0.25	0.25	0.25
Duct efficiency		NA	NA	1.00	1.00	0.95	0.95
Duct weight factor		NA	NA	1.0	1.0	1.0	1.1
Optimized Design Variable Values							
h	Root	0.000	0.000	0.000	0.000	0.000	0.000
	Section 2	0.068	0.069	0.109	0.117	0.113	0.113
	Section 3	0.370	0.372	0.368	0.370	0.371	0.372
	Section 4	0.452	0.453	0.450	0.450	0.450	0.451
	Tip	1.000	1.000	1.000	1.000	1.000	1.000
Chord (ft)	Root	130.0	129.1	126.9	126.3	126.6	126.7
	Section 2	122.0	120.2	113.1	110.8	112.3	112.5
	Section 3	66.8	68.9	55.5	54.1	54.6	54.7
	Section 4	30.0	30.0	30.0	30.0	30.0	30.0
	Tip	10.0	10.0	10.0	10.0	10.0	10.0
t/c	Root	0.17	0.17	0.18	0.18	0.18	0.18
	Section 2	0.18	0.18	0.20	0.20	0.20	0.20
	Section 3	0.13	0.13	0.16	0.16	0.16	0.16
	Section 4	0.10	0.10	0.11	0.11	0.11	0.11
	Tip	0.10	0.10	0.10	0.10	0.10	0.10
Sweep (deg)	Section 1-2	31.21	33.33	34.30	35.85	34.71	34.60
	Section 2-3	29.34	29.81	33.41	33.43	33.24	33.23
	Section 3-4	26.24	24.47	29.97	29.48	29.49	29.49
	Section 4-5	23.37	21.62	24.53	23.73	23.71	23.71
Wing Span (ft)		292.18	290.91	278.04	273.73	274.63	274.57
Average Cruise Altitude (ft)		41411	40400	39585	39273	39270	39267
Total Thrust (lbs)		181140	154265	149376	148479	153156	154342
Fuel Weight (lbs)		269828	271449 (0.60%)	268171 (-0.61%)	261015 (-3.27%)	261861 (-2.95%)	263692 (-2.27%)
Optimum Results							
TOGW (lbs)		928929	918069 (-1.17%)	891905 (-3.99)	878292 (-5.45%)	881630 (-5.09%)	887622.9 (-4.45%)
Wing Weight (lbs)		124406	120476 (-3.16%)	106780 (-14.17)	102998 (-17.2%)	103858 (-16.5%)	103981 (-16.4%)
Reference Area (ft^2)		15197	15179	13741	13453	13562	13579
Aspect Ratio		5.62	5.58	5.63	5.57	5.56	5.55
W/S (lbs/ft^2)		61.13	60.48	64.91	65.28	65.01	65.37
T/W		0.195	0.168	0.167	0.169	0.174	0.174
L/D @ Cruise		29.64	28.95	28.29	27.76	27.81	27.82
Cruise *CL*		0.28	0.26	0.27	0.27	0.27	0.27

Table 6-6: Active constraint comparisons between the conventional BWB design and the distributed propulsion BWB design, together with 'intermediate' optimum designs to show the individual distributed propulsion effects.

Column number	1	2	3	4	5	6
	Conv. BWB design (4 engines)	**Conv. BWB design (8 engines)**	**Dist. Prop. BWB design (induced drag effects only)**	**Dist. Prop. BWB design (perfect duct eff. & no duct weights)**	**Dist. Prop. BWB design (no duct weights)**	**Distributed Propulsion BWB design**
Active constraints						
Range	✓	✓	✓	✓	✓	✓
Fuel volume	✓	✓	✓	✓	✓	✓
Second segment climb gradient	✓	✓	✓	✓	✓	✓
Top of climb rate of climb		✓	✓	✓	✓	✓
Cabin area	✓	✓	✓	✓	✓	✓
Cabin aspect ratio	✓	✓	✓	✓	✓	✓
Root span station thickness	✓	✓	✓	✓	✓	✓
2nd span station thickness	✓	✓	✓	✓	✓	✓
3rd span station thickness	✓	✓	✓	✓	✓	✓
Control constraint at WZF	✓	✓	✓	✓	✓	✓

First compare the optimum conventional BWB design with the optimum distributed propulsion BWB design. These results are listed in Columns 1 and 6 respectively in Table 6-5 and 6-6.We find that both designs have the same aspect ratio of about 5.6, and cruise at nearly the same lift coefficient. Except for the top of climb rate of climb constraint, both aircraft designs have the same active constraints.

In both optimum designs, five of the design variables are at or close to their minimum side constraints. These design variables are:

- Position of the fourth span station
- Chord length of the fourth span station
- Chord length of the tip (fifth) span station
- *t/c* ratio of the forth span station
- *t/c* ratio of the tip (fifth) span station

All five of these design variables relate to the outboard wing sections that do not house the passenger cabin. This suggests that the main cause of the design variables reaching their minimum side constraints relates to the available fuel tank volume within the wings. From Table 6-6, we see that the fuel volume constraint is one of the active constraints in both designs. The optimizer reduces the size of the outboard sections to the smallest possible size, as long as the fuel volume constraint is not violated. In this case, the third wing section has a large volume to carry a majority of the fuel, since the volume at this section is dependant on the *t/c* ratio and chord length of the third wing section.

Both the *t/c* ratio and chord length at this section are limited by the cabin height constraint, therefore creating the volume in the third wing section to carry most of the necessary fuel. This is true because the optimizer is attempting to move the position of the fourth span station as far inboard as possible, and reducing the *t/c* ratio and chord length at this station to its minimum. This is occuring to reduce the size and volume in the third wing section. In addition, thin wing sections with higher aspect ratios allow for higher *L/D* ratios, by reducing wave and induced drag. In the optimum BWB designs the optimizer manages to find a design in which there is no additional unused fuel volume in the wings (i.e. the fuel volume constraint is active) while trying to reduce the size of the outboard wing sections to as much as possible.

In conventional aircraft wings, the chord length and *t/c* ratio of the wing sections are usually constrained by the high structural weight of thin, high aspect ratio wing sections. The BWB is not penalized by a high structural weight because of the large, thick inboard sections that are able to carry large loads. This leads us to consider the load distribution on the wings. In the distributed propulsion BWB MDO program, we assume an elliptical load distribution across the span. However, in reality, the inboard sections will be very lightly loaded due to the large *t/c* ratios, while the outboard sections will be generating much of the aircraft lift. The elliptical load distribution assumption requires the inboard sections to carry too much lift, while making the outboard wing sections to produce less lift. Although the outboard sections generates much lift due to the small chord lengths, as seen in Figure 6-6, it is not as high as it should be. This elliptical loading condition does not incur a large enough structural penalty to constrain the outboard wing chord lengths and *t/c* ratios.

In addition, if a non-elliptical load distribution was adopted, the maximum sectional lift coefficient constraint will cause the outboard chord lengths to increase. To illustrate, consider Figure 6-6, which is the sectional lift coefficient distribution of the conventional BWB design. The sectional lift coefficient distribution constraint is not active in this design as the maximum lift coefficient limit is 0.65 (the maximum lift coefficient for the design is 0.643). However, if a non-elliptical load distribution was adopted, the optimizer would have to increase the chord lengths of the outboard sections to keep the sectional lift coefficient below the maximum limit.

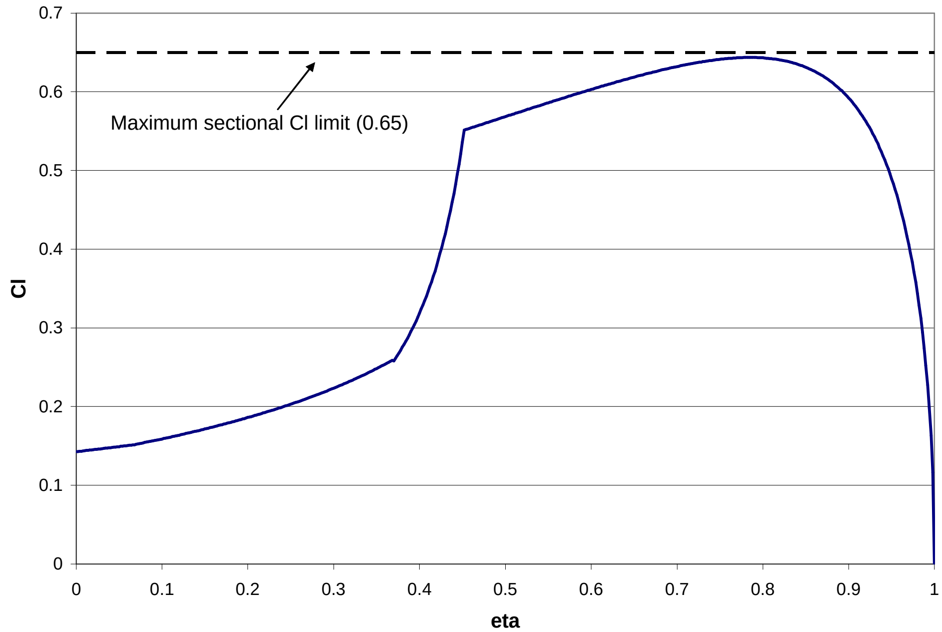

Figure 6-6: Sectional lift coefficient distribution of the conventional BWB design assuming an elliptical load distribution. The maximum lift coefficient is 0.643 at the 80% semi-span location.

The logical question then would be: Is it realistic to assume an elliptical load distribution? Most probably not. With thick inboard wing sections, the airfoil shapes here would have high wave drag if required to carry the elliptical loading. We therefore expect the wing loads to shift towards outboard wing sections, departing from an elliptical load distribution. Such non-elliptic spanloads have been used in Boeing's BWB design and can be found in Reference [19]. We expect that once this non-elliptical load distribution is modeled and implemented, the chord length and *t/c* ratios will increase to reduce structural weight. Currently, this has not been implemented in the distributed propulsion BWB MDO program.

Another logical question would be: Should the minimum side constraints of these design variables be lowered from their current settings? We believe that the answer to this is no. As the wing becomes thinner, there will be less volume in the wings to place necessary systems such as hydraulic control lines, and control actuators. For the distributed propulsion configuration, it would be difficult to install ducts inside these thin sections. In addition to this, it would be more difficult to manufacture much thinner wings, much less design an internal structure at the wing tips to carry the winglets. With the current minimum side constraints, the wing tip maximum thickness is one feet.

We also see that the second segment climb gradient constraint and top of climb rate of climb constraints are active. These two constraints set the thrust level of the aircraft.

Both cabin area and cabin aspect ratio constraints are active, indicating that the optimizer is striving for the smallest cabin size possible. One reason why it is doing this is because the span sections that house the passenger cabin result in high wave drag. Hence, the optimizer is making this section as thin and small as it can be. The same can be said about all three span station thicknesses being active constraints.

It is also interesting to note that the fuel volume constraint is active for both optimum designs. This indicates that there is just enough volume in the wings to hold the require fuel to meet the mission range. It also implies that both designs do not use fuel shifting to control the aircraft CG location to meet the control constraints.

From Table 6-5, we see that the distributed propulsion BWB design is 4.45% lighter than the conventional BWB aircraft. It also requires 2.3% less fuel to perform the same mission. We do see some differences in geometric and other design variables between the two designs. One difference is that the reference area of the optimum distributed propulsion BWB is 10% smaller than the conventional BWB design, while having similar aspect ratios. This means that the optimum distributed propulsion BWB design has a shorter span than the optimum conventional BWB design, and from Table 6-5, this reduction is 6%. In general, the optimum distributed propulsion BWB design has a higher quarter chord sweep and the average cruise altitude is about 2000 ft lower that its comparator. The distributed propulsion BWB design differs from the conventional BWB design in that the chord lengths of the first three sections are smaller. In turn, the *t/c* ratios at these sections are higher to meet the passenger cabin thickness constraints. This results in the distributed propulsion BWB aircraft having a 4% higher wing loading (*W/S*). The distributed propulsion BWB aircraft requires 15% less total thrust, which corresponds to a *T/W* decrease of 11%. Also, the location of the second span station has moved further outboard in the distributed propulsion BWB optimum design.

6.3.2. Effects of the distributed propulsion parameters

Consider Columns 2, 3, 4 and 5 in Table 6-5 and 6-6. They shown the result of individually adding the distributed propulsion effects to the conventional BWB design (optimizing for each case) to produce the final distributed propulsion design.

The design in Column 2 increases the number of engines on the conventional BWB configuration from 4 to 8. This produces a decrease in TOGW by 1.17%. This result is due to a decrease in wing weight of by 3.2%. The required fuel weight for this design is 0.6% (1600 lbs) higher than the conventional (4 engine) BWB optimum design. The design maintains relatively the same aspect ratio, wing loading and cruise *L/D*. There is a decrease in total thrust by almost 15%, which results in a reduction of the *T/W* ratio by almost 14%. One would expect that such a change in total available thrust would have a significant effect on the required fuel weight. However, this is not true as the thrust level of the aircraft is determined by the top of climb rate of climb constraint and the second segment climb gradient constraint while the required fuel weight is determined primarily on the cruise performance of the aircraft.

The design in Column 3 adds the distributed propulsion induced drag effect to the configuration in Column 2. This optimum design is 4% lighter in TOGW than the optimum conventional (4 engines) BWB design (shown in Column 1). This is a 2.8% reduction from the design in Column 2. The wing weight was reduced by 11% from that of the design in Column 2. This reduction is due to a reduction in wing span (by 4.4%), decrease in the wing planform area (by 9.5%) and an increase in *t/c* ratios for the inboard span stations. The results indicate that the optimizer is improving the structural performance of the aircraft to ultimately reduce the TOGW. There is no aerodynamic performance penalty incurred since the reduction in induced drag due to distributed propulsion allows for a smaller wing for the same aerodynamic performance, as indicated by the similar *L/D* ratios and cruise C_L (between designs in Column 2 and 3). The lighter TOGW design results in a 3% lower required thrust.

The design in Column 4 adds the effect of the savings in propulsive efficiency to the design in Column 3. In this configuration, we assumed that 25% of the possible savings in propulsive efficiency can be attained by ‘filling in the wake’ of the aircraft. This effect reduced the TOGW of the aircraft by 1.46% from the design in Column 3.

This is primarily due to a reduction in fuel weight of 2.7% which is a consequence of the improvement in engine efficiency. This is also due to a reduction in wing weight of 3.0%, resultant of an almost 2% smaller wing planform area. The aircraft planform and geometric design remains relatively similar to that of the design in Column 3.

The design in Column 5 adds the effect of the duct efficiency to the configuration in Column 4. As expected, when the duct efficiency was reduced from 100% (condition for the design in Column 4) to 95%, the total required thrust increased by 2.6%. This resulted in a TOGW increase of 0.36% from the design in Column 4. As a result of the increased required thrust, and therefore the increased weight of the propulsion system, the wing weight increased by 0.7% and the required fuel weight increased by 0.3% from the design in Column 4. An increase in planform area of 0.7% is also observed. Otherwise, the general aircraft planform and geometric design remains relatively unchanged.

By comparing the final distributed propulsion BWB design with that on Column 5, we can quantify the effects of the duct weight factor on the distributed propulsion BWB design. Due to the addition of the duct weights (via the use of the duct weight factor), the TOGW of the aircraft increased by 0.64%. This is brought on by a relatively small increase in wing weight of 0.1%. The design maintains relatively similar reference areas, aspect ratios and geometric designs.

Figure 6-7 shows a stacked bar chart with the breakdown of the individual weights of each of the designs as the distributed propulsion effects are added and design optimized.

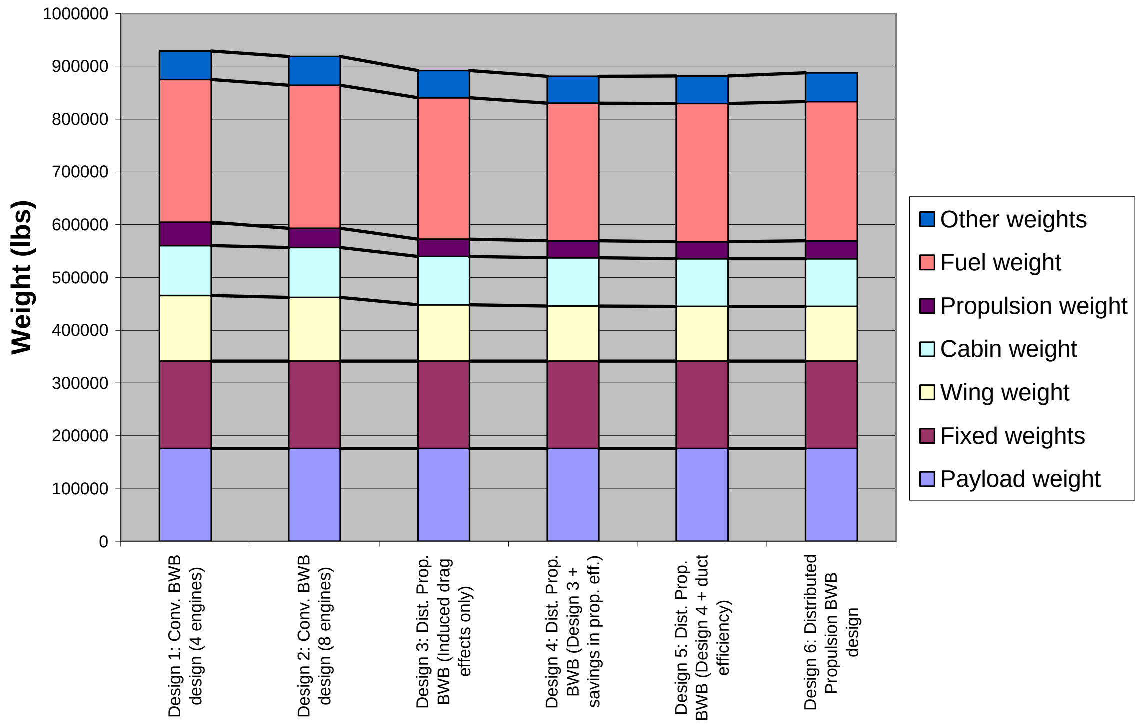

Figure 6-7: Stacked bar chart showing the weight breakdown of each of the designs as the individual distributed propulsion effects are added and design optimized.

6.3.3. Convergence histories

Figure 6-8 and Figure 6-9 show the convergence history of the optimum conventional BWB design and the optimum distributed propulsion BWB design respectively. Both optimizations were started at the same design point. As we can see, the distributed propulsion BWB design converges to its optimum in fewer iterations (by 9 iterations) than the conventional BWB design. For the conventional BWB design, the optimizer stops prematurely at a sub-optimal solution. At this point, the design variables were increased by 1% (except for the fuel weight, which was increased until it satisfied the range constraint) and the optimization restarted. After 13 more iterations, the optimizer reaches the current optimum design. Appendix B gives the iteration history for the distributed propulsion BWB optimization for all the 21 design variables. To ensure convergence all the methods explained in Chapter 4 (Section 4.3.2) were employed on the optimum designs, but no new designs were produced.

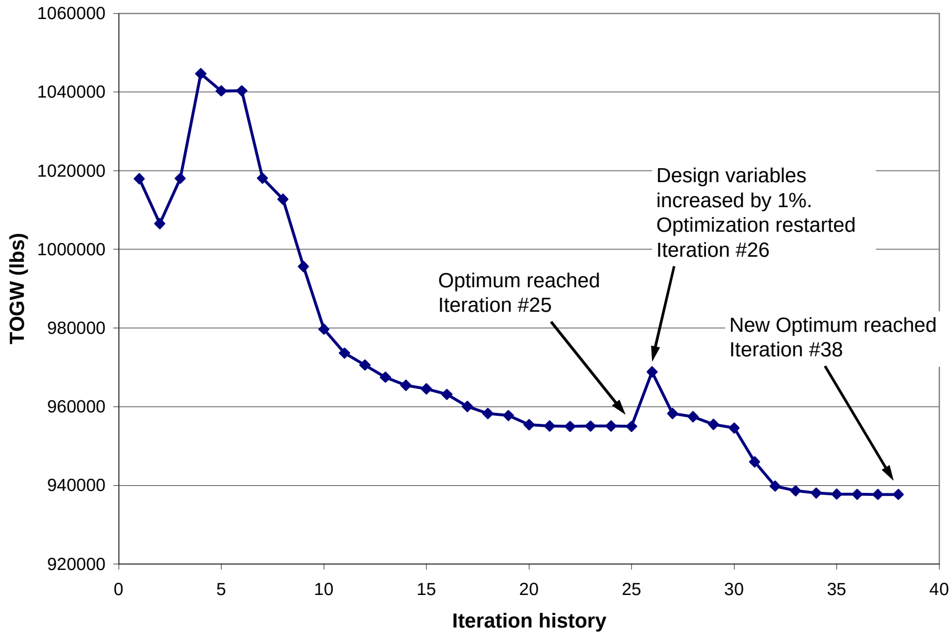

Figure 6-8: Optimization convergence history of the conventional BWB design

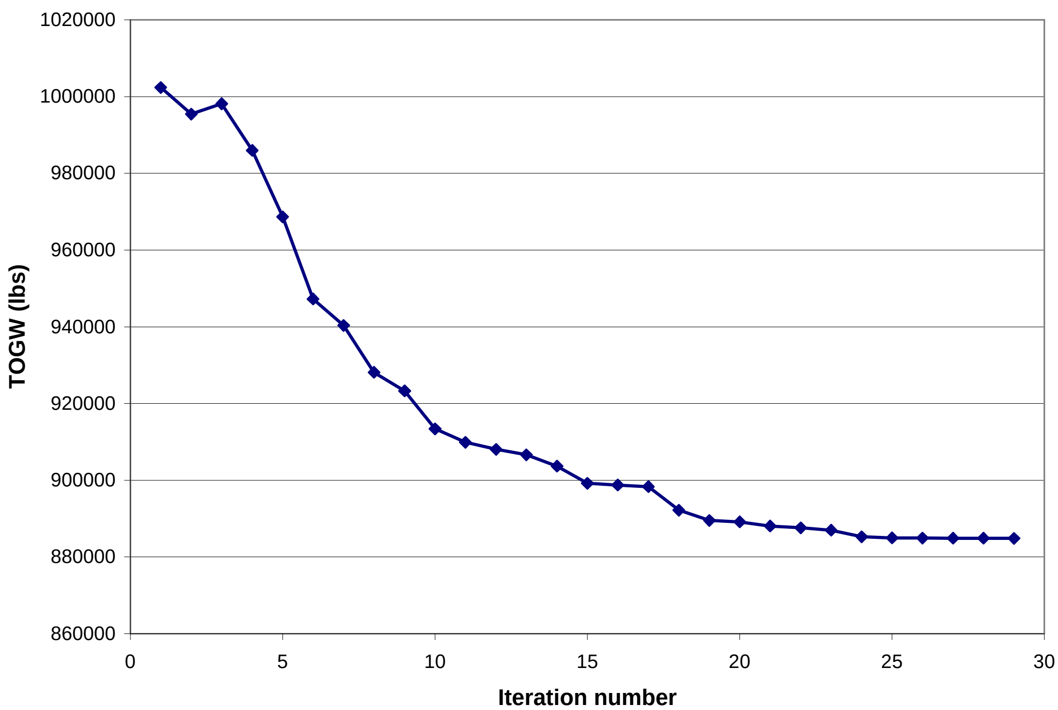

Figure 6-9: Optimization convergence history of the distributed propulsion BWB

6.4. *Parametric sensitivities*

To further understand the effects of distributed propulsion on the BWB design, parametric studies were performed, varying important design parameters that define the distributed propulsion configuration. These studies will provide the design sensitivities and help identify key issues in the distributed propulsion BWB aircraft design.

6.4.1. Duct efficiency

A parametric study was done by varying the duct efficiency. In the MDO process, a duct efficiency factor is applied to the thrust that is diverted from the engines to exhaust out the trailing edge of the aircraft. The duct efficiency will be determined by the detailed duct design parameters such as length of duct, duct cross section shape and size, the number of turns, and the turning angles. By performing this parametric study, we can determine how important the duct efficiency factor is to the distributed propulsion BWB design. In this parametric study, the duct efficiency is varied in 2% intervals from 80% to 100%. At each interval, the distributed propulsion BWB aircraft is optimized to satisfy the constraints and produce the lowest TOGW design.

Figure 6-10 shows the variation of the TOGW with respect to the duct efficiency. In this figure we see that the TOGW of the aircraft decreases with increasing duct efficiency as expected. However, there is only a 1.3% decrease in TOGW for a duct efficiency increase of 20%. This means that for every 1% increase in duct efficiency, there will be a 0.065% (600 lbs) decrease in TOGW. If we extrapolate this result, the duct efficiency will have to be only 2.7% for the distributed propulsion BWB aircraft to have the same TOGW as the conventional BWB baseline. Although we do not expect the effect of the duct efficiency to behave linearly at such an extreme efficiency, it shows that the distributed propulsion BWB aircraft is relatively insensitive to the duct efficiency.

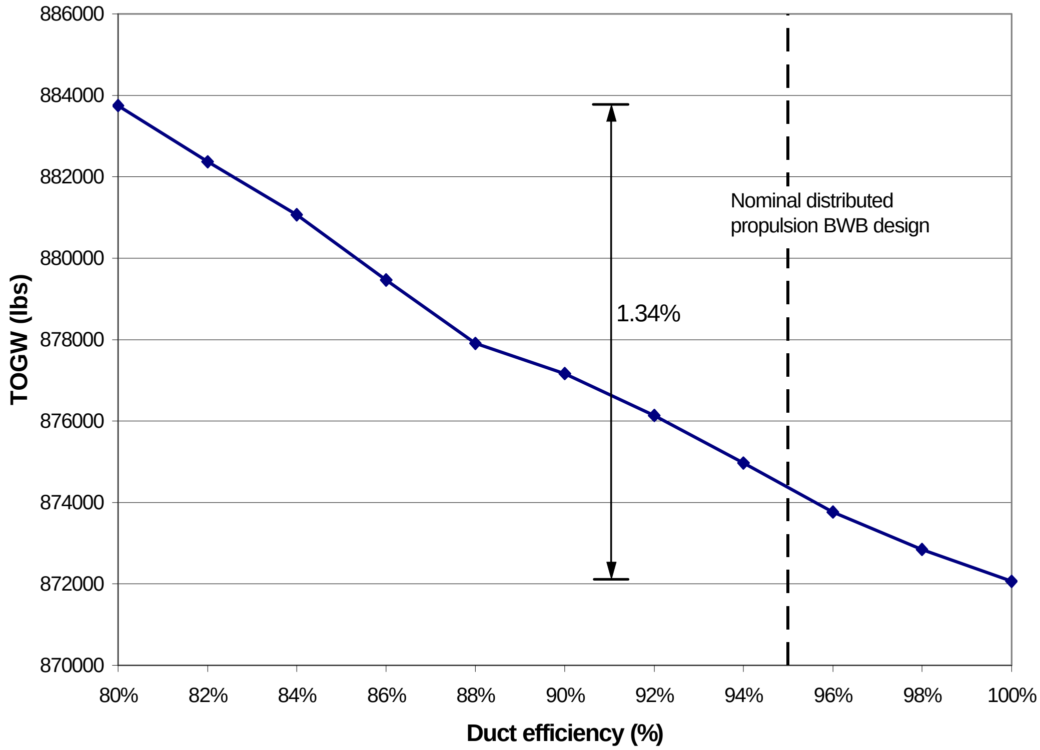

Figure 6-10: Variation of the distributed propulsion BWB aircraft TOGW with duct efficiency

It was found that there is negligible change in the planform shape of the distributed propulsion BWB aircraft with respect to changing the duct efficiency. The planform area varied only 0.7% throughout the 20% range of duct efficiency. However, as expected, there was a change in required engine thrust with varying duct efficiency. As a result of this change in required engine thrust, the amount of required fuel weight was also affected when changing duct efficiency. Figure 6-11 shows this result. We see that for a 20% increase in duct efficiency, the required thrust per engine decreased by 15.6%. Consequently, this resulted in a fuel weight decrease of 2.4%.

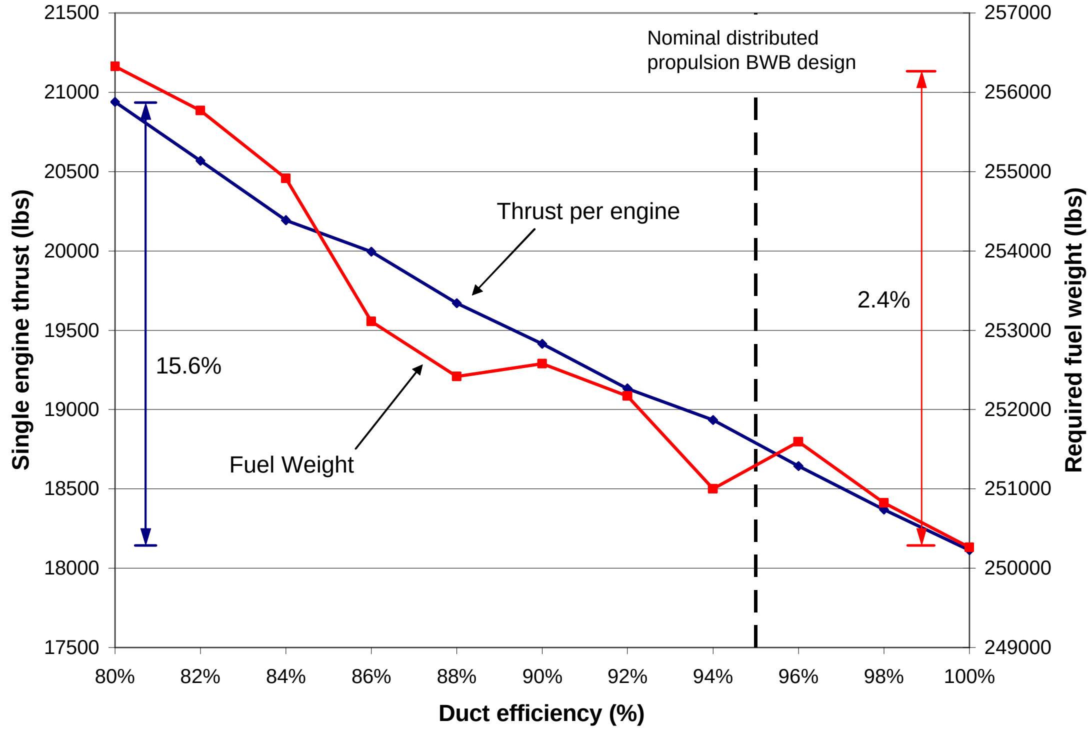

Figure 6-11: Variation of the required fuel weight and thrust per engine for the distributed propulsion BWB aircraft with respect to the duct efficiency

In light of the reduction in engine thrust and fuel weight, the small change in TOGW can be explained. From the optimum distributed propulsion BWB design results, the fuel weight and propulsion weight make up about 30% and 5% of the TOGW respectively. For simplicity, if we assume that the propulsion weight scales with the engine thrust, the reduction in TOGW due to a reduction in propulsion weight will be about 0.78%. The reduction in fuel weight makes a TOGW reduction of 0.72%. The total of these two reductions equal 1.5%, which is about the same level of reduction in TOGW shown in this parametric study.

Looking at Figure 6-11, it is appropriate to comment on the reduction of fuel weight line that is not smooth with changing duct efficiency. Although the trend is not smooth, there is a general trend of a decreasing fuel weight for increasing duct efficiency. The irregularities occur because of the sensitivity of the objective function (in this case, the TOGW) to the fuel weight. At the scale of the irregularities in the fuel weight reduction, the sensitivity of the TOGW to the fuel weight is small enough for the optimizer to disregard such a change. Therefore, it is acceptable to find a non-smooth trend at the small scale that we are considering here.

6.4.2. Savings in propulsive efficiency

A parametric study of varying the amount of savings in propulsive efficiency as a result of 'filling in the wake' was done. For simplicity, we will designate this factor by y. y = 0 corresponds to a case where there is no change in the propulsive efficiency even in a distributed propulsion configuration. Similarly, y = 1.0 corresponds to a case where the distributed propulsion system perfectly fills in the entire wake behind the body. Obviously, a realistic level of savings lies within these two cases. The purpose of this parametric study is to examine the sensitivity of the distributed propulsion BWB aircraft design with respect to y. In this parametric study, y is varied in intervals of 0.1 from 0.0 to 1.0. As with all the parametric studies, the aircraft is optimized at each interval to satisfy the constraints and produce the lowest TOGW design.

Figure 6-12 shows the variation of the aircraft TOGW and engine SFC with respect to y. We find that there is a 5.7% reduction in TOGW from a case where there is no savings in propulsive efficiency to one of a perfect distributed propulsion configuration. This corresponds to a reduction of 49000 lbs over this interval. In terms of engine SFC, there is a reduction of 13.9% over the interval of y. Even if y = 0.1 (i.e. only 10% of the possible savings in propulsive efficiency) is achievable, the reduction in SFC is estimated to be 1.4%. This reduction is significant, considering the mature state engine technology today.

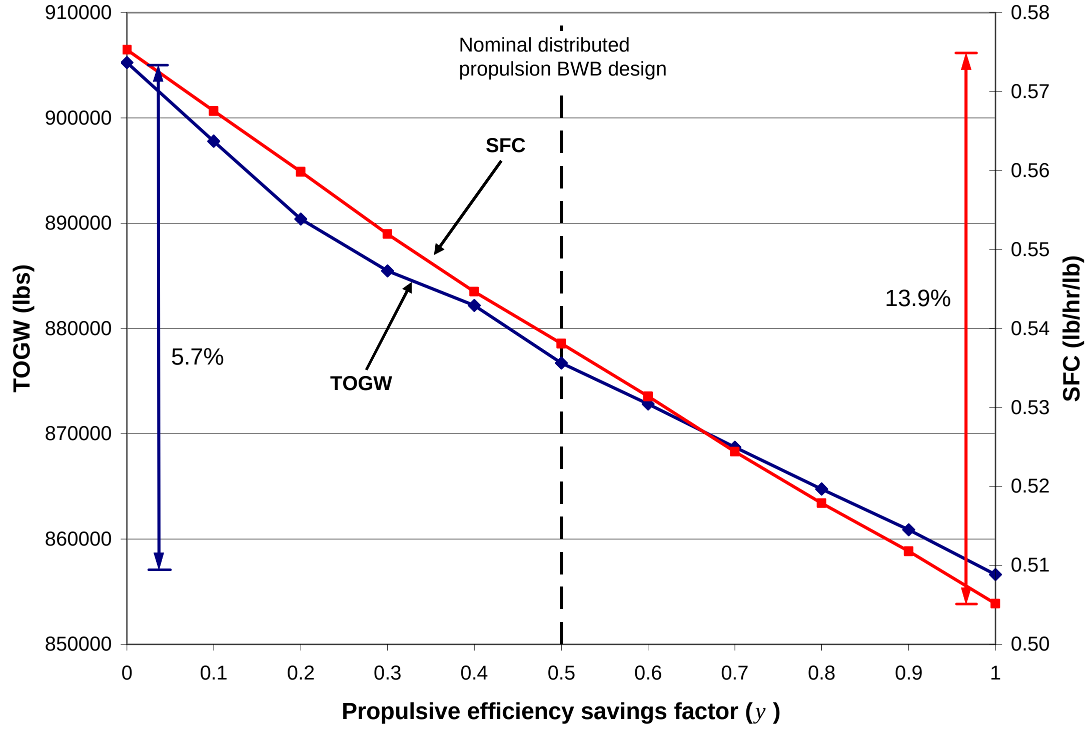

Figure 6-12: Change in TOGW and engine SFC with respect to the propulsive efficiency savings factor.

The change in y also affects the aircraft design significantly. Figure 6-13 shows the change in aspect ratio and average quarter chord sweep of the designs as a function of changes in y. Figure 6-13 also shows a comparison of planform shapes for three different values of y. It is clear that there is a change in design trends at y = 0.3. For designs where y is smaller than 0.3, increasing y causes the optimizer to unsweep the wing, and increase the aspect ratio. This effect is mainly due to the reduction in planform area compared to a small change in the wing span. These two effects can be seen by comparing the planform shapes of y = 0.0 and y = 0.3. A reversal in the trend of the design occurs after y = 0.3. Increasing values of y causes the optimizer to reduce the aspect ratio, and increase the average quarter chord sweep angle (but not as much as it was unswept for y less than 0.3). There is also a significant increase in the *t/c* ratios at the first two span stations, until y = 0.3, where both *t/c* ratios level off at a relatively constant value. This can be seen in Figure 6-14. Although there is a change in the geometric trend of the design, it results in a relatively monotonic reduction in *L/D* at cruise. This reduction can be seen in Figure 6-15. One plausible explanation of this behavior is that at y = 0.3, increasing y allowed the optimizer to take advantage of a different design space topology not previously accessible. This result illustrates the strong coupling between the propulsion and aerodynamics disciplines in the distributed propulsion BWB concept.

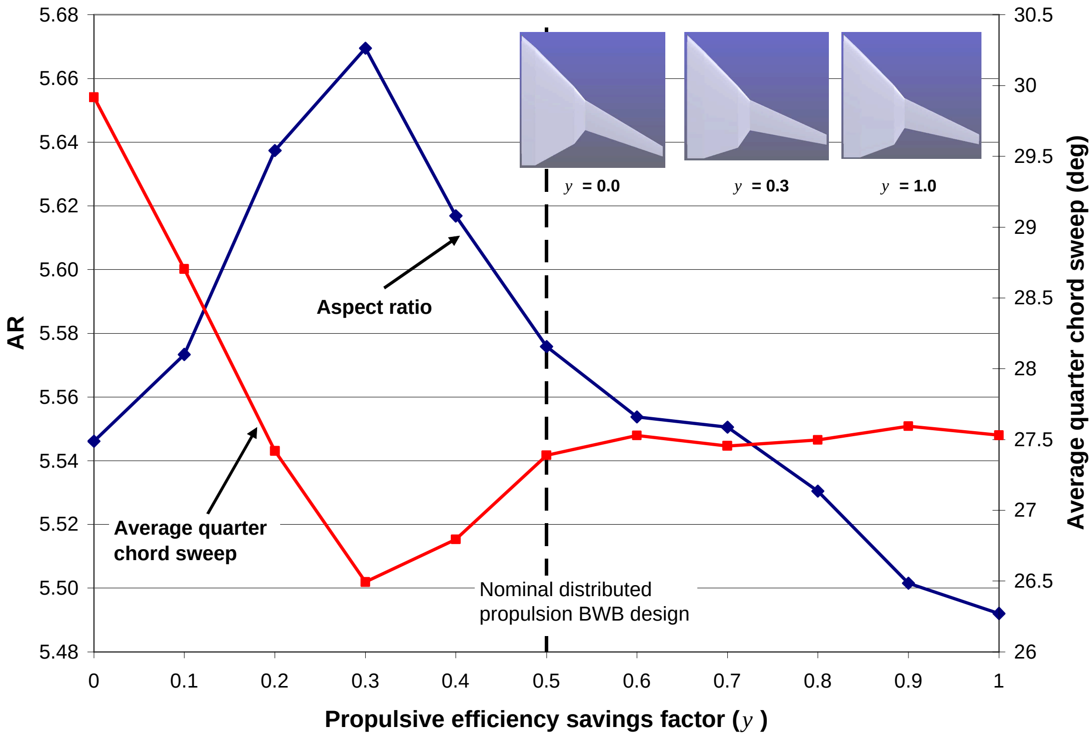

Figure 6-13: Variation of the distributed propulsion BWB aircraft aspect ratio and average quarter chord sweep angle with respect to the propulsive efficiency savings factor. The figure shows that there is a reversal in trends at y = 0.3. A comparison of the planform geometries when y = 0.0, 0.3 and 1.0 is also given.

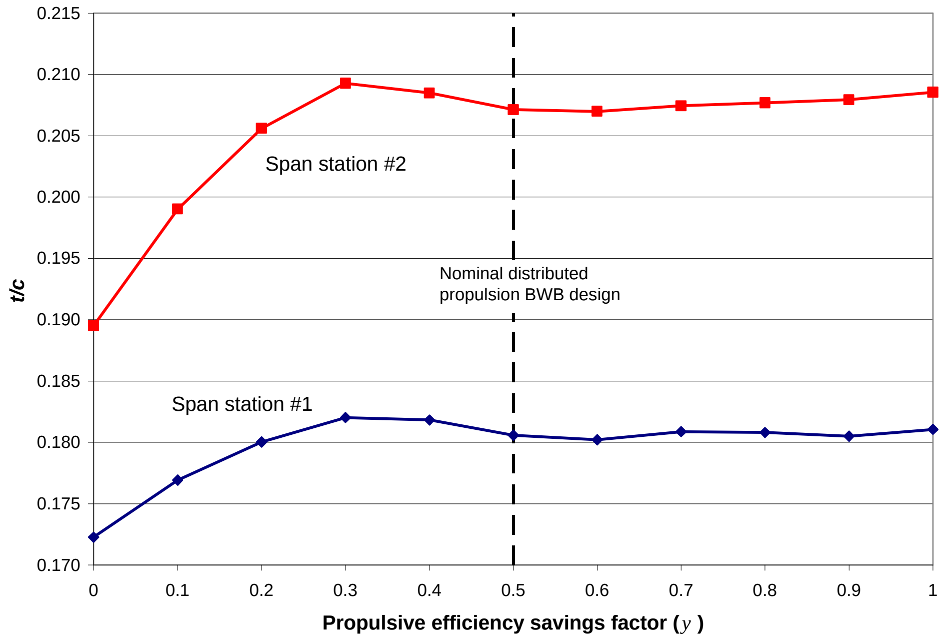

Figure 6-14: Variation in the t/c ratios at the first and second span stations with respect to the propulsive efficiency savings factor. There is an increase in *t/c* ratio values until $y = 0.3$ where the values level off at relatively constant values.

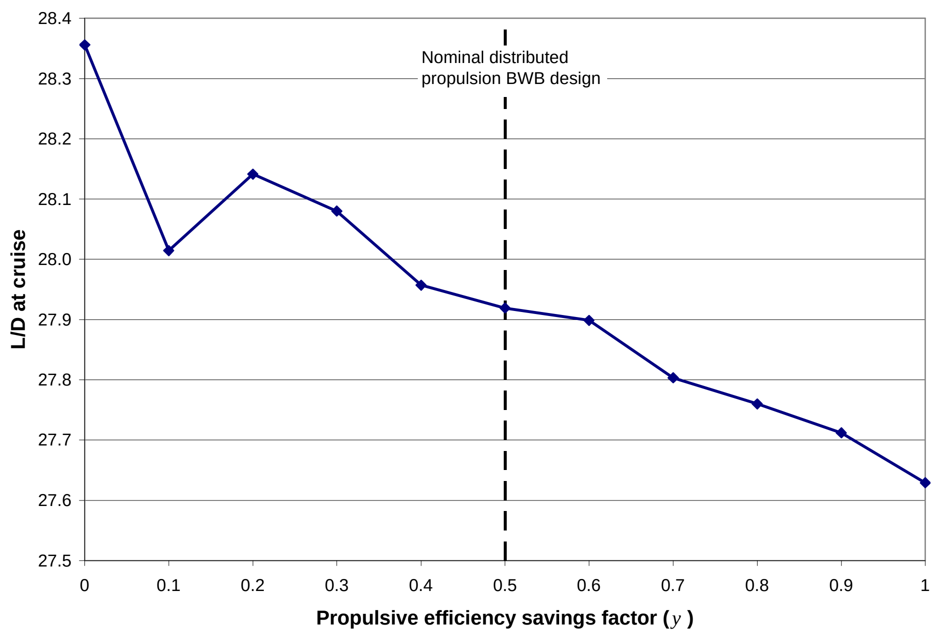

Figure 6-15: Variation of *L/D* at cruise with respect to the propulsive efficiency savings factor. It shows a relatively decreasing *L/D* trend with increasing y.

Although our discussion of the effects of y range up to a factor of 1, based on preliminary CFD results (the same results mentioned in Chapter 5), it seems unlikely that the value of y would be any larger than about 0.5. The restrictions in airfoil trailing edge thickness make it difficult to produce propulsive efficiencies any larger than 85%. It could be possible that at certain sections of the wing where a relatively thin trailing edge is available to exhaust out of, the propulsive efficiencies could be lower than that of the independent engine (i.e. $y < 0$).

It should be noted that in Figure 6-15 the *L/D* value at $y = 0.1$ can be considered as an outlier point, as it does not fall within the general trend across the range of y. Since the TOGW variation in Figure 6-13 does not show any indication of this irregularity, we can conclude that this irregularity is within a range where the optimization objective function is insensitive to a change in value.

6.4.3. Number of engines

A parametric study involving the number of engines was performed. An integral part of the distributed propulsion concept is to investigate the benefits of using smaller, and more engines in place of larger, fewer engines. Hence the design sensitivity with respect to the number of engines is important. In this parametric study, designs with 4, 6 and 8 engines were considered. By only considering an even number of engines, the engine locations on the aircraft can be kept the same. The number of engines is reduced by removing the outboard-most engines. In other words, the first two engine locations on one side of the wing (as a function of semi-span) in the 8 engine configuration are at the same position as the engines in the 4 engine configuration. At each configuration, an optimum distributed propulsion design is obtained.

Figure 6-16 shows the variation in TOGW with respect to the number of engines. It shows that there is a 0.6% (5000 lbs) decrease in TOGW when the number of engines is increased from 4 to 8. This is in part due to the almost 2% decrease in wing weight shown in Figure 6-17. The decrease in wing weight could be attributed to the increased load alleviation as engines are being placed outboard. However, these differences in weights can be considered to be small, and therefore, we can conclude that the aircraft TOGW is fairly insensitive to the number of engines. This will probably be especially true as the number of engines is increased beyond 8. The trend seems to show that the sensitivity of the TOGW with respect to the number of engines tends to decrease with an increasing number of engines.

The decrease in TOGW with respect to the number of engines can also be seen in current transonic transport aircraft. This can be done by considering the fraction of propulsion weight to the TOGW for aircraft with different number of engines. Table 6-7 shows the fraction of the propulsion weight to the TOGW for three different aircraft. It shows that as the number of engines increases, the fraction of propulsion weight to TOGW decreases. It also shows that the extent of this decrease gets smaller for an increasing number of engines.

Table 6-7: Percentage of propulsion weight to gross weight for three transonic transport aircraft with different number of engines [104].

Aircraft	Number of engines	Propulsion dry weight (lbs)	Gross weight (lbs)	% of propulsion weight to gross weight
Boeing 777-300	2	33000	660000	5.0%
Boeing MD-11	3	28200	630500	4.5%
Boeing 747-400	4	37600	875000	4.3%

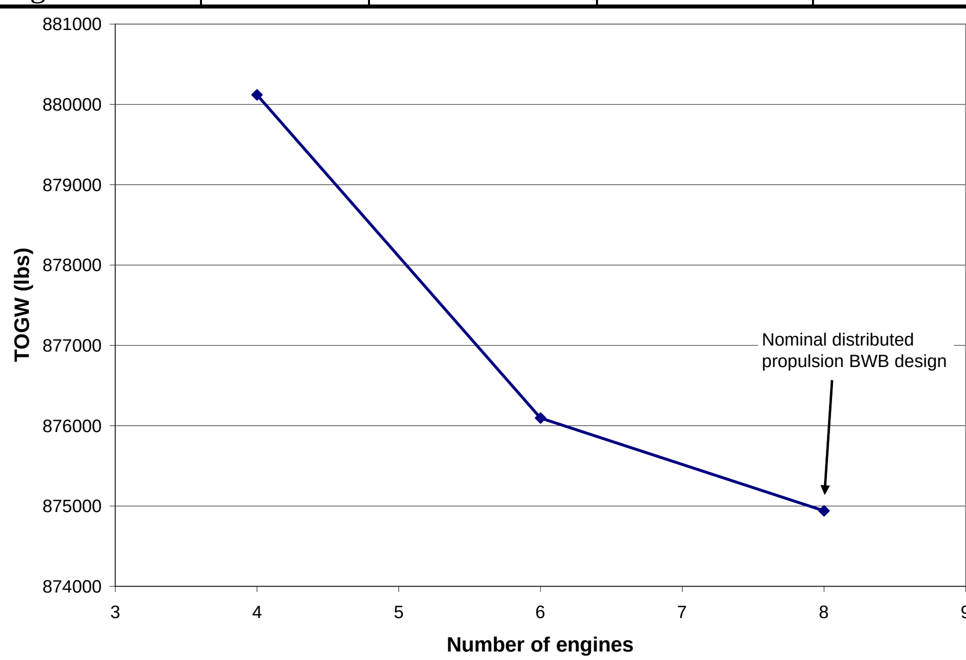

Figure 6-16: Variation of the distributed propulsion BWB TOGW with respect to the number of engines

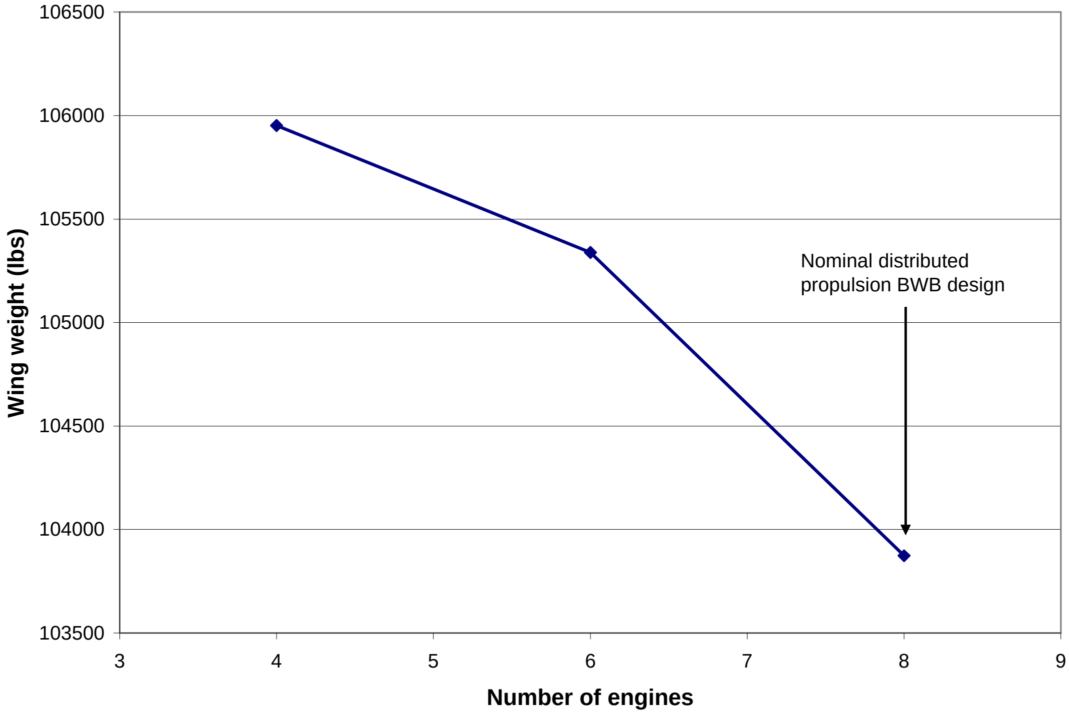

Figure 6-17: Variation of the distributed propulsion BWB wing weight with respect to the number of engines.

6.4.4. Duct weight factor

A parametric study varying the duct weight factor was performed. The duct weight is an integral part of the distributed propulsion BWB aircraft. If the ducts and their associated systems are too heavy, the benefits of distributed propulsion could be surpassed by too heavy duct weights. Therefore, it is important to determine the sensitivity of the aircraft design with respect to the duct weight. Presently, the duct weight is determined by the duct weight factor, which is applied to the propulsion weight. In this study, the duct weight factor will be increased at intervals of 0.1 from a factor of 1.0 to 2.0. Although we do not expect the duct weight to ever be as twice the propulsion weight, we considered this interval to include the 'worst case scenario'. As with the other parametric studies, the aircraft design is optimized at every duct weight factor interval.

Figure 6-18 shows the variation of TOGW with respect to the duct weight factor. We see that there is an 8.15% increase in TOGW if the propulsion system weight is doubled to account for the ducts. This seems like a large increase, but note that it is for a situation where the propulsion weight is doubled. In more realistic terms, the results imply that there is a 0.815%, or approximately 700 lbs for every 1% increase in propulsion weight due to the use of ducts. We expect that the weight of the ducts would at most be about 20% of the engine weight. Therefore, the TOGW will at most increase by 1.6%, or 14000 lbs. This increase is significant, and therefore we can conclude that the TOGW is sensitive to the duct weight factor.

It should be noted here that by modeling the weight of the ducts as an increase in propulsion weight, we are projecting a pessimistic estimation of the effects of the duct weight on the entire aircraft. This is because in formulation, the weight of the ducts is projected as pointwise loads on the wing at the position of the engines. In reality, there will be a distributed load on the wing due to the ducts across the span. We expect that this will result in a lower wing weight.

As a result of increasing the duct weight factor, there is a change in the aircraft design. Figure 6-19 shows the variation of the aircraft span and wing planform area with respect to the duct weight factor. The optimizer scales aircraft planform size to accommodate the additional weight of the ducts, while keeping the aspect ratio constant. The *L/D* ratio of the aircraft also remains constant. Figure 6-20 shows a variation in the average aircraft quarter chord sweep angle with respect to the duct weight factor. It shows that there is almost a 3° change in sweep with the duct weight factor increasing to 2.0 (from 1.0). To accommodate the additional weight, there is also an increase in engine thrust by 6.6%, and as a result, an increase in required fuel weight (by 8.2%) as shown in Figure 6-21.

As noted before in the other parametric studies, the irregularities in some of the trend lines with respect to duct weight factor is expected. This is because the ‘band’ in which these irregularities occur is small compared to their effect on the optimization objective function, which is the TOGW.

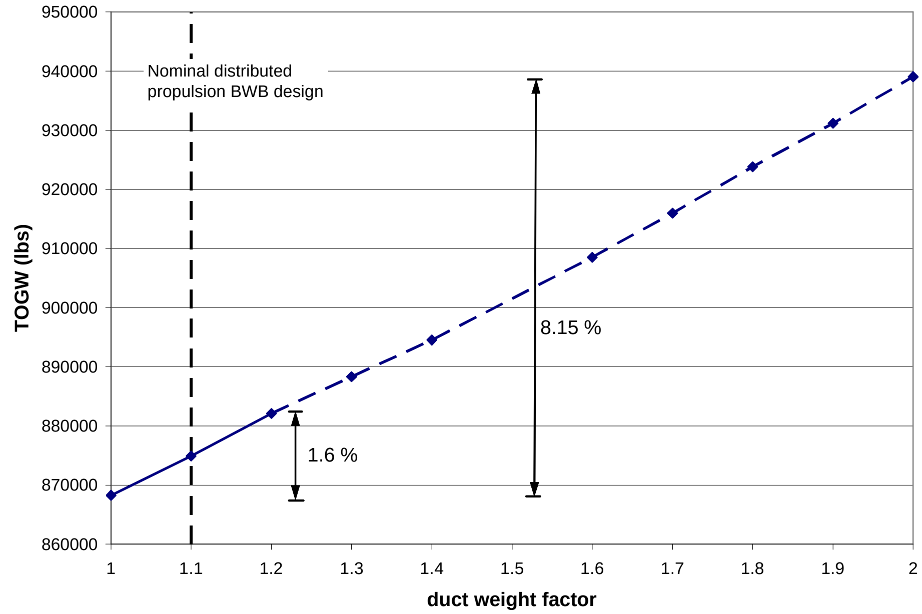

Figure 6-18: Variation of TOGW of the distributed propulsion BWB aircraft with respect to the duct weight factor. Dotted line represents factors too large for realistic duct weights

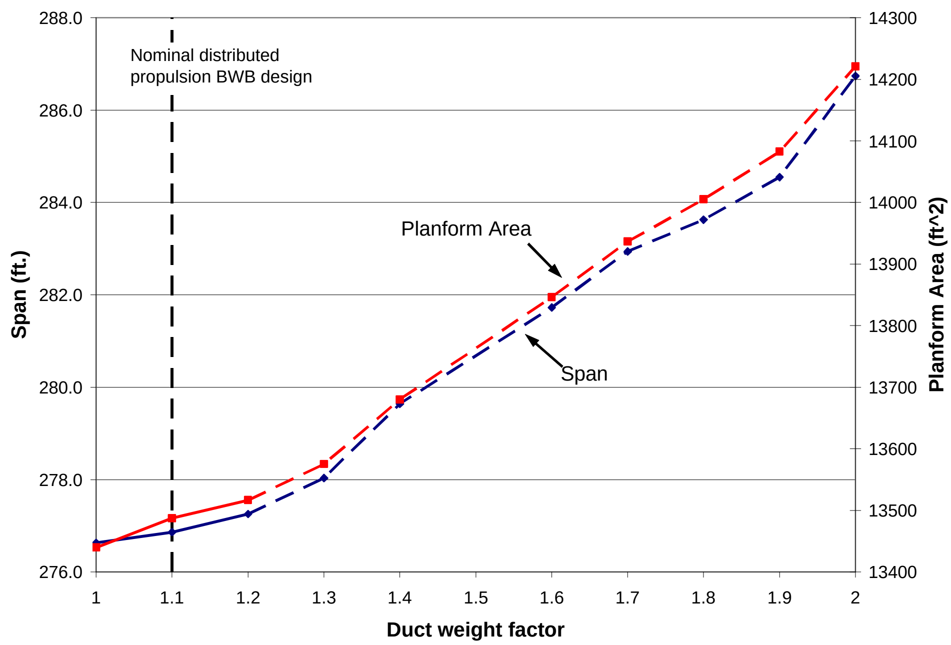

Figure 6-19: The variation in span and planform area of the distributed propulsion BWB aircraft with respect to the duct weight factor. Dotted line represents factors too large for realistic duct weights.

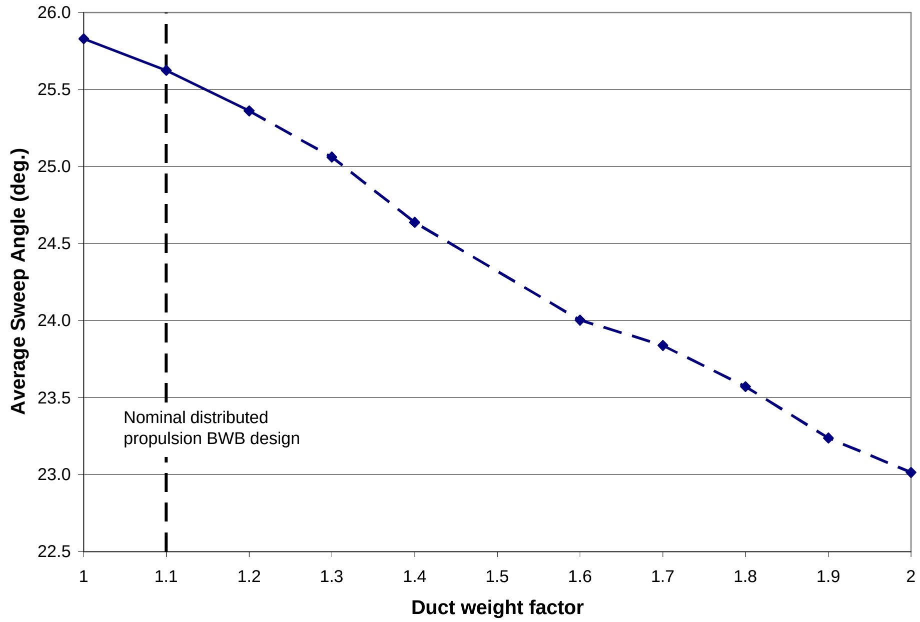

Figure 6-20: Variation of distributed propulsion BWB aircraft average sweep angle with respect to duct weight factor. Dotted line represents factors too large for realistic duct weights.

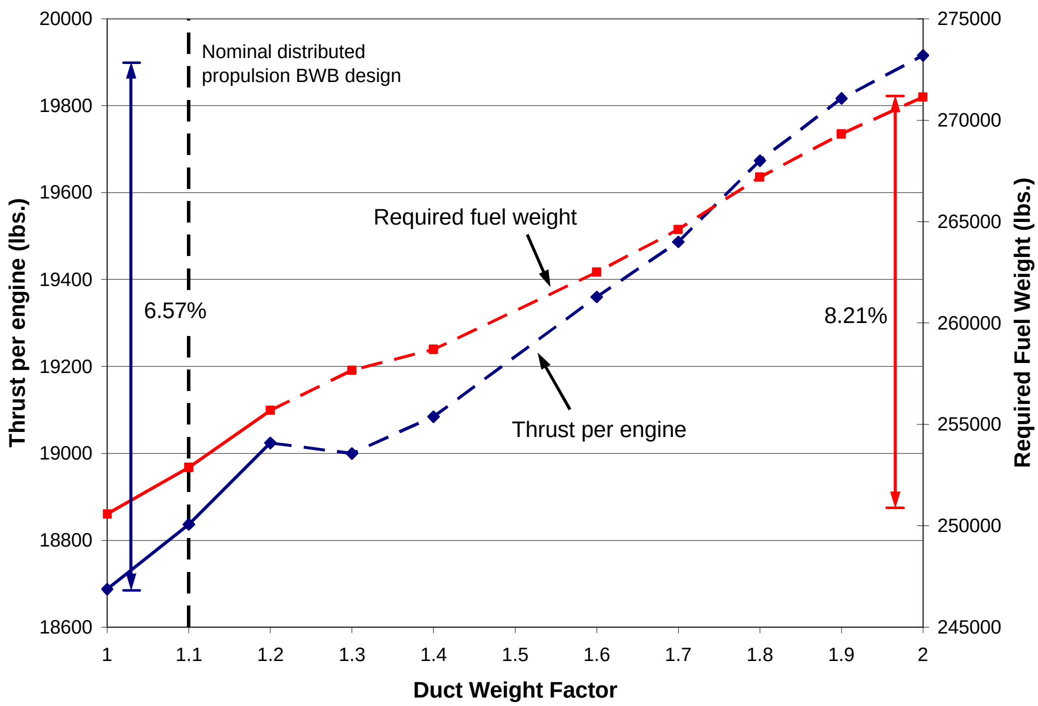

Figure 6-21: Variation of thrust per engine and required fuel weight of the distributed propulsion BWB aircraft with respect to the duct weight factor. Dotted line represents factors too large for realistic duct weights.

Chapter 7: Conclusions

A new model for distributed propulsion has been developed and incorporated into an MDO design formulation. Modeling the various interaction effects of this propulsion system together with other disciplines such as aerodynamics and the control system are important. The Blended-Wing-Body (BWB) aircraft was used as a platform to study the distributed propulsion concept. This dissertation documents the formulation of the fundamental interaction effects of using a distributed propulsion system in an aircraft. In addition, it documents the development of low to medium fidelity methods used to evaluate performance parameters associated with the BWB aircraft and the distributed propulsion concept. MDO studies were then made using this formulation.

The first task was to identify the major interaction effects the distributed propulsion system has on the BWB aircraft. The aerodynamics/propulsion interaction effect was one deemed to be important. One particular effect is the distributed propulsion impact on the propulsive efficiency. It has been theorized that there will an increase in propulsive efficiency when the engine jet is exhausted out the trailing edge of an aircraft wing. Until now, no mathematical assessment has been done to understand the mechanism or to provide quantitative predictions of the change in this efficiency. Starting from first principles, a mathematical formulation describing this effect is presented in this dissertation. By considering simple, idealized, representative cases, and comparing them to a conventional propulsion arrangement, a quantitative assessment of the increase in propulsive efficiency was made. The jet ‘fills in’ the wake behind the body, resulting in a better overall aerodynamic/propulsion system.

To quantify the effects of this increase in efficiency, the limiting cases with which the maximum and minimum benefits of this effect were considered. In the formulation, we assume a minimum propulsive efficiency of 80%, which corresponds to a conventional arrangement where the engine is installed on pylons. The ratio of the jet thrust to the total thrust is determined by setting it equal to the ratio of the friction and form drag to the total drag. This results in a maximum attainable propulsive efficiency of 88% - 90%. By identifying the bounds in attainable propulsive efficiency using a distributed propulsion system, a formulation by which the projected propulsive efficiency of a distributed propulsion system can be determined.

Another aerodynamics/propulsion interaction effect is the impact in reducing induced drag. Spence's Jet Flap theory [99], [100], [101] was used to quantify this effect. By defining the jet coefficient, C_J, a new induced drag can be calculated based on induced drag estimates of a non-distributed propulsion arrangement. It was found that there is only a small savings in induced drag for the distributed propulsion arrangement that is being considered here because C_J is relatively small.

An additional major concept in applying the distributed propulsion concept to the BWB aircraft is the idea of replacing the conventional elevons with a vectored thrust system for longitudinal control. An extension of Spence's Jet Flap theory was developed to estimate the effects of deflecting the distributed propulsion jet exiting the trailing edge on the lift and moment characteristics of the aircraft. This too had not been done before, and the method developed was found to provide a reasonable estimate of the control capability of the distributed propulsion BWB aircraft. It was deemed suitable for use in this MDO design application. Results showed that comparable longitudinal control capability could be achieved with such a system compared to conventional elevon controls.

Other effects that were modeled include estimating the weight of the associated systems and ductwork needed for a distributed propulsion system. By applying a weight factor to the propulsion weight, this additional weight could be simulated in an MDO framework. Thrust losses in the ductwork were also modeled and applied to the MDO framework.

The distributed propulsion concept was applied to the BWB aircraft platform. To do this, an MDO framework to design a BWB aircraft was developed. This framework uses low to medium fidelity analysis methods which were coupled with a gradient based optimization algorithm. Geometric parameters such as chord lengths and quarter chord sweeps together with important performance parameters such as engine thrust and fuel weight were used as design variables. Design constraints such as field performance constraints and cabin height restrictions were imposed on the design. The aircraft TOGW was used as the objective function. However, the MDO design program was developed to be flexible enough to handle other different design variables, constraints and objective functions. With the distributed propulsion effects integrated into the BWB MDO framework, optimum BWB aircraft designs using distributed propulsion or a conventional arrangement can be produced.

The conventional and distributed propulsion BWB configurations were optimized for an 800 passenger load, 0.85 cruise Mach number and 7000 nmi range. It was found that the distributed propulsion BWB aircraft had a 4% lighter TOGW and required 2% less fuel weight to complete the design mission compared to a similar BWB aircraft with a conventional propulsion arrangement. The distributed propulsion aircraft used a total of 8 engines, as oppose to 4 engines used in the comparator conventional BWB aircraft. Although both designs had similar planforms, with similar aspect ratios, the distributed propulsion BWB aircraft has a 10% smaller planform area. This implies smaller chord lengths, which is true at the inboard span stations.

In both the conventional and distributed propulsion BWB designs, the chord lengths and *t/c* ratios at the outboard span stations reached their minimum limit in both designs. This occurred to increase the aircraft *L/D* ratio by increasing the aspect ratio and reducing wave drag, while satisfying the fuel volume constraint. It did not incur a structural weight penalty due to the assumption of an elliptical load distribution which results in the outboard wing sections becoming lightly loaded. This result also indicates that this assumption of an elliptical load distribution might not be realistic.

To satisfy cabin height constraints, the distributed propulsion BWB aircraft has higher *t/c* ratio at the inboard span stations (since now the chord lengths are smaller). The distributed propulsion BWB aircraft requires 17% less total thrust, which corresponds to a *T/W* decrease of 12% compared to the optimum conventional BWB design.

Parametric studies were done to investigate the sensitivity of the distributed propulsion BWB design to certain key design parameters. Four different parameters were considered:

- Duct efficiency
- Amount of savings in propulsive efficiency
- Number of engines
- The duct weight factor

It was found that the distributed propulsion BWB aircraft was insensitive to the duct efficiency and number of engines. Only a decrease of 0.065% in TOGW was observed for every 1% increase in duct efficiency. This is because although a 1% increase in duct efficiency results in a 0.78% decrease in engine thrust and 0.12% decrease in fuel weight, the propulsion weight and fuel weight only account for 5% and 30% of the TOGW respectively. Therefore, the impact on the TOGW is much smaller than that seen by the engine thrust and fuel weight.

The distributed propulsion BWB aircraft was found to be marginally sensitive to the number of engines. A 0.6% reduction in TOGW was observed when the number of engines was increased from 4 to 8. This is consistent with the trends we see in current conventional transport aircraft.

The amount of savings in propulsive efficiency and the duct weight factor however were found to be important parameters. It was found that even if only 10% of the maximum possible savings in propulsive efficiency could be obtained; there will be a 1.4% decrease in engine SFC. In light of the current mature engine technology, this increase is significant. It was also found that a maximum possible reduction of 5.7% in TOGW can be achieved through the distributed propulsion savings in propulsive efficiency.

Since the distributed propulsion aircraft is sensitive to the level of propulsive efficiency savings, quantifying this amount of savings is crucial. Initial CFD studies suggest that due to the small trailing edge thicknesses of the wing sections, it is possible for the propulsive efficiency at some sections be lower than that from an independent engine. This would then result in an undesired effect where the overall propulsive efficiency is lower than that from a conventional BWB design. There are several solutions to this problem. One of them is to thicken the trailing edge at certain sections of the wing to raise the level of propulsive efficiency to a desired one. However, increasing the trailing edge thickness too much could have detrimental effects on the aerodynamics of the wing, and reduce the aerodynamic performance of the aircraft.

The other solution is to regulate the jet velocity exiting the trailing edge such that it is low enough to result in a propulsive efficiency that will never be lower than that from a conventional engine arrangement. In the current configuration, we assume that the thrust from the jet exiting the trailing edge will be used to overcome both the friction and wave drag, while the remaining thrust exited out of a conventional nozzle will be used to overcome the remaining drag (primarily induced drag). The average propulsive efficiency of the two systems will be the overall propulsive efficiency of the aircraft. Therefore, if the efficiency of the distributed propulsion system becomes smaller than that of a conventional engine arrangement, the aircraft overall propulsive efficiency will be less than that for a conventional BWB aircraft. Since the propulsive efficiency is dependant on the jet exit velocity, by regulating the jet exit velocity, we can limit the propulsive efficiency at certain critical sections to a minimum, even thought the thrust produced does not overcome the local friction and wave drag. The reduction in thrust then will be compensated by additional thrust obtained from the conventional engine arrangement. This way, the overall propulsive efficiency will never be below that of a purely conventional engine arrangement.

Regardless of the scheme that will be adopted, determining a nominal value of this factor is critical. This can only be done through CFD or experimental work.

The distributed propulsion BWB aircraft is also sensitive to the duct weight factor. Every 1% increase in propulsion weight due to the ducting system results in a corresponding 0.08% increase in TOGW. This corresponds to an additional 700 lbs in TOGW. We do not expect the duct weight to be any larger than 20% of the propulsion weight. Hence, although important, the duct weight factor will cause the TOGW of the aircraft to change by a maximum of 1.6%.

By identifying the important distributed propulsion design parameters through the use of the sensitivities, decisions as to the research direction of this innovative propulsion concept can be determined. It also provides insight into which interaction effects are more important in a distributed propulsion aircraft configuration.

Aside from the technical challenges of incorporating a new propulsion concept such as the distributed propulsion system, there seems to be promising benefits to such an endeavor. The benefits found here are over and above the potential for reducing airframe noise. If coupled with the use of liquid hydrogen, there will also be a reduction in aircraft emissions. With these projected advantages, further study into the distributed propulsion BWB aircraft is warranted.

Chapter 8: Recommendations

Although this dissertation has shown favorable advantages of the distributed propulsion concept as applied to the BWB aircraft, continued improvements to the analysis methods and MDO framework are still needed. Additional research into the details of the distributed propulsion concept is required to fully understand the interaction effects of this propulsion system concept with the other design disciplines.

8.1. Overall MDO framework

8.1.1. Improvement in optimization speed

There is a need to improve the speed of the optimization process. Currently the greatest improvement in speed can be obtained by speeding up each optimization function evaluation. It is observed that the VLM program (which is used to calculate control derivatives) and the aerodynamics program (which is used to calculate lift and drag coefficients) takes about 40% and 20%-30% of the evaluation time respectively for each function evaluation. Changes to improve the computation time for these two pieces of the MDO framework would impact the overall optimization time greatly.

In addition, better program integration can improve the optimization process. Although we use ModelCenter® to integrate the individual analysis programs, integrating them at the programming level could result in an improvement in computation time. This can happen for two reasons. First, integrating most of the analysis codes in the source code level will allow the computer to run fewer individual programs for each analysis run. This will reduce the number of times the computer will have to communicate with ModelCenter®. In the arrangement where the analysis codes reside and run on one computer, while ModelCenter® runs on another, it is quite possible that this change could reduce the optimization run time. Secondly, it would allow an individual analysis program to use the computer processor more efficiently. In the present framework, the arrangement is for many small programs to start and end in succession. This is less efficient than having an integrated program starting and ending only once.

However, there is a disadvantage to integrating the analysis codes in the source code level. By integrating the codes at the programming level, the benefits of ModelCenter® as a flexible, user-friendly integration tool cannot be fully utilized. Changes to the program will be more difficult as it would involve modifying the analysis code at the programming level.

8.1.2. Expanding the optimization setup

Instead of treating the number of engines and spanwise position of the engines as parameters, the optimization setup should be expanded to include them as design variables. One of the possible challenges to doing this is to adopt an optimization algorithm that takes integer values as design variables. Currently, the optimization algorithms in ModelCenter® do not support integer design variables.

8.2. BWB Modeling

8.2.1. Structures

It was observed in this dissertation that the wing weight formulation obtained from FLOPS tended to over predict the wing weight of the BWB aircraft. A better formulation tailored for the BWB aircraft is required to accurately estimate the BWB aircraft wing weight. Also, as more than 8 engines are being considered for the distributed propulsion configuration, the wing weight formulation should be tailored to estimate the wing weight with many engines at different spanwise locations. In addition to this, the passenger cabin structure should be also taken into account when estimating the wing weight. The method used by Mukhopadhyay et al. [14] should be adopted as it is formulated specifically to estimate the performance and weight of the BWB structure.

With the high wing spans of as much as 300 ft, the wing tip deflection due to a 2g taxi bump should be considered. This should be a constraint in the MDO design to prevent the wingtip from striking the ground at this condition.

In the current formulation, the wing weight model assumes an elliptical load distribution. On the other hand, a load distribution is calculated by idrag in the aerodynamics section. A more accurate wing weight model would use the load distribution calculated by idrag as an input.

8.2.2. Aerodynamics

A higher fidelity method is required to estimate the wave drag of the BWB aircraft. With thick wing sections on the BWB aircraft, the simple formulation of the current wave drag estimation method might not provide accurate results. A better formulation is needed. One option is to perform CFD calculations and integrate them into the aerodynamics calculation using response surfaces.

There is also a need to obtain drag polars for the field performance calculations. Currently, the aerodynamics analysis programs used to estimate drag at cruise conditions are also used to provide drag estimates during takeoff and landing. It is more common to use drag polars for calculations at takeoff and landing configurations as it is in a ‘dirty’ configuration with high lift devices and landing gears deployed as opposed to a ‘clean’ configuration at cruise. Currently, drag due to high lift devices and landing gears are accounted for by increasing the calculated drag coefficient by a reference area scaled nominal drag coefficient.

As discussed in Chapter 6, the assumption of an elliptical load distribution on the wings might not be realistic. A non-elliptical load distribution with more of the span load shifted outboard would be more true to the BWB design. A method to estimate this load distribution should be developed and implemented into the distributed propulsion BWB MDO program.

8.2.3. Weight and CG estimation

The weight and center of gravity estimation could be improved. This can be done by performing a design study to place the individual components in the BWB design. Doing this would provide better confidence in the control constraint calculations.

8.3. *Distributed propulsion*

Computational fluid dynamics (CFD) or experimental testing is required to determine a realistic level of savings in propulsive efficiency due to 'filling in the wake'. The parametric studies performed have shown that this parameter is important in the design of the distributed propulsion BWB aircraft. This testing also is needed to validate the mathematical model that was formulated in this dissertation.

Since we intend to use the deflection of the jet angle for longitudinal control, the effect of the jet deflection on the level of savings in propulsive efficiency should be investigated.

A better model to estimate the duct weights is required. With the current formulation, a factor is applied to the propulsion weight to account for the ducts. However, determining a good value for this factor is required. Also, there is a possibility that the duct weight does not scale with the propulsion weight. It has been suggested that perhaps the duct weight scales better with the jet velocity or the mass flow rate of the engine.

References

[1] Ashley, H., "On Making Things the Best-Aeronautical Uses of Optimization," *Journal of Aircraft*, Vol. 19, No. 1, Jan 1982, pp. 5-28.

[2] Sobieszczanski-Sobieski, J., Haftka, R.T., "Multidisciplinary Aerospace Design Optimization: Survey of Recent Developments," *Structural Optimization*, Vol. 14, No. 1, 1997, pp. 1-23

[3] Kroo, I., "MDO Applications in Preliminary Design: Status and Directions," AIAA 97-1408, 1997.

[4] Giunta, A. A., Golovidov, O., Knill, D. L., Grossman, B., Mason, W. H., Watson, L. T., and Haftka, R. T., "Multidisciplinary Design Optimization of Advanced Aircraft Configurations," *Fifteenth International Conference on Numerical Methods in Fluid Dynamics*, P. Kutler, J. Flores, J.-J. Chattot, Eds., in Lecture Notes in Physics, Vol. 490, Springer-Verlag, Berlin, 1997. pp. 14-34.

[5] Jayaram, S., Mykelbust, A., and Gelhausen, P., "ACSYNT – A Standards-Based System for Parametric Computer Aided Conceptual Design of Aircraft," AIAA Paper 92-1268, 1992.

[6] McCullers, L. A., "Configuration Optimization Including Optimized Flight Profiles," in Proceedings of a Symposium on Recent Experiences in Multidisciplinary Analysis and Optimization, pp. 395-412, April, 1984, J. Sobieski, compiler, NASA CP 2327.

[7] Mason, W. H., Knill, D. L., Giunta, A. A., Grossman, B., Haftka, R. T., and Watson, L. T., "Getting the Full Benefits of CFD in Conceptual Design," AIAA 16th Applied Aerodynamics Conference, Albuquerque, NM, AIAA Paper 98-2513, June 1998.

[8] "Revolutionary Aerospace Systems Concepts: Quiet Green Transport Study," *NASA Fiscal Year 2001 Final Report*.

[9] Attinello, J. S., “The Jet Wing,” IAS Preprint No. 703, IAS 25th Annual meeting, Jan. 28-31, 1957.

[10] Smith, H., *Blended* Wing *Body Airliner – the next generation in civil transport aircraft,* Cranfield College of Aeronautics, http://www.cranfield.ac.uk/coa/tech-avt/avt-4.htm, 1999.

[11] Callaghan, J. T., and Liebeck, R. H., “Some Thoughts on the Design of Subsonic Transport Aircraft for the 21st Century”, SAE Paper No. 901987, October 1990.

[12] Liebeck, R. H., Page, M. A., Rawdon, B. K., Scott, P. W., and Wright, R. A., “Concepts for Advanced Subsonic Transports” NASA CR 4624, Sept. 1994.

[13] Vitali, R., Park, O., Haftka, R. T., Sankar, B. V., Rose, C. A., “Structural Optimization of a Hat-Stiffened Panel Using Response Surfaces,” *Journal of Aircraft*, Vol. 39, No.1, January-February 2002, pp. 158-166.

[14] Mukhopadhyay, V., Sobieszczanski-Sobieski, J., Kosaka, I., Quinn, G., Charpentier, C., “Analysis Design and Optimization of Non-cylindrical Fuselage for Blended-Wing-Body (BWB) Vehicle,” 9th AIAA/ISSMO Symposium on Multidisciplinary Analysis and Optimization, AIAA 2002-5664, Atlanta, GA, September 4-6, 2002.

[15] Wakayama, S., Kroo, I., “The Challenge and promise of Blended-Wing-Body Optimization,” 7th AIAA/USAF/NASA/ISSMO Symposium on Multidisciplinary Analysis and Optimization, AIAA 98-4736, St. Louis, MO, Sept. 2-4, 1998.

[16] Wakayama, S., Page, M., Liebeck, R., “Multidisciplinary optimization on an advanced composite wing,”, 6th AIAA/NASA/ISSMO Symposium on Multidisciplinary Analysis and Optimization, AIAA 96-4003, Reston, VA, Sept. 4-6, 1996.

[17] Wakayama, S., “Blended-Wing-Body Optimization Problem Setup”, 8th AIAA/USAF/NASA/ISSMO Symposium on Multidisciplinary Analysis and Optimization, AIAA-2000-4740, Long Beach, CA, Sept. 6-8, 2000.

[18] Liebeck, R., “Design of the Blended-Wing-Body Subsonic Transport,” 40th AIAA Aerospace Sciences Meeting & Exhibit, AIAA-2002-0002, Reno, NV, Jan. 14-17, 2002.

[19] Potsdam. M. A., Page, M. A., Liebeck, R. H., “Blended Wing Body Analysis and Design,” 15th AIAA Applied Aerodynamics Conference, AIAA-97-2317, Atlanta, GA, June 23-25, 1997.

[20] Cameron, D., “Preliminary Simulation Development for the Quasisteady Aeroelastic Blended-Wing-Body Transport Aircraft,” AIAA Modeling and Simulation Technologies Conference, AIAA-97-3788, New Orleans, LA, Aug. 11-13, 1996.

[21] Liebeck, R. H., Page, M. A., Rawdon, B. K., “Blended-Wing-Body Subsonic Commercial Transport,” 36th Aerospace Sciences Meeting & Exhibit, AIAA-98-0438, Reno, NV, Jan. 12-15, 1998.

[22] Wakayama, S., “Multidisciplinary Design Optimization of the Blended-Wing-Body,” 7th AIAA/USAF/NASA/ISSMO Symposium on Multidisciplinary Analysis and Optimization, AIAA-98-4938, St. Louis, MO, Sept. 2-4, 1998.

[23] Roman, D., Allen, J.B., Liebeck, R. H., “Aerodynamic Design Challenges of the Blended-Wing-Body Subsonic Transport,” 18th AIAA Applied Aerodynamics Conference, AIAA-2000-4335, Denver, CO, Aug. 14-17, 2000.

[24] Cameron, D., Princen, N., “Control Allocation Challenges and Requirements of the Blended Wing Body,” AIAA Guidance, Navigation and Control Conference and Exhibit, AIAA-2000-4539, Denver, CO, 14-17, 2000.

[25] Gilmore, R., Wakayama, S., Roman, D., “Optimization of High-Subsonic Blended-Wing-Body Configurations,” 9th AIAA/ISSMO Symposium on Multidisciplinary Analysis and Optimization, AIAA-2002-5666, Atlanta, GA, Sept. 4-6, 2002.

[26] Rodriguez, D. L., Kroo, I. M., "A 2D Multidisciplinary Design Method for Boundary Layer Ingesting Inlets," 37th AIAA Aerospace Sciences Meeting and Exhibit, AIAA-99-0838, Reno, NV, Jan. 11-14, 1999.

[27] Rodriguez, D. L., "A 3D Multidisciplinary Design Method for Boundary Layer Ingesting Inlets," 38th AIAA Aerospace Sciences Meeting and Exhibit, AIAA-2000-0424, Reno, NV, Jan. 10-13, 2000.

[28] Rodriguez, D. L., "Validation of CFD Methods on a Boundary Layer Ingesting Inlet," 36th AIAA Aerospace Sciences Meeting and Exhibit, AIAA-98-0925, Reno, NV, Jan. 12-15, 1998.

[29] Rodriguez, D. L., "A Multidisciplinary Optimization Method for Designing Inlets using Complex Variables," 8th AIAA/USAF/NASA/ISSMO Symposium on Multidisciplinary Analysis and Optimization, AIAA-2000-4875, Long Beach, CA, Sept. 6-8, 2000.

[30] Rodriguez, D. L., "A Multidisciplinary Optimization Method for Designing Boundary Layer Ingesting Inlets," 9th AIAA/ISSMO Symposium on Multidisciplinary Analysis and Optimization, AIAA-2002-5665, Atlanta, GA, Sept 4-6, 2002.

[31] Anabtawi, A. J., Blackwelder, R., Liebeck, R., Lissaman, P., "Experimental Investigation of Boundary Layer Ingesting Diffusers of a Semi-Circular Cross Section," 36th Aerospace Sciences Meeting & Exhibit, AIAA-98-0945, Reno, NV, Jan. 12-15, 1998.

[32] Anabtawi, A. J., Blackwelder, R. F., Lissaman, P., Liebeck, R.H., "An Experimental Investigation of Boundary Layer Ingestion in a Diffusing S-Duct With and Without Passive Flow Control," 37th AIAA Aerospace Sciences Meeting and Exhibit, AIAA-99-0739, Reno, NV, Jan 11-14, 1999.

[33] Anabtawi, A. J., Blackwelder, R. F., Liebeck, R. H., Lissaman, P., "An Experimental Study of the Effect of Offset on Thick Boundary Layers Flowing

Inside Diffusing Ducts," 30th AIAA Fluid Dynamics Conference, AIAA-99-3590, Norfork, VA, June 28 – July 1, 1999.

[34] Morris, A., "MOB: A European Distributed Multi-Disciplinary Design and Optimisation Project," 9th AIAA/ISSMO Symposium on Multidisciplinary Analysis and Optimization, AIAA-2002-5444, Atlanta, GA, Sept. 4-6, 2002.

[35] Vankan, W., and Laban, M., " A SPINEware Based Computational Design Engine for Integrated Multi-Disciplinary Aircraft Design," 9th AIAA/ISSMO Symposium on Multidisciplinary Analysis and Optimization, AIAA-2002-5445, Atlanta, GA, Sept. 4-6, 2002.

[36] Laban, M., Arendsen, P., Rouwhorst, W., and Vankan, W., "A Computational Design Engine for Multi-Disciplinary Optimisation with Application to a Blended Wing Body Configuration," 9th AIAA/ISSMO Symposium on Multidisciplinary Analysis and Optimization, AIAA-2002-5446, Atlanta, GA, Sept. 4-6, 2002.

[37] La Rocca, G., Krakers, L., van Tooren, M., "Development of an ICAD Generative Model for Blended Wing-Body Aircraft Design," 9th AIAA/ISSMO Symposium on Multidisciplinary Analysis and Optimization, AIAA-2002-5447, Atlanta, GA, Sept. 4-6, 2002.

[38] Qin, N., "Aerodynamic Studies for Blended Wing Body Aircraft,", 9th AIAA/ISSMO Symposium on Multidisciplinary Analysis and Optimization, AIAA-2002-5448, Atlanta, GA, Sept. 4-6, 2002.

[39] Stettner, M., "Aeroelastic, Flight, Mechanic, and Handling Qualities of the MOB BWB Configuration," 9th AIAA/ISSMO Symposium on Multidisciplinary Analysis and Optimization, AIAA-2002-5449, Atlanta, GA, Sept. 4-6, 2002.

[40] Denisov, V. E., Bolsunovsky, A. L., Buzoverya, N. P., Gurevich, B. I., "Recent Investigations of the Very Large Passenger Blended-Wing-Body Aircraft," ICAS 98-4.10.3, 1998.

[41] Bolsunovsky, A. L., Buzoverya, N. P., Gurevich, B. I., Denisov, V. E., Dunaevsky, A. I., Shkadov, L. M., Sonin, O. V., Udzhuhu, A. J., Zhurihin, J. P., "Flying Wing – Problems and Decisions," *Aircraft Design Journal*, Vol. 4, 2001, pp. 193-219.

[42] Pambagjo, T. E., Nakahashi, K., Obayashi, S., Matsushima, K., "Aerodynamic Design of a Medium Size Blended-Wing-Body Airplane," 39th AIAA Aerospace Sciences Meeting & Exhibit, AIAA-2001-0129, Reno, NV, Jan. 8-11, 2001.

[43] *NASA Aeronautics Blueprint: Toward a Bold New Era in Aviation*, NASA, http://www.aerospace.nasa.gov/aero_blueprint/cover.html

[44] Kuchemann, D., *The Aerodynamic Design of Aircraft*, Pergamon Press, New York, 1978, pp. 229.

[45] Davidson, I. M., "The Jet Flap," *Journal of the Royal Aeronautical Society*, Vol. 60, No. 541, January 1956, pp. 25-50.

[46] Kohlman, D. L., *Introduction to V/STOL Airplanes*, Iowa State University Press, Ames, Iowa, 1981, pp 137–144.

[47] Korbacher, G.K., "Aerodynamics of Powered High-Lift Systems," *Annual Review of Fluid Mechanics*, Vol. 6, Palo Alto, CA, 1974, pp. 319-358.

[48] Kimberlin, R. D., "Performance Flight Test Evaluation of the Ball-Bartoe JW-1 JetWing STOL Research Aircraft," *Flight Testing in the Eighties: 11th Annual Symposium Proceedings of the Society of Flight Test Engineers*, Aug 27-29, 1980.

[49] "Assessment of Lift Augmentation Devices," AGARD-LS-42-71, Feb. 1971.

[50] Aiken, T. N., and Cook, A. M., "Results of Full-Scale Wind Tunnel Tests on the H-126 Jet Flap Aircraft," NASA TN D-7252, April 1973.

[51] Ives, D. C., and Melnik, R. E., "Numerical Calculation of the Compressible Flow over an Airfoil with a Jet Flap," 7th AIAA Fluid and Plasma Dynamics Conference, AIAA-74-542, Palo Alto, CA, June 17-19, 1974.

[52] Malmuth, N. D., and Murphy, W. D., "A Relaxation Solution for Transonic Flow over Jet Flapped Airfoils," 13th AIAA Aerospace Sciences Meeting, AIAA-75-82, Pasadena, CA, Jan. 20-22, 1975.

[53] Murphy, W. D., and Malmuth, N. D., "A Relaxation Solution for Transonic Flow over Three-dimensional Jet-flapped Wings," 14th AIAA Aerospace Sciences Meeting, AIAA-76-98, Washington, DC, Jan. 26-28, 1976.

[54] Woan, C. J., "A Three-Dimensional Solution of Flows Over Arbitrary Jet-Flapped Configurations Using a Higher-Order Panel Method," AIAA Applied Aerodynamics Conference, AIAA-83-1846, Danvers, MA, July 13-15, 1983.

[55] Yoshihara, H., Zonars, D., "The transonic Jet Flap – A Review of Recent Results," SAE National Aerospace Engineering and Manufacturing Meeting, SAE-751089, Culver City, LA, Nov. 17-20, 1975.

[56] Clark, L. R., Gerhold, C. H., "Inlet Noise reduction by Shielding for the Blended-Wing-Body Airplane," 33rd AIAA Thermophysics Conference, AIAA-99-1937, Norfolk, VA, June 28 – July 1, 1999.

[57] Lilley, G.M., "The Prediction of Airframe Noise and Comparison with Experiment," *Journal of Sound and Vibration*, 239, No. 4, 2001, pp. 849-859.

[58] Anon, "Jetwing, a Very Quiet Machine," *Professional Pilot*, Vol. 13, Issue 4, 1978, pp. 16-19.

[59] Coles, W.D., "Jet-Engine Exhaust Noise from Slot Nozzles," NASA Technical Note D-60, Lewis Research Center, Sept. 1959.

[60] Maglieri, D. J. and Hubbard, H. H., "Preliinary Measurements of the Noise Characterisitcs of some Jet-Augmented Flap Configurations," NASA Memorandum 12-4-58L, Jan. 1959.

[61] Schrecker, G. O. and Maus, J. R., "Noise Characteristics of Jet Flap Type Exhaust Flows," NASA CR-2342, Feb. 1974.

[62] Green, J.E., "Greener by Design – the technology challenge," *The Aeronautical Journal*, Vol. 106, No. 1056, Feb. 2002.

[63] Allen, J. E., "Global energy issues affecting aeronautics: a reasoned conjecture," *Progress in Aerospace Sciences*, Vol. 35, 1999. pp 413-453.

[64] Sloop, J.L., *Liquid Hydrogen as Propulsion Fuel*, NASA-SP-4404, Washington, D.C., 1978, pg. 95-106, 141-166.

[65] Brewer, G.D., Morris, R.E., Lange, R.H., and Moore, J.W., "Study of the Application of Hydrogen Fuel to Long-Range Subsonic Transport Aircraft," NASA-CR-132558 (Vol. 1), NASA-CR-132559 (Vol. 2), Jan 1975.

[66] Brewer, G.D., Morris, R.E., "Study of LH_2 Fueled Subsonic Passenger Transport Aircraft," NASA-CR-144935, Jan. 1976.

[67] Brewer, G.D., *Hydrogen Aircraft Technology*, CRC Press, Boca Raton, Fl., 1991.

[68] Brewer, G.D., "Configuration Integration for High Altitude Aircraft," AFWAL-TR-86-3063, Vol. 2, Lockheed-California Company, Burbank, Jan. 1987.

[69] Raymer, D. P., *Aircraft Design: A Conceptual Approach*, 2nd Ed., AIAA Education Series, Washington D.C., 1992.

[70] *Improving the Engineering Process with Software Integration*, Technical White Paper, Phoenix Integration, Feb. 2003, Blacksburg, VA. Available at http://www.phoenix-int.com/publications/SoftwareIntegration.pdf.

[71] Vanderplaats, G. N., *Numerical Optimization Techniques for Engineering Design*, Vanderplaats Research & Development, Inc., Colorado Springs, CO.

[72] Grasmeyer, J. M., "A Discrete Vortex Method for Calculating the Minimum Induced Drag and Optimum Load Distribution for Aircraft Configurations with Noncoplanar Surfaces," VPI-AOE-242, Department of Aerospace and Ocean

Engineering, Virginia Polytechnic Institute and State University, Blacksburg, Virginia 24061, January, 1998.

[73] Mason, W. H., "Subsonic Airfoils and Wings," *Configuration Aerodynamic Notes*, March, 2001. Available at: http://www.aoe.vt.edu/~mason/Mason_f/ConfigAeroSubFoilWing.pdf

[74] Mason, W. J., "Analytic Models for Technology Integration in Aircraft Design," AIAA-90-3262, September, 1990.

[75] Malone, B., and Mason, W. H., "Multidisciplinary Optimization in Aircraft Design Using Analytic Technology Models," *Journal of Aircraft*, Vol. 32, No. 2, March-April 1995, pp. 431-438.

[76] Mason, W. H., *FRICTION Code Documentation*, available online at: http://www.aoe.vt.edu/aoe/faculty/Mason_f/CAtxtAppD5.pdf

[77] Braslow, A. L., Maddalon, D. V., Bartlett, D. W., Wagner, R. D., and Collier, F. S., "Applied Aspects of Laminar-Flow Technology," *Viscous Drag Reduction in Boundary Layers*, AIAA, Washington D.C., 1990, pp. 47-78.

[78] Boltz, F. W., Renyon, G. C. and Allen, C. Q., "Effects of Sweep Angle on the Boundary Layer Stability Characteristics of an Untapered Wing at Low Speeds," NASA TN D-338, 1960.

[79] White, F. M., *Viscous Fluid Flow*, McGraw-Hill, New York, 1974, pp. 580-590.

[80] Isikveren, A. T., "Quasi-Analytical Modelling and Optimisation Techniques for Transport Aircraft Design," Ph.D. Dissertation, Royal Institute of Technology (KTH), Department of Aeronautics, Sweden, 1998.

[81] "Aerospace Source Book," *Aviation Week and Space Technology*, Jan. 12, 1998.

[82] *Jane's All the World's Aircraft*, 1990-1991 through 2001-2002, Jane's Information Group Limited, 1990 through 2001.

[83] Svoboda, C., "Turbofan Engine Database as a Preliminary Design Tool," Aircraft Design 3 (2000) 17-31, *Aircraft Design Journal*, 2000.

[84] Hilton, W. F., *High Speed Aerodynamics*, Longmans, Green & Co., London, 1952.

[85] Beltramo, M. N., Trapp, D. L., Kimoto, B. W., Marsh, D. P., "Parametric Study of Transport Aircraft Systems Cost and Weight," NASA CR-151970, April 1977.

[86] McCullers, L.A., FLOPS User's Guide, Release 5.81, NASA Langley Research Center

[87] Gundlach, J.F., "Multidisciplinary Design Optimization and Industry Review of a 2010 Strut-Braced Wing Transonic Transport," MAD 99-06-03. 1999.

[88] Torenbeek, E., *Synthesis of Subsonic Airplane Design*, Delft University Press, delft, The Netherlands, 1982.

[89] Roskam, J., and Lan, C.-T.E., *Airplane Aerodynamics and Performance*, DARCorporation, Lawrence, KS, 1997.

[90] Chai, S. Crisafulli, P., Mason, W. H., "Aircraft Center of Gravity Estimation in Conceptual/Preliminary Design, " 1st AIAA Aircraft Engineering, Technology and Operations Congress, AIAA 95-3882, Los Angeles, Ca., Sept. 19-21, 1995.

[91] Knill, D.L., Giunta, A.A., Baker, C.A., Grossman, B., Mason, W.H., Haftka, R.T. and Watson, L.T., "Response Surface Models Combining Linear and Euler Aerodynamics for Supersonic Transport Design," *Journal of Aircraft*, Vol. 36, No.1, January-February 1999, pp. 75-86.

[92] Ko, Y.-Y. A., "The Role of Constraints and Vehicle Concepts in Transport Design: A Comparison of Cantilever and Strut-Braced Wing Airplane Concepts," MS Thesis, Virginia Polytechnic Institute & State University, April, 2000.

[93] Vanderplaats, G., Malone, B., "Getting the Most Out of ModelCenter® Optimization," Web presentation by Phoenix Integration and Vanderplaats R&D.

Inc., 7 Feb. 2003. Presentation available at:
http://www.vrand.com/DOT_seminar_final.ppt

[94] Gainer, T. G., Yip L. P., and Volger, R. D., "Comparison of Aerodynamic Theory and Experiment for Jet-Flap Wings," *Powered-Lift Aerodynamics and Acoustics*, Jan, 1976, pp. 103-118.

[95] *Marine Engineering*, Vol. 1, Society of Naval Architect & Marine Engineers, Ed. Herbert Lee Seward, pp. 10-11.

[96] Hill, P. and Peterson, C., *Mechanics and Thermodynamics of Propulsion*, 2nd Ed., 1992.

[97] Stinton, D., *The Anatomy of the Airplane*, 2nd Ed., American Institute of Aeronautics and Astronautics, Reston, VA., 1998, pp153.

[98] Harris, C. D., "NASA Supercritical Airfoils: A Matrix of Family Related Airfoils," NASA TP 2969, March 1990.

[99] Spence, D. A., "The Lift Coefficient of a Thin, Jet-Flapped Wing," *Proceedings of the Royal Society of London*, Vol. 238, Issue 1212, Dec. 1956, pp. 46-68.

[100] Spence, D. A., Maskell, E. C., "A Theory of the Jet Flap in Three Dimensions," *Proceedings of the Royal Society of London*, Vol. 251, Issue 1266, June 1959, pp. 407-425.

[101] Spence, D. A., "The Lift Coefficient of a Thin Jet-Flapped Wing. II. A Solution of the Integro-Differential Equation for the Slope of the Jet," *Proceedings of the Royal Society of London*, Vol. 261, Issue 1304, Apr. 1961, pp. 97-118.

[102] Schlichting, H., *Boundary Layer Theory*, McGraw-Hill, New York, 1942, 7th ed. 1979, pp 175-179.

[103] Anderson, J. D., *Fundamentals of Aerodynamics*, 2nd Ed., New York, 1991, pp. 340-345.

[104] "2003 Aerospace Source Book," *Aviation Week and Space Technology*, Jan. 13, 1998.

Appendix A: Aerodynamics/Propulsion interaction effects on propulsive efficiency assuming triangular shaped jets and wakes

Consider a propulsor in a control volume as shown in Figure A-1. We assume that the exit velocity profile of the exhaust is that of a triangle, as shown in Figure A-1. The velocity profile distribution is given in Equation (A.1).

$$
\begin{aligned}
U(y) &= U_\infty && \frac{b}{2} \le y \le h \\
U(y) &= \frac{2(U_\infty - U_J)}{b} y + U_J && 0 \le y \le \frac{b}{2} \\
U(y) &= \frac{2(U_J - U_\infty)}{b} y + U_J && -\frac{b}{2} \le y \le 0 \\
U(y) &= U_\infty && -h \le y \le -\frac{b}{2}
\end{aligned}
\tag{A.1}
$$

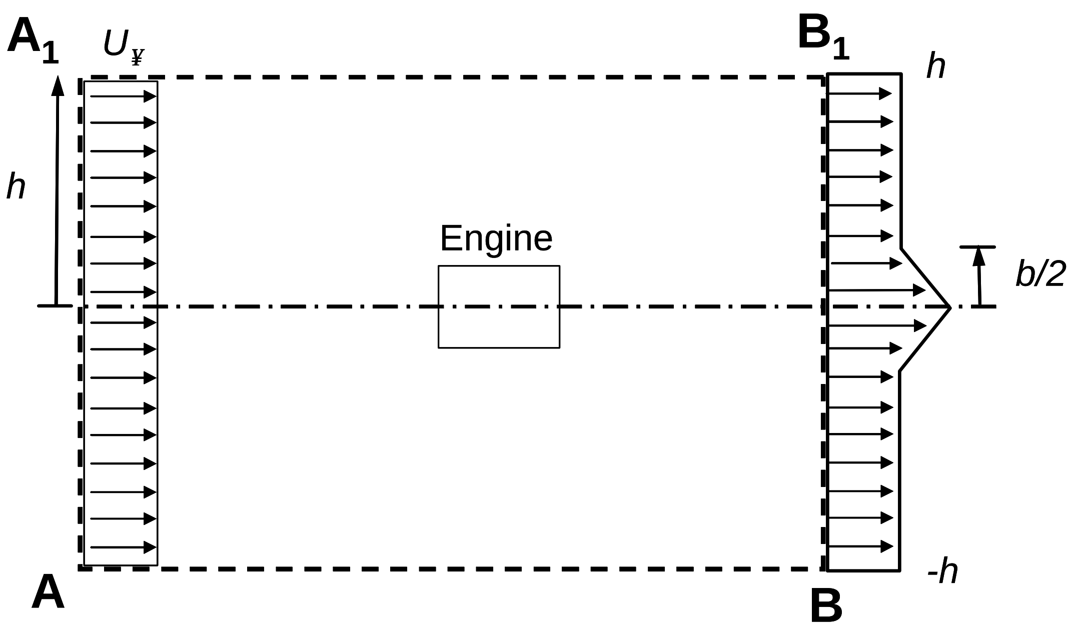

Figure A-1: Control volume for the calculation of propulsive efficiency

The rate of kinetic energy for the flow in the upstream is given by Equation (A.2).

$$KE_{AA_1} = \frac{1}{2} r \int_{-h}^{h} U_\infty{}^3 dy \tag{A.2}$$

The rate of kinetic energy for the flow in the downstream is given by Equation (A.3).

$$KE_{BB_1} = \frac{1}{2} r \left(1 + f\right) \int_{-h}^{h} U\left(y\right)^3 dy \tag{A.3}$$

Hence, assuming negligible fuel mass added to the flow, the net rate of kinetic energy added to the flow is given in Equation (A.4).

$$\begin{aligned} \Delta KE &= KE_{BB_1} - KE_{AA_1} \\ &= \frac{1}{6} r\, bU_\infty \left(U_J^2 + U_\infty U_J - 2U_\infty^2\right) \end{aligned} \tag{A.4}$$

Equation (5.6) in Chapter 5 gives the general form of the thrust equation. Assuming that the fuel mass added to the flow is negligible and the exhaust pressure is equal to the ambient pressure, the thrust of the system simplifies to Equation (A.5).

$$T = \frac{1}{2} r\, bU_\infty \left(U_J - U_\infty\right) \tag{A.5}$$

Therefore, defining the propulsive efficiency as the ratio of the thrust power to the rate of production of propellant kinetic energy, the efficiency of this propulsive system is shown in Equation (A.6).

$$\begin{aligned} h &= \frac{Thrust\, U_\infty}{\Delta KE} \\ &= \frac{3}{2 + \frac{U_J}{U_\infty}} \end{aligned} \tag{A.6}$$

Now, consider a non-distributed propulsion scenario where the propulsor and the body are separate, as shown in Figure A-2.The wake and the jet have no influence on each other, and we assume a triangle shaped jet and wake velocity profile. The velocity distribution at cross section BB_1 is given in Equation (A.7).

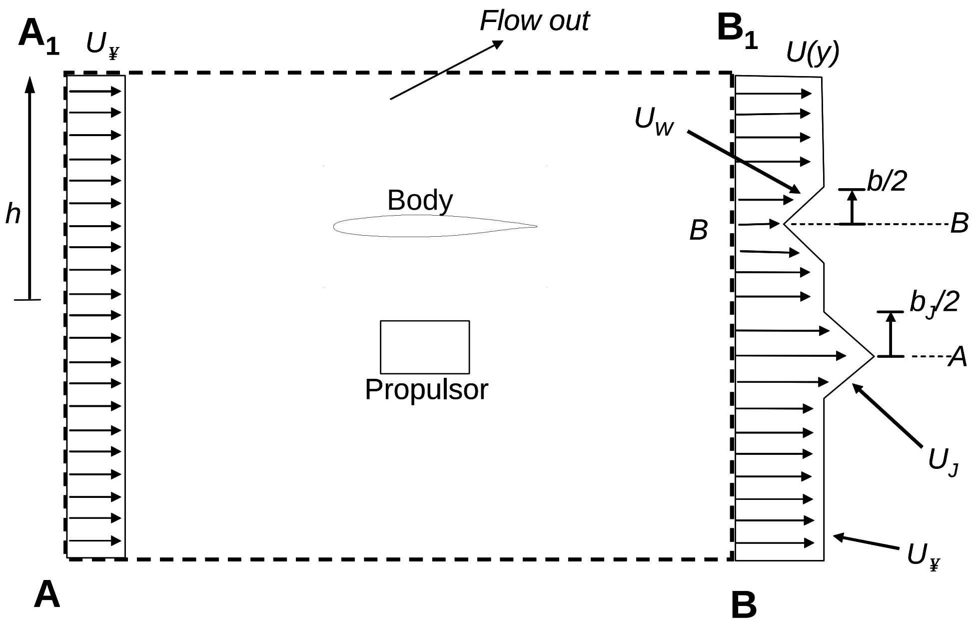

Figure A-2: Control volume of a non-distributed propulsion configuration, assuming a triangular shaped wake and jet

$$
\begin{aligned}
&U(y) = U_\infty && B + \frac{b}{2} \le y \le h \\
&U(y) = \frac{2(U_\infty - U_W)}{b}(y - B) + U_W && B \le y \le B + \frac{b}{2} \\
&U(y) = \frac{2(U_W - U_\infty)}{b}(y - B) + U_W && B - \frac{b}{2} \le y \le B \\
&U(y) = U_\infty && A + \frac{b_J}{2} \le y \le B + \frac{b_J}{2} \\
&U(y) = \frac{2(U_\infty - U_J)}{b_J}(y - A) + U_J && A \le y \le A + \frac{b_J}{2} \\
&U(y) = \frac{2(U_J - U_\infty)}{b_J}(y - A) + U_J && A - \frac{b_J}{2} \le y \le A \\
&U(y) = U_\infty && -h \le y \le A - \frac{b_J}{2}
\end{aligned}
\tag{A.7}
$$

Again, we assume that the pressure along face BB_1 is equal to that along AA_1. Following the momentum equation given in Equation 5.13, The net force in the freestream direction is given in Equation (A.8).

$$
\begin{aligned}
F_x &= r\left[\int_{-h}^{h} u(y)\left[U_\infty - u(y)\right] dy_{BB_1}\right] \\
&= \frac{1}{6} r \left[b_J\left(U_\infty^2 + U_\infty U_J - 2U_J^2\right) + b\left(U_\infty^2 + U_\infty U_W - 2U_W^2\right)\right]
\end{aligned}
\tag{A.8}
$$

By setting Equation (A.8) to zero, for a self-propelled case, we solve for $\frac{U_J}{U_\infty}$. Since we know that $\frac{U_W}{U_\infty} \leq 1$ and $\frac{U_J}{U_\infty} \geq 1$, we take the greater valued solution (from the quadratic solution), shown in Equation (A.9).

$$
\frac{U_J}{U_\infty} = \frac{1}{4} + \frac{1}{4}\sqrt{\left(\frac{b_J}{b}\right)^{-1}\left[9\frac{b_J}{b} + 8\left(1 + \frac{U_W}{U_\infty} - 2\left(\frac{U_W}{U_\infty}\right)^2\right)\right]}
\tag{A.9}
$$

Therefore, by substituting Equation (A.9) into (A.6), the formulation for efficiency in this case is:

$$
h_{Non-DP} = \frac{12\sqrt{\frac{b_J}{b}}}{9\sqrt{\frac{b_J}{b}} + \sqrt{9\frac{b_J}{b} + 8\left[1 + \frac{U_W}{U_\infty} - 2\left(\frac{U_W}{U_\infty}\right)^2\right]}}
\tag{A.10}
$$

Now, consider a distributed propulsion configuration like that shown in Figure A-3. Here the jet overlays the wake. The velocity profile distribution at cross section BB_1 is given in Equation (A.11).

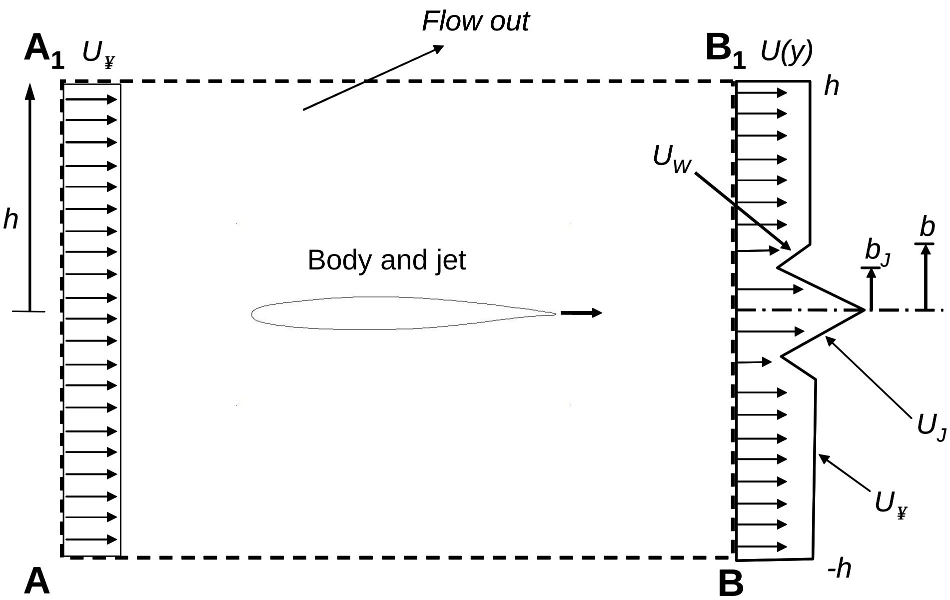

Figure A-3: Control volume of a distributed propulsion configuration, assuming a triangular shaped wake and jet

$$
\begin{aligned}
&U(y) = U_\infty && \frac{b}{2} \le y \le h \\
&U(y) = \frac{2(U_\infty - U_W)}{b} y + U_W && \frac{b_J}{2} \le y \le \frac{b}{2} \\
&U(y) = \frac{2(U_{int} - U_J)}{b_J} y + U_J && 0 \le y \le \frac{b_J}{2} \\
&U(y) = \frac{2(U_J - U_{int})}{b_J} y + U_J && -\frac{b_J}{2} \le y \le 0 \\
&U(y) = \frac{2(U_W - U_\infty)}{b} y + U_W && -\frac{b}{2} \le y \le -\frac{b_J}{2} \\
&U(y) = U_\infty && -h \le y \le -\frac{b}{2} \\
&\textit{where } U_{int} = \frac{b_J}{b}(U_\infty - U_W) + U_W
\end{aligned}
\tag{A.11}
$$

Again, the summation of momentum in the x direction results in Equation (A.12).

$$
F_x = \frac{1}{6}\frac{r}{b}\begin{bmatrix} 2b_J^2(U_\infty - U_W)(U_W - U_J) + b^2\left(U_\infty^2 - U_\infty U_W - 2U_W^2\right) + \\ bb_J(U_J - U_W)(3U_\infty - 2(U_J + 2U_W)) \end{bmatrix} \tag{A.12}
$$

The force equation is set to zero for a self-propelled case and solved for $\frac{U_J}{U_\infty}$. Again, since $\frac{U_W}{U_\infty} \leq 1$ and $\frac{U_J}{U_\infty} \geq 1$, we select the higher valued solution shown in Equation (A.13).

$$\frac{U_J}{U_\infty} = \frac{1}{4\left(\frac{b_J}{b}\right)}\left[\begin{array}{l}\frac{b_J}{b}\left(3-2\frac{U_W}{U_\infty}\right)-2\left(\frac{b_J}{b}\right)^2\left(1-\frac{U_W}{U_\infty}\right)+ \\ \sqrt{\frac{b_J}{b}\left[\begin{array}{l}9\frac{b_J}{b}\left(1-2\frac{U_W}{U_\infty}\right)^2+8\left(1+\frac{U_W}{U_\infty}-2\left(\frac{U_W}{U_\infty}\right)^2\right)+ \\ 4\left(\frac{b_J}{b}\right)^3\left(1-\frac{U_W}{U_\infty}\right)^2-12\left(\frac{b_J}{b}\right)^2\left(1-3\frac{U_W}{U_\infty}+2\left(\frac{U_W}{U_\infty}\right)^2\right)\end{array}\right]}\end{array}\right] \quad \text{(A.13)}$$

By replacing Equation (A.13) into Equation (A.6), the propulsive efficiency of this configuration is given in Equation (A.14).

$$h_{DP} = \frac{12\frac{b_J}{b}}{\frac{b_J}{b}\left(11-2\frac{U_W}{U_\infty}\right)-2\left(\frac{b_J}{b}\right)^2\left(1-\frac{U_W}{U_\infty}\right)+Q}$$

$$where\ Q = \sqrt{\frac{b_J}{b}\left(\begin{array}{l}9\frac{b_J}{b}\left(1-2\frac{U_W}{U_\infty}\right)^2+8\left(1+\frac{U_W}{U_\infty}-2\left(\frac{U_W}{U_\infty}\right)^2\right) \\ +4\left(\frac{b_J}{b}\right)^3\left(1-\frac{U_W}{U_\infty}\right)^2-12\left(\frac{b_J}{b}\right)^2\left(1-3\frac{U_W}{U_\infty}+2\left(\frac{U_W}{U_\infty}\right)^2\right)\end{array}\right)} \quad \text{(A.14)}$$

Figure A-4 shows a plot of the efficiencies from Equation (A.10) and (A.14) for a range of values of $\frac{b_J}{b}$. In this instance, $\frac{U_W}{U_\infty}$ is taken to have a value of 0.5. It shows that the propulsive efficiency of the distributed propulsion configuration exceeds that of the non-distributed propulsion configuration at about efficiency of 78%. The non-distributed propulsion configuration has higher propulsive efficiencies for values of $\frac{b_J}{b}$ smaller than

0.3. However, the difference in propulsive efficiency between the two configurations is small at these values of $\frac{b_J}{b}$.

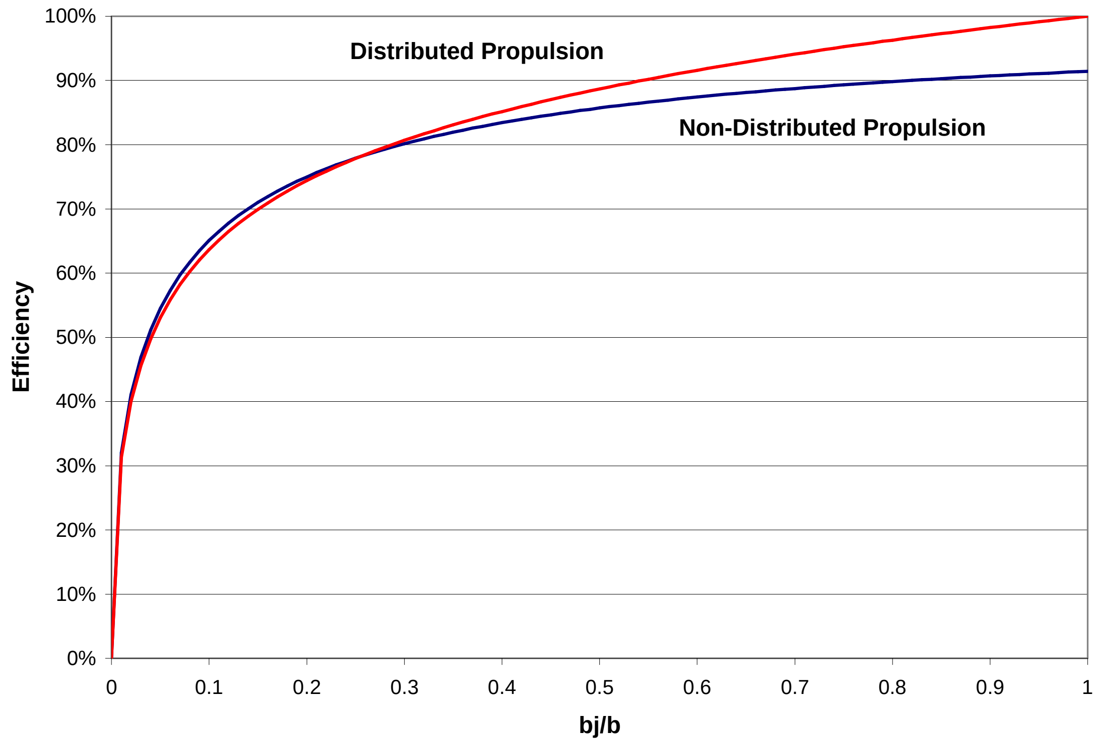

Figure A-4: Figure showing the variation of efficiency for a distributed propulsion and non-distributed propulsion configuration, assuming triangular shaped wakes and jets. $\frac{U_W}{U_\infty} = 0.5$.

Appendix B: Optimization convergence history for the distributed propulsion BWB optimum design

Figures B-1, B-2, and B-3 shows the optimization convergence history of the design variables for the distributed propulsion BWB optimum design. Figure B-1 shows the convergence history of the t/c ratios at each span station. Figure B-2 shows the convergence history of the chord lengths of each span station and the position of the second, third and fourth span stations. Figure B-3 shows the convergence history of the quarter chord sweep at each of the wing sections, and the remaining design variables: fuel weight, average cruise altitude and thrust per engine.

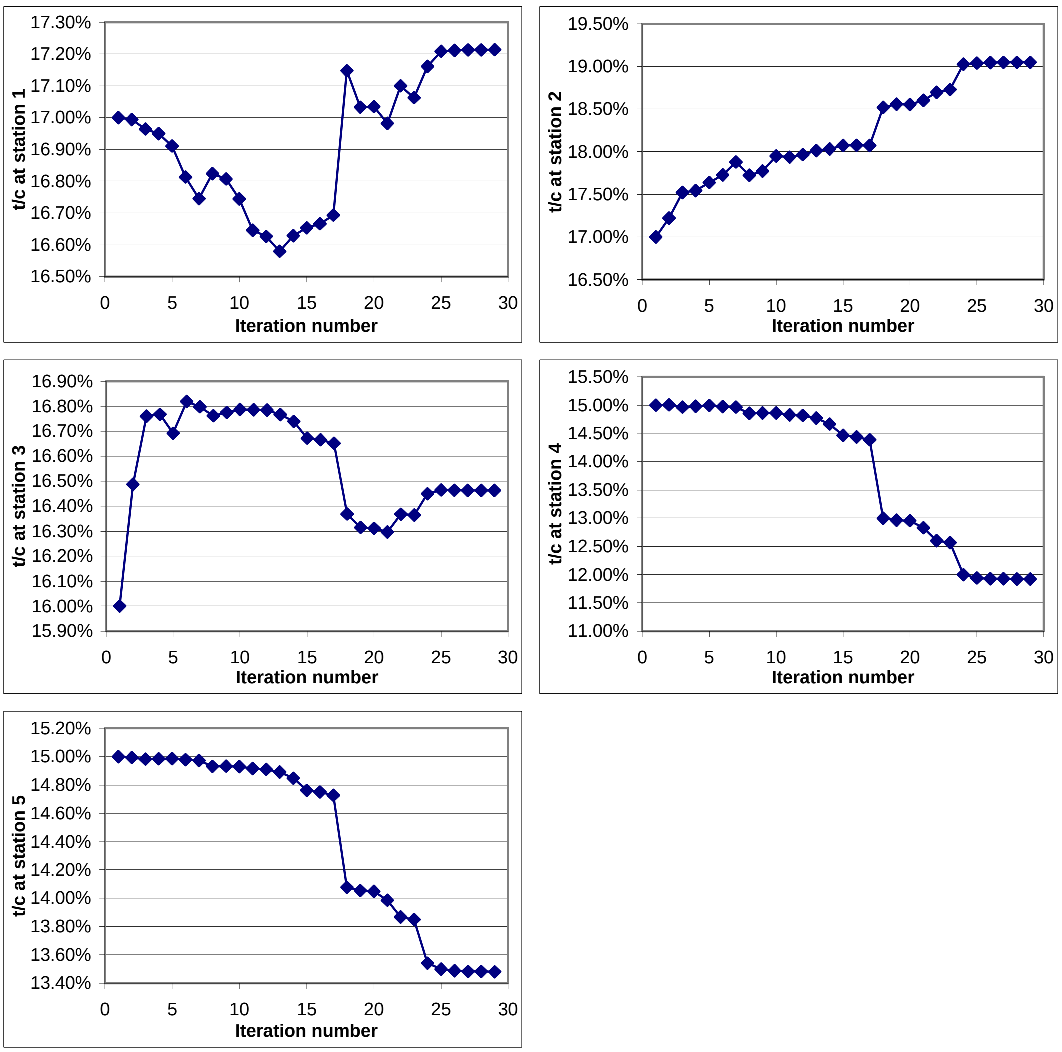

Figure B-1: The optimization convergence history of the *t/c* ratio at each span station for the distributed propulsion BWB optimum design.

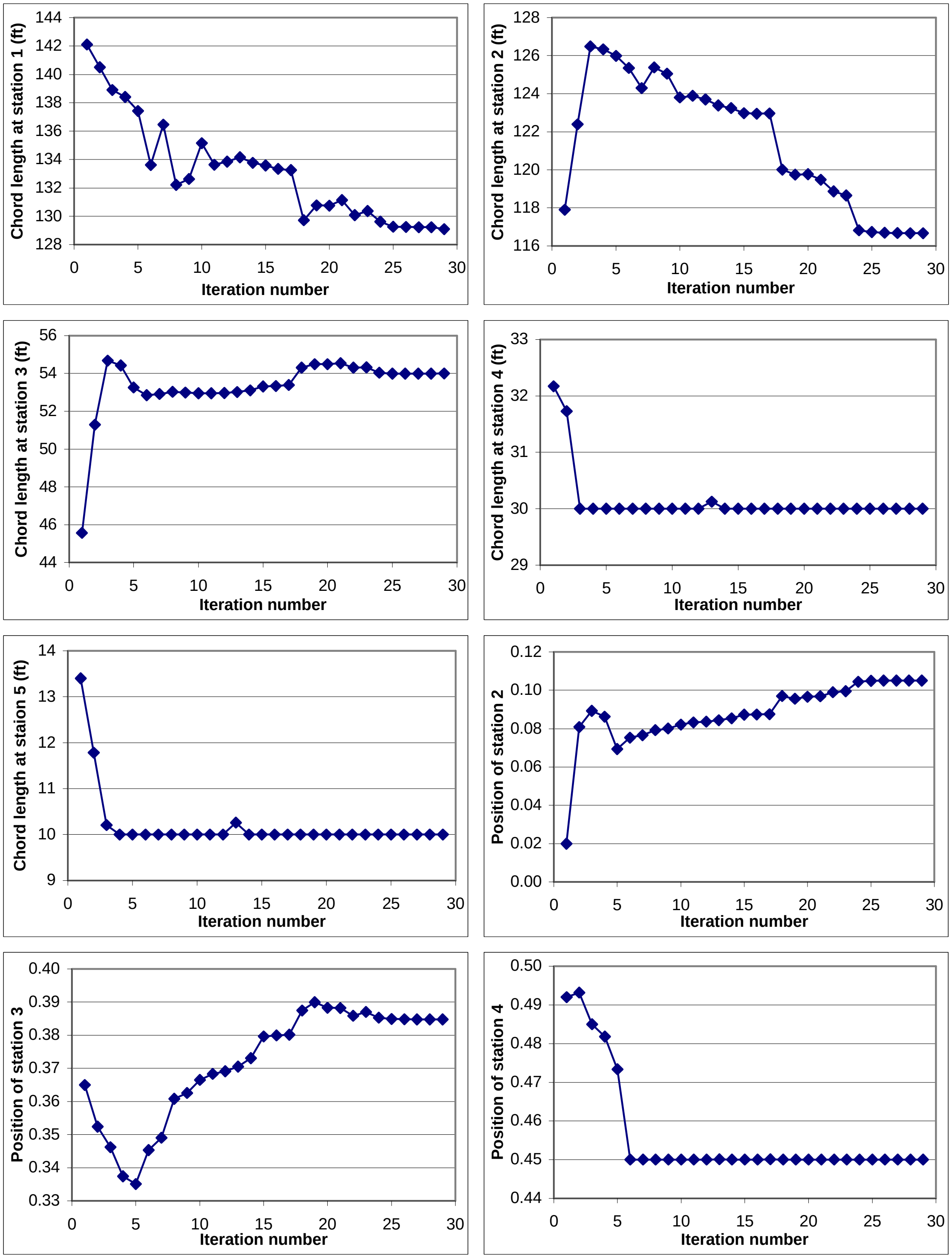

Figure B-2: The optimization convergence history of the chord lengths at each span station and position of the second, third and fourth span station for the distributed propulsion BWB optimum design.

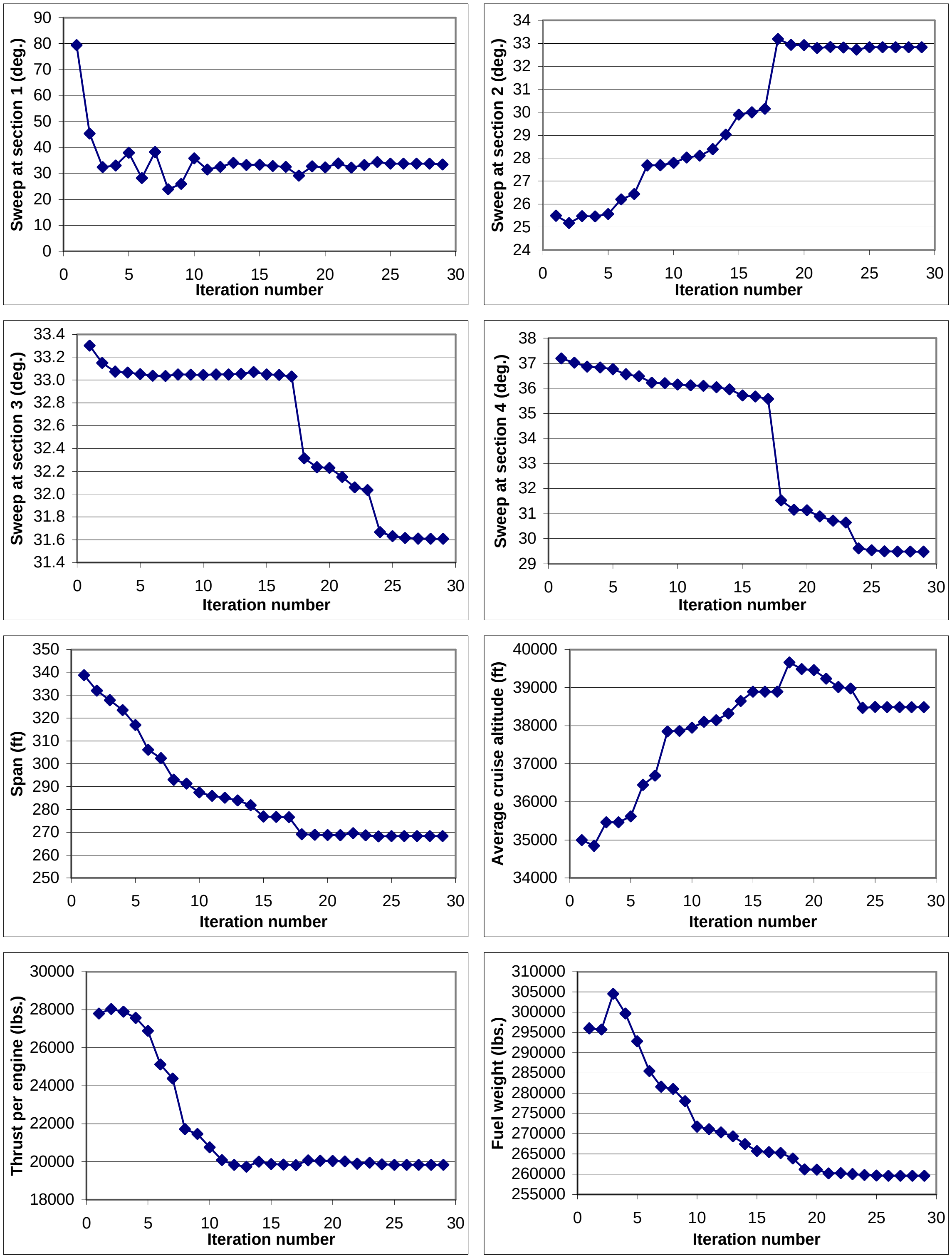

Figure B-3: The optimization convergence history of the quarter chord sweep angles of the wing sections, the wing span, average cruise altitude, thrust per engine and fuel weight for the distributed propulsion BWB optimum design.

Appendix C: Introduction to the use of distributed propulsion on the BWB to reduce external aircraft noise

Early designs of the BWB aircraft noted that the use of buried engines and upper surface inlets have the potential of reduced engine noise due to shielding [18]. To test this hypothesis, a 4% scale model of the BWB was installed in the Anechoic Noise Research Facility at the NASA Langley Research Center to study the engine noise characteristics of the BWB configuration. The tests showed that there were significant reductions in overall noise by the BWB aircraft to an observer on the ground during flyover. This reduction in noise was found to be mainly due to the shielding of the inlet noise. However, there was very little benefit in shielding for the engine exhaust radiated noise. Details of this work can be found in Reference [56].

As mentioned before, the distributed propulsion concept was initially conceived to reduce aircraft noise. Lilley et al. [57] found that the dominant noise source on the airframe arises from the scattering of the noise generated due to the passage of the wing turbulent boundary layers over the wing trailing edge. By modeling the trailing edge of the wing as a jet wing, perhaps the jet wing blowing will act to disrupt this scattering effect. An article in Professional Pilot [58] reported that the Ball Bartoe JW-1 JetWing STOL aircraft was a quiet aircraft. Most jet wing studies focus around the improved high lift aerodynamic characteristics of the concept and not the noise. However, there are experimental results conducted comparing noise characteristics of jets from round and slotted nozzles that found lower noise levels for the slotted jet compared to the round jet at high jet exit velocities. Coles showed in 1959 [59] that the total sound power output from a slotted nozzle of high aspect ratio is half, or 3 dB less, than the output of a circular nozzle having the same exit area and velocity. He also observed reductions in overall noise and a beneficial change in radiation characteristics for high aspect ratio jet flaps. Maglieri and Hubbard [60] observed that there was a considerable noise reduction for long jet flaps. Schrecker and Maus [61] showed experimentally that the overall sound power of a jet flap increases with the fifth or sixth power of the nozzle exit velocity. They also concluded that at higher subsonic exhaust Mach numbers ($M \geq 0.7$), the jet flap radiates as much overall sound power as a circular nozzle of the same area.

Appendix D: The use of hydrogen as a propulsion fuel to reduce emissions

Engine emissions are a major factor in future aircraft design. It is a serious environmental issue at busy airports, and more stringent regulations on air quality are increasing all over the world [62]. The main pollutants from aircraft engines that are limited by these regulations include the oxides of nitrogen, NO and NO_2, collectively termed NO_x. Solely because the BWB aircraft consumes less fuel than its conventional cantilever aircraft counterpart, it will have reduced engine NO_x emissions. However, a more aggressive effort is needed to address engine emission issues. Considering alternative propulsion systems such as hydrogen propulsion is one way to reduce emissions. The world's limited supply of hydrocarbon fuel is also an additional motivation to consider hydrogen propulsion systems. Although it is expected that synthetic kerosene from natural gas would be a much more realistic alternative to hydrocarbon fuels until about 2090 [63], hydrogen propulsion systems should still be considered as an alternative.

From an environmental standpoint, liquid hydrogen (LH_2) is a viable substitute for conventional jet fuel since theoretically it only produces carbon dioxide and water as emission by-products. It is projected that if by 2100, 90% of the world's aircraft fleet used hydrogen, the carbon pollution levels would be reduced by 6% [63]. However, from a design standpoint, LH_2 has a very low mass density (about 10 times smaller than JP4 fuel) which translates to large volumes needed to store the fuel.

Using LH_2 for aircraft propulsion has been considered for the last forty years. In 1956, the Air Force and NACA looked at using hydrogen as aircraft fuel with the start of Project Bee [64]. A test flight of a modified B-57B aircraft using hydrogen as fuel during cruise was made. This test flight demonstrated that hydrogen could be an aircraft fuel alternative. Other tests involving hydrogen fuel were performed at the Lockheed Skunk Works, specifically to test the safety and handling characteristics of liquid hydrogen [64]. It was concluded that LH_2 was much safer than jet fuel in terms of damage due to burning or accidental explosion.

In the 1970s, the Lockheed company performed a study to design a passenger transport aircraft using LH_2 as fuel [65],[66]. It studied two different LH_2 aircraft designs, one with the fuel carried in the fuselage, forward and aft of the passenger compartment, and the other with external fuel tanks mounted on pylons above the wing. A similarly designed conventional aircraft (using jet fuel) was also designed for comparison. It was found that the external fuel tank design did not show any design advantages compared to the internal fuel tank design. Comparing with the conventional aircraft, it was found that for a short range mission (3000 nmi), the performance or weight of a LH_2 aircraft is similar to that of a conventional design, providing no significant advantages. The main advantage occurs for a long range mission (5000 nmi), where the LH_2 aircraft design showed a 40% reduction in TOGW, and a 71% decrease in fuel weight. The LH_2 aircraft requires a smaller wing area, and shorter span. The only disadvantage of this aircraft is that it has a longer and larger fuselage. Other studies performed extensive research into the design of hydrogen engines, pumping and insulation subsystems, and even ground refueling options. A summary of these studies can be found in Reference [67].

A major challenge in using LH_2 fuel in the BWB configuration is the design of the fuel tanks and systems. To store the LH_2 fuel, the fuel tanks have to be pressurized and insulated to prevent boil-off. In the conventional aircraft design, the cylindrical fuselage works well as a structure to house LH_2 fuel tanks. However, in the BWB configuration, no such cylindrical fuselage is present. In fact, the BWB configuration has a high surface area to volume ratio, which presents a storage and insulation challenge.

The storage and insulation challenge is not entirely impossible to overcome. Brewer et al. designed a high altitude, long endurance aircraft for the US Air Force using hydrogen fuel [68]. In this design, all the fuel was stored in the wing sections, much like what would be needed in the BWB aircraft. Several fuel tank options were presented included integral and non-integral pressure tanks.

Based on the research already done on using hydrogen as a propulsion fuel, designing the BWB aircraft to use hydrogen fuel should be a straightforward problem.

Appendix E: The distributed propulsion BWB MDO code User's Manual

Introduction

This manual describes the program which was created to optimize a Distributed Propulsion Blended-Wing-Body (BWB) aircraft configuration as a transonic commercial transport. The code is comprised of individual smaller programs and modules assembled in Phoenix Integration's ModelCenter®. ModelCenter® is a commercial code integration tool. Although the program integrated in ModelCenter® is specific to optimizing BWB aircraft configurations, it is fairly straightforward to reassemble the individual modules to analyze and optimize other aircraft designs. The Distributed Propulsion BWB MDO code is designed to optimize both a conventional BWB configuration, as well as a distributed propulsion BWB configuration.

In the following documentation, it will be assumed that the user is somewhat familiar with ModelCenter®. The program takes advantage of several built-in functions provided in ModelCenter®, and its use will not be documented here. Comprehensive documentation on ModelCenter® can be found under the 'Help' section in the integration program.

A majority of the modules for the code are written in FORTRAN. Some of the modules have been developed specifically for this program. Most of them are written either in FORTRAN 90, or as Visual Basic scripts in ModelCenter®. The other modules have been obtained from other sources, such as from the Virginia Tech SBW code, and the NASA FLOPS (Flight Optimization System) code. These codes are mainly written in FORTRAN 77.

Model/Program Overview

A screenshot of the model in ModelCenter® which serves as the distributed propulsion BWB MDO program is given in **Error! Reference source not found.**. This Model is divided into several sections:

- Code inputs
- Analysis modules
- Constraint calculator
- Optimization tools
- Geometry visualization modules
- Variable Data Monitor

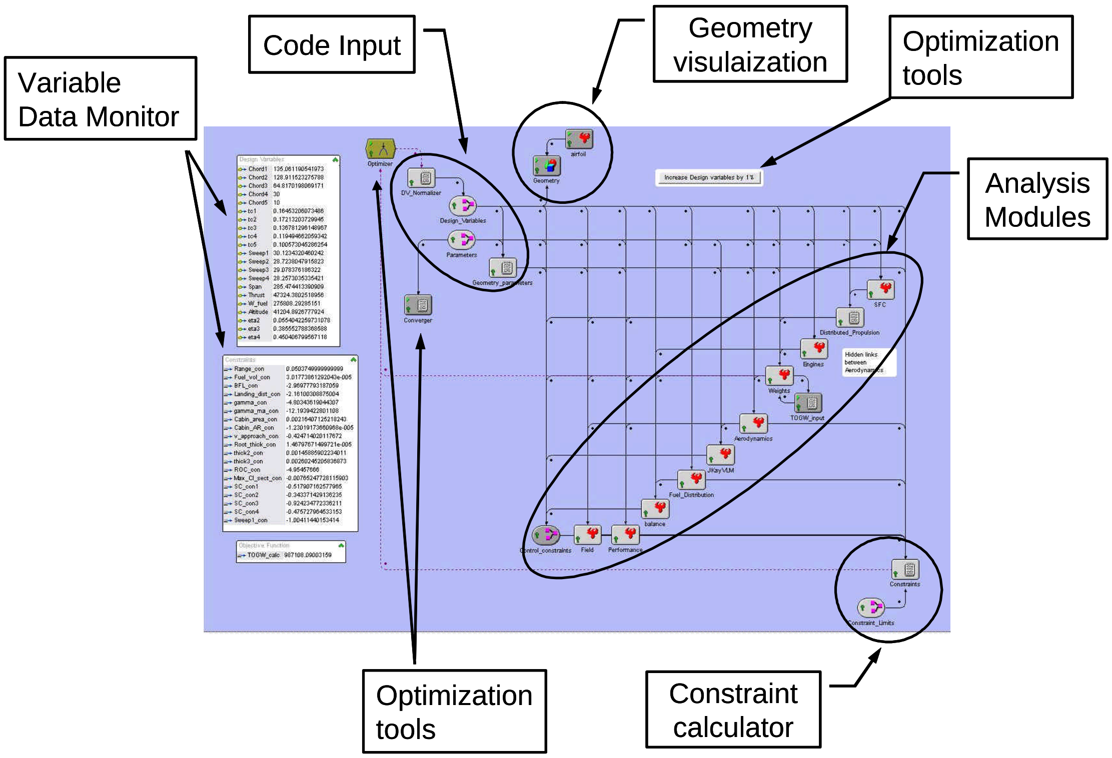

Figure C-1: Model overview of the Distributed Propulsion BWB MDO model

Each ‘block’, called a component, represents an analysis module either obtained from the Analysis Server®[1] or written as a Visual Basic Script.

Code Inputs

The code input components allow the user to specify values for the design variables and parameters that will be used throughout the program. It serves as a ‘starting point’ for the program calculation. This section also calculates basic geometry variables

[1] Analysis Server® is a companion program to ModelCenter® that is used to make available the individual programs to ModelCenter® to integrate.

such as aspect ratio and planform areas from these inputs to be used in the other components. Figure C-2 shows a close up view of the code inputs section.

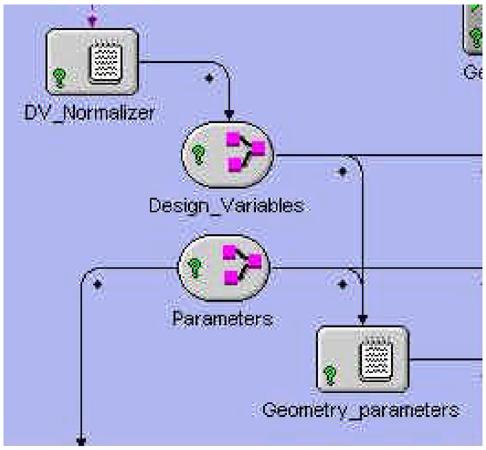

Figure C-2: The code input section of the Distributed Propulsion BWB MDO program

The *DV_Normalizer* component is a Visual Basic script that translates the normalized design variables obtained from the optimizer into their respective design variable quantities. The design variables are normalized so as to place all the design variables manipulated by the optimizer on the same scale. Hence, these values need to be translated back into their respective quantities before being passed on to the analysis routines.

The *Design_Variables* and *Parameters* components serve as a repository for the un-normalized design variables and analysis parameters respectively. It is from here that all the necessary parameters and variables are passed to the analysis components.

The *Geometry_parameters* component calculates general aircraft geometric quantities such as the reference area, wing section thicknesses, and cabin planform area.

Analysis modules

Figure C-3 shows a close up view of the analysis modules. It is here where all of the necessary analysis calculations for the optimizer are performed. Each component is linked and arranged in a 'cascade' arrangement. This 'cascade' visually arranges each component in order of analysis execution and data flow, starting from the top right to the bottom left corner. For example, the *Weights* component receives data from components above it, namely *Engines*, and *Distributed_Propulsion*. Data calculated from the *Weights* component is passed on to other components below it, such as *Aerodynamics* and *balance*. Except for the *Distributed_Propulsion* component, which performs a fixed point iteration scheme with the *Aerodynamics*, *Weights* and *Engines* components, all the other components follow this 'cascade' scheme.

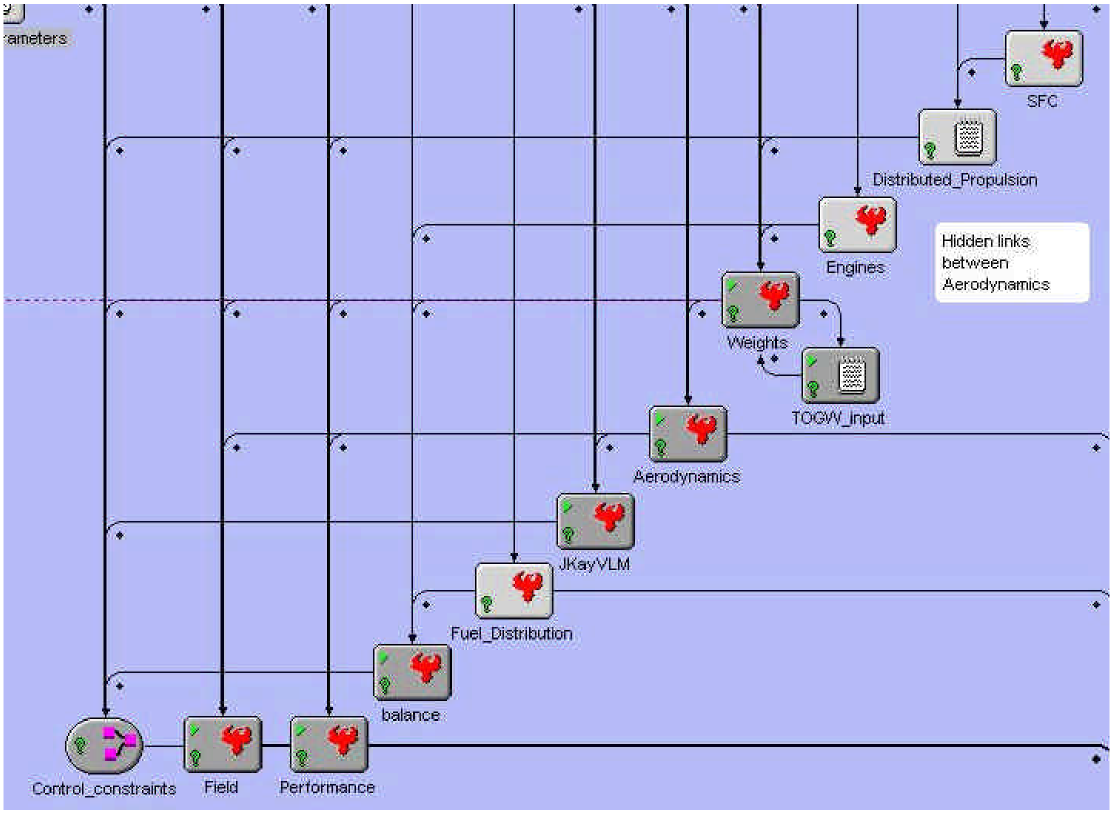

Figure C-3: The analysis components of the Distributed Propulsion BWB MDO program.

The *Distributed_Propulsion* component calculates and applies all the distributed propulsion integration effects explained in Chapter 5 to the other individual analysis components. The *Distributed_Propulsion* component also determines the thrust from the jet exiting the trailing edge of the aircraft. This is calculated based on the ratio of the wave and friction drag to the total drag. However, since the induced drag is affected by the thrust level of the jet, the total drag is dependant on the jet thrust. Hence, we are faced with calculating an implicit solution. The *Distributed_Propulsion* component solves this problem by performing a fixed point iteration scheme with the *Aerodynamics* component. Since some of the input into the *Aerodynamics* component comes from the *Weights* and *Engines* components, they are also included in the iteration scheme. The iteration is stopped when the value of the jet thrust converges within 1 lb (absolute criteria) of its previous calculated value.

The *SFC* component calculates the specific fuel consumption of the propulsion system, while the *Engines* component calculates the weight of the propulsion system. Previous versions included the *SFC* component into the *Engines* component, but it was separated to allow a more efficient execution of the fixed point iteration scheme in the *Distributed_Propulsion* component.

The *Weights* component calculates all the aircraft weights except for that of the propulsion system. The *TOGW_input* component is linked to the *Weights* component to provide a starting guess to the TOGW calculation in the *Weights* component. In Chapter 3, we explained that the calculation of the TOGW requires the use of a Newton Rhapson iteration scheme to solve an implicit formulation. The *TOGW_input* component provides an initial guess to the TOGW based on the converged TOGW value calculated in the previous analysis function evaluation.

The *Aerodynamics* component calculates all the aerodynamic quantities for the aircraft including the *L/D* ratio at cruise, and the maximum sectional lift coefficient.

The *JKayVLM* component is a Vortex Lattice Method program that calculates the longitudinal control derivatives for the conventional BWB configuration and the neutral point location for the distributed propulsion BWB configuration.

The *Fuel_Distribution* component calculates the available fuel volume in the wings, and the center of gravity (CG) locations of the fuel (in a full fuel configuration) in the fuel tanks for the use in the control constraint calculations.

The *balance* component calculates the individual CG locations and the overall CG location of the BWB aircraft at the different weight configurations as documented in Chapter 4 of this dissertation.

The *Field* component calculates field performance parameters such as the balanced field length, second segment climb gradient and the approach velocity.

The *Performance* component calculates the top of climb rate of climb and the aircraft range.

The *Control_Constraints* component is actually an embedded Model whose component integration is shown in Figure C-4. It is responsible for the calculation of the longitudinal control constraints documented in Chapter 4 and 5. The CG_limit_selector component is a Visual Basic script that determines which branch of analysis components are evaluated depending on the BWB configuration. If a conventional BWB configuration is being designed or analyzed, the *CG_limit_calculator_Conv* component will be evaluated. This component calculates the CG limits based on the longitudinal control criteria following the method explained in Chapter 4. If a distributed propulsion BWB configuration is being designed or analyzed, the *Cj_calculator* and *jet_control* components will be evaluated. The *Cj_calculator* component calculates the value of the jet coefficient, C_J. The *jet_control* component calculates the longitudinal control constraints for a distributed propulsion BWB configuration that uses a thrust vectoring system. This calculation method is detailed in Chapter 5 of this dissertation. The *CG_constraints* component calculates the actual longitudinal constraint values based on inputs through the *CG_limit_selector* component.

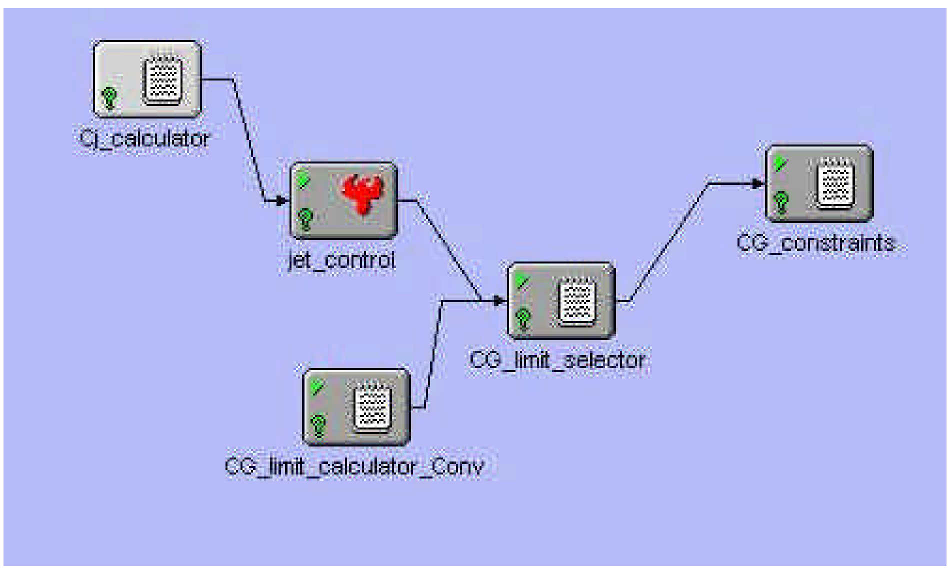

Figure C-4: The control constraints calculation module in the Distributed Propulsion BWB MDO program.

Constraint Calculator

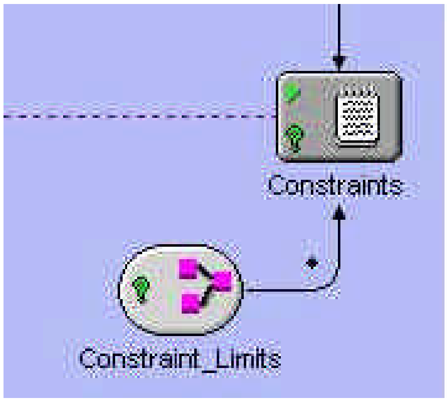

Figure C-5: The constraint calculator section of the Distributed Propulsion BWB MDO program.

The *Constraint* calculator section comprises of two components, shown in Figure C-5. The *Constraints* component receives all the pertinent calculated analysis outputs and calculates the normalized values of the constraints. These constraint values are then used to input into the optimizer. The *Constraints_Limits* serves as a repository with which the limits to the individual constraint (such as the maximum balanced field length, or minimum cabin height) can be input or changed by the user. These values will then be input into the *Constraints* component that will be included in the calculation of the constraint values.

Optimization tools

The optimization tools comprises of two components and a macro tool button. The *Optimizer* and *Converger* components deal with the optimization process while the macro tool button is used to automatically increase the value of the design variables by 1%.

The *Optimizer* component is the built in optimizer provided in ModelCenter®. It is a ModelCenter® version of the DOT tools developed by Vanderplaats R. & D. There are two common ways to perform an optimization. The first is to open the Optimization Tool window by double clicking on the *Optimizer* component. The Optimization Tool window is shown in Figure C-6. Then, by clicking on the ‘Run’ button on the lower left, the optimization will be started and a Data Collector window will be opened. The Data Collector window allows the user to visualize the optimization convergence history as the optimization is being performed. Also, it allows the user to save the iteration history of all the variables used in the model, including the design variables, objective function and constraints. Figure C-7 shows a screen-shot of the data collector. The optimization algorithm, and optimizer parameters can be changed using the ‘Options’ button in the Optimization Tool. Here, the user has the choice of three optimization algorithms: Modified Method of Feasible Direction, Linear Sequential Programming and Quadratic Sequential Programming. The default algorithm for the distributed propulsion BWB MDO program has been set to the Modified Method of Feasible Directions. The optimization parameters such as number of non-changing iterations for convergence can be changed here. The optimization tool window also allows the user to change the optimization parameters such as the objective function and constraints. To change the objective function, the user should ‘drag-and drop’ the particular variable from the Component window into the ‘Objective Definition’ field in the Optimization tool window. The same is true if the user desires to add a constraint or design variable. To delete a constraint or design variable, the user should highlight the particular variable to be deleted and press the ‘Delete’ key on the keyboard. The start value, and side constraints of the design variables can be changed by typing the values directly into the appropriate filed in the window. The same is true if the user would like to set or change the upper and lower constraint bounds.

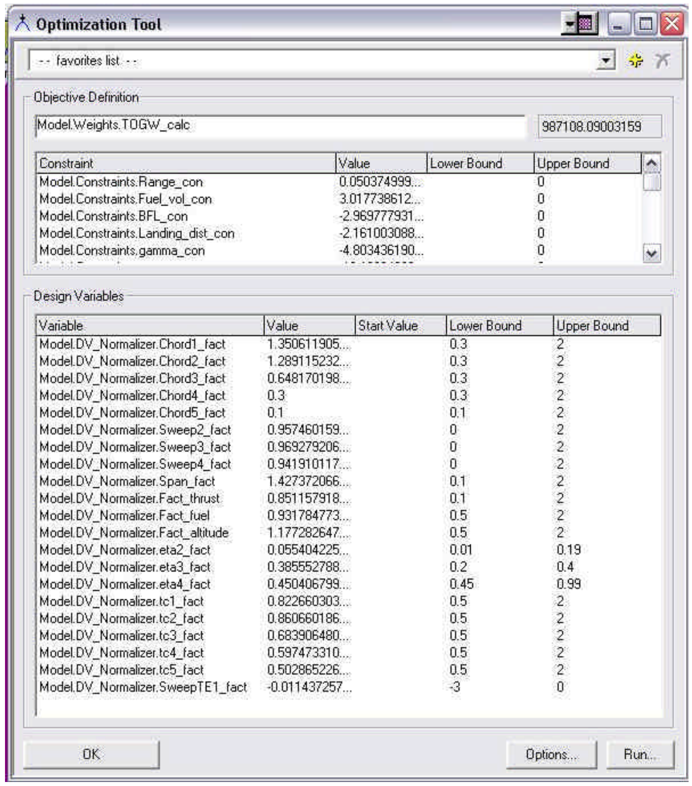

Figure C-6: The Optimization Tool window in the Distributed Propulsion BWB MDO program.

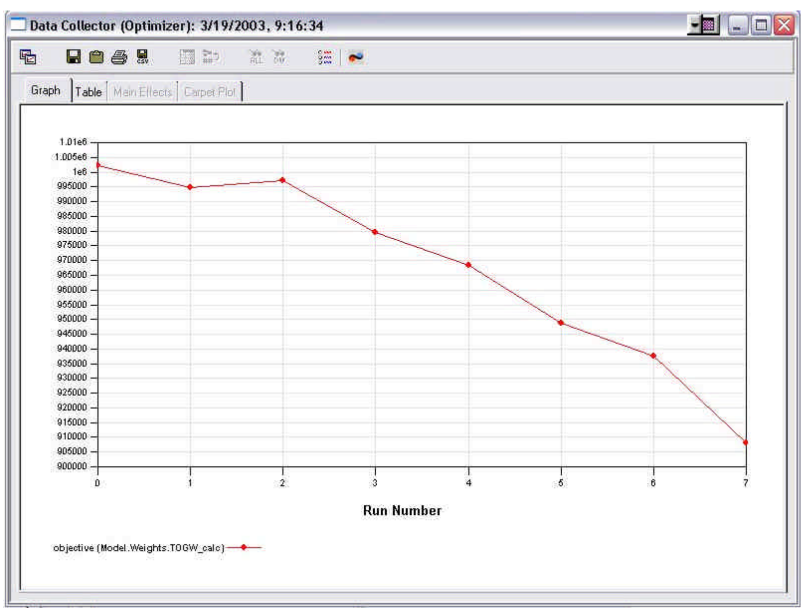

Figure C-7: The Data Collector window in the Distributed Propulsion BWB MDO program.

The other common method to perform the optimization is to click on the 'play' button on the upper left corner of the *Optimizer* component box. This performs the optimization process without showing the Optimization Tool window or the Data Collector window.

The *Converger* component is a Visual Basic script that repeats an optimization run several times until the optimum design produced by consecutive optimization runs converge within a certain objective function tolerance. This procedure is explained in Section 4.3.2.1. Currently, the tolerance (in the TOGW) between consecutive optimization solutions for the script to stop is set at 50 lbs (absolute convergence criteria).

Figure C-8: The Macro tool button in the Distributed Propulsion BWB MDO program

The macro tool button is shown in Figure C-8. Clicking on it will automatically increase all the design variable values by 1%, except for the fuel weight design variable where it will be increased by 2%. This provides the user with an easy method of increasing the design variable values, when adopting the optimization strategy of increasing the design variables and restarting the optimization. This procedure is detailed in Chapter 4 of this dissertation.

Geometry visualization modules

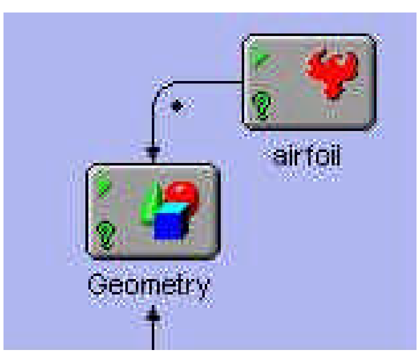

Figure C-9: The geometry visualization components in the Distributed Propulsion BWB MDO program

A screen shot of the geometry visualization modules is shown in Figure C-9. These two components, *Geometry* and *airfoil*, performs the necessary commands to generate a simplified geometry representation of the right half of the BWB aircraft. These components take advantage of the 'Geometry' function in ModelCenter® which allows the user to generate simple three-dimensional images from their models. The *Geometry* component generates the actual commands to generate the geometry image. The *airfoil* component provides baseline airfoil coordinates for use by the *Geometry* component.

Variable Data Monitor

The Variable Data Monitor is a collection of three windows that lists the values of the design variables, constraints and objective function. These values are updated during every function evaluation either during an optimization or in an analysis mode. It provides a way for the user to easily track the variables as the optimization is being performed. A screen shot of the Variable Data Monitor is given in Figure C-10.

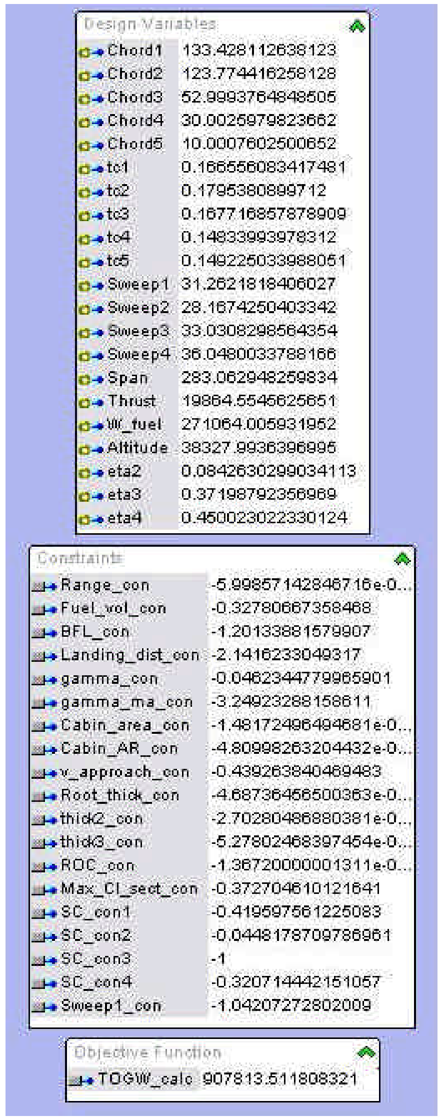

Figure C-10: The variable data monitor windows in the Distributed Propulsion BWB MDO program

Component Details

The following tables list the input and output variable details of each component in the Distributed Propulsion BWB MDO program in ModelCenter®. It will also document the links between the components. For the input variables, the 'link from' is noted, while for the output variables, the 'link to' is noted.

DV_Normalizer

Variable	Type	Description	Linked to/from
Inputs			
eta2_fact	Double	Normalized position of second span station	Optimizer
eta3_fact	Double	Normalized position of third span station	Optimizer
eta4_fact	Double	Normalized position of fourth span station	Optimizer
tc1_fact	Double	Normalized *t/c* ratio at first span station	Optimizer
tc2_fact	Double	Normalized *t/c* ratio at second span station	Optimizer
tc3_fact	Double	Normalized *t/c* ratio at third span station	Optimizer
tc4_fact	Double	Normalized *t/c* ratio at fourth span station	Optimizer
tc5_fact	Double	Normalized *t/c* ratio at fifth span station	Optimizer
Chord1_fact	Double	Normalized chord length at first span station	Optimizer
Chord2_fact	Double	Normalized chord length at second span station	Optimizer
Chord3_fact	Double	Normalized chord length at third span station	Optimizer
Chord4_fact	Double	Normalized chord length at fourth span station	Optimizer
Chord5_fact	Double	Normalized chord length at fourth span station	Optimizer
SweepTE1_fact	Double	Normalized trailing edge sweep at the first wing section	Optimizer
Sweep1_fact	Double	Normalized quarter chord sweep at the first wing section	Not used
Sweep2_fact	Double	Normalized quarter chord sweep at the second wing section	Optimizer
Sweep3_fact	Double	Normalized quarter chord sweep at the third wing section	Optimizer
Sweep4_fact	Double	Normalized quarter chord sweep at the fourth wing section	Optimizer
Span_fact	Double	Normalized aircraft span	Optimizer
Fact_thrust	Double	Normalized thrust per engine	Optimizer
Fact_fuel	Double	Normalized required fuel weight	Optimizer
Fact_altitude	Double	Normalized average cruise altitude	Optimizer

Outputs			
eta2	Double	Semi-span position of second span station	Design_Variables
eta3	Double	Semi-span position of third span station	Design_Variables
eta4	Double	Semi-span position of fourth span station	Design_Variables
tc1	Double	t/c ratio at first span station	Design_Variables
tc2	Double	t/c ratio at second span station	Design_Variables
tc3	Double	t/c ratio at third span station	Design_Variables
tc4	Double	t/c ratio at fourth span station	Design_Variables
tc5	Double	t/c ratio at fifth span station	Design_Variables
Chord1	Double	Chord length at the first span station (ft)	Design_Variables
Chord2	Double	Chord length at the second span station (ft)	Design_Variables
Chord3	Double	Chord length at the third span station (ft)	Design_Variables
Chord4	Double	Chord length at the fourth span station (ft)	Design_Variables
Chord5	Double	Chord length at the fifth span station (ft)	Design_Variables
Sweep1	Double	Quarter chord sweep at the first wing section (deg)	Design_Variables
Sweep2	Double	Quarter chord sweep at the second wing section (deg)	Design_Variables
Sweep3	Double	Quarter chord sweep at the third wing section (deg)	Design_Variables
Sweep4	Double	Quarter chord sweep at the fourth wing section (deg)	Design_Variables
Span	Double	Aircraft span (ft)	Design_Variables
Thrust	Double	Engine thrust per engine (lbs)	Design_Variables
W_fuel	Double	Required fuel weight (lbs)	Design_Variables
Altitude	Double	Average cruise altitude (ft)	Design_Variables

Design_Variables

Variable	Type	Description	Linked to
eta1	Double	Semi-span position of first span station	Geometry_parameters Weights Aerodynamics Constraints Geometry balance Fuel_Distribution jet_control

eta2	Double	Semi-span position of second span station	Geometry_parameters Weights Aerodynamics Constraints Geometry balance Fuel_Distribution jet_control
eta3	Double	Semi-span position of third span station	Geometry_parameters Weights Aerodynamics Constraints Geometry balance Fuel_Distribution jet_control
eta4	Double	Semi-span position of fourth span station	Geometry_parameters Weights Aerodynamics Constraints Geometry balance Fuel_Distribution jet_control
eta5	Double	Semi-span position of the fifth span station	Geometry_parameters Weights Aerodynamics Constraints Geometry balance Fuel_Distribution jet_control
Chord1	Double	Chord length at the first span station (ft)	Geometry_parameters Weights Aerodynamics Constraints Geometry balance Fuel_Distribution jet_control

Chord2	Double	Chord length at the second span station (ft)	Geometry_parameters Weights Aerodynamics Constraints Geometry balance Fuel_Distribution jet_control
Chord3	Double	Chord length at the third span station (ft)	Geometry_parameters Weights Aerodynamics Constraints Geometry balance Fuel_Distribution jet_control
Chord4	Double	Chord length at the fourth span station (ft)	Geometry_parameters Weights Aerodynamics Constraints Geometry balance Fuel_Distribution jet_control
Chord5	Double	Chord length at the fifth span station (ft)	Geometry_parameters Weights Aerodynamics Constraints Geometry balance Fuel_Distribution jet_control
tc1	Double	t/c ratio at first span station	Geometry_parameters Weights Aerodynamics Geometry Fuel_Distribution

tc2	Double	t/c ratio at second span station	Geometry_parameters Weights Aerodynamics Geometry Fuel_Distribution
tc3	Double	t/c ratio at third span station	Geometry_parameters Weights Aerodynamics Geometry Fuel_Distribution
tc4	Double	t/c ratio at fourth span station	Geometry_parameters Weights Aerodynamics Geometry Fuel_Distribution
tc5	Double	t/c ratio at fifth span station	Geometry_parameters Weights Aerodynamics Geometry Fuel_Distribution
Sweep1	Double	Quarter chord sweep at the first wing section (deg)	Geometry_parameters Weights Aerodynamics Constraints Geometry balance Fuel_Distribution jet_control
Sweep2	Double	Quarter chord sweep at the second wing section (deg)	Geometry_parameters Weights Aerodynamics Constraints Geometry balance Fuel_Distribution jet_control

Sweep3	Double	Quarter chord sweep at the third wing section (deg)	Geometry_parameters Weights Aerodynamics Constraints Geometry balance Fuel_Distribution jet_control
Sweep4	Double	Quarter chord sweep at the fourth wing section (deg)	Geometry_parameters Weights Aerodynamics Constraints Geometry balance Fuel_Distribution jet_control
Span	Double	Aircraft span (ft)	Geometry_parameters Weights Aerodynamics Constraints Geometry balance Fuel_Distribution jet_control
Thrust	Double	Engine thrust per engine (lbs)	Aerodynamics Engines Distributed_propulsion
W_fuel	Double	Required fuel weight (lbs)	Weights Aerodynamics Performance Field balance Fuel_Distribution CG_limit_calculator_ Conv jet_control Constraints
Altitude	Double	Average cruise altitude (ft)	Aerodynamics Performance Engines SFC

Parameters

Variable	Type	Description	Linked to
npass	Integer	Number of passengers	Weights
neng	Integer	Number of engines	Weights Aerodynamics Performance Field Distributed_Propulsion
n	Double	Ultimate load factor	Weights
Mach	Double	Design Mach number	Aerodynamics Performance Engines SFC
laminar_tf	Double	Laminar flow technology factor	Aerodynamics
airfoil_tf	Double	Airfoil technology factor (0.87 for NACA 6-series, 0.95 for a supercritical section	Aerodynamics
Clmax_to	Double	Maximum lift coefficient at take-off	Aerodynamics Field
Cl_max	Double	Maximum cruise lift coefficient	Aerodynamics
Reserve_Range	Double	Reserve range (nmi)	Performance
v_loss_factor	Double	Volume loss factor in fuel tanks	Fuel_Distribution
Fuel_density	Double	Fuel density (lbs/gal)	Fuel_Distribution
to_alt	Double	Takeoff altitude (ft)	Field
mu_brk	Double	Landing braking fricion coefficient	Field
temp_grd	Double	Ground temperature at takeoff (°F)	Field
cd_gear	Double	Drag coefficient for a nominal landing gear	Field
sref_gear	Double	Surface area for a nominal landing gear (ft^2)	Field
wldg_factor	Double	Landing weight/TOGW ratio	Field
v2_factor	Double	Second segment climb velocity factor	Field
hto	Double	Height of obstacle at take-off (ft)	Field
h_ldg	Double	Height of obstacle at landing (ft)	Field
Transition1	Double	Transition location on the first wing section (x/c), negative value implies internally calculated	Aerodynamics
Transition2	Double	Transition location on the second wing section (x/c), negative value implies internally calculated	Aerodynamics

Transition3	Double	Transition location on the third wing section (x/c), negative value implies internally calculated	Aerodynamics
Transition4	Double	Transition location on the fourth wing section (x/c), negative value implies internally calculated	Aerodynamics
de_max	Double	Maximum elevon deflection angle (deg)	CG_limit_calculator_Conv jet_control
alpha_max	Double	Maximum angle of attack (deg)	CG_limit_calculator_Conv jet_control
q_SL	Double	Dynamic pressure at sea level (slug/(ft s^2))	CG_limit_calculator_Conv Cj_calculator jet_control
SFC_static	Double	Static engine specific fuel consumption (lb/hr/lb)	Engines SFC
Flap1	Double	Ratio of the flap chord to the wing chord in the first wing section	Geometry_parameters JKayVLM
Flap2	Double	Ratio of the flap chord to the wing chord in the second wing section	Geometry_parameters JKayVLM
Flap3	Double	Ratio of the flap chord to the wing chord in the third wing section	Geometry_parameters JKayVLM
Flap4	Double	Ratio of the flap chord to the wing chord in the fourth wing section	Geoemtery_parameters JKayVLM
Eng_pos1	Double	Semi-spanwise position of the first engine	Weights
Eng_pos2	Double	Semi-spanwise position of the second engine	Weights
Eng_pos3	Double	Semi-spanwise position of the third engine	Weights
Eng_pos4	Double	Semi-spanwise position of the fourth engine	Weights
Dist_prop_flag	Integer	Distributed propulsion configuration selector (0 = conventional BWB design, 1 = distributed propulsion BWB design)	Aerodynamics Engines CG_limit_selector Distributed_Propulsion
dist_prop_factor	Double	Percentage of savings in propulsive efficiency due to ‘filling in the wake’	Converger Distributed_Propulsion
cbar	Double	The reference chord used to calculate the control performance for a distributed propulsion system	jet_control
Xgap	Double	The distance between the reference axis to the leading edge of the wing (used for the control performance calculation for a distributed propulsion system)	jet_control

Duct_efficiency	Double	Duct efficiency in the distributed propulsion system	Converger Distributed_propulsion
Duct_weight_factor	Double	Duct weight factor applied to the propulsion weight to account for the duct weight	Weights

Geometry_parameters

Variable	Type	Description	Linked to/from
Inputs			
Flap1	Double	Ratio of the flap chord to the wing chord in the first wing section	Parameters
Flap2	Double	Ratio of the flap chord to the wing chord in the second wing section	Parameters
Flap3	Double	Ratio of the flap chord to the wing chord in the third wing section	Parameters
Flap4	Double	Ratio of the flap chord to the wing chord in the fourth wing section	Parameters
eta(5)	Array double	Array of semi-spanwise position of the span stations	Design_Variables
Chord(5)	Array double	Array of chord lengths of the span stations (ft)	Design_Variables
Span	Double	Aircraft span (ft)	Design_Variables
tc(5)	Array double	Array of *t/c* ratio of the span stations (ft)	Design_Variables
Sweep(4)	Array double	Array of quarter chord sweeps at the wing span stations (deg)	Design_Variables
deck_factor	Integer	Number of passenger decks in the passenger cabin in the first wing section	
Outputs			
Sref	Double	Reference planform area (ft^2)	Weights Aerodynamics Performance JKayVLM CG_limit_calculator_Conv Cj_calculator jet_control
AR	Double	Aspect ratio	Aerodynamics Field jet_control
Root_thick	Double	Passenger cabin height at the first span station (ft)	Constraints
thick2	Double	Passenger cabin height at the second span station (ft)	Constraints

thick3	Double	Passenger cabin height at the third span station (ft)	Constraints
Scabin	Double	Passenger cabin deck area (ft^2)	Constraints
flapr	Double	Ratio of the flap area to the planform area	Weights
TE1	Double	Trailing edge sweep angle at the first wing section (deg)	

Converger

Variable	Type	Description	Linked to/from
Inputs			
dist_prop_factor	Double	Percentage of savings in propulsive efficiency due to 'filling in the wake'	Parameters
duct_efficiency	Double	Duct efficiency in the distributed propulsion system	Parameters
Outputs			
TOGW1	Double	TOGW of the last third optimization run	
TOGW2	Double	TOGW of the last second optimization run	
TOGW3	Double	TOGW of the last optimization run	
index	Integer	Number of optimization runs performed	

Geometry

Variable	Type	Description	Linked to/from
Inputs			
eta1	Double	Semi-span position of first span station	Design_Variables
eta2	Double	Semi-span position of second span station	Design_Variables
eta3	Double	Semi-span position of third span station	Design_Variables
eta4	Double	Semi-span position of fourth span station	Design_Variables
eta5	Double	Semi-span position of the fifth span station	Design_Variables
Chord1	Double	Chord length at the first span station (ft)	Design_Variables
Chord2	Double	Chord length at the second span station (ft)	Design_Variables
Chord3	Double	Chord length at the third span station (ft)	Design_Variables
Chord4	Double	Chord length at the fourth span station (ft)	Design_Variables
Chord5	Double	Chord length at the fifth span station (ft)	Design_Variables
tc1	Double	t/c ratio at first span station	Design_Variables
tc2	Double	t/c ratio at second span station	Design_Variables
tc3	Double	t/c ratio at third span station	Design_Variables
tc4	Double	t/c ratio at fourth span station	Design_Variables
tc5	Double	t/c ratio at fifth span station	Design_Variables

Sweep1	Double	Quarter chord sweep at the first wing section (deg)	Design_Variables
Sweep2	Double	Quarter chord sweep at the second wing section (deg)	Design_Variables
Sweep3	Double	Quarter chord sweep at the third wing section (deg)	Design_Variables
Sweep4	Double	Quarter chord sweep at the fourth wing section (deg)	Design_Variables
Span	Double	Aircraft span (ft)	Design_Variables
x(80)	Array Double	X-coordinate array of airfoil coordinates	Airfoil
y(80)	Array Double	Y-coordinate array of airfoil coordinates	Airfoil
Outputs			
geom	Text	Instruction file for geometry tool	

Airfoil

Variable	Type	Description	Linked to/from
Outputs			
No_points	Integer	Number of airfoil coordinates	
tc_nom	Double	t/c ratio of reference airfoil	
x[80]	Double	X-coordinate array of airfoil coordinates	Geometry
y[80]	Double	Y-coordinate array of airfoil coordinates	Geometry

SFC

Variable	Type	Description	Linked to/from
Inputs			
sfc_static	Double	Static engine specific fuel consumption (lb/hr/lb)	Parameters
Mach	Double	Cruise Mach number	Parameters
Altitude	Double	Average cruise altitude (ft)	Design_Variables
Outputs			
SFC	Double	Specific fuel consumption (lb/hr/lb)	Distributed_Propulsion

Distributed Propulsion

Variable	Type	Description	Linked to/from
Inputs			
dist_prop_flag	Integer	Distributed propulsion configuration selector (0 = conventional BWB design, 1 = distributed propulsion BWB design)	Parameters
dist_prop_fact	Double	Percentage of savings in propulsive efficiency due to ‘filling in the wake’	Parameters

duct_efficiency	Double	Duct efficiency in the distributed propulsion system	Parameters
Thrust	Double	Engine thrust per engine (lbs)	Design_Variables
neng	Integer	Number of engines	Parameters
sfc	Double	Specific fuel consumption (lb/hr/lb)	SFC
Outputs			
Tuseful	Double	Thrust per engine corrected for duct losses (distributed propulsion configuration only)	Weights Performance Field
sfc_new	Double	Specific fuel consumption corrected for distributed propulsion (lb/hr/lb)	Performance
Jet	Double	Distributed propulsion jet thrust (lbs)	Control_constraints Aerodynamics (scripted)

Engines

Variable	Type	Description	Linked to/from
Inputs			
Thrust	Double	Engine thrust per engine (lbs)	Design_Variables
Mach	Double	Cruise Mach number	Parameters
Altitude	Double	Average cruise altitude (ft)	Design_Variables
sfc_static	Double	Static engine specific fuel consumption (lb/hr/lb)	Parameters
dist_prop_flag	Integer	Distributed propulsion configuration selector (0 = conventional BWB design, 1 = distributed propulsion BWB design)	Parameters
Outputs			
Wpropulsion		Propulsion weight per engine (lbs)	Weights balance
SFC		Specific fuel consumption (lb/hr/lb)	Not Used

Weights

Variable	Type	Description	Linked to/from
Inputs			
npass	Integer	Number of passengers	Parameters
neng	Integer	Number of engines	Parameters
Chord(5)	Array Double	Array of chord lengths of the span stations (ft)	Design_Variables
eta(5)	Array Double	Array of semi-spanwise position of the span stations	Design_Variables

tc(5)	Array Double	Array of *t/c* ratio of the span stations (ft)	Design_Variables
Sweep(4)	Array Double	Array of quarter chord sweeps at the wing span stations (deg)	Design_Variables
Eng_pos(4)	Array Double	Array of engine position as a function of semi-span	Parameters
Span	Double	Aircraft span (ft)	Design_Variables
Area	Double	Aircraft planform area (ft^2)	Geometry_parameters
n	Double	Ultimate load factor	Parameters
Thrust	Double	Engine thrust per engine (lbs)	Distributed_Propulsion
W_fuel	Double	Required fuel weight (lbs)	Design_Variables
TOGW_in	Double	TOGW first guess (lbs)	TOGW_input
Wpropulsion	Double	Propulsion weight per engine (lbs)	Engines
flapr	Double	Flap ratio	Geometry_parameters
Duct_weight_factor	Double	Duct weight factor applied to the propulsion weight to account for the duct weight	Parameters
Outputs			
MEW	Double	Manufacturer's Empty Weight (lbs)	
OEW	Double	Operational Empty Weight (lbs)	Control_constraints
WZF	Double	Zero Fuel Weight (lbs)	balance Control_constraints
TOGW_calc	Double	Calculated Takeoff Gross Weight (lbs)	Aerodynamics TOGW_input Performance Field Optimizer
Cabin_area	Double	Passenger cabin deck area (ft^2)	Not Used
Wing_weight	Double	Wing weight (lbs)	balance
Cabin_weight	Double	Passenger cabin weight (lbs)	balance
Afterbody_weight	Double	Afterbody weight (lbs)	balance
AI_weight	Double	Anti-Icing weight (lbs)	balance
Pneumatics_weight	Double	Pneumatics_weight (lbs)	balance
Aux_pwr_weight	Double	Auxiliary power weight (lbs)	balance
Electrical_weight	Double	Electrical weight (lbs)	balance
AC_weight	Double	Air-conditioning weight (lbs)	balance
Furnishing_weight	Double	Furnishing weight (lbs)	balance
Avionics_weight	Double	Avionics weight (lbs)	balance
Instruments_weight	Double	Instruments weight (lbs)	balance
Controls_weight	Double	Controls weight (lbs)	balance
Payload_weight	Double	Payload weight (lbs)	balance

LG_weight	Double	Landing gear weight (lbs)	balance
STATUS	Integer	TOGW convergence status indicator (1=TOGW calculation converged, 0=TOGW not found)	

TOGW_input

Variable	Type	Description	Linked to/from
Inputs			
TOGW_calc	Double	Calculated Takeoff Gross Weight (lbs)	Weights
Outputs			
TOGW_in	Double	TOGW first guess (lbs)	Weights

Aerodynamics

Variable	Type	Description	Linked to/from
Inputs			
eta(5)	Array Double	Array of semi-spanwise position of the span stations	Design_Variables
Chord(5)	Array Double	Array of chord lengths of the span stations (ft)	Design_Variables
tc(5)	Array Double	Array of *t/c* ratio of the span stations (ft)	Design_Variables
Sweep(4)	Array Double	Array of quarter chord sweeps at the wing span stations (deg)	Design_Variables
Span	Double	Aircraft span (ft)	Design_Variables
neng	Integer	Number of engines	Parameters
Altitude	Double	Average cruise altitude (ft)	Design_Variables
W_fuel	Double	Required fuel weight (lbs)	Design_Variables
Mach	Double	Cruise Mach number	Parameters
laminar_tf	Double	Laminar flow technology factor	Parameters
airfoil_tf	Double	Airfoil technology factor (0.87 for NACA 6-series, 0.95 for a supercritical section	Parameters
clmax_to	Double	Maximum lift coefficient at take-off	Parameters
Cl_max	Double	Maximum cruise lift coefficient	Parameters
cm_design	Double	Design moment coefficient	Design_Variables
Dist_prop_flag	Integer	Distributed propulsion configuration selector (0 = conventional BWB design, 1 = distributed propulsion BWB design)	Parameters
AR	Double	Aspect ratio	Geometry_parameters
re_trans_nacelle	Double	Nacelle transition Reynolds number	

Thrust	Double	Engine thrust per engine (lbs)	Design_Variables
Jet	Double	Distributed propulsion jet thrust	
engine_expose_fact	Double	Fraction of nacelle surface area exposed to the airflow	
Sref	Double	Reference planform area (ft^2)	Geometry_parameters
TOGW	Double	Takeoff Gross Weight (lbs)	Weights
Transition_loc(4)	Array Double	Array of transition locations for the wing sections	Parameters
Outputs			
Cl_TOGW	Double	Lift coefficient at TOGW configuration	
Cl_cruise	Double	Lift coefficient at cruise condition	Performance
Cl_climb	Double	Lift coefficient at climb condition	
Cl_ma	Double	Lift configuration at missed approach condition	
Cl_landing	Double	Lift configuration at landing condition	
Cd_TOGW	Double	Drag coefficient at TOGW configuration	
Cd_cruise	Double	Drag coefficient at cruise condition	
Cd_climb	Double	Drag coefficient at climb condition	Field
Cd_ma	Double	Drag coefficient at missed approach condition	Field
Cd_landing	Double	Drag coefficient at landing condition	Field
LD_TOGW	Double	Lift to drag ratio at TOGW configuration	
LD_cruise	Double	Lift to drag ratio at cruise condition	Performance
LD_climb	Double	Lift to drag ratio at climb condition	
LD_ma	Double	Lift to drag ratio at missed approach condition	
LD_landing	Double	Lift to drag ratio at landing condition	
Cl_sect_max	Double	Maximum sectional lift coefficient	Constraints
Induced_drag	Double	Induced drag coefficient at cruise condition	
Friction_drag	Double	Friction drag coefficient at cruise condition	
Wave_drag	Double	Wave drag coefficient at cruise condition	
X1(4)	Array Double	X-coordinates for first wing section to input into JKayVLM	JKayVLM
Y1(4)	Array Double	Y-coordinates for first wing section to input into JKayVLM	JKayVLM
Z1(4)	Array Double	Z-coordinates for first wing section to input into JKayVLM	JKayVLM
X2(4)	Array Double	X-coordinates for second wing section to input into JKayVLM	JKayVLM
Y2(4)	Array Double	Y-coordinates for second wing section to input into JKayVLM	JKayVLM
Z2(4)	Array Double	Z-coordinates for second wing section to input into JKayVLM	JKayVLM
X3(4)	Array Double	X-coordinates for third wing section to input into JKayVLM	JKayVLM

Y3(4)	Array Double	Y-coordinates for third wing section to input into JKayVLM	JKayVLM
Z3(4)	Array Double	Z-coordinates for third wing section to input into JKayVLM	JKayVLM
X4(4)	Array Double	X-coordinates for fourth wing section to input into JKayVLM	JKayVLM
Y4(4)	Array Double	Y-coordinates for fourth wing section to input into JKayVLM	JKayVLM
Z4(4)	Array Double	Z-coordinates for fourth wing section to input into JKayVLM	JKayVLM
X5(4)	Array Double	X-coordinates for fifth wing section to input into JKayVLM	JKayVLM
Y5(4)	Array Double	Y-coordinates for fifth wing section to input into JKayVLM	JKayVLM
Z5(4)	Array Double	Z-coordinates for fifth wing section to input into JKayVLM	JKayVLM

JKayVLM

Variable	Type	Description	Linked to/from
Inputs			
Mach_control	Double	Mach number at control constraint calculation condition	
Area	Double	Reference planform area (ft^2)	Geometry_parameters
Span	Double	Aircraft span (ft)	Design_Variables
Sections	Integer	Number of wing sections	
X1(4)	Array Double	X-coordinates for first wing section	Aerodynamics
Y1(4)	Array Double	Y-coordinates for first wing section	Aerodynamics
Z1(4)	Array Double	Z-coordinates for first wing section	Aerodynamics
X2(4)	Array Double	X-coordinates for second wing section	Aerodynamics
Y2(4)	Array Double	Y-coordinates for second wing section	Aerodynamics
Z2(4)	Array Double	Z-coordinates for second wing section	Aerodynamics
X3(4)	Array Double	X-coordinates for third wing section	Aerodynamics
Y3(4)	Array Double	Y-coordinates for third wing section	Aerodynamics
Z3(4)	Array Double	Z-coordinates for third wing section	Aerodynamics

X4(4)	Array Double	X-coordinates for fourth wing section	Aerodynamics
Y4(4)	Array Double	Y-coordinates for fourth wing section	Aerodynamics
Z4(4)	Array Double	Z-coordinates for fourth wing section	Aerodynamics
X5(4)	Array Double	X-coordinates for fifth wing section	Aerodynamics
Y5(4)	Array Double	Y-coordinates for fifth wing section	Aerodynamics
Z5(4)	Array Double	Z-coordinates for fifth wing section	Aerodynamics
Flap1	Double	Percent chord position of flap hinge line from the trailing edge for the first wing section	Parameters
Flap2	Double	Percent chord position of flap hinge line from the trailing edge for the second wing section	Parameters
Flap3	Double	Percent chord position of flap hinge line from the trailing edge for the third wing section	Parameters
Flap4	Double	Percent chord position of flap hinge line from the trailing edge for the fourth wing section	Parameters
Outputs			
CL0	Double	Zero angle of attack lift coefficient	CG_limit_calculator_Conv
Cm0	Double	Zero angle of attack moment coefficient	CG_limit_calculator_Conv
Cl_alpha	Double	Lift coefficient curve slope wrt. angle of attack (rad^{-1})	CG_limit_calculator_Conv jet_control
Cm_alpha	Double	Moment coefficient curve slope wrt. angle of attack (rad^{-1})	CG_limit_calculator_Conv jet_control
Neg_neutral_pt	Double	The negative of the neutral point location	
CL_delta2	Double	Lift coefficient curve slope wrt. second wing section flap angle (rad^{-1})	CG_limit_calculator_Conv
Cm_delta2	Double	Moment coefficient curve slope wrt. second wing section flap angle (rad^{-1})	CG_limit_calculator_Conv
CL_delta3	Double	Lift coefficient curve slope wrt. third wing section flap angle (rad^{-1})	CG_limit_calculator_Conv
Cm_delta3	Double	Moment coefficient curve slope wrt. third wing section flap angle (rad^{-1})	CG_limit_calculator_Conv

Fuel_Distribution

Variable	Type	Description	Linked to/from
Inputs			
eta(5)	Array Double	Array of semi-spanwise position of the span stations	Design_Variables

Chord(5)	Array Double	Array of chord lengths of the span stations (ft)	Design_Variables
tc(5)	Array Double	Array of *t/c* ratio of the span stations (ft)	Design_Variables
Sweep(4)	Array Double	Array of quarter chord sweeps at the wing span stations (deg)	Design_Variables
Span	Double	Aircraft span (ft)	Design_Variables
v_loss_factor	Double	Volume loss factor in fuel tanks	Parameters
Fuel_density	Double	Fuel density (lbs/gal)	Parameters
Fuel_weight	Double	Required fuel weight (lbs)	Design_Variables
Outputs			
Tank_cap	Double	Fuel tank capacity (lbs)	Constraints
CG_fuel_in	Double	CG location of fuel when shifted inboard	balance
CG_fuel_out	Double	CG location of fuel when shifted outboard	balance

Balance

Variable	Type	Description	Linked to/from
Inputs			
eta(5)	Array Double	Array of semi-spanwise position of the span stations	Design_Variables
Chord(5)	Array Double	Array of chord lengths of the span stations (ft)	Design_Variables
Sweep(4)	Array Double	Array of quarter chord sweeps at the wing span stations (deg)	Design_Variables
Span	Double	Aircraft span (ft)	Design_Variables
Wing_weight	Double	Wing weight (lbs)	Weights
Cabin_weight	Double	Passenger cabin weight (lbs)	Weights
Afterbody_weight	Double	Afterbody weight (lbs)	Weights
AI_weight	Double	Anti-Icing weight (lbs)	Weights
Pneumatics_weight	Double	Pneumatics_weight (lbs)	Weights
Aux_weight	Double	Auxiliary power weight (lbs)	Weights
Electric_weight	Double	Electrical weight (lbs)	Weights
AC_weight	Double	Air-conditioning weight (lbs)	Weights
Furnishing_weight	Double	Furnishing weight (lbs)	Weights
Avionics_weight	Double	Avionics weight (lbs)	Weights
Instrument_weight	Double	Instruments weight (lbs)	Weights
Control_weight	Double	Controls weight (lbs)	Weights
Payload_weight	Double	Payload weight (lbs)	Weights
Prop_weight	Double	Propulsion weight per engine (lbs)	Engines

LG_weight	Double	Landing gear weight (lbs)	Weights
WZF	Double	Zero fuel weight (lbs)	Weights
Fuel_weight	Double	Required fuel weight (lbs)	Design_Variables
CG_fuel_in	Double	CG location of fuel when shifted inboard	Fuel_Distribution
CG_fuel_out	Double	CG location of fuel when shifted outboard	Fuel_Distribution
Outputs			
CG_nopay_fuel_in	Double	Aircraft CG when fuel is shifted inboard without any payload	CG_constraints
CG_nopay_fuel_out	Double	Aircraft CG when fuel is shifted outboard without any payload	CG_constraints
CG_TOGW_fuel_in	Double	Aircraft CG when fuel is shifted inboard at TOGW condition	CG_constraints
CG_TOGW_fuel_out	Double	Aircraft CG when fuel is shifted outboard at TOGW condition	CG_constraints

Field

Variable	Type	Description	Linked to/from
Inputs			
Span	Double	Aircraft span (ft)	Design_Variables
W_fuel	Double	Required fuel weight (lbs)	Design_Variables
Thrust	Double	Engine thrust per engine (lbs)	Distributed_Propulsion
neng	Integer	Number of engines	Parameters
to_alt	Double	Takeoff altitude (ft)	Parameters
mu_brk	Double	Landing braking fricion coefficient	Parameters
temp_grd	Double	Ground temperature at takeoff (°F)	Parameters
cd_gear	Double	Drag coefficient for a nominal landing gear	Parameters
sref_gear	Double	Surface area for a nominal landing gear (ft^2)	Parameters
wldg_factor	Double	Landing weight/TOGW ratio	Parameters
V2_factor	Double	Second segment climb velocity factor	Parameters
hto	Double	Height of obstacle at take-off (ft)	Parameters
Cl_maxto	Double	Height of obstacle at landing (ft)	Parameters
Cl_max	Double	Maximum cruise lift coefficient	Aerodynamics
h_ldg	Double	Height of obstacle at landing (ft)	Parameters
TOGW	Double	Takeoff gross weight (lbs)	Weights
Sref	Double	Reference planform area (ft^2)	Aerodynamics
AR	Double	Aspect ratio	Geometry_parameters
cd_climb	Double	Drag coefficient at climb condition	Aerodynamics
cd_ma	Double	Drag coefficient at missed approach condition	Aerodynamics
cd_grd	Double	Ground drag coefficient	Aerodynamics

Outputs			
BFL	Double	Balanced Field Length (ft)	Constraints
v_approach	Double	Approach velocity (knots)	Constraints
Landing_dist	Double	Landing distance (ft)	Constraints
v2	Double	Second segment velocity (ft/s)	
gamma	Double	Second segment climb gradient	Constraints
gamma_ma	Double	Missed approach climb gradient	Constraints

Performance

Variable	Type	Description	Linked to/from
Inputs			
W_fuel	Double	Required fuel weight (lbs)	Design_Variables
Reserve_range	Double	Reserve range (nmi)	Parameters
Altitude	Double	Average cruise altitude (ft)	Design_Variables
Mach	Double	Cruise Mach number	Parameters
Cl_cruise	Double	Lift coefficient at cruise condition	Aerodynamics
Sref	Double	Reference planform area (ft^2)	Geometry_parameters
Thrust	Double	Engine thrust per engine (lbs)	Distributed_Propulsion
neng	Integer	Number of engines	Parameters
SFC	Double	Specific fuel consumption (lb/hr/lb)	Distributed_Propulsion
LD_cruise	Double	Lift to drag ratio at cruise condition	Aerodynamics
TOGW	Double	Takeoff gross weight (lbs)	Weights
Outputs			
Range_calc	Double	Calculated Range	Constraints
ROC	Double	Top of climb rate of climb	Constraints

Cj_calculator

Variable	Type	Description	Linked to/from
Inputs			
Jet	Double	Distributed propulsion jet thrust (lbs)	Distributed_Propulsion
q_SL	Double	Dynamic pressure at sea level (slug/(ft s^2))	Parameters
Sref	Double	Reference planform area (ft^2)	Geometry_parameters
Outputs			
Cj	Double	Distributed propulsion jet coefficient	jet_control

Jet_control

Variable	Type	Description	Linked to/from
Inputs			
Cj	Double	Distributed propulsion jet coefficient	Cj_calculator
Chord(5)	Array Double	Array of chord lengths of the span stations (ft)	Design_Variables
Sweep(4)	Array Double	Array of quarter chord sweeps at the wing span stations (deg)	Design_Variables
eta(5)	Array Double	Array of semi-spanwise position of the span stations	Design_Variables
Span	Double	Aircraft span (ft)	Design_Variables
Sref	Double	Reference planform area (ft^2)	Geometry_parameters
AR	Double	Aspect ratio	
cbar	Double	The reference chord used to calculate the control performance for a distributed propulsion system	Parameters
Xgap	Double	The distance between the reference axis to the leading edge of the wing (used for the control performance calculation for a distributed propulsion system)	Parameters
q	Double	Dynamic pressure at sea level (slug/(ft s^2))	Parameters
de_max	Double	Maximum jet deflection angle (deg)	Parameters
alpha_max	Double	Maximum angle of attack (deg)	Parameters
CL_VLM	Double	Lift coefficient curve slope wrt. angle of attack (rad^{-1})	JKayVLM
Cm_VLM	Double	Moment coefficient curve slope wrt. angle of attack (rad^{-1})	JKayVLM
OEW	Double	Operational empty weight (lbs)	Weights
W_fuel	Double	Fuel weight (lbs)	Design_Variables
WZF	Double	Zero fuel weight (lbs)	Weights
Outputs			
XCG_OEW_Cond1A	Double	Aft CG limit at OEW for full jet deflection down	CG_limit_selector
XCG_OEW_Cond1B	Double	Forward CG limit at OEW for full jet deflection up	CG_limit_selector
XCG_OEW_Cond2	Double	Forward CG limit at OEW at maximum angle of attack	CG_limit_selector
XCG_OEWfuel_Cond1A	Double	Aft CG limit at OEW + Fuel weight for full jet deflection down	CG_limit_selector
XCG_OEWfuel_Cond1B	Double	Forward CG limit at OEW + Fuel weight for full jet deflection up	CG_limit_selector

XCG_OEWfuel_Cond2	Double	Forward CG limit at OEW + Fuel weight at maximum angle of attack	CG_limit_selector
XCG_WZF_Cond1A	Double	Aft CG limit at WZF for full jet deflection down	CG_limit_selector
XCG_WZF_Cond1B	Double	Forward CG limit at WZF for full jet deflection up	CG_limit_selector
XCG_WZF_Cond2	Double	Forward CG limit at WZF at maximum angle of attack	CG_limit_selector
XCG_TOGW_Cond1A	Double	Aft CG limit at TOGW for full jet deflection down	CG_limit_selector
XCG_TOGW_Cond1B	Double	Forward CG limit at TOGW for full jet deflection up	CG_limit_selector
XCG_TOGW_Cond2	Double	Forward CG limit at TOGW at maximum angle of attack	CG_limit_selector

CG_limit_calculator_Conv

Variable	Type	Description	Linked to/from
Inputs			
OEW	Double	Operational empty weight (lbs)	Weights
WZF	Double	Zero fuel weight (lbs)	Weights
W_fuel	Double	Required fuel weight (lbs)	Design_Variables
q	Double	Dynamic pressure at sea level (slug/(ft s^2))	Parameters
S	Double	Reference planform area (ft^2)	Geometry_parameters
Cm0	Double	Zero angle of attack moment coefficient	JKayVLM
Cm_alpha	Double	Moment coefficient curve slope wrt. angle of attack (rad^{-1})	JKayVLM
CL0	Double	Zero angle of attack lift coefficient	JKayVLM
CL_alpha	Double	Lift coefficient curve slope wrt. angle of attack (rad^{-1})	JKayVLM
de_max	Double	Maximum elevon deflection angle (deg)	Parameters
alpha_max	Double	Maximum angle of attack (deg)	Parameters
CL_delta2	Double	Lift coefficient curve slope wrt. second wing section flap angle (rad^{-1})	JKayVLM
CL_delta3	Double	Lift coefficient curve slope wrt. third wing section flap angle (rad^{-1})	JKayVLM
Cm_delta2	Double	Moment coefficient curve slope wrt. second wing section flap angle (rad^{-1})	JKayVLM
Cm_delta3	Double	Moment coefficient curve slope wrt. third wing section flap angle (rad^{-1})	JKayVLM
Outputs			
CG_OEW_Cond1A	Double	Aft CG limit at OEW for full elevon deflection down	CG_limit_selector

CG_OEW_Cond1B	Double	Forward CG limit at OEW for full elevon deflection up	CG_limit_selector
CG_OEW_Cond2	Double	Forward CG limit at OEW at maximum angle of attack	CG_limit_selector
CG_OEWfuel_Cond1A	Double	Aft CG limit at OEW + Fuel weight for full elevon deflection down	CG_limit_selector
CG_OEWfuel_Cond1B	Double	Forward CG limit at OEW + Fuel weight for full elevon deflection up	CG_limit_selector
CG_OEWfuel_Cond2	Double	Forward CG limit at OEW + Fuel weight at maximum angle of attack	CG_limit_selector
CG_WZF_Cond1A	Double	Aft CG limit at WZF for full elevon deflection down	CG_limit_selector
CG_WZF_Cond1B	Double	Forward CG limit at WZF for full elevon deflection up	CG_limit_selector
CG_WZF_Cond2	Double	Forward CG limit at WZF at maximum angle of attack	CG_limit_selector
CG_TOGW_Cond1A	Double	Aft CG limit at TOGW for full elevon deflection down	CG_limit_selector
CG_TOGW_Cond1B	Double	Forward CG limit at TOGW for full elevon deflection up	CG_limit_selector
CG_TOGW_Cond2	Double	Forward CG limit at TOGW at maximum angle of attack	CG_limit_selector

CG_limit_selector

Variable	Type	Description	Linked to/from
Inputs			
dist_prop_flag	Integer	Distributed propulsion configuration selector (0 = conventional BWB design, 1 = distributed propulsion BWB design)	Parameters
CG_OEW_Cond1A_Conv	Double	Aft CG limit at OEW for full elevon deflection down (Conventional BWB configuration)	CG_limit_calculator_Conv
CG_OEW_Cond1B_Conv	Double	Forward CG limit at OEW for full elevon deflection up (Conventional BWB configuration)	CG_limit_calculator_Conv
CG_OEW_Cond2_Conv	Double	Forward CG limit at OEW at maximum angle of attack (Conventional BWB configuration)	CG_limit_calculator_Conv

CG_OEWfuel_Cond1A_Conv	Double	Aft CG limit at OEW + Fuel weight for full elevon deflection down (Conventional BWB configuration)	CG_limit_calculator_Conv
CG_OEWfuel_Cond1B_Conv	Double	Forward CG limit at OEW + Fuel weight for full elevon deflection up (Conventional BWB configuration)	CG_limit_calculator_Conv
CG_OEWfuel_Cond2_Conv	Double	Forward CG limit at OEW + Fuel weight at maximum angle of attack (Conventional BWB configuration)	CG_limit_calculator_Conv
CG_WZF_Cond1A_Conv	Double	Aft CG limit at WZF for full elevon deflection down (Conventional BWB configuration)	CG_limit_calculator_Conv
CG_WZF_Cond1B_Conv	Double	Forward CG limit at WZF for full elevon deflection up (Conventional BWB configuration)	CG_limit_calculator_Conv
CG_WZF_Cond2_Conv	Double	Forward CG limit at WZF at maximum angle of attack (Conventional BWB configuration)	CG_limit_calculator_Conv
CG_TOGW_Cond1A_Conv	Double	Aft CG limit at TOGW for full elevon deflection down (Conventional BWB configuration)	CG_limit_calculator_Conv
CG_TOGW_Cond1B_Conv	Double	Forward CG limit at TOGW for full elevon deflection up (Conventional BWB configuration)	CG_limit_calculator_Conv
CG_TOGW_Cond2_Conv	Double	Forward CG limit at TOGW at maximum angle of attack (Conventional BWB configuration)	CG_limit_calculator_Conv
CG_OEW_Cond1A_Jet	Double	Aft CG limit at OEW for full jet deflection down (Distributed propulsion BWB configuration)	jet_control
CG_OEW_Cond1B_Jet	Double	Forward CG limit at OEW for full jet deflection up (Distributed propulsion BWB configuration)	jet_control
CG_OEW_Cond2_Jet	Double	Forward CG limit at OEW at maximum angle of attack (Distributed propulsion BWB configuration)	jet_control
CG_OEWfuel_Cond1A_Jet	Double	Aft CG limit at OEW + Fuel weight for full jet deflection down (Distributed propulsion BWB configuration)	jet_control

CG_OEWfuel_Cond1B_Jet	Double	Forward CG limit at OEW + Fuel weight for full jet deflection up (Distributed propulsion BWB configuration)	jet_control
CG_OEWfuel_Cond2_Jet	Double	Forward CG limit at OEW + Fuel weight at maximum angle of attack (Distributed propulsion BWB configuration)	jet_control
CG_WZF_Cond1A_Jet	Double	Aft CG limit at WZF for full jet deflection down (Distributed propulsion BWB configuration)	jet_control
CG_WZF_Cond1B_Jet	Double	Forward CG limit at WZF for full jet deflection up (Distributed propulsion BWB configuration)	jet_control
CG_WZF_Cond2_Jet	Double	Forward CG limit at WZF at maximum angle of attack (Distributed propulsion BWB configuration)	jet_control
CG_TOGW_Cond1A_Jet	Double	Aft CG limit at TOGW for full jet deflection down (Distributed propulsion BWB configuration)	jet_control
CG_TOGW_Cond1B_Jet	Double	Forward CG limit at TOGW for full jet deflection up (Distributed propulsion BWB configuration)	jet_control
CG_TOGW_Cond2_Jet	Double	Forward CG limit at TOGW at maximum angle of attack (Distributed propulsion BWB configuration)	jet_control
Outputs			
CG_OEW_Cond1A	Double	Aft CG limit at OEW for full elevon/jet deflection down	CG_constraints
CG_OEW_Cond1B	Double	Forward CG limit at OEW for full elevon/jet deflection up	CG_constraints
CG_OEW_Cond2	Double	Forward CG limit at OEW at maximum angle of attack	CG_constraints
CG_OEWfuel_Cond1A	Double	Aft CG limit at OEW + Fuel weight for full elevon/jet deflection down	CG_constraints
CG_OEWfuel_Cond1B	Double	Forward CG limit at OEW + Fuel weight for full elevon/jet deflection up	CG_constraints
CG_OEWfuel_Cond2	Double	Forward CG limit at OEW + Fuel weight at maximum angle of attack	CG_constraints
CG_WZF_Cond1A	Double	Aft CG limit at WZF for full elevon/jet deflection down	CG_constraints
CG_WZF_Cond1B	Double	Forward CG limit at WZF for full elevon/jet deflection up	CG_constraints

CG_WZF_Cond2	Double	Forward CG limit at WZF at maximum angle of attack	CG_constraints
CG_TOGW_Cond1A	Double	Aft CG limit at TOGW for full elevon/jet deflection down	CG_constraints
CG_TOGW_Cond1B	Double	Forward CG limit at TOGW for full elevon/jet deflection up	CG_constraints
CG_TOGW_Cond2	Double	Forward CG limit at TOGW at maximum angle of attack	CG_constraints

CG_constraints

Variable	Type	Description	Linked to/from
Inputs			
OEW_CG	Double	Aircraft CG location at operational empty weight (ft)	balance
WZF_CG	Double	Aircraft CG location at zero fuel weight (ft)	balance
CG_nopay_fuel_in	Double	Aircraft CG when fuel is shifted inboard without any payload	balance
CG_nopay_fuel_out	Double	Aircraft CG when fuel is shifted outboard without any payload	balance
CG_TOGW_fuel_in	Double	Aircraft CG when fuel is shifted inboard at TOGW condition	balance
CG_TOGW_fuel_out	Double	Aircraft CG when fuel is shifted outboard at TOGW condition	balance
CG_OEW_Cond1A	Double	Aft CG limit at OEW for full elevon/jet deflection down	Control_constraints
CG_OEW_Cond1B	Double	Forward CG limit at OEW for full elevon/jet deflection up	Control_constraints
CG_OEW_Cond2	Double	Forward CG limit at OEW at maximum angle of attack	Control_constraints
CG_OEWfuel_Cond1A	Double	Aft CG limit at OEW + Fuel weight for full elevon/jet deflection down	Control_constraints
CG_OEWfuel_Cond1B	Double	Forward CG limit at OEW + Fuel weight for full elevon/jet deflection up	Control_constraints
CG_OEWfuel_Cond2	Double	Forward CG limit at OEW + Fuel weight at maximum angle of attack	Control_constraints
CG_WZF_Cond1A	Double	Aft CG limit at WZF for full elevon/jet deflection down	Control_constraints
CG_WZF_Cond1B	Double	Forward CG limit at WZF for full elevon/jet deflection up	Control_constraints
CG_WZF_Cond2	Double	Forward CG limit at WZF at maximum angle of attack	Control_constraints
CG_TOGW_Cond1A	Double	Aft CG limit at TOGW for full elevon/jet deflection down	Control_constraints

CG_TOGW_Cond1B	Double	Forward CG limit at TOGW for full elevon/jet deflection up	Control_constraints
CG_TOGW_Cond2	Double	Forward CG limit at TOGW at maximum angle of attack	Control_constraints
Outputs			
Con_OEW	Double	Longitudinal control constraint value at Operational empty weight	Constraints
Con_OEWfuel	Double	Longitudinal control constraint value at Operational empty weight + Fuel weight	Constraints
Con_WZF	Double	Longitudinal control constraint value at Zero fuel weight	Constraints
Con_TOGW	Double	Longitudinal control constraint value at Takeoff gross weight	Constraints

Constraints

Variable	Type	Description	Linked to/from
Inputs			
Chord(5)	Array Double	Array of chord lengths of the span stations (ft)	Design_Variables
eta(5)	Array Double	Array of semi-spanwise position of the span stations	Design_Variables
Sweep1	Double	Quarter chord sweep angle of the first wing section (deg)	Design_Variables
W_fuel	Double	Required fuel weight (lbs)	Design_Variables
BFL	Double	Balanced Field Length (ft)	Field
v_approach	Double	Approach velocity (knots)	Field
Landing_dist	Double	Landing distance (ft)	Field
gamma	Double	Second segment climb gradient	Field
gamma_ma	Double	Missed approach climb gradient	Field
Range_calc	Double	Calculated range (nmi)	Performance
Cabin_area	Double	Passenger cabin area (ft^2)	Geometry_parameters
tank_cap	Double	Fuel tank capacity (lbs)	Fuel_Distribution
BFL_max	Double	Maximum balanced field length (ft)	Constraint_Limits
v_approach_max	Double	Maximum approach velocity (knots)	Constraint_Limits
gamma_min	Double	Minimum second segment climb gradient	Constraint_Limits
gamma_ma_min	Double	Minimum missed approach climb gradient	Constraint_Limits
Range	Double	Minimum range (nmi)	Constraint_Limits
Cabin_area_min	Double	Minimum cabin area (ft^2)	Constraint_Limits
Root_thick	Double	Passenger cabin height at the first span station (ft)	Geometry_parameters

Root_thick_min	Double	Minimum cabin height at the first span station(ft)	Constraint_Limits
thick2	Double	Passenger cabin height at the second span station (ft)	Geometry_parameters
thick2_min	Double	Minimum cabin height at the second span station (ft)	Constraint_Limits
thick3	Double	Passenger cabin height at the third span station (ft)	Geometry_parameters
thick3_min	Double	Minimum cabin height at the third span station (ft)	Constraint_Limits
ROC	Double	Calculated top of climb rate of climb (ft/s)	Performance
ROC_min	Double	Minimum top of climb rate of climb (ft/s)	Constraint_Limits
Cl_sect_max	Double	Maximum sectional lift coefficient	Aerodynamics
Cl_sect_max_lim	Double	Maximum sectional lift coefficient limit	Constraint_Limits
Span	Double	Aircraft span (ft)	Design_Variables
Cabin_AR_min	Double	Minimum passenger cabin aspect ratio	Constraint_Limits
Con_OEW	Double	Longitudinal control constraint value at Operational empty weight	Control_constraints
Con_WZF	Double	Longitudinal control constraint value at Operational empty weight + Fuel weight	Control_constraints
Con_OEWfuel	Double	Longitudinal control constraint value at Zero fuel weight	Control_constraints
Con_TOGW	Double	Longitudinal control constraint value at Takeoff gross weight	Control_constraints
Outputs			
Fuel_vol_con	Double	Fuel volume constraint value	Optimizer
BFL_con	Double	Balanced Field length constraint value	Optimizer
Landing_dist_con	Double	Landing distance constraint value	Optimizer
gamma_con	Double	Second segment climb gradient constraint value	Optimizer
gamma_ma_con	Double	Missed approach second segment climb gradient constraint value	Optimizer
Range_con	Double	Range constraint value	Optimizer
Cabin_area_con	Double	Cabin area constraint value	Optimizer
v_approach_con	Double	Approach velocity constraint value	Optimizer
Root_thick_con	Double	Cabin height at the first span station constraint value	Optimizer
thick2_con	Double	Cabin height at the second span station constraint value	Optimizer
thick3_con	Double	Cabin height at the third span station constraint value	Optimizer
ROC_con	Double	Top of climb rate of climb constraint value	Optimizer
Max_Cl_sect_con	Double	Maximum sectional lift coefficient constraint value	Optimizer

Cabin_AR_con	Double	Cabin aspect ratio constraint value	Optimizer
SC_con1	Double	Longitudinal control constraint value at Operational empty weight	Optimizer
SC_con2	Double	Longitudinal control constraint value at Operational empty weight + Fuel weight	Optimizer
SC_con3	Double	Longitudinal control constraint value at Zero fuel weight	Optimizer
SC_con4	Double	Longitudinal control constraint value at Takeoff gross weight	Optimizer
Sweep1_con	Double	Quarter-chord sweep at the first wing section constraint value	Optimizer
Cabin_AR	Double	Cabin aspect ratio	

Constraint_Limits

Variable	Type	Description	Linked to
BFL_max	Double	Maximum balanced field length (ft)	Constraints
v_approach_max	Double	Maximum approach velocity (knots)	Constraints
gamma_min	Double	Minimum second segment climb gradient	Constraints
gamma_ma_min	Double	Minimum missed approach climb gradient	Constraints
Range	Double	Minimum range (nmi)	Constraints
Cabin_area_min	Double	Minimum cabin area (ft^2)	Constraints
Root_thick_min	Double	Minimum cabin height at the first span station(ft)	Constraints
thick2_min	Double	Minimum cabin height at the second span station (ft)	Constraints
thick3_min	Double	Minimum cabin height at the third span station (ft)	Constraints
ROC_min	Double	Minimum top of climb rate of climb (ft/s)	Constraints
Cl_sect_max_lim	Double	Maximum sectional lift coefficient limit	Constraints
Cabin_AR_min	Double	Minimum passenger cabin aspect ratio	Constraints

Optimizer setup

The following table gives the optimizer setup, documenting the objective function, constraints and design variables for the distributed propulsion BWB MDO program.

Inputs			
Variable	**Type**	**Description**	**Linked from**
TOGW	Double	Calculated takeoff gross weight (lbs)	Weights

Constraints				
Variable	**Description**	**Lower Bound**	**Upper Bound**	**Linked from**
Range_con	Range constraint		0	Constraints
Fuel_vol_con	Fuel volume constraint		0	Constraints
BFL_con	Balanced Field Length constraint		0	Constraints
Landing_dist_con	Landing distance constraint		0	Constraints
gamma_con	Second segment climb gradient constraint		0	Constraints
gamma_ma_con	Missed approach climb gradient constraint		0	Constraints
Cabin_area_con	Cabin area constraint		0	Constraints
Cabin_AR_con	Cabin aspect ratio constraint		0	Constraints
v_approach_con	Approach velocity constraint		0	Constraints
Root_thick_con	Cabin height at first span station constraint		0	Constraints
thick2_con	Cabin height at second span station constraint		0	Constraints
thick3_con	Cabin height at third span station constraint		0	Constraints
Max_Cl_sect_con	Maximum sectional lift coefficient constraint		0	Constraints
SC_con1	Longitudinal control constraint at OEW		0	Constraints
SC_con2	Longitudinal control constraint at OEW + Fuel weight		0	Constraints
SC_con3	Longitudinal control constraint value at Zero fuel weight		0	Constraints
SC_con4	Longitudinal control constraint value at Takeoff gross weight		0	Constraints
Sweep1_con	Quarter chord sweep angle at the first wing section		0	Constraints
Design Variables				
Chord1_fact	Normalized chord length at first span station	0.3	2.0	DV_Normalizer
Chord2_fact	Normalized chord length at second span station	0.3	2.0	DV_Normalizer
Chord3_fact	Normalized chord length at third span station	0.3	2.0	DV_Normalizer
Chord4_fact	Normalized chord length at fourth span station	0.3	2.0	DV_Normalizer
Chord5_fact	Normalized chord length at fifth span station	0.1	2.0	DV_Normalizer
SweepTE1_fact	Normalized railing edge sweep angle at the first wing section	-3.0	0.0	DV_Normalizer
Sweep2_fact	Normalized quarter chord sweep angle at the second wing section	0	2.0	DV_Normalizer

Sweep3_fact	Normalized quarter chord sweep angle at the third wing section	0	2.0	DV_Normalizer
Sweep4_fact	Normalized quarter chord sweep angle at the fourth wing section	0	2.0	DV_Normalizer
Span_fact	Normalized aircraft span	0.1	2.0	DV_Normalizer
Fact_thrust	Normalized thrust per engine	0.1	2.0	DV_Normalizer
Fact_fuel	Normalized required fuel weight	0.5	2.0	DV_Normalizer
Fact_altitude	Normalized average cruise altitude	0.5	2.0	DV_Normalizer
eta2_fact	Normalized semi-span position of the second span station	0.01	0.19	DV_Normalizer
eta3_fact	Normalized semi-span position of the third span station	0.2	0.4	DV_Normalizer
eta4_fact	Normalized semi-span position of the fourth span station	0.45	0.99	DV_Normalizer
tc1_fact	Normalized *t/c* ratio at the first span station	0.5	2.0	DV_Normalizer
tc2_fact	Normalized *t/c* ratio at the second span station	0.5	2.0	DV_Normalizer
tc3_fact	Normalized *t/c* ratio at the first third station	0.5	2.0	DV_Normalizer
tc4_fact	Normalized *t/c* ratio at the first fourth station	0.5	2.0	DV_Normalizer
tc5_fact	Normalized *t/c* ratio at the first fifth station	0.5	2.0	DV_Normalizer

Vita

Yan-Yee Andy Ko was born on August 31, 1975 in Petaling Jaya, Malaysia. He grew up in Cameron Highlands with his parents, Wing-Wah and Geok-Lan, and his older sister, Sharon. At the age of 16, he moved to Singapore, to attend Victoria School, and later, Victoria Junior College, earning his General Cambridge Examination (GCE) “O” and “A” Level certificates. In 1995, he began his Bachelor’s degree at Mississippi State University in the United States. He graduated Summa Cum Laude in May of 1998, earning a Bachelor of Science degree in Aerospace Engineering. During his time at Mississippi State University, he worked part-time at the Raspet Flight Laboratories, doing research into robotics and ultrasonic non-destrictive testing. In August of 1998, he joined the Multidisciplinary Analysis and Design (MAD) Center at Virginia Tech as a graduate student. He obtained his M.S. degree in the Fall of 2000, investigating the design of a strut-braced wing transonic transport aircraft. Upon completion of his doctoral studies, he will be working as a volunteer science and mathematics teacher at the Blacksburg Christian School for one year. He is married to Teresa Edwards Ko since November 2001.